Flapping Wing Micro Air Vehicles: An Analysis of the Importance of the Mass of the Wings to Flight Dynamics, Stability, and Control

by

Christopher T. Orlowski

A dissertation submitted in partial fulfillment
of the requirements for the degree of
Doctor of Philosophy
(Aerospace Engineering)
in The University of Michigan
2011

Doctoral Committee:

Assistant Professor Anouck R. Girard, Chair
Professor Semyon M. Meerkov, Cognate Member
Professor Luis P. Bernal
Professor Pierre T. Kabamba
Professor Wei Shyy

For my mother, who gave me my love of numbers.

For my father, who always stressed the importance of school.

For my grandfather, who gave me the love for engineering.

For my boys, you are my greatest accomplishments.

ACKNOWLEDGEMENTS

The dissertation could not have been completed without the exceptional guidance of my advisor, Assistant Professor Anouck Girard. Prof. Girard provided the guidance and intent to successfully execute research and add to the body of engineering knowledge. She allowed me to execute in the way I have been trained as an Army Officer. Prof. Girard is one of the best supervisors that I have ever had the pleasure of working for and am honored to have worked with her over the past three years. Professor Wei Shyy provided exceptional guidance into flapping wing fliers during the early phases of the research and provided the initial concept for the flight dynamics model. Prof. Shyy's guidance and instruction not only allowed me to grow as a student, but will benefit me in the Army as well.

Thanks as well to the other members of my dissertation committee, Professor Luis Bernal, Professor Pierre Kabamba, and Professor Semyon Meerkov, who provided excellent insight and guidance during the research process. Thanks to Professor Emeritus Donald Greenwood and Dr. Michael Bolender, from the United States Air Force Research Lab at Wright-Patterson AFB, for assistance with the development of the flight dynamics model. Special thanks to the many colleagues and peers who let me bounce ideas off them at any time, even when they were busy with their own work. The list is long, but Justin 'Jack' Jackson, Tony D'Amato, Baro Hyun, Zahid Hasan, Johnhenri Richardson, and Kurt Swieringa deserve special mention. Special thanks are also due to Dr. Hikaru Aono, Dr. Pat Trizila, Dr. Chang-Kwon Kang, and Dr. Abhijit Gogulapti for enhancing my understanding of flapping wing aerodynamics.

Finally, and most importantly, thanks to my wonderful wife, Eva. I could have not completed the dissertation without her love, support, and understanding.

TABLE OF CONTENTS

LIST OF FIGURES

Figure

LIST OF TABLES

Table

LIST OF APPENDICES

Appendix

ABSTRACT

Flapping Wing Micro Air Vehicles: An Analysis of the Importance of the Mass of the Wings to Flight Dynamics, Stability, and Control

by

Christopher T. Orlowski

Chair: Anouck R. Girard

The flight dynamics, stability, and control of a model flapping wing micro air vehicle are analyzed with a focus on the inertial and mass effects of the wings on the position and orientation of the body. A multi-body, flight dynamics model is derived from first principles. The multi-body model predicts significant differences in the position and orientation of the flapping wing micro air vehicle, when compared to a flight dynamics model based on the standard aircraft, or six degree of freedom, equations of motion. The strongly coupled, multi-body equations of motion are transformed into first order form using an approximate inverse and appropriate assumptions. Local (naïve) averaging of the first order system does not produce an accurate result and a new approximation technique named 'quarter-cycle' averaging is proposed. The technique is effective in reducing the error by at least an order of magnitude for three reference flight conditions. A stability analysis of the local averaged equations of motions, in the vicinity of a hover condition, produces a modal structure consist with the most common vertical takeoff or landing structure and independent stability analyses of the linearized flight dynamics of insect models. The inclusion of the wing

effects produces a non-negligible change in the linear stability of a hawkmoth-sized model. The hovering solution is shown, under proper control, to produce a limit cycle. The control input to achieve a limit cycle is different if the flight dynamics model includes the wing effects or does not include the wing effects. Improper control input application will not produce the desired limit cycle effects. A scaling analysis is used to analyze the relative importance of the mass of the wings, based on the quarter-cycle approximation. The conclusion of the scaling analysis is that the linear momentum effects of the wings are always important in terms of the inertial position of the flapping wing micro air vehicle. Above a flapping frequency of approximately 30-40 Hz, the mass and inertial effects of the wings on the orientation of the body can be neglected.

CHAPTER 1

Introduction

1.1 Introduction

For millions of years, man has been fascinated by flight. Over the past century, significant advances have been made in powered flight. Arguably, humans have pushed the technological boundaries of flight with the development of supersonic and rotary wing aircraft. Recent research efforts focus on increased efficiency, increased performance, and increased ability to evade radar. However, two areas of flight are still being explored at the boundary of flight regimes: the very small and the very fast. The focus of this work is the dynamics, stability, and control of the very small. The contribution of the dissertation will be an analysis, and the associated conclusions, on how important (or not important) the mass of the wings of flapping wing micro air vehicles is for dynamics, stability, and control studies.

The first step is the development of a multi-body flight dynamics model capable of replicating insect flight. The second step is the distillation of that model into first order equations of motion. The first order equations of motion are approximated in order to enable analysis of reference flight conditions (equilibrium conditions), stability derivatives, and limit cycles. The analyses of the limit cycles and stability derivatives naturally allow for the determination of when the wings are important. The analysis will focus on the mass of the wings as the key parameter. As a general

rule, the mass percentage of the wings of insects decreases, as total percentage of insect body mass, as the insects decrease in mass. Also, as a general rule, the flapping frequency of the wings of insects increases as the mass of the wing decreases. Therefore, it can be concluded that mass percentage of the wings of insects decreases as the flapping frequency of the wings increases.

Insect flight has evolved over millions of years. Current estimates place the number of insect species at over 10 million, with many of the species yet to be discovered [1]. The evolution of insects produced fliers that make adjustments to changing flight conditions within one wing stroke [2] or species that complete 180 degree turns in as little as three wing strokes [3]. The potential benefits for insect-like flapping wing micro air vehicles are numerous. The hovering ability of insects, coupled with the ability for a quick transition to forward flight, provide an ideal reconnaissance platform for search and rescue, law enforcement, and military efforts. The potential benefits of using insects as a model for flapping wing micro air vehicles (FWMAVs) has been covered extensively, especially by Ellington in [4]. Recent advances in flapping wing micro air vehicle technology have produced very capable fliers [5, 6, 7, 8, 9]. The ultimate goal is to make the aircraft autonomous with a limited payload. Arguably the best prototype is the Nano Hummingbird produced by Aerovironment under a DARPA contract [9]. However, the Nano Hummingbird is still remote controlled. In order for FWMAVs to be autonomous with a limited payload, the processing power dedicated to control calculations needs to be as minimal as possible. The wings may be important in this calculation. The first step towards determining how important is presented in the following material.

1.2 Insect Flight

The study of flapping wing micro air vehicles is not complete without the initial studies, largely produced by biologists, of insect flight. In nature, there are two general

types of flapping flight: bird flight and insect flight [10]. Bird flight, alternatively referred to as ornithopter flight, is generally defined by a main flapping motion of the wings with passive rotation of portions of the wing. The wings only have two degrees of freedom: the main flapping motion and slight deviation from the stroke plane defining the mean motion of the wing. Insect flight is defined by three degrees of freedom for each wing. The main motion of the wings is defined according to a stroke plane. The wing can actively pitch about the wing root and deviate from the stroke plane. The three degrees of freedom of the wing can be defined such the wing tip traces a figure-8 pattern with respect to the wing root. A lateral view of the stroke plane is represented in Figure 1.1. Insect flight is also defined by the wing 'flipping'

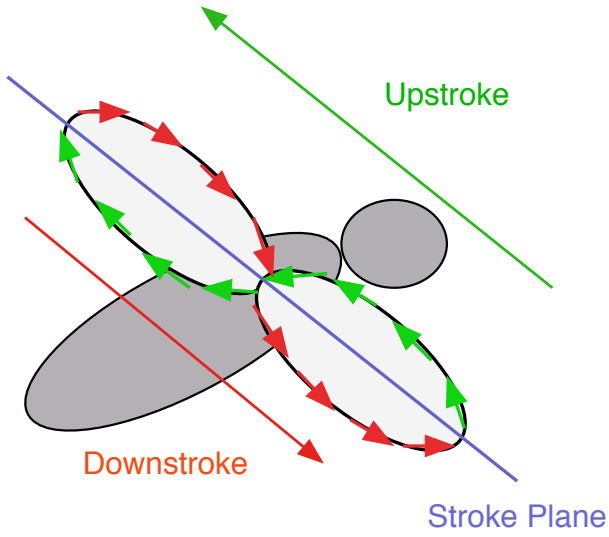

Figure 1.1: Insect Flight: Lateral View of Stroke Plane

during the wing stroke. The wing stroke is decomposed into two halves: the upstroke and downstroke. If the rotation of the wing occurs at the end of each half-stroke, then the rotation of the wings is coined 'normal rotation.' If the rotation of the wing occurs before the end of the half-stroke, after the mid-stroke, then the rotation is advanced. If the rotation occurs after the end of the half-stroke, but before the mid-stroke, then the rotation is delayed. The insect wing kinematics in this study will be

based on normal rotation. Even with normal rotation, there are two general types of insect wing kinematics: water treading and normal hovering. In normal hovering, the geometric pitch angle of the wing is a maximum at the mid-stroke and the wing has a geometric angle of attack of 90° at the end of each half-stroke. The normal hovering mode is illustrated in Figure 1.2. Water treading mode is defined by a maximum

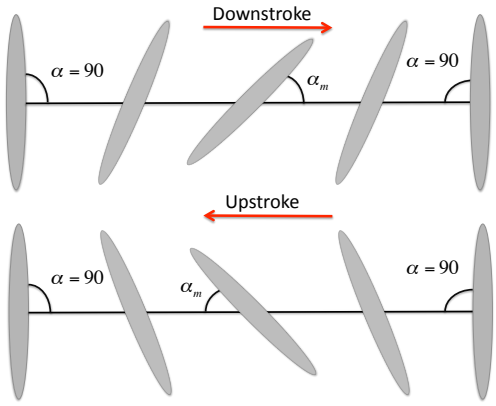

Figure 1.2: Normal Hovering Mode

geometric angle of attack at the mid-stroke and an angle of attack of zero at the end of each half-stroke. A depiction of the angle of attack in the stroke plane is shown in Figure 1.3. A detailed discussion of both modes is available in [10]. Other seminal literature on the biology of insect flight are books written by Dudley in [1], Vogel in [11], and Azuma in [12]. Insect flight is also described by Tennekes in [13].

Weis-Fogh published one of the first attempts to analyze the lift and power requirements of hovering animals in [14]. Weis-Fogh studied the hovering flight of hummingbird and insects in the *Drosophila* family. Weis-Fogh concluded that hovering flight could be explained by steady-state aerodynamics and that nonsteady effects, such as delayed stall and the Wagner effect, probably average out over the course of a flapping cycle. Weis-Fogh expanded the work to a wider range of insects in [15] and came to the same general conclusion in regards to steady-state aerodynamics. The

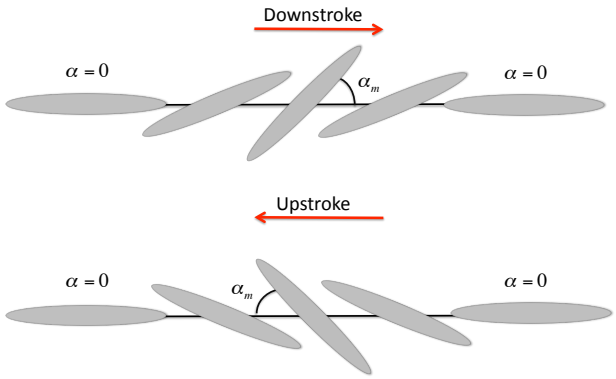

Figure 1.3: Water Treading Hovering Mode

conclusions made by Weis-Fogh are largely disproved by Ellington, in his seminal work in [2, 16, 17, 18, 19, 20]. Ellington claimed that Weis-Fogh's approximations in [14] and [15] were off by up to 30%. One of Ellington's key contributions is that the lift required for an insect cannot be explained by steady-state aerodynamics alone, The generation of lift must be aided by unsteady effects. Weis-Fogh discussed nonsteady effects, but did not consider them important for the majority of insects.

Ellington's seminal work was divided into six parts. The first section put forth a blade-element/quasi-steady theory for the aerodynamics of insect flight [2]. The blade-element/quasi-steady analysis assumes that each section of the wing sees steady flight according to classic aerodynamics theory. The effects are integrated over blade elements along the radial component of the wing. The total results are then used to analyze the lift and thrust generated by the motion of the insect wings. In the same work, Ellington also conducted a study of the morphological parameters of insects [16], the wing stroke kinematics in [17], and the unsteady aerodynamic mechanisms contributing to the lift generation of the wings in [18]. The lift produced by insects exceeded the predictions of classical aerodynamic theory and Ellington produced one of the first theories of the unsteady mechanisms contributing to insect flight in [19].

Finally, Ellington produced a work predicting the lift and power requirements of insect flight in [20].

The literature expanded after Ellington's six part work to other specific insect species, describing the lift and power requirements for various species, as well as the morphological parameters and wing kinematics. The morphological relationship between the wings and the body of insects is studied and published for various species, such as hawkmoths in [21, 22], dragonflies in [3, 23, 24], and bumblebees in [25, 26]. The wings of insects are generally less than 6% of their total body mass. For example, the mass of the wings of the desert locust *Schistocerca gregaria* is less than 4% of the total body mass [27]. In the study of hawkmoths by Willmott and Ellington, the wing mass of the specimens studied ranged between 4.8 and 5.8% [21]. Insects can flap their wings from approximately 10-26 Hz, for hawkmoths, to upwards of 200 Hz in fruitflies and bumblebees, and even higher for gnats and mosquitoes.

The initial work covering insect flight and theorizing on the lift and thrust generation naturally expanded into the field of aerodynamics. The theory put forth by Ellington in [19] included circulation effects into the calculation of the aerodynamic forces. Dickinson et al. added the effects of wing rotation in [28] to the aerodynamic knowledge of insects, which provided the basis for a blade-element/quasi-steady aerodynamic model presented in [29] and [30]. At this point in the wide research field, the unsteady mechanisms of insect flight are well understood. The effects include rapid pitch rotation, wake capture, delayed stall, vortex generation, and a passive pitching mechanism [31]. Comprehensive reviews of insect flight and progress in aerodynamic modeling are available from Sane in [32], Wang in [33], Ansari et al. in [34], and Shyy et al. in [10, 31, 35].

The aerodynamic models are generally divided into two areas: blade-element and computational fluid dynamics models. Numerous blade-element, and usually quasi-steady, models have been developed, with varying degrees of accuracy. Blade-element

aerodynamic models sacrifice accuracy and fidelity for speed, when compared to computational fluid dynamics models. Sane and Dickinson developed a blade-element model incorporating unsteady effects and added mass effects in [29] and [30]. Berman and Wang developed a blade-element aerodynamic model in [36] that produces quantitatively similar results to CFD results as presented in [37]. Other blade-element aerodynamic models include those developed by Doman et al. in [38] and Deng et al. in [39]. Arguably the most complex blade-element model is that developed by Ansari in [40, 41]. The Ansari model includes wake capture and vortex effects, but is computationally costly.

Recent aerodynamic efforts have focused on surrogate modeling, improved efficiency in calculations, and quantification of the flexibility effects of the wings in the generation of aerodynamic forces and moments. Surrogate modeling is presented by Trizila et al. in [42, 43]. Efforts to improve the efficiency of aerodynamics calculations is presented in [44]. Flexibility effects have been presented by Kang et al. in [45] and Gogulapti and Friedmann in [46]. The focus of the dissertation is for dynamics, stability, and control studies. All aerodynamic models are simplifications of the true physics, with varying degrees of fidelity. Blade-element/quasi-steady aerodynamic models will be used for computational efficiency and analytical tractability.

Research has also focused on the effects of the wings on flapping flight, specifically on the effects of the wing kinematics and wing geometry. The reported research areas have involved experimental and theoretical work into the determination of the effects of wing kinematics and geometry on the lift and thrust generation of flapping wings. Ansari et al. provide a comprehensive examination on the effects of wing kinematics in [47] and wing geometry in [48]. Khan and Agrawal calculate optimal wing kinematics using a robotic flapper in conjunction with an aerodynamic model in [49]. Chabalko et al. conduct a similar analysis to [49] by using CFD models in [50].

The following section will provide a comprehensive review of the studies involving

dynamics, stability, and control of flapping wing micro air vehicles. The literature review will set the basis for the contribution to the field of knowledge regarding the flight dynamics, stability, and control of flapping wing micro air vehicles. The review will be separated into three sections, covering dynamics, stability, and control studies.

1.3 Literature Review

It is generally impossible to distinguish between dynamics and stability studies of insects and flapping wing micro air vehicles. The dynamics and stability of flying systems are inherently tied together. However, the literature review will at least attempt to distinguish, with lines of grey, between those studies that are generated with a goal of determining stability or those developing a dynamic model for further study. Furthermore, the control analysis of insects, biomimetic vehicles, or flapping wing micro air vehicles cannot be conducted without the inclusion of a flight dynamics model. The dynamics will be addressed first, but the majority of the significant works are in the area of stability and control, to be discussed in Sections 1.3.2 and 1.3.3, respectively.

1.3.1 Dynamics Studies

From an extensive review, we discovered very few models of the flight dynamics of flapping wing micro air vehicles that treated the inertial/mass effects of the wings on the central body, and by extension, the entire system. Many of the dynamics models present in the literature focus on the standard aircraft model and neglect the inertial effects of the mass of the wings. The standard aircraft equations of motion, to included the linearized model resulting from small perturbation theory, is extensively developed in [51]. For example, Khan and Agrawal present the modeling and simulation of flapping wing micro air vehicles based on the standard aircraft model in [52]. Simulations are presented for a hover condition by utilizing a quasi-steady

aerodynamic model. The aerodynamic forces generated by the wings are transformed from the wing frames to the body frame by using 2-3-1 Euler angles, but the inertial effects of the wings are neglected. An aerodynamic model is developed, based on [29], that includes rotational and leading edge vortex effects. The coefficients for the aerodynamic model are determined from a robotic flapper. The wing dimensions from the robotic flapper and the mathematical model are used to present simulations of the FWMAV in a hover condition. Many of the uses of the standard aircraft model for flapping wing flight dynamics are tied to research areas conducting control research. For example, Duan and Li developed the flight dynamics model for an ornithopter in [53] for the purpose of attitude control.

In [54] and [55], Lasek and Sibilski and Buler et al., respectively, derive the equations of motion for a flapping wing micro air vehicle using the Gibbs-Appel Equations. The model developed by Lasek and Sibilski is one of the first multi-body models of flapping wing flight and is used to model ornithopters. Lasek and Sibilski develop a simulation architecture in [54] and limit the wings to two degrees of freedom: flapping and lagging. Alternatively, flapping is the deviation angle and lagging is the flapping (sweep) angle. The feathering, or pitch angle, remains fixed in the study. Buler et al. model a flapping wing micro air vehicle with two degrees of freedom for each wing: sweep in the stroke plane and an angle of attack relative to the stroke plane in [55]. The authors derived a flight dynamics model with six degrees of freedom for the central body and two holonomically constrained degrees of freedom for each wing, resulting in a system with 10 degrees of freedom. Buler et al. use the model to numerically calculate a Jacobian linearization of the system around a desired trajectory and present a linear quadratic regulator control solution to track the trajectory. In [56], Jackson et al. present a trajectory optimization problem for a flapping wing micro air vehicle. The FWMAV is modeled as a system of three bodies, but the central body is modeled as a point mass. The inertial effects of the wings are included,

but without the presence of a rigid body for the central body, the inertial coupling between the wings and the central body is not accounted for in the simulations and trajectory optimization problem.

In [57] and [58], Grauer and Hubbard derived the equations of motion of an ornithopter using the Boltzman-Hamel equations and five rigid bodies: one for the central body, one for each wing, and two determining the linkage for the tail. The work is motivated to provide control of a relatively larger vehicle; namely an ornithopter with a four foot wingspan. Each linked rigid body is allowed one degree of freedom. The angle of attack of the wings is due to passive rotation and a quasi-steady aerodynamic model is used for simulation efforts. Additionally, the equations of motion are transformed into a form found often in spacecraft and robotics control in order to allow for the integration of nonlinear control techniques. Grauer et al. have recently expanded the use of the model to the testing and system identification of an ornithopter in [59].

Bolender derived the equations of motion for a flapping wing micro air vehicle using Kane's Equations in [60]. The novel approach conducted by Bolender is to derive the equations of motion with four rigid bodies: a central body, a tail, and two wings. The tail is used for pitch control of the central body. Bolender includes the derivation of the inertial and active forces, necessary for Kane's equations, but limits the derivation of the wings. The wings are allotted two degrees of freedom, but the effects of the wings on the central body can be reconfigured through tilting of the stroke plane. The simulations presented in [60] are for the dynamic model with wing effects included and are simulated in an open loop fashion. Furthermore, the presented simulations include the motion of the tail. The equations show that without control, the magnitude of the pitch velocity of the central body steadily increases.

In [61], Gebert et al. derive the equations of motion for a flapping wing micro air vehicle using Newtonian methods, which requires the calculation of the constraint

forces between the wings and the body. The wings are not neglected, but simulations are not presented to validate the efforts. Furthermore, Sun et al. claim in [62] that the equations of motion derived in [61] contain errors and cannot be used. Dickson et al. present simulation efforts for a model insect based on *Drosophila* that includes the mass effects of the wings in [63] and [64]. The method chosen uses physics engine software, similar to that used to make video games and animated features, to model the wings and body. Simulations are presented using the physics engine. If equations of motion were developed, which may be important for the development of relevant control algorithms, the equations are not presented.

1.3.2 Stability Studies

The initial studies of the dynamics and stability of insect flight, and by extension flapping wing micro air vehicles, started with the analysis of the flight dynamics of specific insect species. The first formal analysis of the dynamic stability of insects, by Taylor and Thomas in [27], studied the dynamics of the desert locust *Schistocerca gregaria*. The mass of the wings, and the associated coupling terms, are neglected due to the assumption that the wings beat fast enough to not excite the rigid body modes of the central body. The stability derivatives are obtained from experimental methods and through the use of the standard aircraft equations of motion, available from [51]. The authors acknowledge that the linearized system may not be the best approximation of the flight behavior of the desert locust. Furthermore, the stability derivatives are not for an unperturbed system. The study is conducted on actual insects and the authors found it impossible to distinguish between the active and passive stability mechanisms of the desert locust. Taylor and Thomas state that the rigid body approximation is only valid if the wingbeat frequency is at least 10 times higher than the fastest rigid body mode. Furthermore, the authors conclude that a linear system may not be the best way to approximate an inherently nonlinear

system. Taylor et al. expand the work presented in [27] to nonlinear longitudinal dynamics of the desert locust in [65]. The authors present a combination of stability and control derivatives obtained from experiments. The derivatives are combined due to the inability to distinguish between active and passive stability in insects. The derivatives are then used for a nonlinear time-periodic (NLTP) model of the longitudinal dynamics. Both the linear and NLTP model neglect the mass effects of the wings and are longitudinal models only.

In [66], Sun and Xiong use the same rigid body approximation as in [27] to analyze the hovering flight stability of a bumblebee. The stability derivatives are obtained from computational fluid dynamics using flight data from [25]. The aerodynamic forces and moments are cycle-averaged; the resultant forces over one flapping cycle are used to determine the equilibrium flight condition in the vicinity of a hover condition. The analysis results in the determination that, based on the linearized system, the bumblebee has an unstable oscillatory mode for the longitudinal axis. In an open loop setting, the aerodynamic pitching moment destabilizes the longitudinal axis. Improper phasing between the pitching and flapping motion of the wings will enhance the destabilizing effects of the pitching moment.

Sun et al. expand the analysis presented in [66] to four additional insect species in [62]. The same methodology is used: coupling of the standard aircraft, rigid body equations of motion with aerodynamic derivatives calculated from computational fluid dynamics techniques. Sun et al. provided a justification for use of the standard aircraft equations of motion after presenting a Newton-Euler multi-body derivation of the equations of motion in [62]. The standard aircraft equations of motion are justified by assuming that either or the gyroscopic effects of the wings are small, compared to the body effects, or that the effects averaged over one flapping cycle are identically zero. The simulation model is used to determine the equilibrium solution for hovering for the four insect species: dronefly, cranefly, hoverfly, and hawkmoth.

The authors determine an eigenvalue modal structure identical to that of [66]. The modal structure has two stable subsidence modes, one fast and one slow, and one unstable, oscillatory mode. Sun et al. conclude that the rigid body approximation may not be accurate for the larger insect species studied (the cranefly and hawkmoth). Furthermore, Sun et al. conclude that the assumptions at the core of the analysis, namely that the effects of the wings are either small or time-average to zero, need to be validated with additional analysis.

Xiong and Sun continue the work presented in [66] and apply the methodology to forward flight for a bumblebee in [67]. The linear stability analysis is conducted at various forward flight speeds, ranging from 0 m/s to 4.5 m/s. The authors determined that at slow forward flight speeds of less than 1.0 m/s, the modal structure of the system matrix is qualitatively similar with the structure obtained in [62, 66]. At forward flight speeds of approximately 2.5 m/s, the modal structure for the longitudinal flight dynamics is approximately neutrally stable. The eigenvalues exist in two pairs and both are stable, although the magnitudes are close to the $j\omega$-axis and noted as marginally stable. As forward flight continues to increase, the modal structure switches back to the structure near hover. The final modal structure contains four real eigenvalues: two stable and two unstable. The results differ from those presented in [27]. In [27], the analysis predicted a modal structure identical to the hovering modal structure for even faster forward flight speeds. However, it is important to note that the studies are conducted for two separate insect species and used different methods for the determination of the aerodynamic derivatives.

The analysis used in [62, 66, 67] is expanded in [68] to allow for oscillations of the central body. Wu et al. present a method of obtaining the hover solution for two model insects, the dronefly and hawkmoth, by coupling the equations of motion with the Navier-Stokes equations. The work is significantly different from [62, 66] because the body is no longer assumed to be fixed. Wu et al. present a method of

solving the required parameters by using a 'shooting' method. The hover condition is solved for the longitudinal equations of motion; the lateral motion of the insect model is neglected. The results for the hover condition are qualitatively consistent with results obtained from biological studies of droneflies and hawkmoths. Although the derivation presented in [62] is mentioned, the hover solution is obtained while neglecting the coupling effects of the wings.

The validity of the assumptions made by Sun et al. in [62] is evaluated by Zhang and Sun in [69]. The validity of the assumptions is examined by comparing the solutions obtained in [62] for hovering using the approximate theory to the solutions obtained in [68]. Numerical simulations are presented that show, under the effects of the disturbances from the hover condition, that the models are close for three flapping cycles. The results are similar for the hawkmoth and the dronefly. Zhang and Sun conclude that due to the relatively low flapping frequency of the hawkmoth (26 Hz), the approximate model should be valid for all insects.

The results presented by Sun et al. in [62, 66, 67] are obtained independently, and using a different method, by Faruque and Humbert in [70]. In [70], Faruque and Humbert model an insect using the standard aircraft equations of motion and cycle-averaged forces and moments. The forces and moments are calculated using a quasi-steady/blade-element aerodynamic model, as opposed to the CFD aerodynamic model used in [66]. The system matrix and control inputs matrix, in vicinity of a hover condition, are obtained using frequency-based system identification techniques. Faruque and Humbert obtain the same modal structure as presented in [62] and [66] for an open loop system: two subsidence modes (one fast and one slow) and one unstable, oscillatory pair. With halteres providing sensing and feedback applied, the unstable oscillatory mode become stable. The stable modal structure is independently obtained by Gao et al. in [71]. Gao et al. conduct a numerical analysis of hawkmoth hovering using coupling of computational fluid dynamics with the standard aircraft

equations of motion. As opposed to the work presented in [66] and [70], Gao et al. do not assume simple sinusoidal motion for the wing stroke. Instead, actual wing kinematics from [21, 22] are used. The numerical analysis results in two subsidence modes, one fast and one slow, and a stable oscillatory mode. The stable oscillatory mode is small in magnitude and close to the $j\omega$-axis. The authors attribute the difference in the stability of the oscillatory mode to the choice of wing kinematics.

Faruque and Humbert expand their work to lateral stability, in the vicinity of hover, in [72]. Zhang and Sun present a similar approach to the analysis of the stability derivatives for lateral motion in [73]. The lateral stability derivatives are determined for the standard aircraft equations of motion, in the vicinity of a hover condition, using computational fluid dynamics. Zhang and Sun's analysis reveals three natural modes for the dronefly model: one unstable (fast) subsidence mode, one stable (slow) subsidence mode, and a stable (slow) oscillatory mode. Faruque and Humbert use the same techniques as outlined in [70]: a standard aircraft flight dynamics model, a quasi-steady aerodynamic model, and frequency based techniques to identify the stability derivatives. They explicitly include a passive damping term, as determined by Hedrick et al. in [74], named flapping counter torque (FCT). Faruque and Humbert determine the closed-loop lateral system to be stable with three natural modes: two subsidence modes, one fast and one slow, and one stable oscillatory mode. The difference in results between the two studies, a stable versus unstable system, may be due to the inclusion of the flapping counter torque by Faruque and Humbert.

Bolender examines the open loop stability of a flapping wing micro air vehicle in hover in [75]. The analysis is conducted by examining the orbital stability of the flapping wing micro air vehicle, due to the periodicity of the flapping wing system. The vehicle is modeled as a point mass with a quasi-steady, two-dimensional aerodynamic model transformed from the wing frames. The body of the flapping wing micro air vehicle is first modeled as a point mass and the stability analysis is conducted using

Floquet Theory. The calculation determines that the orbit of the point mass model is unstable. The analysis is also conducted with a multi-body model, with the central body modeled as a rigid body. The orbit for the multi-body model is also unstable.

The standard aircraft model is used to analyze the stability of the flight dynamics of an ornithopter by Dietl and Garcia in [76, 77, 78]. In [76, 77], the vehicle dynamics model is presented along with the aerodynamic model. Dietl and Garcia present the longitudinal dynamics, trim solutions and a limit cycle. The aerodynamic model used is developed in [36] and used throughout [76, 77, 78]. The longitudinal dynamics are decoupled from the lateral dynamics in the standard model. In [78], in addition to an analysis of the dynamics of the vehicle, control solutions are presented, based on the discrete-time eigenvalues resulting from the periodic solution. The periodic solution and stability analysis are conducted using Floquet Theory, as in [75]. The analysis of the dynamics neglects the inertial effects of the wings on the central body and limits the wings to bird-like flapping: one degree of freedom with passive rotation of the wings due to aerodynamic pressure on the wing.

The stability studies are summarized in Table 1.1. The stability studies have a general consensus. For both nonlinear and linear systems, in the absence of active control, flapping wing micro air vehicle models are unstable. The addition of active control can stabilize the system for linear systems, for both time-invariant and time-varying systems. The development of stabilization methods for nonlinear systems, both time-invariant and time-varying, will be discussed. The stabilization methods will be discussed in Section 1.3.3. For reference, 'LTV' in Table 1.1 is short for linear time-varying. 'NLTV' is short for nonlinear time-varying. The majority of the stability studies are for longitudinal flight. A flight system only has three degrees of freedom under the appropriate assumptions for longitudinal flight. The distinction has been made between longitudinal flight and full, six degree of freedom flight where applicable. The results in [70] and [72] are condensed into one entry. In actuality, the

stability analyses in [70, 72] produced two separate three degree of freedom models to analyze the linear stability of the six degree of freedom system in the vicinity of a hover condition.

Authors	Dynamics Model	Aero Model	Stability (type)	Flight Condition
Taylor and Thomas, 2003	Linear (3DOF)	Experimental	Unstable (open loop)	Forward Flight
Sun and Xiong, 2005 Sun et al., 2008	Linear (3DOF)	CFD	Unstable (open loop)	Hover (longitudinal)
Xiong and Sun, 2008	Linear (3DOF)	CFD	Unstable (open loop)	Forward Flight
Gao et al., 2009	Linear (3DOF)	CFD	Stable (open loop)	Hover (longitudinal)
Faruque and Humbert, 2010	Linear (6DOF)	Quasi-steady	Unstable (open) Stable (closed)	Hover
Zhang and Sun, 2009	Linear (6DOF)	CFD	Unstable (open loop)	Hover (lateral)
Bolender, 2010	NLTV (1DOF,3DOF)	Quasi-steady	Unstable (open loop)	Hover (longitudinal)
Dietl and Garcia, 2008	LTV (3DOF)	Quasi-steady	Unstable (open loop)	Hover (longitudinal)

Table 1.1: Summary Table of Stability Studies

1.3.3 Control Studies

In [38] and [79], Doman et al. present modeling and control of a flapping wing micro air vehicle based on the 'RoboFly' developed by Wood and presented in [80]. The aerodynamic model used in the simulations is developed in [38] and based on the work of Sane and Dickinson in [29] and [30]. The cycle-averaged aerodynamic forces and moments are presented in detail, along with calculation of the control derivatives based on the dynamic and aerodynamic models. The authors present a method of controlling the six degrees of freedom of the central body through the use of split-cycle frequency modulation and a bob-weight to control the pitch. Split-cycle frequency

modulation varies the frequency of the wing stroke during either the upstroke or downstroke. The result is asymmetric thrust forces and body moments, allowing for control of the system. The work is expanded on and presented in [81]. Doman et al. neglect the mass of the wings and their associated effects due to basing the work on the RoboFly, where the mass of the wings comprises less than 1% of the total vehicle mass. The work is expanded in [82, 83, 84] to include wing bias. The addition of wing bias increases the number of control inputs to four from the previous model using only split cycle frequency modulation. The wing bias changes the midpoint of the wingstroke and enables six degree of freedom control, without the bobweight as detailed in [79].

The research efforts into six degree of freedom control in [81, 84] are expanded to robust nonlinear control by Serrani et al. in [85, 86]. Serrani presents a method for the robust control of a 1-DOF flapping wing micro air vehicle in [85]. In [86], Serrani presents the robust control of a 3-DOF FWMAV. The flight dynamics model is based on the work by Bolender in [60], but restricted to the longitudinal plane. The control is achieved through the use of varying the wingbeat frequency and stroke plane angle. Through the use of decomposing the system dynamics into different time scales, the x and z position of the FWMAV can be controlled directly and the pitch attitude stabilized. Simulation results show the control is effective, by achieving the set point tracking command, in about 60 seconds. The solution is achieved by allowing the pitch angle to oscillate, but by stabilizing the oscillations so that they are bounded.

Deng et al. use the standard aircraft model and time-averaged forces and moments to derive a switching controller for a biomimetic insect in [87]. The controller is used, with success, to control the biomimetic insect in the vicinity of a hover condition. Schenato et al. present a controllability study of a biomimetic insect using the standard aircraft equations in [88]. In [39, 89], Deng, Schenato, et al. develop a mathematical model for the dynamics of a FWMAV. An aerodynamic model is

developed and based on the 'Robot Fly' experiments by Sane and Dickinson in [29] and [30]. The dynamics of the actuators are included, as well as the required sensors for effective flight. The wings are given three degrees of freedom, but parameterized into one single degree of freedom. The averaged dynamics and aerodynamic inputs are presented and used as a basis for controller and sensor design. Using averaging and linear quadratic regulator theory, a control strategy for ensuring proper stroke kinematics is presented resulting in good tracking of a reference flight condition.

Hu et al. develop a control mechanic in [90] based on the work of Deng, Schenato et al. in [39, 89]. Using four control inputs, the authors demonstrate control combinations that enable six degree of freedom control of a flapping wing micro air vehicle. The controls for each wing are flip-start timing, alternatively referred to as advanced or delayed rotation, and change in the mid-stroke angle of attack. The control mechanic developed in [90] is expanded to develop the control parameters in [91]. The choice of control is parameterized and the parameterized controls are coupled using random input choices and system identification techniques. The system identification produces a control input matrix and demonstrates the controllability of the system. Simulation results demonstrate successful control of the flapping wing micro air vehicle. The results are expanded in [92] to the use of time-periodic, feedback control to stabilize the attitude of a flapping wing micro air vehicle. Using the time-average forces and moments, as well as time-averaged dynamics, the controller is able to stabilize the system as long as the number of control inputs is equal to the numbers of degrees of freedom in the system. Hu et al. discuss controllability issues with flapping wing micro air vehicles in [93]. The effects of various choices of flip-start timing and mid-stroke angle of attack are evaluated. The mean forces and moments are detailed as a result of the various input choices.

Sun and Wang use the analysis from [66] to stabilize a hovering model insect in [94]. The stabilization is achieved on the linear time-invariant model using four controls:

change in stroke (flap) amplitude, change in stroke (flap) offset, an equal change in the angle of attack, and a differential change in the angle of attack. Xiong and Sun in [95] use the analysis presented in [66] and [67] to apply stabilization control to the linear, time-invariant models of bumblebee flight previously developed. Stabilization is applied to both hovering and forward flight. CFD models are used to calculated the control derivatives given the following set of control inputs: changes in the stroke (flap) amplitude, change in the mean stroke (flap) position with respect to the body, an equal change in the angle of attack, and a differential change in the angle of attack for each wing. The authors concluded that for the forward flight speeds presented in the study that the system is controllable and therefore using linear systems theory, the system is stable in the presence of active control. The control work is expanded by Wu and Sun in [96] to include determining the controls necessary, based on the linear models for both the system and control inputs, to transition from hovering to slow, forward flight speeds. Change in the mean stroke angles enables forward or backwards translation. An equal change in the stroke amplitude or angle of attack enables vertical flight. Coupling the two controls enables full, six degree of freedom flight.

Cheng and Deng present a derivation of the linear dynamics and control near hover in [97]. The wings are modeled with two degrees of freedom relative to the stroke plane, the deviation is neglected, and the body is modeled as three rigid body ellipsoids. The intent of the work is to mimic the flight of the fruit fly *Drosophila*. The effects of the change in angle of attack on the aerodynamic forces are neglected due to being in vicinity of a hover condition. The method develops estimations of the stability and control derivatives based on flapping-counter forces (FCFs) and flapping-counter torques (FCTs) presented in [74]. The control inputs are chosen to be an equal change in mean position of the left and right wings, differential change in stroke amplitudes, and differential change in stroke plane angle. The open loop system

is unstable and the system is stabilizable using proper choices of only proportional control, based on the chosen control inputs.

Rifaï et al. control a model flapping wing micro air vehicle using bounded, nonlinear state feedback in [98]. The dynamics model is based on the standard aircraft equations of motion with quaternions used to describe the orientation of the central body. Average forces and moments, as well as averaged dynamics, are used to compute the control law for the time-varying system. The developed controller is effective in bringing the flapping wing model to an equilibrium condition, under the presence of disturbances, from a significant initial condition. Humbert and Faruque expand the analysis presented in [70] to a reachability analysis in [99]. Faruque and Humbert demonstrate that controllability is achieved through the choice of two of the following control inputs: stroke plane, flapping offset (similar to wing bias), and change in the angle of attack between the upstroke and downstroke. For a proper choice of control inputs, the most effective choice is the combination of stroke plane changes and changes in the angle of attack between the upstroke and downstroke. Geder et al. present a model that includes the sensors and actuators in [100]. Control for hovering, forward flight, and turning maneuvers is achieved through the use of PID-control and an extended Kalman filter. Fuzzy neural networks have also been investigated for control schemes for flapping wing micro air vehicles. Guo et al. developed a neural network controller, in [101], that effectively stabilizes the position and orientation of a biomimetic robot, based on the work presented in [93]. Other control techniques include control through engineered central pattern generators in [102] and the evolution of analog neuromorphic devices in [103].

The control of insect-like flapping wing micro air vehicles is widely studied and continuing to expand. The significant control studies are summarized in Table 1.2. The following abbreviations, not previously defined, are relevant. 'DTLTI' stands for discrete-time linear time-invariant. 'LTI' stands for linear time-invariant. The

flapping amplitude input is shortened to 'flap amp' and angle of attack is shortened to 'AoA.' 'LQR' refers to linear quadratic regulator and 'LQG' refers to linear quadratic Gaussian. In regards to linear gains: 'P' is proportional, 'I' is integral, and 'D' is derivative.

Authors	Dynamics Model	Control	Technique	Inputs
Deng, Schenato et al., 2006	DTLTI (3DOF)	Linear	LQR/LQG	Flap amp. AoA
Doman et al., 2010	NLTV (6DOF)	Linear	Pseudo-inverse allocation	Split-cycle Wing bias
Serrani, 2010	NLTV (3DOF)	Nonlinear Robust	Time scale separation	Flap frequency Stroke plane
Sun et al., 2007 Xiong et al., 2009	LTI (3DOF)	Linear	Modal decomp. LQR	Flap and AoA Offset and Diff
Rifaï et al., 2008	NLTV (6DOF)	Nonlinear	Bounded Feedback	Flap amp. AoA
Cheng and Deng, 2010	LTI (3DOF)	Linear	Linear Gains: PD	Flap amp./bias Stroke plane
Geder et al., 2010	NLTV (6DOF)	Linear	Linear Gains: PID	Flap amp./bias Stroke plane

Table 1.2: Summary Table of Control Studies

None of the control results presented in Table 1.2 include the mass and inertia effects of the wings in the control algorithms. The robust control schemes developed by Rifaï, in [98], and Serrani, in [85, 86], may be able to handle to the mass of the wings. All of the control studies discussed are not only a wealth of knowledge for feasible control inputs, but control strategies as well.

1.4 Conclusions

The many dynamics models previously discussed in the literature review are summarized in Table 1.3. The dynamics of flapping wing micro air vehicles is widely stud-

Authors	Dynamics Model	Wing Effects	Aero-dynamics	Applicability
Taylor and Thomas, 2003	Linear	No	Experimental	Desert locusts
Sun and Xiong, 2005	Linear	No	CFD	Honeybees
Doman et al., 2009	6DOF	No	Blade-element	Robot Fly
Deng, Schenato et al., 2006	6DOF	No	Blade-element	Insects
Khan & Agrawal, 2005	6DOF	No	Blade-element	Insects
Loh & Cook, 2003	Multi-body	2 DOFs	Blade-element	Insects
Bolender, 2009	Multi-body	2 DOFs	Berman Wang	Insects
Sun et al., 2008	6DOF	No	Navier-Stokes	Insects
Buler et al., 2004	Multi-body	2 DOFs	Not specified	Ornithopters
Grauer et al., 2009	Multi-body	1 DOF	Blade-element	Ornithopters
Orlowski et al., 2011	Multi-body	3 DOFs	Blade-element	Insects

Table 1.3: Summary Table of Dynamics Models

ied from the aspect of a rigid body approximation. However, studying the multiple-body nonlinear system, with mass and inertia coupling effects from the wings, has not been widely reported. In [60], Bolender makes the claim that the effects of the wings need to be included for proper control studies. The aerodynamic models used by Doman and Oppenheimer in [81, 84] and by Deng, Schenato et al. in [39, 88, 89] are based on the experiments of Sane and Dicksinson in [29, 30]. The lift and drag coefficients used by Doman et al. are derived from model wing experiments in an oil tank. The model wing is based off of the common fruit fly, *Drosophila melanogaster*, but the wings are scaled to a semi-span of 25 *cm* and mean chord of 6.7 *cm*. Sane and Dickinson conducted their experiments at a Reynolds number of 115, whereas hawkmoths operate in a flow regime with a Reynolds number of approximately 6,000 - 8,000 [10, 21, 22]. The dynamics models derived by Taylor and Thomas in [27], Sun and Xiong in [66], and by Doman in [38, 82] are directly tied to the aerodynamics models presented in the papers. Especially in [27, 62, 66], the dynamic and aerodynamic results are specifically tied to the insect species presented in the specific studies.

In regards to the the other studies presented, the work is not tied to a specific aerodynamic model. The aerodynamic models are chosen as inputs. In [39, 88, 89], the control results are tied to the aerodynamic model, but the dynamics presentations allows for the implementation of different aerodynamic models. However, the presented results neglect the mass of the wings. The work by Lasek and Sibiliski in [54], Buler et al. in [55], and Grauer and Hubbard in [58] include the mass effects of the wings, but the formulation is limited to ornithopter flight and not true insect flight. Bolender, in [60], included the wing effects in the derivation and simulations, but the wings only have two degrees of freedom relative to the stroke plane. Shyy et al. state that the third degree of freedom, relative to the stroke plane, is important for the transition from hover to forward flight for insect-like flapping [10]. The results presented by Sun and Xiong in [62, 66, 67] are presented without the mass effects of the wings and the linear solutions are based upon the calculations performed using the Navier-Stokes equations. The aerodynamic model used is most likely more accurate, but the method is computationally expensive.

Throughout all of the previous references discussed, the work is presented for a single aerodynamic model and the effects of the mass of the wings is either included, or neglected. An analysis of how the wings may affect the central body is largely absent from the literature. Furthermore, since every aerodynamic model is an approximation (of varying degrees of fidelity) of the actual aerodynamic forces and moments generated by the wings, there has not been an attempt to quantify, or qualify, the effects of choosing a different aerodynamic model. The main issue is the availability of computationally efficient aerodynamic models for dynamics, control, and stability studies. The most accurate modeling of flapping wings is obtained from computational fluid dynamics methods, but to obtain data is computationally expensive. Tying these models to a dynamics model will further increase the computational time. Quasi-steady/blade-element models are computationally inexpensive, but their accuracy is

debatable. The model used for previous simulations, developed by Berman and Wang in [36], achieves decent accuracy for calculations when compared to the CFD efforts by Sun and Du in [37]. However, the point of this study is to determine the inertial effects of the wings on the dynamics of the central body for stability and control studies. A quasi-steady aerodynamic model will suffice. Specifically, the goal is to develop and analyze model that includes the inertial coupling effects of the wings on the central body, due to the continuous motion of the wings. The model must be able to replicate true insect flight with three degrees of freedom relative to a stroke plane. All effects of the wings on the body, and vice versa, are included in the derivation. None of the effects will be neglected or simplified.

Once the multi-body model is developed, it can be used to analyze the relative importance of the wings. In order to analyze the relative importance of the wings, the first order equations of motion needed to be obtained from the multi-body model. Once the first order equations of motion are determined, the equations of motion need to be properly approximated. Even in first order form, the equations of motion are quite complex and equilibrium (or reference flight) conditions are not immediately apparent. With proper approximation, the importance of the wings can be analyzed and included in dynamics and stability studies.

1.5 Original Contributions

- The derivation, from first principles, of a multi-body flight dynamics capable of modeling true insect flight. The flight dynamics model allows for three degrees of freedom relative to a stroke plane. The flight dynamics model is the only model in the literature with three degrees of freedom, the stroke plane, and multi-body dynamics. The multi-body flight dynamics model is capable of modeling configurations with two wings, two wings with a tail and/or a control mass, and four wings. The technique is easily expanded to configurations with

more wings.

- The multi-body, flight dynamics model is used to analyze the open loop effects of the mass and inertial effects of the wings on the position and orientation of the central body. The multi-body model predicts behavior different from the standard aircraft model for the same aerodynamic inputs. The differences in behavior manifest in both the position and orientation.

- The derivation of approximate first order equations of motion for flapping wing micro air vehicles. The first order equations of motion are approximated from the multi-body, flight dynamics model. The first order equations of motion can be written as the standard aircraft equations of motion plus perturbations of the wing mass. First order equations of motion, with the wing effects included, did not previously exist in the literature.

- The development of an approximation technique for a periodic system, in context of flapping wing micro air vehicles, coined quarter-cycle averaging. The new approximation technique is necessary due to the lack of an analytical solution for the standard aircraft equations of motion. The quarter-cycle techniques reduces the error in approximation by over an order of magnitude when compared to local (naïve) averaging.

- The development of an analytically tractable method of determining the stability derivatives for a flapping wing micro air vehicle in vicinity of a hover condition. The results are qualitatively consistent with independent numerical efforts.

- The development of a method for determining the relative importance of the wing mass effects on the position and orientation of a flapping wing model. The method predicts that the linear momentum effects are always important,

but the angular momentum effects can be neglected greater than a flapping frequency of approximately 30-40 Hz.

1.6 Dissertation Organization

The dissertation will start with the detailed derivation, from first principles, of the multi-body, flight dynamics model in Chapter 2. Certain portions of the derivation are presented in Appendix A to maintain a consistent flow. Chapter 2 will present a simulation comparison of the multi-body and the standard aircraft (6DOF) equations of motion in Section 2.5.2. The multi-body model is also used to show system behavior with different aerodynamic inputs (2.5.3) and decreasing wing mass for a fixed body mass (2.5.4). Chapter 3 presents a derivation of the first order equations of motion for the multi-body dynamics, with certain details presented in Appendices B and C. The first order equations of motion derived in Chapter 3 are approximated using local averaging and a new approximation technique coined 'quarter-cycle' averaging in Section 3.4. The quarter-cycle averaging techniques are presented for three reference flight conditions: hovering flight (3.4.1), forward flight (3.4.2), and vertical flight (3.4.3).

The equations of motion and approximation techniques developed in Chapters 2 and 3 will be used to evaluate the stability and limit cycles of the multi-body, flapping wing micro air vehicle system in Chapter 4. An analytically tractable method for obtaining the stability derivatives of a flapping wing micro air vehicle in the vicinity of a hover condition will be presented in Section 4.2. The stability results will be presented for models with and without wing effects. Linear and nonlinear control analysis in the vicinity of a hover condition, to include limit cycle conditions, will be presented in Sections 4.4 and 4.5. Finally, Chapter 5 will present scaling relationships that examine the relative importance of the wings. Chapter 5 will include an analysis of certain scaling relationships for insects and application of the

scaling relationships to the linear and angular momentum effects of the wings on the position and orientation of the body.

CHAPTER 2

Multi-Body Dynamics for Insect-like Flapping Wing Micro Air Vehicles

2.1 Introduction

As detailed in Chapter 1, the majority of the reported studies regarding the dynamics and stability of flapping wing micro air vehicles neglect the mass of the wings and their associated coupling effects. Various multi-body models have been developed, but all of the models lack, to a certain degree, the desired flexibility for the analysis of an insect-like, flapping wing micro air vehicle. The models developed by Lasek and Sibilski in [54], Buler et al. in [55], and Grauer and Hubbard in [57, 58] are based on ornithopter models. The multi-body models developed by Loh and Cook in [104] and Bolender in [60] allow for only two degrees of freedom of the wings, relative to the stroke plane. The third degree of freedom, the deviation angle, is important for the transition from hovering to forward flight [10]. Furthermore, the derivation in [104] is lacking the majority of the pertinent details.

The inclusion of three degrees of freedom relative to the stroke plane is not a new development. The work is previously presented in [52], but the flight dynamic model development is limited to the transformation of forces from the wing frames and does not include multi-body considerations. Gebert et al. in [61] and Sun et

al. in [62] develop multi-body models with three degrees of freedom for each wing. However, the models are developed with Newton-Euler techniques. Some of the required implementation details are not presented in [61] and [62]. Furthermore, the use of Newton-Euler requires the calculation of the constraint forces between two bodies, which is quite cumbersome given bodies in continuous motion. The following derivation will present a multi-body, flight dynamics model for a flapping wing micro air vehicle that includes three degrees of freedom for each wing relative to the stroke plane. The model will enable the study of the flight dynamics of insect-like flapping micro air vehicles and a determination of the (relative) importance of the inertial coupling effects of the wings on the position and orientation of the vehicle.

2.2 Derivation of the Equations of Motion

2.2.1 Method

The derivation of a dynamic model that encompasses the mass and inertial effects of the wings, as well as allowing three degrees of freedom for the wings relative to the stroke plane, is now presented. The method chosen for the derivation is D'Alembert's Principle for Multiple Rigid Bodies, alternatively presented as the 'general form of the equations of motion for multiple rigid bodies' in [105]. The derivation method is presented in [105, 106, 107]. The chosen method is a hybrid of Euler and Lagrange techniques and is akin to Kane's Equations and the Gibbs-Appel Equations [107]. The flight dynamics model to be developed is presented in [108, 109, 110, 111]. The main equation, governing the derivation, is:

$$\sum_{i=1}^{n} \left[\dot{\mathbf{p}}_i \cdot \bar{\gamma}_{\mathbf{ij}} + \left(\dot{\mathbf{H}}_i + m_i \bar{\rho}_{\mathbf{ci}} \times \dot{\mathbf{v}}_i \right) \cdot \bar{\beta}_{\mathbf{ij}} \right] = Q_j, \tag{2.1}$$

where i denotes the number of rigid bodies and j denotes the number of generalized coordinates (with associated quasi-velocities). In Equation (2.1), linear momentum is

defined as $\bar{\mathbf{p}}_i$ and angular momentum is $\bar{\mathbf{H}}_i$. For completeness, the linear momentum rate and angular momentum rate of the ith rigid body are defined as

$$\dot{\bar{\mathbf{p}}}_i = m_i \left(\dot{\bar{\mathbf{v}}} + \dot{\bar{\rho}}_{ci} \right) \quad \text{and} \quad \dot{\bar{\mathbf{H}}}_i = \mathbf{I_i} \cdot \dot{\bar{\omega}}_\mathbf{i} + \bar{\omega}_\mathbf{i} \times \mathbf{I_i} \cdot \bar{\omega}_\mathbf{i}. \tag{2.2}$$

The method has a few main advantages. One, since the principle of virtual work is used to calculate the forces and moments for each generalized coordinate, the constraint forces between the wing and the central body are neglected, as constraint forces do not perform virtual work. Two, the method allows for the choice of reference points for the velocity of each body. The wings are assumed to be attached to the central body by joints that allow three degrees of freedom. To simplify the derivation, and eliminate the need for tracking the absolute velocity and acceleration of the wings in an inertial frame, the velocity reference points for the wings are chosen to be the respective wing joints. Finally, the inertia tensor for the individual bodies is calculated with respect to the reference point and does not need to be calculated at the time-varying center of mass of the system.

2.2.2 Reference Frames

In order to accurately describe the motion of the body with respect to an inertial frame, and the motion of the wings with respect to the body, six reference frames are required. The first reference frame is an inertial (fixed) frame. The absolute velocity and position of the flapping wing micro air vehicle (FWMAV) are described with respect to the inertial frame. The B frame is a body-fixed frame attached to the body (fuselage) of the FWMAV with origin at the center of mass of the body. The B frame is depicted in Fig. 2.1a. The frame is oriented with positive x-axis along the longitudinal axis of the central body. The y-axis is perpendicular to the x-axis and is positive out of the right side of the vehicle. The z-axis is positive downward and

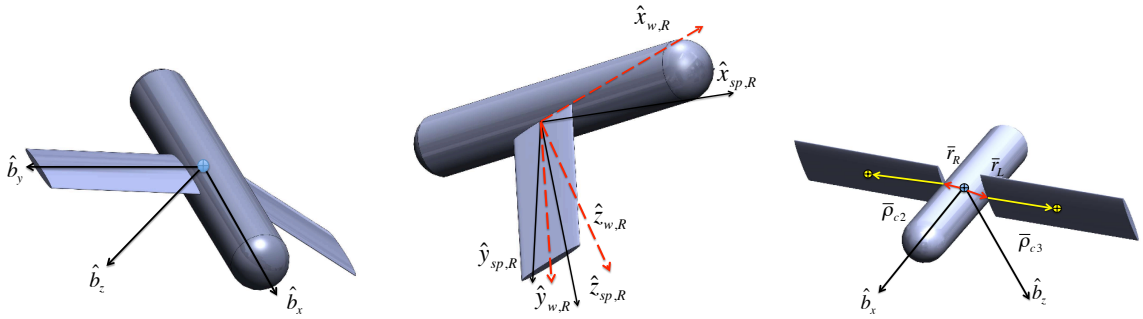

(a) B Frame

(b) Right Stroke Plane and Wing Frames

(c) Reference Vectors

Figure 2.1: Model Representation with Reference Frames and Reference Vectors

perpendicular to the $x-y$ plane. The unit vectors of the B frame are denoted by $\hat{b}_x, \hat{b}_y$, and $\hat{b}_z$. An $x-z$ plane of mass symmetry is assumed for the body. In addition to the B frame, the stroke plane frames are two body fixed-frames originated at the wing joints. The stroke plane frames are denoted by R_{sp} and L_{sp} and have initial orientation parallel to the B frame. The orientation is rotated by an angle β about the $\hat{b}_y$-axis of the B frame to the stroke plane. The stroke plane defines the mean motion of the wing. The stroke plane angle defines the orientation of the stroke plane relative to the longitudinal axis of the central body. The y-axis of the stroke plane frames will always remain parallel to the B frame. The x and z axes of R_{sp} and L_{sp} will be rotated by the fixed angles β_R and β_L. The last two frames are fixed frames attached to the wings. The initial orientation of the wing frames is parallel to the stroke plane frames with an origin coincident with the wing joint. The wing frames, R_w and L_w, move with the rotation of the wings and enable the calculation of the wings' orientations with respect to the stroke plane, and by extension, the central body. The right stroke plane frame and wing frame are depicted in Fig. 2.1b. The stroke plane frame is represented by solid lines and unit vectors with the subscript sp, R. The wing frame is represented by dashed lines and unit vectors with the subscript w, R.

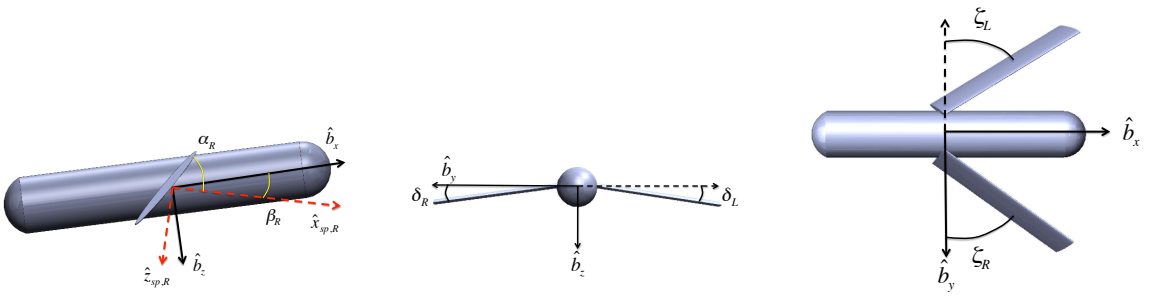

(a) α_R and β_R (b) δ_R and δ_L (c) ζ_R and ζ_L

Figure 2.2: Wing Angles and Stroke Plane Angles

2.2.2.1 Orientation

The orientation of the central body is determined by 3-2-1 Euler angles with respect to the inertial (fixed) frame. The nomenclature for the angles is consistent with the NASA standard for aircraft [107]. The orientation of the stroke plane with respect to the body is denoted by the angles β_R and β_L and is fixed for a given flight condition. The stroke plane is defined relative to the longitudinal axis of the body and not an inertial (fixed) frame, as is the common practice in the biology literature. The orientation of the wings with respect to the stroke plane is determined by the deviation, pitch, and flap angles of the wings. The wing angles are δ, α, and ζ. The stroke plane angle and angle of attack are shown in Fig. 2.2a. A common, although not completely accepted, nomenclature choice for the deviation (elevation) and flap (sweep) angles are θ and ϕ, respectively. Here, δ is chosen for the deviation angle and ζ is chosen for the sweep angle to avoid confusion with the pitch and roll angles of the central body. The relation of the δ and ζ angles to the central body are shown in Figs. 2.2b and 2.2c.

Positive rotations are consistent with the right hand rule. A positive angle of attack is 'up' in the stroke plane frame. A positive deviation (elevation) angle is down and a positive flap (sweep) angle is forward. The kinematics of the wings, usually sinusoidal functions to be discussed later, will always be set so that positive motion is 'forward' and 'down.'

2.2.2.2 Rotation Matrices

The rotation matrix from the inertial frame to the body frame, $\mathbf{R}_B$, is determined by proper combination of the 3-2-1 Euler angles. The standard combination can be found in [51] and [107]. The rotation matrix from the body to the stroke plane frame is

$$\mathbf{R}_\beta = \begin{bmatrix} \cos\beta & 0 & -\sin\beta \\ 0 & 1 & 0 \\ \sin\beta & 0 & \cos\beta \end{bmatrix}, \tag{2.3}$$

where β_R and β_L are substituted for the proper stroke plane frame. The orientation for the right and left wings with respect to the R_{sp} and L_{sp} frames is determined by the 3-1-2 Euler angles, where $\zeta = 3$, $\alpha = 2$, and $\delta = 1$. The choice of 3-1-2 Euler angles matches the requirements of the system in a physical sense. For example, the radial position of a point on the wing can be tracked in the stroke plane frame using spherical coordinates with the angles ζ and δ (please see Equation (A.4)). The choice of 3-1-2 Euler angles gives spherical coordinates for a radial (y) position of the wing when transformed from the wing frame to the stroke plane frame. The singularity for 3-1-2 Euler angles, using the chosen nomenclature, is at $\delta = \pm\frac{\pi}{2}$ and will not be reached by the wing stroke kinematics. The rotation matrices for the right wing are

$$\mathbf{R}_{\delta_R} = \begin{bmatrix} 1 & 0 & 0 \\ 0 & \cos\delta_R & \sin\delta_R \\ 0 & -\sin\delta_R & \cos\delta_R \end{bmatrix}, \mathbf{R}_{\alpha_R} = \begin{bmatrix} \cos\alpha_R & 0 & -\sin\alpha_R \\ 0 & 1 & 0 \\ \sin\alpha_R & 0 & \cos\alpha_R \end{bmatrix},$$

and

$$\mathbf{R}_{\zeta_R} = \begin{bmatrix} \cos\zeta_R & -\sin\zeta_R & 0 \\ \sin\zeta_R & \cos\zeta_R & 0 \\ 0 & 0 & 1 \end{bmatrix}. \tag{2.4}$$

The rotation matrices are combined according to

$$\mathbf{R}_R = \mathbf{R}_{\alpha_R}\mathbf{R}_{\delta_R}\mathbf{R}_{\zeta_R}. \tag{2.5}$$

The rotation matrices for the left wing, with respect to the left stroke plane, are combined in the same manner as in Equation (2.5). The rotation matrices for the left wing are presented in Equation (A.1). The negative signs for the rotation matrices for the ζ and δ angles are interchanged for the right and left wings. The sign change is due to the fact that 'positive' motion of the wings is forward, which is a positive rotation for the left wing by the angle ζ_L, but a negative rotation for the right wing by the angle ζ_R. Likewise, 'positive' downward motion is a positive rotation of the angle δ_R for the right wing, but a negative rotation by the angle δ_L for the left wing. The correct sign ensures proper cancellation of forces and moments in the B frame when the flapping is symmetrical, which will be discussed in Section 2.2.7.

2.2.3 Generalized Coordinates

A flapping wing micro air vehicle truly only has six degrees of freedom: the three translational and rotational degrees of freedom of the central body. However, each of the wings has three holonomically constrained degrees of freedom relative to the central body. Combining the six true degrees of freedom and six holonomically constrained degrees of freedom, we can view the system as having twelve independent degrees of freedom [54, 55, 106]. As a result, we need twelve generalized coordinates to accurately describe the system. The inertial position is described by X, Y, and Z. The orientation of the body with respect to an inertial frame is determined by the angles ψ (yaw), θ (pitch), and ϕ (roll). The orientation of the right wing is described by the angles δ_R, α_R, and ζ_R. The orientation of the left wing is described by the angles δ_L, α_L, and ζ_L. Sum total, the twelve degrees of freedom for the system are

described by the generalized coordinates, $\mathbf{q}_j$, listed together as

$$\mathbf{q}_j = \begin{bmatrix} X & Y & Z & \psi & \theta & \phi & \delta_R & \alpha_R & \zeta_R & \delta_L & \alpha_L & \zeta_L \end{bmatrix}. \tag{2.6}$$

The associated quasi-velocities of the system, $\mathbf{u}_j$, are

$$\mathbf{u}_j = \begin{bmatrix} u & v & w & p & q & r & p_{RW} & q_{RW} & r_{RW} & p_{LW} & q_{LW} & r_{LW} \end{bmatrix}. \tag{2.7}$$

The variables u, v, and w describe the translational velocity of the central body in the B frame. The variables p, q, and r describe the angular velocity of the central body in the B frame. The final six quasi-velocities are the angular velocity components of the wings in the stroke plane and are expressed in the B frame.

2.2.4 Reference Vectors

The reference vectors are denoted by $\bar{\rho}_{ci}$ in Equation (2.1). For each body, a reference point is chosen. The reference vectors denote the position of the center of mass of the ith body with respect to the reference point. For the central body, the reference point is chosen to be its center of mass. As a direct result, the reference vector $\bar{\rho}_{c1}$ is identically zero. The reference points for each of the wings are chosen to be the respective wing joints. We assume that each wing is rigid. The vectors describing the position of the wing center of mass relative to the wing joint, in the wing frame, are $\bar{\rho}_{c2,w}$ and $\bar{\rho}_{c3,w}$. To express the reference vectors in the body frame, the vectors are transformed from the wing frame according to

$$\bar{\rho}_{c2} = \mathbf{R}_{\beta_R}{}^{\mathrm{T}}\mathbf{R}_R{}^{\mathrm{T}}\bar{\rho}_{c2,w} \quad \text{and} \quad \bar{\rho}_{c3} = \mathbf{R}_{\beta_L}{}^{\mathrm{T}}\mathbf{R}_L{}^{\mathrm{T}}\bar{\rho}_{c3,w}. \tag{2.8}$$

The required accelerations of the reference vectors are denoted by $\ddot{\bar{\rho}}_{ci}$. The acceleration of the reference vector for the central body is identically zero. The acceleration

vectors for the right and left wing reference vectors are obtained according to the following derivation. The reference vectors are defined according to Equation (2.8). The velocity of the reference vectors is obtained from

$$\dot{\bar{\rho}}_{c2} = \frac{\partial}{\partial t}\left({\mathbf{R}_{\beta_R}}^{\mathrm{T}}{\mathbf{R}_R}^{\mathrm{T}}\bar{\rho}_{c2,w}\right) + \bar{\omega}_2 \times \bar{\rho}_{c2}. \tag{2.9}$$

The angular velocities of the wings in the B frame, $\bar{\omega}_2$ for the right wing and $\bar{\omega}_3$ for the left wing, are calculated according to Equation (2.19) with appropriate substitutions made for the left wing. The time derivative of the right wing reference vector is

$$\frac{\partial}{\partial t}\left({\mathbf{R}_{\beta_R}}^{\mathrm{T}}{\mathbf{R}_R}^{\mathrm{T}}\bar{\rho}_{c2,w}\right) = {\mathbf{R}_{\beta_R}}^{\mathrm{T}}\left(\dot{\mathbf{R}}_R^{\mathrm{T}}\bar{\rho}_{c2,w} + {\mathbf{R}_R}^{\mathrm{T}}\dot{\bar{\rho}}_{c2,w}\right), \tag{2.10}$$

where the stroke plane angle, β_R, is assumed to be constant and the derivative of the reference vector, in the wing frame, is zero. The result is

$$\frac{\partial}{\partial t}\left({\mathbf{R}_{\beta_R}}^{\mathrm{T}}{\mathbf{R}_R}^{\mathrm{T}}\bar{\rho}_{c2,w}\right) = {\mathbf{R}_{\beta_R}}^{\mathrm{T}}\left(\dot{\mathbf{R}}_R^{\mathrm{T}}\bar{\rho}_{c2,w}\right). \tag{2.11}$$

The time derivative of the transpose of the rotation matrix, $\dot{\mathbf{R}}_R^{\mathrm{T}}$, is obtained from the relationship between angular velocity and rotation matrices [105]. The time derivative of the transpose of the rotation matrix is equal to

$$\dot{\mathbf{R}}_R^{\mathrm{T}} = {\mathbf{R}_R}^{\mathrm{T}}\tilde{\omega}_{2,sp}, \tag{2.12}$$

where $\tilde{\omega}_{2,sp}$ denotes the skew-symmetric (or cross) matrix of the angular velocity of the right wing with respect to the stroke plane frame, which will be defined in Equation (2.18). A similar procedure is used to derive the acceleration of the left wing reference vector. The acceleration of the reference vectors, with respect to the inertial frame

and expressed in the B frame, is calculated according to

$$\bar{\ddot{\rho}}_{c2} = \frac{\partial}{\partial t}\dot{\bar{\rho}}_{c2} + \dot{\bar{\omega}}_2 \times \bar{\rho}_{c2} + \bar{\omega}_2 \times (\bar{\omega}_2 \times \bar{\rho}_{c2}). \tag{2.13}$$

The full representation of $\bar{\ddot{\rho}}_{c2}$ is presented in Equation (A.14). Additionally, wing joint vectors are defined from the center of mass of the body frame to the wing joints. Since the central body is assumed to be rigid, then the wing joint vectors are fixed and their respective components are constant. The vector from the origin of the B frame to the right wing joint is $\bar{r}_R$ and to the left wing joint is $\bar{r}_L$. The wing reference vectors and wing joint reference vectors are depicted in Fig. 2.1c. Depending on the configuration of the flapping wing aircraft, $\bar{r}_R$ and $\bar{r}_L$ may, or may not, have components in all directions in the B frame. The components of the vectors $\bar{r}_R$ and $\bar{r}_L$ are defined by R_x, R_y, R_z, L_x, L_y, and L_z.

2.2.5 Velocities

The velocities of each of the rigid bodies are defined in the B frame, with respect to the inertial frame. The translational velocity of the body is

$$\bar{\mathbf{v}}_1 = u\,\hat{b}_x + v\,\hat{b}_y + w\,\hat{b}_z\,. \tag{2.14}$$

The angular velocity of the body is

$$\bar{\omega}_1 = p\,\hat{b}_x + q\,\hat{b}_y + r\,\hat{b}_z\,. \tag{2.15}$$

Since the wing joints are chosen to be the reference points, the reference velocity, for each of the wings, is the velocity of the respective wing joint in the B frame. The

velocities of the right and left wing joints are

$$\bar{\mathbf{v}}_2 = \bar{\mathbf{v}}_1 + \bar{\omega}_1 \times \bar{\mathbf{r}}_R \quad \text{and} \quad \bar{\mathbf{v}}_3 = \bar{\mathbf{v}}_1 + \bar{\omega}_1 \times \bar{\mathbf{r}}_L. \tag{2.16}$$

The angular velocities of the wings are a function of the wing angles and angular rates. The angular velocities of the wings, with respect to the stroke plane, are calculated according to the 3-1-2 Euler angle relationship. The angular velocity of the right wing is calculated according to

$$\bar{\omega}_{2,sp} = \mathbf{R}_R \begin{bmatrix} 0 \\ 0 \\ -\dot{\zeta}_R \end{bmatrix} + \mathbf{R}_{\alpha_R}\mathbf{R}_{\delta_R} \begin{bmatrix} \dot{\delta_R} \\ 0 \\ 0 \end{bmatrix} + \mathbf{R}_{\alpha_R} \begin{bmatrix} 0 \\ \dot{\alpha}_R \\ 0 \end{bmatrix}. \tag{2.17}$$

In component form, the angular velocity of the right wing with respect to the stroke plane, is

$$\bar{\omega}_{2,sp} = \begin{bmatrix} p_{RW} \\ q_{RW} \\ r_{RW} \end{bmatrix} = \begin{bmatrix} (cos\alpha_R)\dot{\delta}_R + (\sin\alpha_R \cos\delta_R)\dot{\zeta}_R \\ \dot{\alpha}_R - (\sin\delta_R)\dot{\zeta}_R \\ (\sin\alpha_R)\dot{\delta}_R - (\cos\alpha_R \cos\delta_R)\dot{\zeta}_R \end{bmatrix}. \tag{2.18}$$

The total angular velocity of the right wing with respect to the inertial frame, and expressed in the B frame, is

$$\bar{\omega}_2 = \bar{\omega}_1 + {\mathbf{R}_{\beta_R}}^{\mathrm{T}} \bar{\omega}_{2,sp}. \tag{2.19}$$

A similar procedure is used to develop the angular velocity of the left wing and is presented in Equations (A.6) and (A.7). The total angular velocity of the right wing, expressed in Equation (2.19), is the angular velocity of the wing expressed in the body frame with respect to the inertial frame. It's important to note, consistent with the development of the orientation of the wings with respect to the stroke planes and the right hand rule, that the signs are opposite for $\dot{\delta}_R$ and $\dot{\delta}_L$ and $\dot{\zeta}_R$ and $\dot{\zeta}_L$, which

results (for symmetric flapping) in $-p_{LW} = p_{RW}$ and $r_{LW} = -r_{RW}$ in the B frame.

2.2.6 Velocity and Angular Velocity Coefficients

Velocity and angular velocity coefficients arise from the calculation of virtual work performed by forces and moments [106]. Each velocity and angular velocity coefficient is a vector. The velocity and angular velocity coefficients are calculated according to

$$\bar{\gamma}_{ij} = \frac{\partial \bar{\mathbf{v}}_i}{\partial \mathbf{u}_j} \quad \text{and} \quad \bar{\beta}_{ij} = \frac{\partial \bar{\omega}_i}{\partial \mathbf{u}_j}. \tag{2.20}$$

The velocities and angular velocities for the ith rigid body are defined in Section 2.2.5. The system quasi-velocities, $\mathbf{u}_j$, are detailed in Section 2.2.3. Since each coefficient is a vector, the coefficients are combined with the other elements of the equations generated by Equation (2.1) according to inner product rules. With twelve coordinates and three rigid bodies, the total number of velocity coefficients and angular velocity coefficients is thirty-six each. The velocity coefficients for all three rigid bodies, due to the translational motion of the central body, can be summarized as

$$\begin{bmatrix} \bar{\gamma}_{11} \\ \bar{\gamma}_{12} \\ \bar{\gamma}_{13} \end{bmatrix} = \begin{bmatrix} \bar{\gamma}_{21} \\ \bar{\gamma}_{22} \\ \bar{\gamma}_{23} \end{bmatrix} = \begin{bmatrix} \bar{\gamma}_{31} \\ \bar{\gamma}_{32} \\ \bar{\gamma}_{33} \end{bmatrix} = \mathbb{I}^{3\text{x}3} \begin{bmatrix} \hat{b}_x \\ \hat{b}_y \\ \hat{b}_z \end{bmatrix}. \tag{2.21}$$

The velocity coefficients of the right wing and left wings, due to the angular velocity of the central body are

$$\begin{bmatrix} \bar{\gamma}_{24} \\ \bar{\gamma}_{25} \\ \bar{\gamma}_{26} \end{bmatrix} = \begin{bmatrix} 0 & -R_z & R_y \\ R_z & 0 & -R_x \\ -R_y & R_x & 0 \end{bmatrix} \begin{bmatrix} \hat{b}_x \\ \hat{b}_y \\ \hat{b}_z \end{bmatrix} \text{ and } \begin{bmatrix} \bar{\gamma}_{34} \\ \bar{\gamma}_{35} \\ \bar{\gamma}_{36} \end{bmatrix} = \begin{bmatrix} 0 & -L_z & L_y \\ L_z & 0 & -L_x \\ -L_y & L_x & 0 \end{bmatrix} \begin{bmatrix} \hat{b}_x \\ \hat{b}_y \\ \hat{b}_z \end{bmatrix}. \tag{2.22}$$

The velocity coefficients due to the angular velocity components of the wings are all identically zero, for each rigid body. The non-zero angular velocity coefficients for the central body and the wings are

$$\begin{bmatrix} \bar{\beta}_{14} \\ \bar{\beta}_{15} \\ \bar{\beta}_{16} \end{bmatrix} = \begin{bmatrix} \bar{\beta}_{24} \\ \bar{\beta}_{25} \\ \bar{\beta}_{26} \end{bmatrix} = \begin{bmatrix} \bar{\beta}_{34} \\ \bar{\beta}_{35} \\ \bar{\beta}_{36} \end{bmatrix} = \mathbb{I}^{3\text{x}3} \begin{bmatrix} \hat{b}_x \\ \hat{b}_y \\ \hat{b}_z \end{bmatrix}. \tag{2.23}$$

The angular velocity coefficients for the central body due to the angular velocity of the wings and translational velocity of the central body are identically zero. Since the total angular velocity of the wings is a combination of the angular velocity of the central body and the angular velocity of the wings with respect to the body frame, the angular velocity coefficients from the wings due to the angular velocity of the central body are identical. The angular velocity coefficients for the right wing, due to the angular velocity of the right wing, and the angular velocity coefficients of the left wing, due to the angular velocity of the left wing, are

$$\begin{bmatrix} \bar{\beta}_{2,7} \\ \bar{\beta}_{2,8} \\ \bar{\beta}_{2,9} \end{bmatrix} = \mathbf{R}_{\beta_R}{}^{\mathrm{T}} \begin{bmatrix} \hat{b}_x \\ \hat{b}_y \\ \hat{b}_z \end{bmatrix} \quad \text{and} \quad \begin{bmatrix} \bar{\beta}_{3,10} \\ \bar{\beta}_{3,11} \\ \bar{\beta}_{3,12} \end{bmatrix} = \mathbf{R}_{\beta_L}{}^{\mathrm{T}} \begin{bmatrix} \hat{b}_x \\ \hat{b}_y \\ \hat{b}_z \end{bmatrix}. \tag{2.24}$$

The angular velocity coefficients of the right wing, due to the angular velocity of the left wing, are identically zero. The same is true for the angular velocity coefficients of the left wing due to the angular velocity of the right wing.

2.2.7 Forces

The forces are calculated according to the principle of virtual work. The principle of virtual work calculates the generalized forces and moments acting on the system due to an arbitrary virtual displacement. The derivation of the principle of virtual

work is detailed in [105, 106, 107]. The generalized forces and moments are calculated according to

$$Q_j = \sum_{i=1}^{n} \left(\mathbf{F}_i \cdot \bar{\gamma}_{ij} + \mathbf{M}_i \cdot \bar{\beta}_{ij} \right), \tag{2.25}$$

for each jth coordinate. The resultant forces, $\mathbf{F}_i$, and moments, $\mathbf{M}_i$ are determined for each rigid body. The resultant forces acting on the central body are due to the acceleration due to gravity and the aerodynamic forces generated on the central body due to its translation. There are zero resultant moments acting directly on the central body. The resultant forces acting on the wings are the aerodynamic forces generated by the motion of the wings, acting at the wing center of pressure, and the gravity force, acting at the center of mass of the wing. The resultant moments on the wings are calculated with respect to the wing joints and include contributions from the aerodynamic forces, the gravity force, and the control moments applied to obtain the desired wing motion. The generalized forces affecting the translation of the central body are

$$\begin{bmatrix} Q_1 \\ Q_2 \\ Q_3 \end{bmatrix} = \begin{bmatrix} F_x \\ F_y \\ F_z \end{bmatrix} + (m_1 + m_2 + m_3)\mathbf{R}_B \begin{bmatrix} 0 \\ 0 \\ g \end{bmatrix}. \tag{2.26}$$

The generalized forces affecting the rotation of the central body are

$$\begin{bmatrix} Q_4 \\ Q_5 \\ Q_6 \end{bmatrix} = \bar{M}_{aero} + \bar{M}_g. \tag{2.27}$$

where $\bar{M}_{aero}$ is the vector of aerodynamic moments acting on the central body and $\bar{M}_g$ is the moments due to gravity of the wings on the central body. The moments due to gravity are calculated according to

$$\bar{M}_g = \bar{M}_{g,R} + \bar{M}_{g,L}, \tag{2.28}$$

where the moments due to gravity for the right wing and left wing are calculated according to

$$\bar{M}_{g,R} = (\bar{r}_R + \bar{\rho}_{c2}) \times (m_2)\mathbf{R}_B \begin{bmatrix} 0 \\ 0 \\ g \end{bmatrix} \quad \text{and} \quad \bar{M}_{g,L} = (\bar{r}_L + \bar{\rho}_{c3}) \times (m_3)\mathbf{R}_B \begin{bmatrix} 0 \\ 0 \\ g \end{bmatrix}. \quad (2.29)$$

The generalized forces Q_7, Q_8, and Q_9 are the control moments for the right wing. Q_{10}, Q_{11}, Q_{12} are the control moments for the left wing. Q_8 and Q_{11} control the angle of attack of the wings, right and left wing respectively. Q_7 and Q_{10} control the deviation angle of the wings, while Q_9 and Q_{12} control the flap angle of the wings. The control moments are required to produce the desired motion of the wings. The forces and moments produced by the wings will be the result of aerodynamic modeling of the wing. For the moment, we will assume the motion will produce a force normal, F_N, and tangential, F_T, to the wing. The forces will be calculated in the wing frame and transformed to the stroke plane and body frame. We define the total aerodynamic forces acting on the body, expressed in the B frame as

$$\bar{F}_{aero} = F_x\,\hat{b}_x + F_y\,\hat{b}_y + F_z\,\hat{b}_z. \quad (2.30)$$

The total aerodynamic moments are defined as

$$\bar{M}_{aero} = L\,\hat{b}_x + M\,\hat{b}_y + N\,\hat{b}_z. \quad (2.31)$$

Assuming a normal and tangential force produced by each wing, the forces expressed in the body frame are calculated according to

$$\begin{bmatrix} F_{x,R} \\ F_{y,R} \\ F_{z,R} \end{bmatrix} = \mathbf{R}_{\beta_R}{}^{\mathrm{T}} \mathbf{R}_R{}^{\mathrm{T}} \begin{bmatrix} F_{T,R} \\ 0 \\ F_{N,R} \end{bmatrix} \text{ and } \begin{bmatrix} F_{x,L} \\ F_{y,L} \\ F_{z,L} \end{bmatrix} = \mathbf{R}_{\beta_L}{}^{\mathrm{T}} \mathbf{R}_L{}^{\mathrm{T}} \begin{bmatrix} F_{T,L} \\ 0 \\ F_{N,L} \end{bmatrix}. \tag{2.32}$$

If the chosen aerodynamic model produces identical normal and tangential forces for the right and left wings, then in the body frame the F_x and F_z forces are the same and the F_y forces will perfectly cancel each other out, when the flapping is symmetrical with respect to the central body. A rotation from the stroke plane will not change the F_y forces and will only change the magnitude/combination of the F_x and F_z forces. The aerodynamic centers of pressure of the wings are calculated based on the morphology of the wings. The x- and y-positions of the aerodynamic centers of pressure, in the wing frame, are obtained with the assistance of following equations

$$\hat{r}_2 = \sqrt{\frac{\int_0^R c(r) r^2 dr}{R^2 A_w}} \text{ and } \hat{c} = \frac{\int_0^R c^2(r) r dr}{\hat{r}_2 R A_w c_{max}}, \tag{2.33}$$

which are based on the geometry of the wings [39, 89]. The resulting aerodynamic center is at the following coordinates in the wing frames

$$\bar{\rho}_{ac,R,w} = \begin{bmatrix} \frac{c_R}{4} \\ \hat{r}_{2,R} b_R \\ 0 \end{bmatrix} \quad \text{and} \quad \bar{\rho}_{ac,L,w} = \begin{bmatrix} \frac{c_L}{4} \\ -\hat{r}_{2,L} b_L \\ 0 \end{bmatrix}. \tag{2.34}$$

In Equation (2.34), c_R and c_L are the chords of the respective wings, b_R and b_L are the semi-spans of the wings and $\hat{r}_2$ denotes the normalized aerodynamic center of pressure. The aerodynamic centers are transformed into the B frame in the same manner as the forces are transformed in Equation (2.32). The total aerodynamic

moment in the B frame, for each wing, is given by:

$$\bar{M}_{aero,R} = (\bar{r}_R + \bar{\rho}_{ac,R}) \times \bar{F}_{aero,R} \text{ and } \bar{M}_{aero,L} = (\bar{r}_L + \bar{\rho}_{ac,L}) \times \bar{F}_{aero,L}. \tag{2.35}$$

In component form, the total aerodynamic moments in the B frame are

$$\begin{bmatrix} L \\ M \\ N \end{bmatrix} = \begin{bmatrix} \rho_{RW,y}F_{z,R} - \rho_{RW,z}F_{y,R} + \rho_{LW,y}F_{z,L} - \rho_{LW,z}F_{y,L} \\ \rho_{RW,z}F_{x,R} - \rho_{RW,x}F_{z,R} + \rho_{LW,z}F_{x,L} - \rho_{LW,x}F_{z,L} \\ \rho_{RW,y}F_{x,R} - \rho_{RW,x}F_{y,R} + \rho_{LW,y}F_{x,L} - \rho_{LW,x}F_{y,L} \end{bmatrix}, \tag{2.36}$$

where $\bar{\rho}_{RW} = \bar{r}_R + \bar{\rho}_{ac,R}$ and $\bar{\rho}_{LW} = \bar{r}_L + \bar{\rho}_{ac,L}$. For symmetrical flapping, we showed previously that $F_{y,R} = -F_{y,L}$. Similarly, under the constraint of symmetrical flapping, $\rho_{ac,R,y} = -\rho_{ac,L,y}$. Good engineering design will place the y components of $\bar{r}_R$ and $\bar{r}_L$ equal and opposite, or asymmetric moments result. Therefore, if the flapping is symmetric and the stroke plane angles are equal, we can perform proper cancellations and obtain

$$\begin{bmatrix} L \\ M \\ N \end{bmatrix} = \begin{bmatrix} 0 \\ \rho_{RW,z}F_{x,R} - \rho_{RW,x}F_{z,R} + \rho_{LW,z}F_{x,L} - \rho_{LW,x}F_{z,L} \\ 0 \end{bmatrix}, \tag{2.37}$$

which is expected if the flapping is perfectly symmetrical, the normal and tangential forces are identical for both wings when symmetrical flapping occurs, and the wings have the same morphological parameters.

2.2.8 Equations of Motion

The equations of motion are now summarized for each of the generalized coordinates. The equations of motion governing the translation of the central body are

$$\mathbb{I}^{3x3}\left(\sum_{i=1}^{3}\left(m_i+\ddot{\bar{\rho}}_{ci}\right)\right)=\begin{bmatrix}Q_1 & Q_2 & Q_3\end{bmatrix}^{\mathrm{T}}. \tag{2.38}$$

The equations of motion governing the rotation of the central body are

$$m_2\bar{r}_R\times(\dot{\bar{\mathbf{v}}}_2+\ddot{\bar{\rho}}_{c2})+m_3\bar{r}_L\times(\dot{\bar{\mathbf{v}}}_3+\ddot{\bar{\rho}}_{c3})+\sum_{i=1}^{3}(\dot{\bar{\mathbf{H}}}_i+m_i\bar{\rho}_{\mathbf{ci}}\times\dot{\bar{\mathbf{v}}}_i)=\begin{bmatrix}Q_4 & Q_5 & Q_6\end{bmatrix}^{\mathrm{T}}. \tag{2.39}$$

The equations of motion governing the motion of the right wing are

$$\mathbf{R}_{\beta_R}{}^{\mathrm{T}}\left(\mathbf{I}_2\dot{\bar{\omega}}_2+\bar{\omega}_2\times\mathbf{I}_2\bar{\omega}_2+m_2\bar{\rho}_{c2}\times\dot{\bar{\mathbf{v}}}_2\right)=\begin{bmatrix}Q_7 & Q_8 & Q_9\end{bmatrix}^{\mathrm{T}}. \tag{2.40}$$

The equations of motion governing the motion of the left wing are

$$\mathbf{R}_{\beta_L}{}^{\mathrm{T}}\left(\mathbf{I}_3\dot{\bar{\omega}}_3+\bar{\omega}_3\times\mathbf{I}_3\bar{\omega}_3+m_3\bar{\rho}_{c3}\times\dot{\bar{\mathbf{v}}}_3\right)=\begin{bmatrix}Q_{10} & Q_{11} & Q_{12}\end{bmatrix}^{\mathrm{T}}. \tag{2.41}$$

2.3 Standard Aircraft Model

The standard aircraft equations of motion, alternatively known as the six degree of freedom (6DOF) aircraft equations of motion, can be summarized according to:

$$\begin{aligned}\dot{\bar{\mathbf{v}}}_b&=\tfrac{1}{m_b}\left(\bar{W}_b+\bar{F}_{aero}\right)+\bar{\omega}_b\times\bar{\mathbf{v}}_b\\ \dot{\bar{\omega}}_b&=\mathbf{I}_b{}^{-1}\left(\bar{\omega}_b\times\mathbf{I}_b\bar{\omega}_b+\bar{M}_{aero}\right).\end{aligned} \tag{2.42}$$

In Equation (2.42), $\bar{\omega}_b$ denotes the angular velocity of the central body, $\bar{\mathbf{v}}_b$ is the translational velocity of the central body, m_b is the mass of the central body, $\mathbf{I}_b$ is

the inertia tensor of the central body about its respective center of mass, and $\bar{W}_b$ is the weight vector of the body expressed in a body frame. The standard aircraft model neglects the inertial and mass effects of the wings on the central body. The wings' motion is solely included to generate aerodynamic forces and moments on the central body. The set of equations in Equation (2.42) are simulated when combined with an aerodynamic model using the traditional equations of motion for six degree of freedom, rigid body flight.

From the derivation of the full nonlinear equations previously presented, we can make the following substitutions into Equation (2.42): $\bar{\omega}_1 = \bar{\omega}_b$, $\mathbf{I}_1 = \mathbf{I}_b$, and $\bar{\mathbf{v}}_1 = \bar{\mathbf{v}}_b$. The mass of the body will equal the entire mass of the system, both central body and wings. The inertia tensor will be calculated based on the mass of the system, adding the mass of the wings to that of the central body. Additionally, the aerodynamic forces and moments generated by the wings will be calculated in the same manner as previously presented. The multi-body model will be simulated against the standard aircraft model.

2.4 Simulation

2.4.1 Body Parameters

The FWMAV is modeled after a hawkmoth as presented in [21]. The specific specimen chosen is F1. A hawkmoth is chosen because, according to Willmott and Ellington in [21], the wingstrokes can be considered the most 'representative' of insect wingstrokes. Additionally, the flapping frequency for hawkmoths is generally between 24 and 26 Hz, which can be replicated by current technology (as opposed to using a bumblebee or fruitfly, where the flapping frequency is on the order of 150 and 200 Hz, respectively). The total mass of the FWMAV will be set at 1648 mg, with the wings accounting for 5.7% of the total body mass.

2.4.1.1 Central Body

The central body is modeled as a cylinder with a constant radius. The mass of the body is set at 1554 mg, with a length of 42.1 mm, and a constant radius of 6 mm. The parameters are similar to those used in [112]. The length is calculated based off of the $\hat{L}$ parameter in [21]. The radius is calculated from the $\hat{l}_1$ parameter in [21]. Since the body is modeled as a cylinder, the inertia tensor for the central body will be diagonal. The wings are assumed to be mounted at wing joints with components such that $R_y = r_1$ and $L_y = -r_1$, where r_1 denotes the constant radius of the central body.

2.4.1.2 Wings

The wings are modeled as thin, flat plates with a constant chord. The wing semi-span (b, the span of each wing) is set at 51.9 mm. With an aspect ratio of 5.65 for both wings, the chord is set at 18.4 mm. The wings are mounted at the wing joints at the mid-point of the wing, such that the center of mass of the wing is along the y-axis of the respective wing frame. The inertia tensors for the wings are calculated at the wing joint according to (using the right wing as an example),

$$\mathbf{I}_{2,w} = \begin{bmatrix} \frac{m_2}{3}{b_2}^2 & 0 & 0 \\ 0 & \frac{m_2}{12}{c_2}^2 & 0 \\ 0 & 0 & m_2\left(\frac{1}{3}{b_2}^2 + \frac{1}{12}{c_2}^2\right) \end{bmatrix}. \tag{2.43}$$

The inertia tensor for the left wing, $\mathbf{I}_{3,w}$, is identical to the inertia tensor for the right wing in the wing frames. For aerodynamic force and moment calculations, the thickness of the wings is set at 0.076% of the wing semi-span. The mass of each of the wings is set at 47 mg. The inertia tensor for the wing in Equation (2.43) is expressed in the wing frame. In order to express the inertia tensor in the stroke plane frame,

the inertia tensors in the wing frames are transformed according to

$$\mathbf{I}_{2,sp} = {\mathbf{R}_R}^{\mathrm{T}} \mathbf{I}_{2,w} \mathbf{R}_R \quad \text{and} \quad \mathbf{I}_{3,sp} = {\mathbf{R}_L}^{\mathrm{T}} \mathbf{I}_{3,w} \mathbf{R}_L. \tag{2.44}$$

When the stroke plane is non-zero, the inertia tensors in the stroke plane frames are transformed to the B frame according to

$$\mathbf{I}_2 = {\mathbf{R}_{\beta_R}}^{\mathrm{T}} \mathbf{I}_{2,sp} \mathbf{R}_{\beta_R} \quad \text{and} \quad \mathbf{I}_3 = {\mathbf{R}_{\beta_L}}^{\mathrm{T}} \mathbf{I}_{3,sp} \mathbf{R}_{\beta_L}. \tag{2.45}$$

No further transformation of the inertia tensors is necessary. The derivation method only requires calculation of the inertia tensors with respect to the reference points for each rigid body.

2.4.2 Aerodynamic Model

The model used for the majority of the simulations is the quasi-steady/blade-element model developed by Berman and Wang and presented in [36]. The model is slightly modified from that presented in [36] and [60] in order to properly fit the presented dynamics. The reference directions are changed to fit our representation of the dynamics, e.g. from r_1 and r_3 in [60] to r_x and r_z. Furthermore, notation is changed to fit with model development previously presented. The model includes linear and circulation terms, but does not include leading edge vortex or wake capture effects, which have been previously shown through CFD results to enhance lift. The morphological parameters for the FWMAV simulations to be presented are based off of a hawkmoth. In [36], Berman and Wang use the drag coefficients obtained by Usherwood and Ellington in [113, 114]. Usherwood and Ellington used model hawkmoth wings, scaled to $0.5m$, at a Reynolds number of 8071, to obtain the drag coefficients used in the simulations.

The Berman and Wang model is chosen for the aerodynamic model because the

drag coefficients are calculated for a Reynolds number equivalent to the Reynolds number of the wings in the simulation results. Although the model does not include wake capture effects or vortex sheddings effects, Sane and Dickinson determined in [29] that as high as 80% of the lift and drag generated in a hover condition are due to translation and rotational effects. Hedrick and Daniel state in [112] that a computationally efficient model for aerodynamics, including wake and vortex effects, is not presently available. The Ansari blade-element aerodynamic model, presented in [40] and [41], includes wake and vortex effects, but high fidelity runs are not computationally efficient for control studies. Quasi-steady aerodynamic models have been used in multi-body simulations presented in [54, 55, 58, 60]. The intent of this study is to provide the basis for dynamics studies from a stability and control standpoint. Therefore, a complicated, complex aerodynamic model with a large computation time will not result in practical calculations.

A velocity of a point on the wing is required to calculate the aerodynamic forces and moments. The velocity on a point of the wing, relative to the body, is calculated in the following manner. The position of a point along the center of the wing, expressed in the B frame, is given by

$$\bar{r}_{RW} = r_w \, \mathbf{R}_{\beta_R}{}^{\mathrm{T}} \begin{bmatrix} \cos\delta_R \sin\zeta_R \\ \cos\delta_R \cos\zeta_R \\ \sin\delta_R \end{bmatrix} \tag{2.46}$$

for the right wing, where r_w denotes the position along the wing in the stroke plane frame. The velocity of the wing is calculated according to the transport theorem such that

$$\dot{\bar{r}}_{RW} = \frac{\partial \bar{r}_{RW}}{\partial t} + \bar{\omega}_2 \times \bar{r}_{RW}. \tag{2.47}$$

The acceleration of the wing is

$$\ddot{\bar{r}}_{RW} = \frac{\partial \dot{\bar{r}}_{RW}}{\partial t} + \bar{\omega}_2 \times \dot{\bar{r}}_{RW}. \tag{2.48}$$

A similar procedure is used to develop the velocity and acceleration of the left wing. The angular velocities of the right and left wings, $\bar{\omega}_2$ and $\bar{\omega}_3$, are obtained from Equation (2.18), which define the angular velocity of the wing with respect to the stroke plane frame. The force generation for a wing in the x-direction is

$$dF_x = \left\{ \left[\left(\frac{-c(r)}{\bar{c}R} m_w + m_{22} \right) \dot{\alpha} + \rho\Gamma \right] \dot{\bar{r}}_z - m_{11} \ddot{\bar{r}}_x \right\} dr \tag{2.49}$$

and in the z-direction is

$$dF_z = \left\{ \left[\left(\frac{-c(r)}{\bar{c}R} m_w + m_{11} \right) \dot{\alpha} + \rho\Gamma \right] \dot{\bar{r}}_x - m_{11} \ddot{\bar{r}}_z \right\} dr, \tag{2.50}$$

where $c(r)$ denotes the chord as a function of the radial position of the wing, m_{11} and m_{22} are added mass terms, m_w is the mass of the wing, and Γ is the circulation term. The added mass terms are calculated according to

$$m_{11} = \frac{\pi}{4} \rho \bar{t}^2 \quad \text{and} \quad m_{22} = \frac{\pi}{4} \rho c(r)^2. \tag{2.51}$$

The circulation term is calculated according to the equation

$$\Gamma = -\tfrac{1}{2} C_T c(r) ||\dot{\bar{r}}_W||_2 \sin(2\alpha) + \tfrac{1}{2} C_R c(r)^2 \dot{\alpha} \ . \tag{2.52}$$

The viscous effects on the wings are calculated by

$$dF_x^{\nu} = \frac{1}{2} \rho c(r) \left(C_{D_o} \cos^2\alpha + C_{D_{\pi/2}} \sin^2\alpha \right) ||\dot{\bar{r}}||_2 \dot{\bar{r}}_x \tag{2.53}$$

and

$$dF_z^{\nu} = \frac{1}{2}\rho c(r)\left(C_{D_o}\cos^2\alpha + C_{D_{\pi/2}}\sin^2\alpha\right)||\dot{\bar{r}}||_2\dot{\bar{r}}_z. \tag{2.54}$$

C_T, C_{D_o}, and $C_{D_{\pi/2}}$ are coefficients to fit the lift and drag of each wing. The constants used for simulation purposes are those for the hawkmoth presented in [36] and are obtained from experiments on model hawkmoth wings presented in [113]. The method does not calculate lift and drag directly, but the resultant forces in the x and z directions in the wing frames [60]. The normal and tangential forces on the wings are calculated according to

$$dF_T = dF_x - dF_x^{\nu} \quad \text{and} \quad dF_N = dF_z - dF_z^{\nu}. \tag{2.55}$$

For simulation purposes, five slices of the wing are used at each time step to integrate and calculate the resultant normal and tangential forces. Five slices are chosen based on the results presented in [112]. The lift, drag, and lateral forces generated by each wing in the B frame are calculated according to Equation (2.32). The resultant pitch, roll, and yaw moments are calculated using the results from Equations (2.32) and (2.35). A summary of the simulation framework is presented in Figures 2.3 and 2.4. Figure 2.3 details the inputs to the system, including the calculation of the mass matrix, aerodynamic forces and moments, body forces and moments, and control moments. The calculation of the mass matrix is necessary, as the **ode15s** suite in MATLAB is used for simulation purposes. Figure 2.4 details the outputs of the system. The simulation involves two sets of integrations. First, systems quasi-velocities are integrated using the mass matrix and the forces and moments. After the results are obtained for the system quasi-velocities, the system generalized coordinates are obtained using the proper representation from Euler angle relationships. Although not specifically detailed in Figures 2.3 and 2.4, the quasi-velocities and generalized coordinates calculated at each time step are also inputs to the next simulation step.

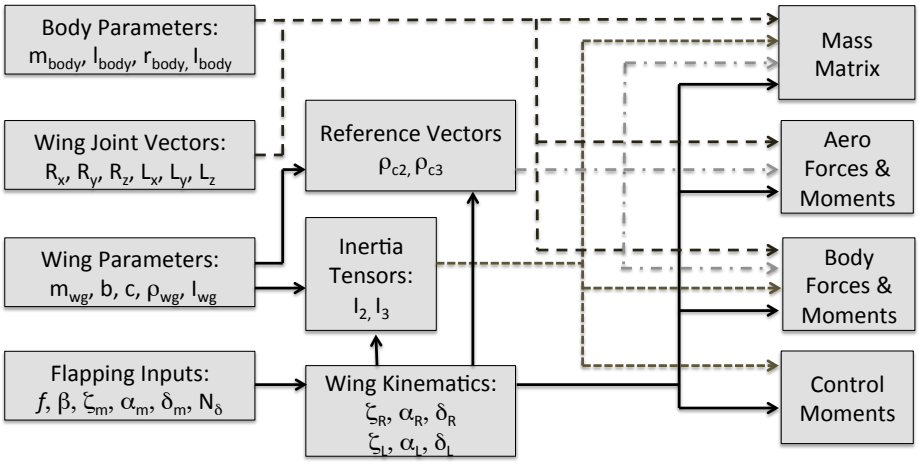

Figure 2.3: Simulation Framework: Model Inputs

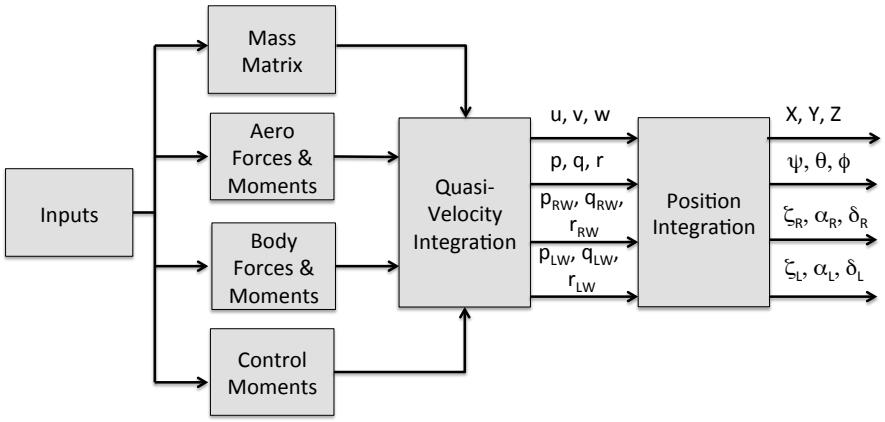

Figure 2.4: Simulation Framework: Model Outputs

2.5 Results

2.5.1 Simulation Parameters

The wing kinematics are based off of the biological flight mechanics of specimen F1 in [21]. The deviation angle of the right and left wings is set at

$$\delta(t) = \delta_m \sin\left(2\pi N_\delta f t\right). \tag{2.56}$$

The parameter N_δ is a shape parameter, which is set to 2 to ensure a proper figure 8 pattern for the wings. The specimen F1 has an average deviation angle of 0.9 degrees. As a result, δ_m will be set to one degree to approximate the kinematic pattern of hawkmoth. The flap angle will be governed by the equation

$$\zeta(t) = \zeta_m \sin(2\pi f t). \tag{2.57}$$

Hawkmoths, like most insect species, generally exhibit a total flapping (stroke) amplitude of approximately 120 degrees, therefore ζ_m will be set to 60 degrees. The stroke plane angle and the flapping frequency will be varied for the simulations, as well as the initial pitch angle. A summary table of the pertinent wing morphological parameters, for aerodynamic calculations, is shown Table 2.1. The positions of the aerodynamic centers of pressure are shown for their fixed position in the respective wing frames.

Wing	Semi-span	Chord	x-pos of c.p.	y-pos of c.p.	Reynolds number
Right	51.9 mm	18.4 mm	4.6 mm	29.6 mm	8000
Left	51.9 mm	18.4 mm	4.6 mm	-29.6 mm	8000

Table 2.1: Summary of Wing Morphological Parameters

2.5.2 Dynamic Model Comparison - Water Treading Mode

The dynamic model comparison will be presented for the water treading mode previously discussed in Chapter 1.2. The motion of the angle of attack is described by the motion

$$\alpha(t) = \alpha_m \sin(2\pi f t + \Phi_\alpha), \tag{2.58}$$

where Φ_α is a phase shift to ensure the proper mid-stroke angle of attack. For the simulations presented, the amplitude is set at 45 degrees and the phase shift is set at $\frac{\pi}{2}$. A phase shift of $\frac{\pi}{2}$ ensures that the angle of attack is positive during the down

stroke and that the mid-stroke angle of attack is 45 degrees. Additionally, the angle of attack will be -45 degrees during the upstroke, but since the wing is moving in the opposite direction, the magnitude of the angle of attack is still correct. A phase of $\frac{3\pi}{2}$ will have the wing rotated in the wrong direction (negative on the downstroke, positive on the upstroke) and produce 'positive' lift, quickly driving the vehicle into the ground. It's important to note that during the upstroke, the center of pressure of the wing is at a x-coordinate of $-\frac{c}{4}$ in the wing frame since the wing is 'flipped' over [38]. The angle of attack presented in [39, 89] uses a water-treading mode. Simulations, for three flapping cycles, are presented in Figs. 2.5, 2.6, and 2.7. For each of the plots, the solid line represents the full nonlinear model and dot-dash line represents the standard aircraft model. The FWMAV starts at an initial altitude of 5 m with zero initial body velocities. The flapping frequency, initial pitch angle, and the stroke plane angle vary for the four cases presented. In all Figures 2.5-2.7, the multi-body model is denoted by 'MB' and represented by the solid line. The standard aircraft model is denoted by '6DOF' and represented by the dash-dot line. Table 2.2 presents a summary of the flapping inputs for the dynamic model comparison.

Case	Initial Pitch Angle $\theta_o\,(^\circ)$	Stroke Plane $\beta\,(^\circ)$	Flapping Frequency $f\,(Hz)$
1	34.9	-10	26
2	20.0	-20	26
3	15	-25	26
4	5	-5	24

Table 2.2: Summary of Input Parameters for Dynamic Model Comparison Simulations, Presented in Figures 2.5-2.7

The inertial position, in Fig. 2.5, shows that the inertial effects of the wings push the vehicle away from the initial starting point and the vehicle gains altitude. The total lift, in the absence of inertial coupling effects, is enough for the standard aircraft model to slowly gain altitude. With no control, the resultant drag (thrust) forces pushed the vehicle models away from a hover condition. However, the direction

of the displacement from the initial conditions differs between the two models. In Figs. 2.5(a) and 2.5(d), the standard aircraft models moves in a negative direction, while the multi-body model moves in a positive direction. The models move in the same direction in Figs. 2.5(b) and 2.5(c). For Case 4, presented in Fig 2.5(d), the standard aircraft model not only translates in the opposite direction, but gains altitude. The addition of the inertial coupling effects actually increases the amount of lift generation required for flapping wing micro air vehicle model.

In [68], the authors estimate that the peak-to-peak displacement of the center of mass of the hawkmoth in a hover condition is 4 mm. Furthermore, Hedrick and Daniel in [112] found the maximum deviation of a hawkmoth center of mass in a true hover condition is 6.5 mm. The simulations presented here are open loop, and not exhibiting a controlled, true hover condition. An average horizontal displacement of approximately 10 mm per flapping cycle, over the four cases, is qualitatively consistent with the previous studies. Fig. 2.6 shows the pitch angle and Fig. 2.7 shows the pitch velocity of the FWMAV simulations. The wings are started, for simulation purposes, at midstroke of the downstroke. The initial gravity moment is nose down, while the initial aerodynamic pitching moment is nose up.

The greatest difference between the two models is exhibited in the pitch angle, and as a direct cause, the pitch velocity. At the end of the three flapping cycles, the average difference between the pitch angle prediction is approximately 42.9° (0.75 radians). Furthermore, as depicted in Figure 2.6(d), the multi-body model predicts a nearly nose up orientation ($\theta = \frac{\pi}{2}$) after the three flapping cycles, while the standard aircraft model is only halfway to the nose up orientation.

The simulations show a marked difference for the standard aircraft model in regards to the pitch velocity. Both sets of simulations show a steadily increasing magnitude in the pitch velocity, consistent with the results presented by Bolender in [60]. However, the difference in magnitude between the two models, directly due to the

inclusion of the inertial effects of the wings, results in the difference in orientation prediction presented in Fig. 2.7(d). The simulation results lead to the conclusion that the inertial effects of the wings need to be included for dynamics, stability, and control studies of flapping wing micro air vehicles.

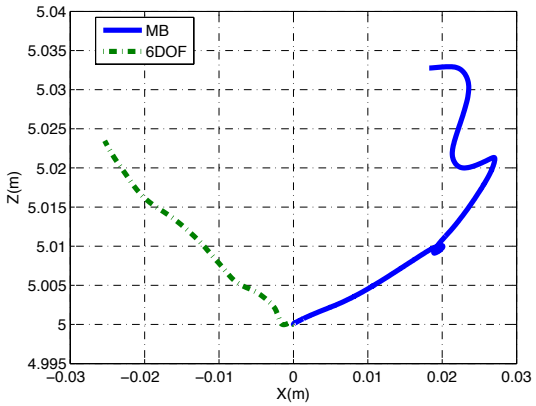

(a) Case 1: $\theta_o = 34.9°$, $\beta = -16°$, $f = 26$ Hz

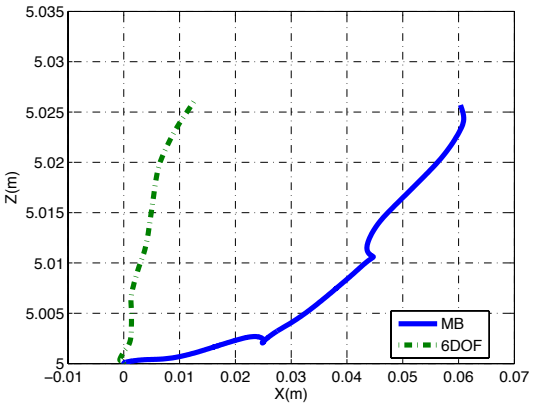

(b) Case 2: $\theta_o = 20.0°$, $\beta = -20°$, $f = 26$ Hz

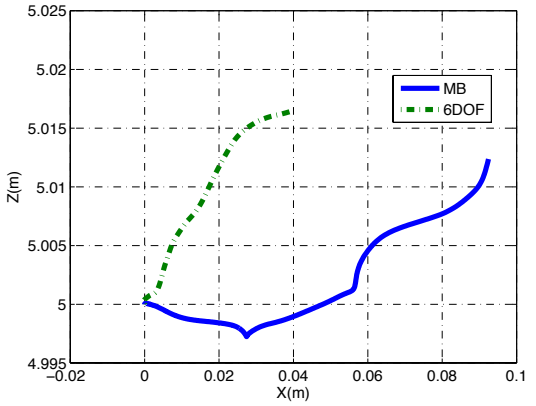

(c) Case 3: $\theta_o = 15°$, $\beta = -25°$, $f = 26$ Hz

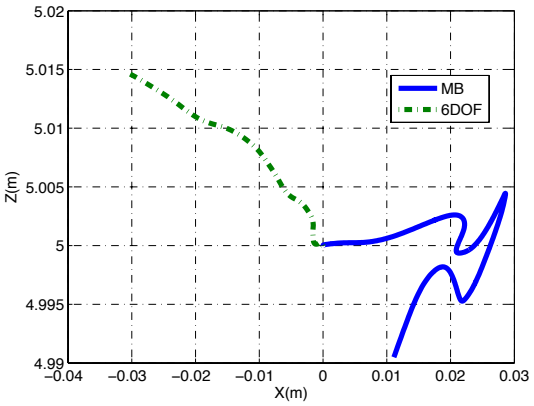

(d) Case 4: $\theta_o = 5°$, $\beta = -5°$, $f = 24$ Hz

Figure 2.5: Inertial Position Results for Dynamic Model Comparison with $\alpha_m = 45°$, $\zeta_m = 60°$

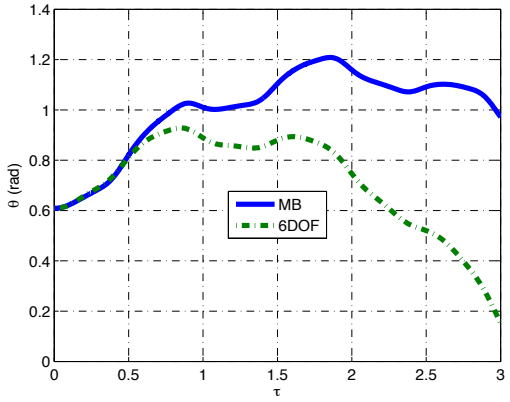

(a) Case 1: $\theta_o = 34.9°$, $\beta = -16°$, $f = 26$ Hz

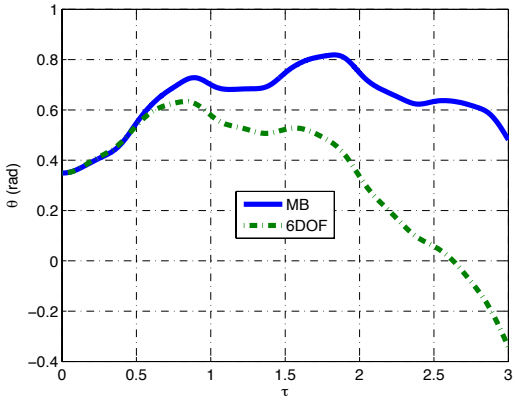

(b) Case 2: $\theta_o = 20.0°$, $\beta = -20°$, $f = 26$ Hz

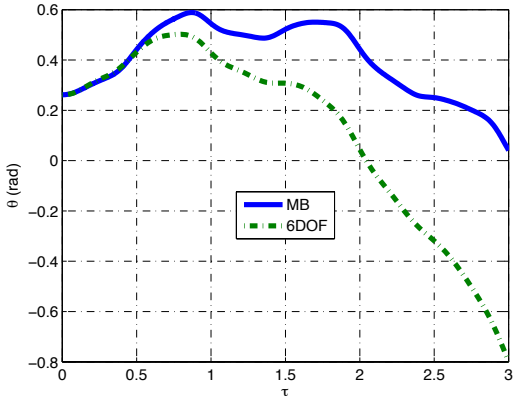

(c) Case 3: $\theta_o = 15°$, $\beta = -25°$, $f = 26$ Hz

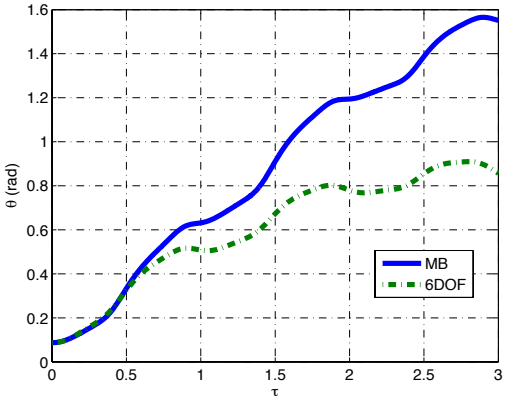

(d) Case 4: $\theta_o = 5°$, $\beta = -5°$, $f = 24$ Hz

Figure 2.6: Pitch Orientation Results for Dynamic Model Comparison with $\alpha_m = 45°$, $\zeta_m = 60°$

2.5.3 Dynamic Model Comparison - Aerodynamic Model Comparison

The following simulations will show that the qualitative performance of the flight dynamics models, for both the model presented in this paper and the standard aircraft model, is similar for different aerodynamic models. The two flight dynamics models previously presented will be compared with different aerodynamic models: the Berman and Wang model previously discussed and the blade-element/quasi-steady model used in [39, 89]. The model in [39, 89] is a combination of a quasi-steady model from the Sane and Dickinson 'Robot Fly' experiments and empirically matched data. The model includes delayed stall and rotational lift effects, but does not include wake

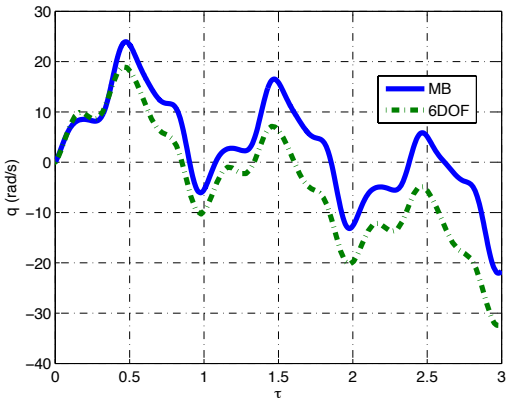

(a) Case 1: $\theta_o = 34.9°$, $\beta = -16°$, $f = 26$ Hz

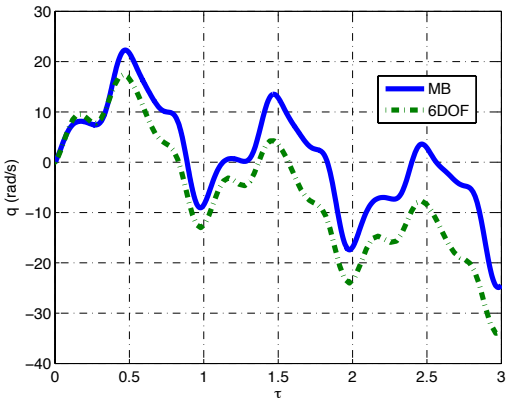

(b) Case 2: $\theta_o = 20.0°$, $\beta = -20°$, $f = 26$ Hz

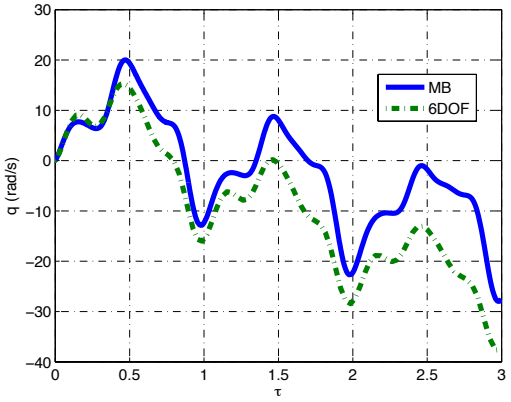

(c) Case 3: $\theta_o = 15°$, $\beta = -25°$, $f = 26$ Hz

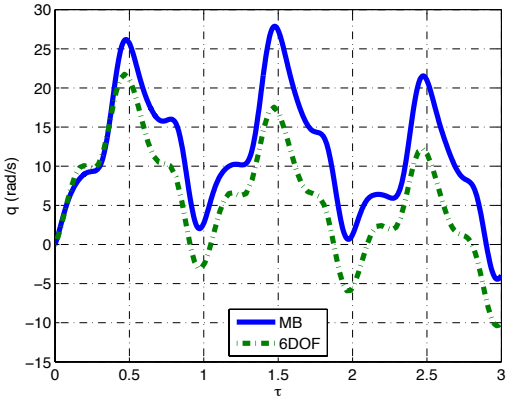

(d) Case 4: $\theta_o = 5°$, $\beta = -5°$, $f = 24$ Hz

Figure 2.7: Pitch Velocity Results for Dynamic Model Comparison with $\alpha_m = 45°$, $\zeta_m = 60°$

capture or leading edge vortex effects. The model calculates normal and tangential forces on the wing. The forces due to the translation of the wing are

$$F_{tr,N}(t) = \frac{1}{2}\rho A_w C_N(\alpha(t)) U_{cp}^2(t) \quad \text{and} \quad F_{tr,T}(t) = \frac{1}{2}\rho A_w C_T(\alpha(t)) U_{cp}^2(t). \tag{2.59}$$

The normal force on the wing, due to the rotation of the wing, is

$$F_{rot,N}(t) = \frac{1}{2}\rho A_w C_{rot} c_{max} \dot{\alpha}(t) U_{cp}(t). \tag{2.60}$$

In Equations (2.59) and (2.60), A_w is the area of the wing, C_N and C_T are the normal and tangential force coefficients, $U_{cp}(t)$ is the velocity of the center of pressure, and C_{rot} is the rotational lift coefficient. The normal and tangential forces are transformed into the B frame according to Equation (2.32).

The comparison simulations are presented in Figs. 2.8 and 2.9. The simulation of the model with wing effects and the Berman and Wang model is represented by the solid line. The simulations of the full nonlinear model with the comparison aerodynamic model, denoted 'UCB', is shown by the dash-dot line. The standard aircraft simulation results with the Berman and Wang model are represented by the dashed line and the results with the comparison model are represented by the dashed line. Simulations with the multi-body model are denoted by 'MB.' Simulations with the standard aircraft model are denoted by '6DOF.' The presented simulations are for a wing mass of 47 mg per wing. The stroke plane angle is set at -16° and the initial pitch angle is 16°. The initial orientation of the wings is parallel to the ground in the inertial frame. A summary of the input parameters for the aerodynamic model comparison simulations is presented in Table 2.3.

Case	Mid-stroke Angle of Attack $\alpha_m(^\circ)$	Flapping Amplitude $\zeta_m(^\circ)$	Flapping Frequency $f\,(Hz)$
1	45	60	24
2	40	60	24
3	45	58	23
4	40	58	23

Table 2.3: Summary of Input Parameters for Aerodynamic Model Comparison Simulations, Presented in Figures 2.8 and 2.9

The models with wing effects exhibit similar dynamic behavior, independent of the aerodynamic model. Likewise, the standard aircraft model exhibits similar behavior with different aerodynamic models. Both models produce a significant quantitative difference in position after three wing strokes. The inertial position shows a qualitative similarity between the two dynamics models. The inertial position results are

presented in Figure 2.8. The difference in aerodynamic models is significant in the inertial position of the FWMAV, when compared with the standard aircraft model. As shown in Section 2.5.2, there is a marked difference in the position of the two models after three wing beats when the Berman and Wang aerodynamic model is used. However, the UCB model also predicts a significant difference in position. The difference is even greater, approximately 0.5 body lengths after three flapping cycles. The results show that the multi-body dynamics model predicts different behavior, independent of the aerodynamic model being used to generate the aerodynamic forces and moments. The multi-body dynamics, from the simulation results, seem less susceptible to difference in position when given a choice of aerodynamic model, than the standard aircraft dynamics. The multi-body flight dynamics predict translation in the same direction and the most significant error is in altitude (or height). The standard aircraft model, on the other hand, does not have predictions that are consistent in the same direction for the cases presented.

The pitch orientation results for the aerodynamic model comparison are presented in Figure 2.9. The aerodynamic models produce qualitatively similar behavior in the angular position of the central body between the two dynamics models. However, the quantitative difference is significant and predicts different behavior. The pitch angle of the model with wing effects increases at a faster rate with the 'UCB' model than with the Berman and Wang model. After three flapping cycles, the 'UCB' model predicts a continuing increase in the pitch angle of the central body for both the standard aircraft and multi-body model. The models using the Berman and Wang model predict a decreasing pitch angle.

The 'UCB' model does not predict a significant difference in the attitude of the FWMAV when the wing effects are included, but the position still exhibits a large difference, on the order of 1.5 body lengths in three flapping cycles. The Berman and Wang aerodynamic model predicts different behavior in both position and orientation,

when the wing effects are included. The 'UCB' model exhibits similar behavior in attitude, but different behavior in position, when the wing effects are included. In fact, the difference between the position of the two models for the 'UCB' model is approximately 50% greater than that of the two dynamics models when the Berman and Wang model is used. The aerodynamic model comparison shows that despite the choice of different aerodynamic models, the flight dynamics difference between the standard aircraft model and the multi-body model are significant. Furthermore, different aerodynamics models can predict significant differences when the standard aircraft model is used for the flight dynamics model.

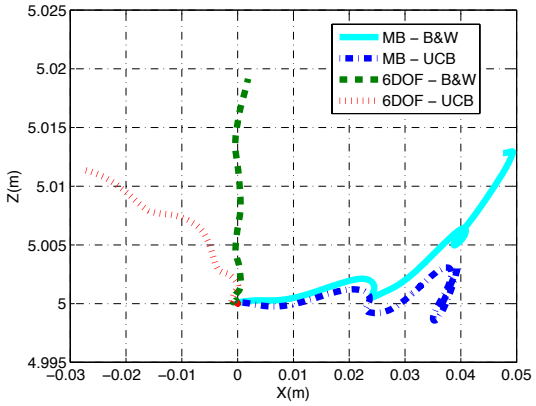

(a) Case 1: $\alpha_m = 45°$, $\zeta_m = 60°$, $f = 24$ Hz

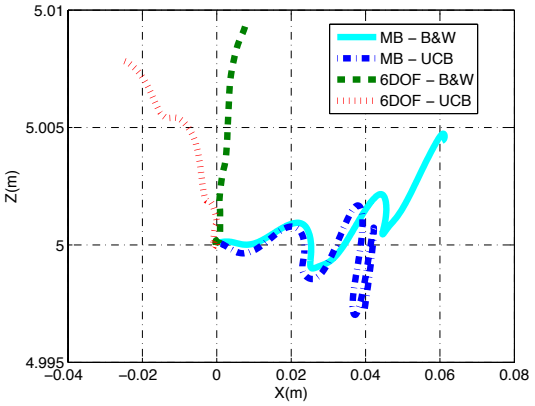

(b) Case 2: $\alpha_m = 40°$, $\zeta_m = 60°$, $f = 24$ Hz

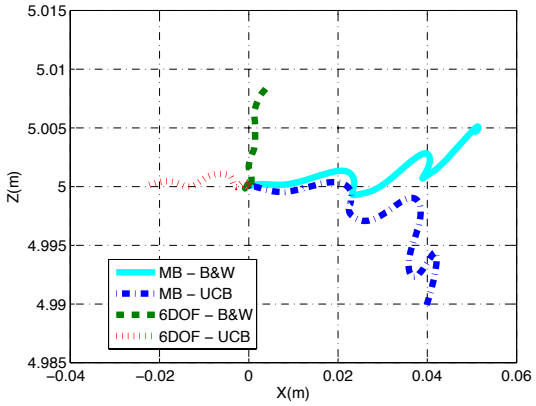

(c) Case 3: $\alpha_m = 45°$, $\zeta_m = 58°$, $f = 23$ Hz

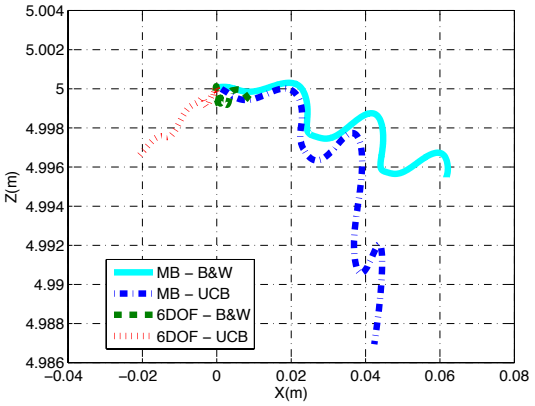

(d) Case 4: $\alpha_m = 45°$, $\zeta_m = 58°$, $f = 23$ Hz

Figure 2.8: Inertial Position Results for Aerodynamic Model Comparison: $\theta_o = 16°$, $\beta = -16°$

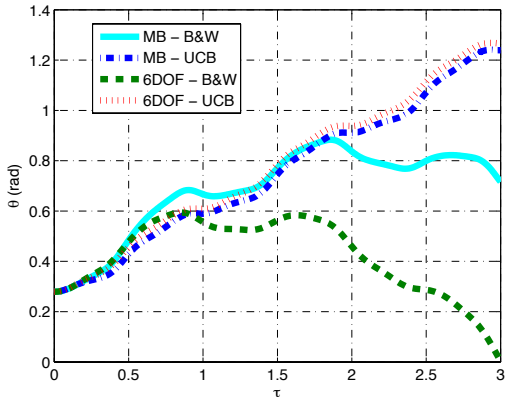

(a) Case 1: $\alpha_m = 45°$, $\zeta_m = 60°$, $f = 24$ Hz

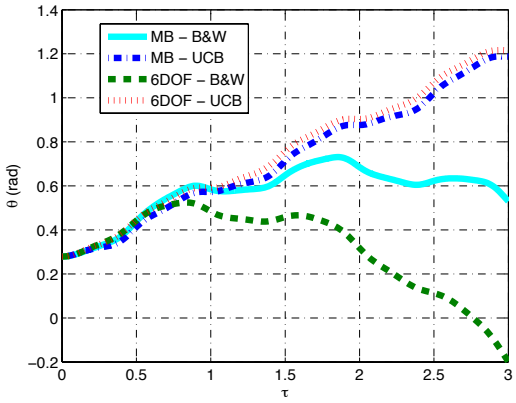

(b) Case 2: $\alpha_m = 40°$, $\zeta_m = 60°$, $f = 24$ Hz

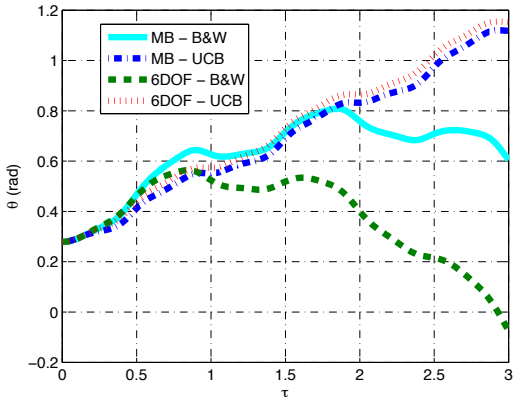

(c) Case 3: $\alpha_m = 45°$, $\zeta_m = 58°$, $f = 23$ Hz

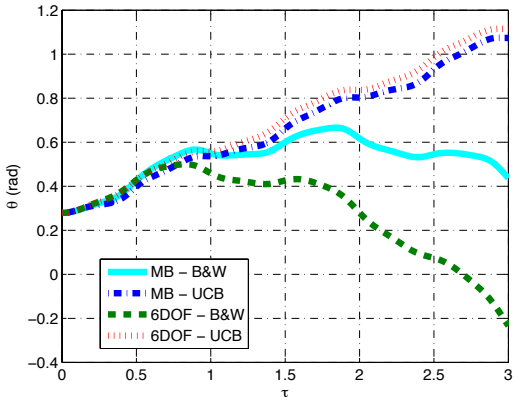

(d) Case 4: $\alpha_m = 45°$, $\zeta_m = 58°$, $f = 23$ Hz

Figure 2.9: Pitch Orientation Results for Aerodynamic Model Comparison: $\theta_o = 16°$, $\beta = -16°$

2.5.4 Dynamic Model Comparison - Decreased Wing Mass

The following simulations results show the comparison between the nonlinear model with wing effects and the standard aircraft model, with the mass of the wings decreased from the previous water treading simulations. The simulations use the same initial conditions for velocity as the previous simulation results. The aerodynamic model used is the model presented in [36]. Each set of simulations presented

shows results for different number of flapping cycles and different conditions for the initial pitch angle, stroke plane angle, and flapping frequency. The first set of simulations shows the inertial position, pitch angle and pitch velocity with the wing mass reduced by one half to 23.5 mg per wing. The $^1/_2$ wing mass simulations are represented by the dash-dot line. The second set of comparison simulations presents results with the wing mass reduced to $^1/_8$ of the initial wing mass, or approximately 5.875 mg for each wing, and is represented by the dashed line. The solid line represents the full wing mass. The simulation results for zero wing mass, alternatively the standard aircraft model, are represented by the dotted line. Figure 2.10 shows the simulation results for the inertial position of the FWMAV. The input parameters for the decrease wing mass simulations is presented in Table 2.4.

Case	Initial Pitch Angle $\theta_o\,(^\circ)$	Stroke Plane $\beta\,(^\circ)$	Flapping Frequency $f\,(Hz)$	Number of Flapping Cycles
1	0	0	22	4
2	15	-15	24	3
3	22.5	-22.5	23	2
4	45	-45	25	2.5

Table 2.4: Summary of Input Parameters for Decreased Wing Mass Simulations, Presented in Figures 2.10-2.12

The simulation results show that as the mass of the wings is decreased, relative to the central body, the multi-body dynamics model approaches the standard aircraft model. The simulation results for pitch orientation in Figure 2.11 and pitch velocity in Figure 2.12 present a similar trend. In nature, the mass of insects tends to decrease with increase flapping frequency. Also, as a general trend to be shown in Chapter 5, the relative mass of the wings of insects also tends to decrease with the mass of insects. A vehicle of the size presented here, with a total mass of approximately 1.6 grams, does not usually have wings with a combined mass of only 11.5 mg.

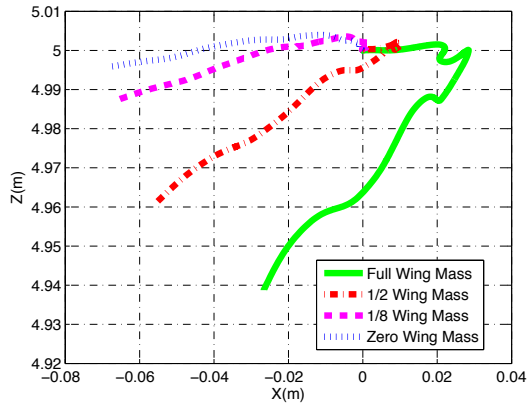

(a) Case 1: $\theta_o = 0°$, $\beta = 0°$

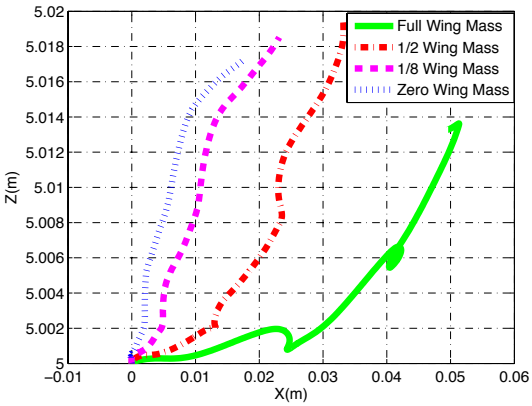

(b) Case 2: $\theta_o = 15.0°$, $\beta = -15°$

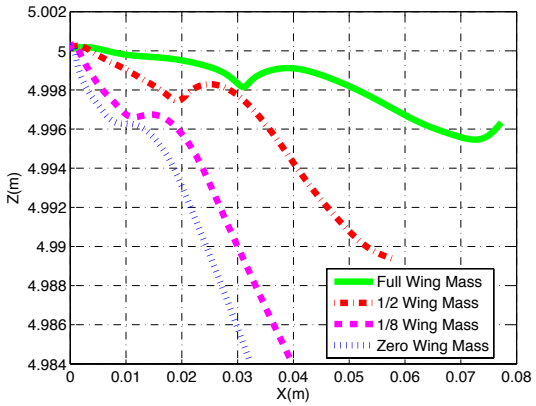

(c) Case 3: $\theta_o = 45°$, $\beta = -45°$

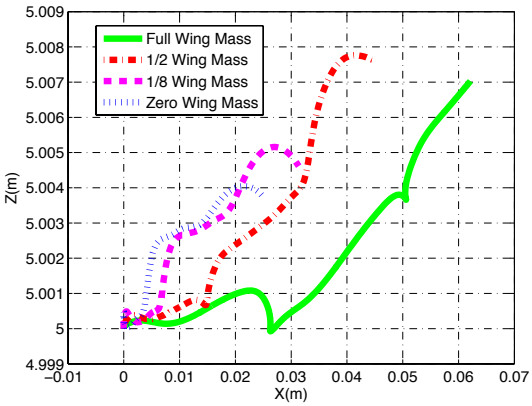

(d) Case 4: $\theta_o = 22.5°$, $\beta = -22.5°$

Figure 2.10: Inertial Position Results for Mass Comparison $\alpha_m = 45°$, $\zeta_m = 60°$.

The simulation results presented in Figs. 2.10-2.12 show that as the mass of the wings relative to the central body decreases, the simulation results from the full nonlinear model approach the results of the model with simple nonlinear dynamics. However, there are still differences in simulation results when the wings total only 0.71% of the total body mass, especially in the inertial position of the central body. The simulations presented with full wing mass showed that the wings may reduce the destabilizing effect of the aerodynamic pitching moment. As the mass of the wings is reduced relative to the central body, the aerodynamic pitching moment seems to have more of an effect on the attitude of the central body. The simulation results lead to the conclusion that the relative importance of the mass of the wings, from a

dynamics standpoint, should decrease as the mass of the wings decrease relative to the total mass of the flapping wing micro air vehicle.

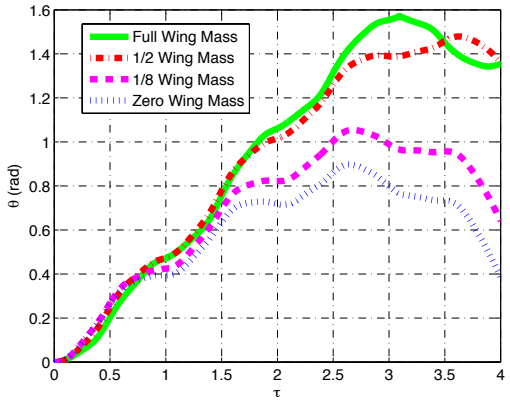

(a) Case 1: $\theta_o = 0°$, $\beta = 0°$

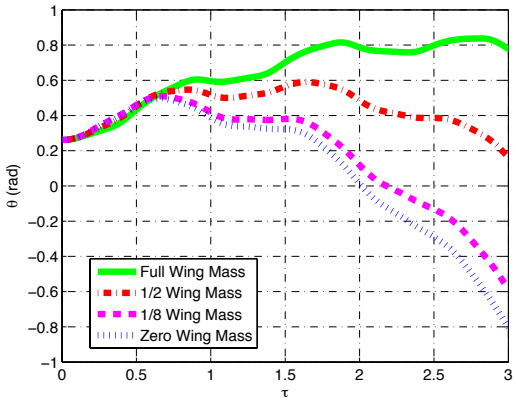

(b) Case 2: $\theta_o = 15.0°$, $\beta = -15°$

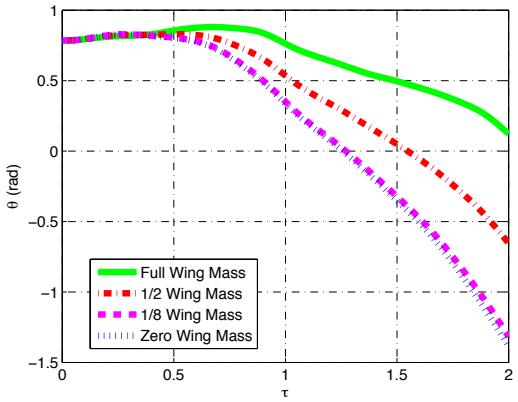

(c) Case 3: $\theta_o = 45°$, $\beta = -45°$

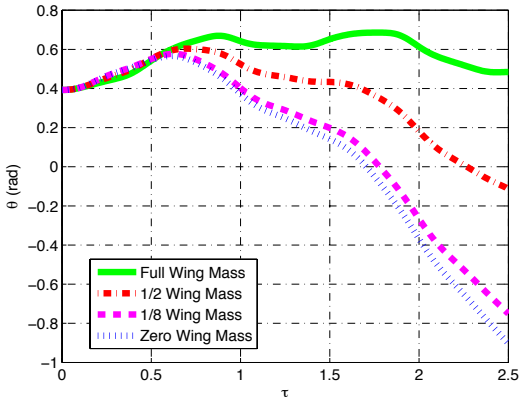

(d) Case 4: $\theta_o = 22.5°$, $\beta = -22.5°$

Figure 2.11: Pitch Orientation Results for Mass Comparison $\alpha_m = 45°$, $\zeta_m = 60°$.

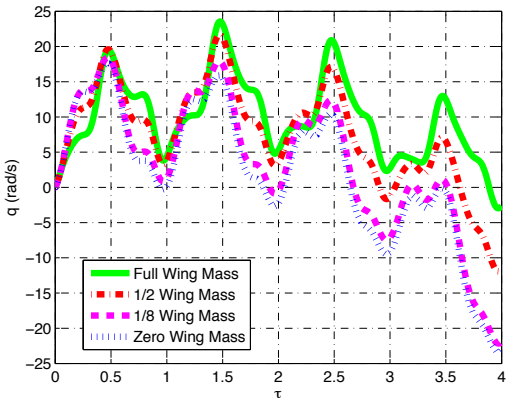

(a) Case 1: $\theta_o = 0°$, $\beta = 0°$

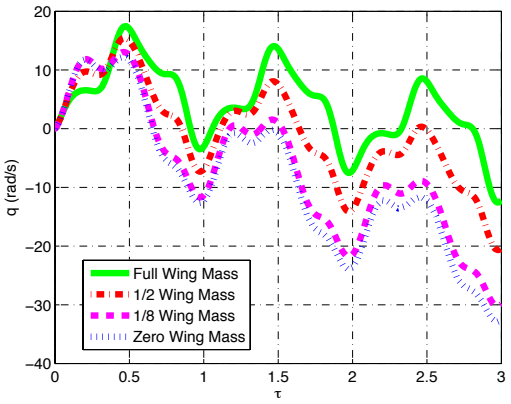

(b) Case 2: $\theta_o = 15.0°$, $\beta = -15°$

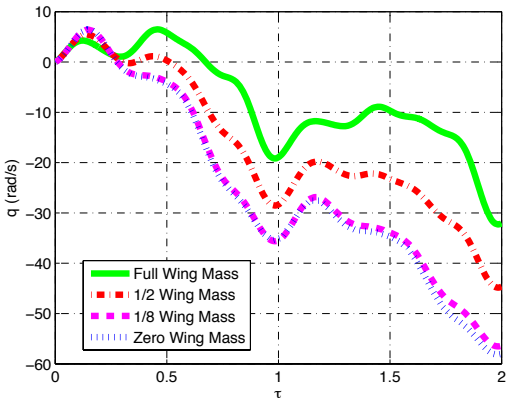

(c) Case 3: $\theta_o = 45°$, $\beta = -45°$

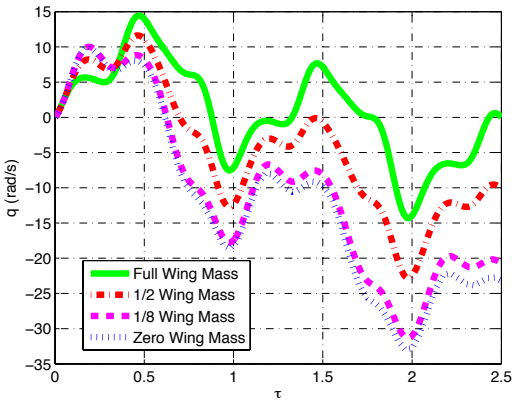

(d) Case 4: $\theta_o = 22.5°$, $\beta = -22.5°$

Figure 2.12: Pitch Velocity Results for Mass Comparison $\alpha_m = 45°$, $\zeta_m = 60°$.

2.6 Conclusions

The chapter presented the derivation and simulation of the nonlinear dynamics of a flapping wing micro air vehicle with three degrees of freedom. The dynamic model includes the mass and inertia effects of the wings. The simulations show that the common practice of neglecting the mass of the wings produces a vastly different result from when mass coupling effects of the wings are included. Additionally, the choice of aerodynamic model, and the associated underlying assumptions, can make a substantial difference in the predicted behavior of the system. The total wing mass is 5.7% for the initial set of simulations, on the outside of the range of wing mass

values that lead to neglecting the effects of the wings. However, the inertial position (and translational velocity) results are vastly different for the full nonlinear model and the standard aircraft models. For the same flapping frequency in a water treading hovering mode, the full nonlinear model climbs and translates forward, while the standard aircraft models continue to ascend and translate backwards. Changing the aerodynamic model produces qualitatively similar results. A difference in behavior between the flight dynamics model with wing effects, and the model without, is present for a total wing mass of 0.7% of the body mass.

From a simulation standpoint, neglecting the mass effects of the wings on the central body of a FWMAV may be foolhardy for flight stability and controls studies of a flapping wing aircraft. Some, if not all, of the mass effects of the wings need to be included for a representative model of the aircraft dynamics and performance. The wing effects, as detailed in this study, are important in an open loop setting. When active controls are added to the system, the result may change. Furthermore, the relative importance of the effects of the wings on the motion of the central body needs to be examined. The following chapter will presents a method of approximating the dynamics of flapping wing micro air vehicles, in order to enable studies of the relative importance of the mass of the wings.

CHAPTER 3

Averaging of the Nonlinear Dynamics of Flapping Wing Micro Air Vehicles for Symmetrical Flapping

3.1 Introduction

In order to analyze the importance of the mass coupling effects of the wings on the position and orientation of the body of a FWMAV, the multi-body model presented in Chapter 2 needs to be transformed to first order form. Once transformed into first order form, an approximation technique of some form may be used to enable analysis of the larger system. Numerous techniques are available for approximations of nonlinear systems. A natural choice, due to the periodic nature of the system, is averaging theory. Averaging, in the traditional sense, involves equations of the following form

$$\dot{x} = \varepsilon\, f(x,t), \tag{3.1}$$

where ε is a small parameter. Classical averaging theory applies to equations of the form of Equation (3.1), commonly referred to as averaging in the standard form. Averaging in the non-standard form involves equations of the following form:

$$\dot{x} = f^{(0)}(x,t) + \varepsilon^1 f^{(1)}(x,t) + \varepsilon^2 f^{(2)}(x,t) + \cdots + \varepsilon^n f^{(n)}(x,t), \tag{3.2}$$

where $\varepsilon^1 \ldots \varepsilon^n$ are perturbations of order $1 \ldots n$ and we used the notation of Bogoliubov and Mitropolsky in [115] and [116]. According to [117], local (naïve) averaging is not encouraged due to inaccurate results. Local averaging involves equations of motion of the form of either Equation (3.1) or Equation (3.2) and integrating according to

$$\bar{f}(x) = \frac{1}{T} \int_{t}^{t+T} f(x,t)dt \tag{3.3}$$

where T is the desired period for integration. In order to place an equation of the form in Equation (3.2) in the standard form, the analytical solution of the unperturbed system is required [117]. The equation of the form in Equation (3.2), to ε precision, is solved for $\varepsilon = 0$ and a given initial condition. The explicit solution, denoted by $x = h(y,t)$, is then composed into the ε portion of the equation according to the method of the variation of constants. The formula is

$$\frac{\partial h(t,y)}{\partial t} + \left[\frac{\partial h}{\partial y}(y,t)\right] \frac{dh}{dt} = f^{(0)}\left(h(y,t),t\right) + \varepsilon f^{(1)}\left(h(y,t),t,\varepsilon\right), \tag{3.4}$$

where $\left[\frac{\partial h}{\partial y}\right]$ denotes the Jacobian of the solution $x = h(y,t)$. The first terms on the left and right sides of the equation cancel out and the resultant perturbation problem in the standard form is [117]

$$\dot{h} = \varepsilon \left[\frac{\partial h}{\partial y}(y,t)\right]^{-1} f^{(1)}\left(h(y,t),t,\varepsilon\right). \tag{3.5}$$

Once the equation is placed in the standard form, $\dot{h}$ can then be averaged in the traditional sense.

A classic technique for dealing with nonlinear elements in dynamics systems is the method of describing functions. Originally developed by Krylov and Bogoliubov in [115], the method replaces nonlinear elements in an otherwise linear system with constant gains. The gains are based on the frequency and/or amplitude of the input

to the nonlinear 'block.' Further treatment of the method of describing functions is available in [118], [119], and [120]. Describing functions does not fit as an approximation technique because the method requires that the nonlinear elements are odd functions. The method would immediately eliminate many of the nonlinearities in the equations of motions, simply because the functions are even functions.

Asymptotic methods of approximation do not fit the problem, either. The regular perturbation problem, is described by the dynamical system

$$\dot{x} = f\left(t, x, \varepsilon\right), \tag{3.6}$$

where ε is a 'small' parameter. The regular perturbation problem is covered extensively in [115], [116], and [121]. The regular perturbation method uses Taylor series expansions to approximate the exact solution and is often applied to weakly coupled systems. The interactions between the wings and the body in the flight dynamics model of a flapping wing micro air vehicle are strongly coupled and may exist at different time scales. A method of approximating a strongly coupled nonlinear system, often with multiple time scales, is the singular perturbation method. The singular perturbation method involves systems of equations of the form

$$\begin{aligned} \dot{x} &= f\left(t, x, z, \varepsilon\right) \\ \varepsilon\dot{z} &= g\left(t, x, z, \varepsilon\right), \end{aligned} \tag{3.7}$$

where ε is the small parameter. The singular perturbation method does not necessarily fit the applications of the system, either. As detailed in [121], [122], and [123], the singular perturbation method requires exponential stability of the boundary layer system ($g(.)$). Furthermore, for control applications as detailed in [123], the equilibrium point of the 'slow' system ($f(.)$) needs to be asymptotically stable without control. Unfortunately, the flapping wing equations of motion are not asymptotically

stable without control.

The chapter will present the derivation of the first order equations of motion. Using the mass of the wings as the 'small' parameter, the equations of motion can be transformed into the form of Equation (3.2). The equations of motion are the standard aircraft equations of motion with first and second order perturbations due to the mass of the wings. Local averaging will be used to obtain a poor solution, as predicted by [117]. Classical averaging techniques are not available since the general analytical solution of the standard aircraft equations of motion, when $\varepsilon \equiv 0$, does not exist. An approximation technique, coined 'quarter-cycle' averaging, will be used to approximate the equations of motion. The technique results in greater than an order of magnitude improvement in the approximation error in the system versus local averaging for three different flight conditions: hovering, forward flight, and vertical flight. The derivation of the first order equations of motion and the subsequent approximation technique will allow for the analysis of the (relative) importance of the wings in the dynamics, stability, and control of flapping wing micro air vehicles.

3.2 First Order Equations of Motion

In order to conduct any analysis using averaging theory, the equations of motion presented in Chapter 2 need to be decoupled and placed into first-order form. The equations of motion can be placed into the following form

$$\mathbf{M}\dot{\mathbf{u}}_j = \begin{bmatrix} \bar{F}_{aero} + \bar{F}_g - \sum_{i=1}^{3} \left(\dot{\bar{\mathbf{v}}}_{i,red} + \ddot{\bar{\rho}}_{ci,red} \right) \\ \bar{M}_{aero} + \bar{M}_g - \sum_{i=1}^{3} \left(\mathbf{I}_i \bar{\omega}_1 \times \bar{\omega}_i + \bar{\omega}_i \times \mathbf{I}_i \bar{\omega}_1 + m_i \bar{\rho}_{ci} \times \dot{\bar{\mathbf{v}}}_{i,red} \right) \\ Q_{RW} - \left(\mathbf{I}_2 \bar{\omega}_1 \times \bar{\omega}_2 + \bar{\omega}_2 \times \mathbf{I}_2 \bar{\omega}_2 + m_2 \bar{\rho}_{c2} \times \dot{\bar{\mathbf{v}}}_{2,red} \right) \\ Q_{LW} - \left(\mathbf{I}_3 \bar{\omega}_1 \times \bar{\omega}_3 + \bar{\omega}_3 \times \mathbf{I}_3 \bar{\omega}_3 + m_3 \bar{\rho}_{c3} \times \dot{\bar{\mathbf{v}}}_{3,red} \right) \end{bmatrix}, \qquad (3.8)$$

with $\dot{\mathbf{u}}_j \in \mathbb{R}^{12\text{x}1}$ and $\mathbf{M} \in \mathbb{R}^{12\text{x}12}$. The vector $\dot{\mathbf{u}}_j$ contains the time derivatives of the quasi-velocities presented in Chapter 2. $\mathbf{M}$ in Equation (3.8) is a time-varying mass matrix describing the coupling between the time rate of change of the various quasi-velocities. The terms $\ddot{\bar{\rho}}_{ci,red}$ and $\dot{\bar{\mathbf{v}}}_{i,red}$ represent the reduced forms of the terms defined in Chapter 2. The terms contain the components of the vectors $\ddot{\bar{\rho}}_{ci}$ and $\dot{\bar{\mathbf{v}}}_i$ that do not contain time-derivatives of the quasi-velocities. The details are in Appendix A. Traditionally, the first-order form for equations of motion is obtained by inverting the matrix $\mathbf{M}$. However, the analytical inversion of a 12x12 matrix with symbolic inputs is computationally intractable.

In order to obtain the first order equations of motion, an approximate inverse is used to decouple the equations of motion. The approximate inverse has the form

$$\mathbf{M}^{-1} = (\mathbf{A} + \varepsilon\mathbf{E})^{-1} = \mathbf{A}^{-1} + \varepsilon\mathbf{A}^{-1}\mathbf{E}\mathbf{A}^{-1}. \tag{3.9}$$

In this case, the mass of the wings is considered as the small parameter ε. All of the terms in $\mathbf{E}$ contain the mass of the wings. If the mass of the wings is equal to zero, then $\mathbf{E} \equiv 0$. The details of the composition of the approximate inverse are contained in Appendix B. The analysis will be based on symmetrical flapping with respect to the body. Symmetrical flapping is achieved with identical stroke plane angles ($\beta_R = \beta_L$), identical flapping angles ($\zeta_R = \zeta_L$), identical deviation angles ($\delta_R = \delta_L$), and identical pitch angles ($\alpha_R = \alpha_L$). Furthermore, if the following initial conditions are met: $p = r = 0$, $\psi = \phi = 0$, then the FWMAV will maintain longitudinal flight given proper choices of the wing motion. Identical wing angles, and associated time derivatives of the wing angles, produces angular velocities where $p_{RW} = -p_{LW}$, $q_{RW} = q_{LW}$, and $-r_{RW} = r_{LW}$. Furthermore, with symmetrical flapping and wings with the same length and mass parameters, the inertia terms for $I_{xy,w}$ and $I_{yz,w}$ are equal in magnitude and opposite sign (where the appropriate wing is substituted for

w). The remaining inertia tensor terms ($I_{xx,w}, I_{xz,w}, I_{yy,w}$, and $I_{zz,w}$) are equal in both sign and magnitude.

The assumptions enable simplification of various terms and enable the derivation of first order equations of motion. The assumptions, when combined with the approximate inverse defined in Equation (3.9), produce the first order equations of motion. The inverse also enables the calculation of the control moments of the wings. Alternatively, the control moments can be defined as the required accelerations of the wing angular velocities to produce the required wing angles and, by extension, the necessary aerodynamic forces and moments to maneuver the FWMAV. Using the approximate matrix inversion, we can calculate the control moments required to achieve the desired values for the time derivatives of the angular velocities of the wings. The control moments for the right wing and left wing are calculated according to

$$Q_{RW} = \mathbf{R}_{\beta_R}{}^{\mathrm{T}} \mathbf{I}_2 \mathbf{R}_{\beta_R}{}^{\mathrm{T}} \begin{bmatrix} \dot{p}_{RW,d} \\ \dot{q}_{RW,d} \\ \dot{r}_{RW,d} \end{bmatrix} \text{ and } Q_{LW} = \mathbf{R}_{\beta_L}{}^{\mathrm{T}} \mathbf{I}_3 \mathbf{R}_{\beta_L}{}^{\mathrm{T}} \begin{bmatrix} \dot{p}_{LW,d} \\ \dot{q}_{LW,d} \\ \dot{r}_{LW,d} \end{bmatrix}. \tag{3.10}$$

For future reference, we define the following

$$\Omega_{RW,d} = \begin{bmatrix} \dot{p}_{RW,d} \\ \dot{q}_{RW,d} \\ \dot{r}_{RW,d} \end{bmatrix} \quad \text{and} \quad \Omega_{LW,d} = \begin{bmatrix} \dot{p}_{LW,d} \\ \dot{q}_{LW,d} \\ \dot{r}_{LW,d} \end{bmatrix}, \tag{3.11}$$

where d in the subscript denotes the desired values of the time derivatives of the wing angular velocities. Based on the calculation of the control moments, we assume that the system will produce the desired wing motion. Therefore, the system of equations can be reduced to a longitudinal system of equations with the wing effects included in the equations governing the translational and rotational behavior of the body.

3.2.1 $\dot{u}$ - Longitudinal Velocity of the Body

The first equation governs the longitudinal velocity of the body. Putting the $\dot{u}$ equation in the form of Equation (3.2), we can write

$$\dot{u} = \dot{x}_1 = f_1^{(0)}(x,t) + \varepsilon f_1^{(1)}(x,t) + \varepsilon^2 f_1^{(2)}(x,t). \tag{3.12}$$

The first term, $f_1^{(0)}$ represents the longitudinal equation of motion for an aircraft in the absence of yawing and rolling motion:

$$f_1^{(0)} = \frac{1}{m_{sys}} F_x - g\sin\theta - qw. \tag{3.13}$$

The second term, $f_1^{(1)}$, represents the first order effects of the wings on the motion of the central body:

$$\begin{aligned} f_1^{(1)} &= \frac{1}{m_{sys}}\Big(\left(\tilde{\rho}_{c2}^{\mathrm{T}} \mathbf{R}_{\beta_R}{}^{\mathrm{T}} + \mathbf{R}_{\beta_R}{}^{\mathrm{T}} \Theta_{RW}\right) \Omega_{RW,d} \\ &\quad + \left(\tilde{\rho}_{c3}^{\mathrm{T}} \mathbf{R}_{\beta_L}{}^{\mathrm{T}} + \mathbf{R}_{\beta_L}{}^{\mathrm{T}} \Theta_{LW}\right) \Omega_{LW,d}\Big) \cdot \hat{b}_x \\ &\quad + \left(\left(\rho_{c2,z} + \rho_{c3,z}\right) \frac{\left(M_R + M_L\right)}{m_{sys} I_{yy,sys}} \right) - \frac{1}{m_{sys}} \left(\ddot{\bar{\rho}}_{c2,red} + \ddot{\bar{\rho}}_{c3,red}\right) \cdot \hat{b}_x. \end{aligned} \tag{3.14}$$

The third term, $f_1^{(2)}$ represents the second order effects of the wings on the motion of the central body. The second order effects are

$$\begin{aligned} f_1^{(2)} &= \frac{\left(\rho_{c2,z} + \rho_{c3,z}\right)}{m_{sys} I_{yy,sys}} \Bigg(\Big(\overline{M}_g \\ &\quad - \sum_{i=2}^{3} \left(\bar{\omega}_1 \times \mathbf{I}_i \bar{\omega}_i + \bar{\omega}_i \times \mathbf{I}_i \bar{\omega}_i + m_i \bar{\rho}_{ci} \times \dot{\bar{\mathbf{v}}}_{i,red} \right) \Big) \cdot \hat{b}_y \Bigg). \end{aligned} \tag{3.15}$$

3.2.2 $\dot{w}$ - Vertical Velocity of the Body

As with the equation for $\dot{u}$, we wish to write $\dot{w}$ in the following form:

$$\dot{w} = \dot{x}_2 = f_2^{(0)}(x,t) + \varepsilon f_2^{(1)}(x,t) + \varepsilon^2 f_2^{(2)}(x,t). \tag{3.16}$$

The first term of $\dot{x}_2$ has the same form as the standard aircraft equations of motion for vertical velocity:

$$f_2^{(0)} = \frac{1}{m_{sys}} F_z + g\cos\theta + qu. \tag{3.17}$$

The first order effects of the wings on the vertical translation of the central body are

$$\begin{aligned} f_2^{(1)} \;=\; & \frac{1}{m_{sys}}\Big(\left(\tilde{\rho}_{c2}^{\mathrm{T}} \mathbf{R}_{\beta_R}{}^{\mathrm{T}} + \mathbf{R}_{\beta_R}{}^{\mathrm{T}} \Theta_{RW}\right) \Omega_{RW,d} \\ & + \left(\tilde{\rho}_{c3}^{\mathrm{T}} \mathbf{R}_{\beta_L}{}^{\mathrm{T}} + \mathbf{R}_{\beta_L}{}^{\mathrm{T}} \Theta_{LW}\right) \Omega_{LW,d} \Big) \cdot \hat{b}_z \\ & - \left(\left(\rho_{c2,x} + \rho_{c3,x}\right) \frac{(M_R + M_L)}{m_{sys} I_{yy,sys}} \right) - \frac{1}{m_{sys}} \left(\ddot{\bar{\rho}}_{c2,red} + \ddot{\bar{\rho}}_{c3,red}\right) \cdot \hat{b}_z \end{aligned} \tag{3.18}$$

The second order effects of the wings on the vertical translation of the central body are

$$\begin{aligned} f_2^{(2)} \;=\; & \frac{\left(\rho_{c2,x} + \rho_{c3,x}\right)}{m_{sys} I_{yy,sys}} \Bigg(\Big(- \overline{M}_g \\ & + \sum_{i=2}^{3} \left(\bar{\omega}_1 \times \mathbf{I}_i \bar{\omega}_i + \bar{\omega}_i \times \mathbf{I}_i \bar{\omega}_i + m_i \bar{\rho}_{ci} \times \dot{\bar{\mathbf{v}}}_{i,red} \right) \Big) \cdot \hat{b}_y \Bigg). \end{aligned} \tag{3.19}$$

3.2.3 $\dot{q}$ - Pitch Velocity of the Body

The equations of motion for $\dot{q}$ can be placed in the same form as $\dot{u}$ and $\dot{w}$, such that

$$\dot{q} = \dot{x}_3 = f_3^{(0)}(x,t) + \varepsilon f_3^{(1)}(x,t) + \varepsilon^2 f_3^{(2)}(x,t). \tag{3.20}$$

The first term, $f_3^{(0)}$, is simply defined by the aerodynamic pitching moment and is calculated according to

$$f_3^{(0)} = \frac{M_R + M_L}{I_{yy,sys}}. \tag{3.21}$$

The first order effects of the mass of the wings on the pitch velocity of the central body are

$$\begin{aligned} f_3^{(1)} &= \frac{1}{m_{sys} I_{yy,sys}} \Big(\left(\rho_{c2,z} + \rho_{c3,z}\right) \left(F_x - m_{sys} \left(g \sin\theta + qw\right)\right) \\ &\quad - \left(\rho_{c2,x} + \rho_{c3,x}\right) \left(F_z + m_{sys} \left(g \cos\theta + qu\right)\right) \Big) \\ &\quad + \frac{1}{I_{yy,sys}} \left(\overline{M}_g - \sum_{i=2}^{3} \left(\bar{\omega}_1 \times \mathbf{I}_i \bar{\omega}_i + \bar{\omega}_i \times \mathbf{I}_i \bar{\omega}_i + m_i \bar{\rho}_{ci} \times \dot{\bar{\mathbf{v}}}_{i,red} \right) \right) \cdot \hat{b}_y \\ &\quad + \frac{1}{I_{yy,sys}} \left({A_{22}}^{-1} E_{23} \Omega_{RW,d} + {A_{22}}^{-1} E_{24} \Omega_{LW,d} \right) \cdot \hat{b}_y, \end{aligned} \tag{3.22}$$

where A_{22}, E_{23}, and E_{24} are defined in Appendix B and represent the wing acceleration contribution to the pitch angle of the flapping wing micro air vehicle. The second order effects of the mass of the wings on the pitch velocity of the central body are

$$\begin{aligned} f_3^{(2)} &= \frac{1}{m_{sys} I_{yy,sys}} \Big(\left(\rho_{c2,x} + \rho_{c3,x}\right) \left(\left(\ddot{\bar{\rho}}_{c2,red} + \ddot{\bar{\rho}}_{c3,red}\right) \cdot \hat{b}_z \right) \\ &\quad - \left(\rho_{c2,z} + \rho_{c3,z}\right) \left(\left(\ddot{\bar{\rho}}_{c2,red} + \ddot{\bar{\rho}}_{c3,red}\right) \cdot \hat{b}_x \right) \Big). \end{aligned} \tag{3.23}$$

3.3 Averaging Results

The local averaging of the dynamic equations is obtained from the following equation

$$\dot{\bar{x}}(t) = \bar{f}^{(0)}(\bar{x}) + \varepsilon \bar{f}^{(1)}(\bar{x}) = \frac{1}{T} \int_0^T \dot{x}(t) dt = \frac{1}{T} \int_0^T f^{(0)}\left(x,t\right) + \varepsilon f^{(1)}(x,t) dt, \tag{3.24}$$

where the implicit functions of time are assumed to remain constant and explicit functions of time are integrated over a specified period, T. For a hover condition, we make the assumption that only two degrees of freedom per wing are needed, such that the deviation angle from the stroke plane will remain zero, e.g. $\delta_R = \delta_L \equiv 0$. The assumption reduces the complexity of several terms in the equations of motion, including the resultant aerodynamic forces and moments, the inertia tensors of the wings when expressed in the body frame, and the orientation of the centers of mass of the wings with respect to the origin of the body frame.

3.3.1 Aerodynamic Model

In order to average the equations of motion, an aerodynamic model is required. The aerodynamic model chosen is based on the model developed and presented by Deng, Schenato, et al. in [39] and [89] and previously presented in Section 2.5.3. We assume that the flapping angle, ζ, and the pitch angle of the wing, α, have the following form

$$\zeta(t) = \zeta_m \sin(2\pi f t) \quad \text{and} \quad \alpha(t) = \alpha_m \operatorname{sgn}\left(\dot{\zeta}\right). \tag{3.25}$$

The angle of attack is constant during each half-stroke. As a direct result, the time rate of change of the pitch angle is zero ($\dot{\alpha} \equiv 0$). The choice is made to simplify the calculation of the various integrals used to obtain the $^1/_4$-cycle equations to be presented and present an analytical solution. If the assumption is not made, the majority of the integrals to be calculated can only be evaluated numerically. It is important to note that a pitch angle of the form $\alpha(t) = \alpha_m \cos(2\pi f t)$ will produce qualitatively similar results. The velocity of the center of pressure of the wing, $U_{cp}(t)$, is assumed to act at the center of pressure calculated from Equation (2.33). The

velocity of the center of pressure can be written as

$$U_{cp}(t) = \hat{r}_2 b_w \dot{\zeta} = (\hat{r}_2 b_w)(\omega \zeta_m)\cos(\omega\, t), \tag{3.26}$$

where b_w denotes the semi-span of the wings (the span of one wing). The value for $U_{cp}(t)$ can be substituted into Equation (2.59) to obtain the normal and tangential forces on the wing generated by the motion of the wings:

$$F_T = \frac{1}{2}\rho_{sl} A_w C_T \left(\hat{r}_2 b_w \omega \zeta_m\right)^2 \cos^2(\omega t) \tag{3.27}$$

and

$$F_N = \frac{1}{2}\rho_{sl} A_w C_N \left(\hat{r}_2 b_w \omega \zeta_m\right)^2 \cos^2(\omega t)\,. \tag{3.28}$$

The rotational force contribution, previously defined in Equation (2.60), is identically zero since $\dot{\alpha} \equiv 0$. In Equations (3.27) and (3.28), $\hat{r}_2 b_w$ denotes the aerodynamic center of pressure of the wing for velocity calculations and $\omega = 2\pi f$, denotes the flapping frequency. The coefficients in Equations (3.27) and (3.28) are calculated according to

$$C_T = -0.4\,\mathrm{sgn}\left(\dot{\zeta}\right)\cos^2(2\alpha) \text{ and } C_N = -3.4\,\mathrm{sgn}\left(\dot{\zeta}\right)\sin(\alpha). \tag{3.29}$$

In Equation (3.29), the signum function is used to ensure proper orientation of the forces on the wings. Based on the assumption for the form of the pitch angle, $\alpha(t)$, the coefficients in Equation (3.29) can be simplified to

$$C_T = -0.4\,\mathrm{sgn}\left(\dot{\zeta}\right)\cos^2(2\alpha_m) \text{ and } C_N = -3.4\,\sin(\alpha_m). \tag{3.30}$$

The flapping velocity of the wings is assumed to be much greater than the velocity of the freestream air, since the FWMAV is considered to be at (or near) a hovering condition. Therefore, the velocity of the body of the FWMAV and the change in the

true angle of attack of the wing are neglected.

3.3.2 Averaged Forces

Rotating from the stroke plane frame to the body frame will not alter the time average of the aerodynamic forces, just the orientation of the forces in the body frame. We can examine, individually, the thrust and lift forces in the body frame for a parallel (to the longitudinal axis) stroke plane frame without loss of generality. The resultant thrust and lift forces are

$$F_x = (\cos\alpha\cos\zeta)\,F_T + (\sin\alpha\cos\zeta)\,F_N \tag{3.31}$$

and

$$F_z = -(\sin\alpha)\,F_T + (\cos\alpha)\,F_N \tag{3.32}$$

The average of the forces is obtained according to

$$\overline{F}_x = \frac{1}{2\pi}\int_0^{2\pi} F_x\,dt \quad \text{and} \quad \overline{F}_z = \frac{1}{2\pi}\int_0^{2\pi} F_z\,dt\,. \tag{3.33}$$

The thrust and lift forces are not continuous over the interval $[0,\, 2\pi]$, but are continuous over each quarter-stroke, due to the choice of representation of the normal and tangential force coefficients. The average of the lift and thrust forces is calculated by a summation of four integrals, each integral over a quarter-stroke: $\left[0,\, \frac{1}{2}\pi\right]$, $\left[\frac{1}{2}\pi,\, \pi\right]$, $\left[\pi,\, \frac{3}{2}\pi\right]$, and $\left[\frac{3}{2}\pi,\, 2\pi\right]$. The average of the thrust force in the stroke plane is identically zero. For simplicity in presentation, the following constants are defined (based on the averaged values):

$$k_T = 0.2\rho_{sl}A_w\cos^2(2\alpha_m)\,(\hat{r}_2 b_w\omega\zeta_m)^2 \text{ and } k_N = 1.7\rho_{sl}A_w\sin(\alpha_m)\,(\hat{r}_2 b_w\omega\zeta_m)^2\,. \tag{3.34}$$

The average of the lift force in the stroke plane is calculated according to

$$\overline{F}_{z,sp} = \frac{1}{2} k_T \sin(\alpha_m) - \frac{1}{2} k_N \cos(\alpha_m). \tag{3.35}$$

The integrals of individual terms are calculated using assistance from [124, 125, 126]. Figure 3.1 shows the instantaneous lift force and the averaged lift force for a flapping frequency of 21 Hz, a flapping amplitude of 60 degrees, and a maximum angle of attack of 34.4212 degrees. The wings are considered to be thin, flat plates with constant chord. The dimensions of the wings are set to 51.9 mm for the semi-span and 18.9 mm for the chord, based off of hawkmoth specimen F1 from [21]. The wings have the same dimensions as in the results presented previously in Chapter 2. The average

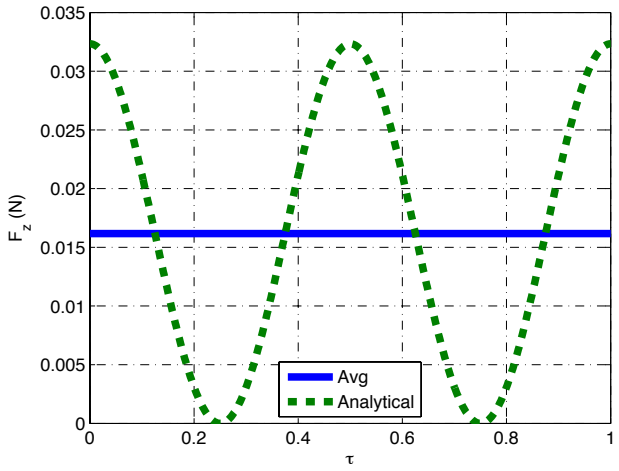

Figure 3.1: Instantaneous Lift Force and Average Lift Force

of the aerodynamic pitching moment is zero, over one flapping cycle, consistent with [38] and [82].

3.3.3 Averaged Equations and Simulation Results

To achieve the averaged equations of motion, we assume that the control moments produce the desired equations of motion of the wings. Therefore, we can define the

angular velocity of the wings according to

$$\begin{bmatrix} p_{RW} \\ q_{RW} \\ r_{RW} \end{bmatrix} = \begin{bmatrix} \sin\alpha_R\dot{\zeta}_R \\ 0 \\ -\cos\alpha_R\dot{\zeta}_R \end{bmatrix} \quad \text{and} \quad \begin{bmatrix} p_{LW} \\ q_{LW} \\ r_{LW} \end{bmatrix} = \begin{bmatrix} -\sin\alpha_L\dot{\zeta}_L \\ 0 \\ \cos\alpha_L\dot{\zeta}_L \end{bmatrix}. \tag{3.36}$$

With symmetrical flapping, $p_{RW} = -p_{LW}$ and $-r_{RW} = r_{LW}$. The period for the calculation of the averaged equations is set to be $\frac{1}{f}$, where f denotes the flapping frequency. The local averaging produces the following equations of motion for the translation of the central body, where the averaged variables are denoted by a 'bar,'

$$\begin{aligned} \dot{\bar{u}} &= \frac{\bar{F}_x}{m_{sys}} - g\sin\bar{\theta} - \bar{q}\bar{w} + \frac{2}{m_{sys}} m_w\rho_w\omega\zeta_m\sin(\alpha_m)\cos\beta\left(\frac{2}{\pi}\frac{\sin(\zeta_m)}{\zeta_m}\right)\bar{q} \quad (3.37) \\ &+ \frac{m_w\rho_w\hat{r}_2 b_w}{m_{sys}I_{yy,sys}}\big(k_T\sin(\alpha_m) - k_N\cos(\alpha_m)\big)\sin\beta\big(1 - \mathbf{J}_0(2\zeta_m) - \mathbf{J}_2(2\zeta_m)\big) \end{aligned}$$

and

$$\begin{aligned} \dot{\bar{w}} &= \frac{\bar{F}_z}{m_{sys}} + g\cos\bar{\theta} + \bar{q}\bar{u} - \frac{2}{m_{sys}} m_w\rho_w\omega\zeta_m\sin(\alpha_m)\sin\beta\left(\frac{2}{\pi}\frac{\sin(\zeta_m)}{\zeta_m}\right)\bar{q} \quad (3.38) \\ &- \frac{m_w\rho_w\hat{r}_2 b_w}{m_{sys}I_{yy,sys}}\big(k_T\sin(\alpha_m) - k_N\cos(\alpha_m)\big)\cos\beta\big(1 - \mathbf{J}_0(2\zeta_m) - \mathbf{J}_2(2\zeta_m)\big), \end{aligned}$$

where the terms ρ_w and m_w denote the distance to the center of mass of the wing from the wing joint and the mass of the wing, respectively. Through the calculation of numerous individual integrals, over the period T, the majority of the effects of the wings on the central body are zero, which is consistent with the method and results in [62]. In order to calculate the average of the equation for $\dot{q}$, the term $I_{yy,sys}$ is averaged separately in order to obtain some form of an analytical averaging solution. The time-varying form of $I_{yy,sys}$, for symmetrical flapping, is

$$I_{yy,sys} = I_{yy,1} + 2\left(I_{yy,w}\cos^2(\zeta) + \big(I_{xx,w}\cos^2(\alpha) + I_{zz,w}\sin^2(\alpha)\big)\sin^2(\zeta)\right). \tag{3.39}$$

The averaged result is

$$\begin{aligned} \bar{I}_{yy,sys} &= I_{yy,1} + \left(I_{xx,w}\cos^2(\alpha_m) + I_{zz,w}\sin^2(\alpha_m)\right)\left(1 - \mathbf{J}_0\left(2\zeta_m\right)\right) \\ &\quad + I_{yy,w}\left(1 + \mathbf{J}_0\left(2\zeta_m\right)\right). \end{aligned} \tag{3.40}$$

As stated previously, the average of the aerodynamic pitching moment, over one flapping-cycle, is identically zero. Likewise, the average over one flapping cycle of all of the terms in $f_3^{(1)}$ is also identically zero. As a direct result, the averaged equation for the pitch velocity is

$$\dot{\bar{q}} = 0 \tag{3.41}$$

The numerical solutions for the perturbed system, to precision of ε, and the averaged system are presented in Figures 3.2. The morphological parameters of the FWMAV are based off a hawkmoth and are consistent with those used in previous multi-body simulations. The flapping amplitude, ζ_m, is equal to 60° and the pitch angle, α_m, is equal to 34.4212°. The flapping frequency is set at 22 Hz. The simulation results are for a stroke plane parallel to the inertial frame, $\beta = -10°$, and an initial pitch angle of 10°. The simulations are started with zero body velocities and an initial altitude of 5 m.

The results are presented in Fig 3.2. The numerical results in Fig. 3.2 are poor. The averaged equations do not match the first order equations of motion. In Fig. 3.2(a), the FWMAV model climbs vertically, but the averaged model does not predict the translation in the negative x direction. Of special concern is the pitch angle of the FWMAV. Averaging, based on the first order equations of motion, predicts the change in the pitch attitude of the FWMAV to be zero for symmetrical flapping. Without control, the pitch angle of the non-averaged system continues to increase (Fig 3.2(b)), while the pitch angle of averaged system remains constant. Furthermore, the pitch

velocity of the FWMAV remains at zero for the averaged system, while the pitch velocity changes drastically during each flapping cycle for the ε^1 system. Section 3.4 will present a method for approximating the dynamics of the FWMAV that will closely match the predicted behavior of the nonlinear, time-varying dynamics of the system.

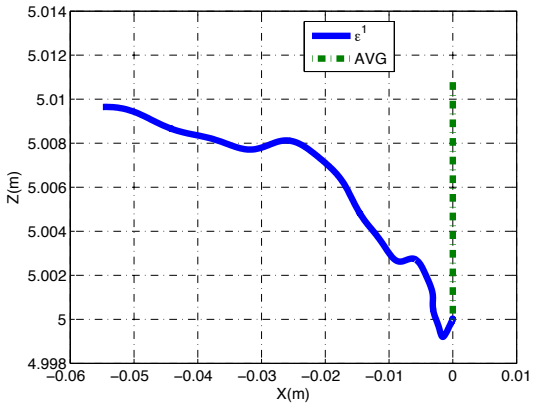

(a) Inertial Position

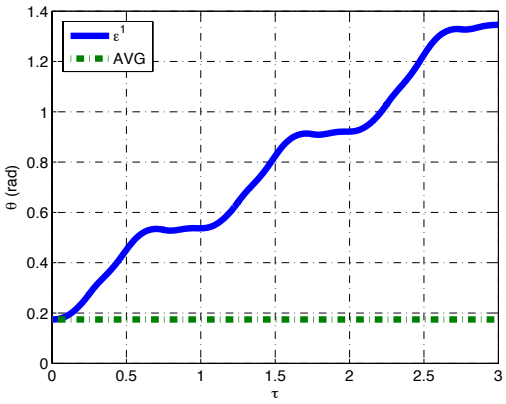

(b) Pitch Orientation

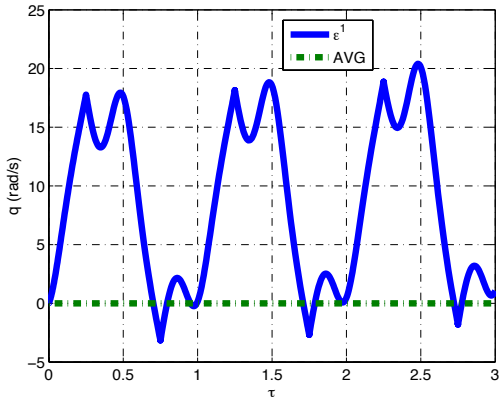

(c) Pitch Velocify

Figure 3.2: Simulation Results for Local Averaging in the Vicinity of Hovering, $\beta = -10°$, $\theta_o = 10°$

3.4 Quarter-Cycle Averaging Results

Obviously, the results from local averaging are poor. The error between the predicted pitch angle from averaging and the actual pitch angle is 100%. The error in the x-position of the FWMAV is also 100%. To provide a better approximation of the system behavior, we propose a method coined 'quarter-cycle' averaging. Essentially, all of the integrals that evaluated to zero over the course of one flapping cycle in Section 3.3.3 are re-written as piecewise continuous, constant functions. The time average, over the course of one flapping cycle, is still zero. The method results in a set of four step, discrete, autonomous equations of motion. The quarter-cycle results for the equations of motion presented in Section 3.2 are detailed in Appendix C. The integrals are broken up over quarter-cycles because of the desire to obtain an analytical solution. Integral tables, available in [124], [125], [126] and Wolfram Alpha, contain anayltical results for many complicated integrals over the interval $\left[0 \quad \frac{\pi}{2}\right]$. The necessary analytical results do not exist for intervals less than $\frac{\pi}{2}$ in length. Furthermore, the integrals are readily defined, analytically, for the intervals $\left[\frac{\pi}{2} \quad \pi\right]$, $\left[\pi \quad \frac{3\pi}{2}\right]$, and $\left[\frac{3\pi}{2} \quad 2\pi\right]$. A summary of the integrals that arose in the derivation process and the appropriate quarter-cycle representations are presented in Appendix D.

The issue with the perturbation problem in the standard form is the analytical solution of the unperturbed system. The general analytical solution of the longitudinal aircraft equations of motion does not exist. An additional issue is that the aerodynamic forces and moments are generated by piecewise continuous explicit functions of time. The approach, presented here, is to utilize the knowledge of dynamic changes during a flapping cycle and use that knowledge to construct piecewise continuous equations that will accurately approximate the dynamics of the flapping micro air vehicle. The results will take one of four forms: constant over the entire flapping cycle, sign changes consistent with a sine wave, sign changes consistent with a cosine wave, and sign changes consistent with a sine wave at twice the normal flapping frequency.

Flapping amplitude and flapping velocity can be written as the following

$$\zeta(t) = \zeta_m \sin(\omega t) \quad \text{and} \quad \dot{\zeta}(t) = \omega \zeta_m \cos(\omega t). \tag{3.42}$$

where $\omega = 2\pi f$. Functions that are consistent with a sine wave are positive over the interval $(0 \quad \pi)$ and negative over the interval $(\pi \quad 2\pi)$. Functions consistent with a sine wave will be denoted by $\text{sgn}(\zeta)$. Functions the are consistent with a cosine wave are positive over the interval $\left(0 \quad \frac{\pi}{2}\right)$, negative over the interval $\left(\frac{\pi}{2} \quad \frac{3\pi}{2}\right)$, and positive over the interval $\left(\frac{3\pi}{2} \quad 2\pi\right)$. Functions consistent with a cosine wave will be denoted by $\text{sgn}\left(\dot{\zeta}\right)$. Functions consistent with a sine wave at twice the normal flapping frequency are positive over the intervals $\left(0 \quad \frac{\pi}{2}\right)$ and $\left(\pi \quad \frac{3\pi}{2}\right)$ and negative over the intervals $\left(\frac{\pi}{2} \quad \pi\right)$ and $\left(\frac{3\pi}{2} \quad 2\pi\right)$. These functions will be denoted by $\text{sgn}(\text{s}(2\omega))$.

For example, in Section 3.3.3, the thrust force, in the stroke plane, and the aerodynamic pitching moment are identically zero when averaged over a flapping cycle. The thrust force may be written as

$$\overline{F}_{x,sp,QC} = \frac{1}{2}\text{sgn}\left(\dot{\zeta}\right)\left(k_T \cos(\alpha_m) + k_N \sin(\alpha_m)\right)\left(\mathbf{J}_0(\zeta_m) + \mathbf{J}_2(\zeta_m)\right), \tag{3.43}$$

where $\mathbf{J}_n$ denotes a Bessel function of the first kind, order n. The aerodynamic pitching moment, for one wing, may be written as

$$M = (\sin\alpha \sin\zeta)\hat{r}_2 b_w F_T - (\cos\alpha \sin\zeta)\hat{r}_2 b_w F_N - \text{sgn}\left(\dot{\zeta}\right)\frac{c_w}{4}(\cos\zeta)F_N. \tag{3.44}$$

When averaged over the four quarter-cycles, the result is

$$\begin{aligned} \overline{M}_{aero,QC} &= \text{sgn}(\zeta)\hat{r}_2 b_w \frac{1}{\zeta_m}\mathbf{H}_1(\zeta_m)\left(k_N \cos(\alpha_m) - k_T \sin(\alpha_m)\right) \\ &\quad + \frac{1}{8}\text{sgn}\left(\dot{\zeta}\right) c_w k_N \left(\mathbf{J}_0(\zeta_m) + \mathbf{J}_2(\zeta_m)\right). \end{aligned} \tag{3.45}$$

$\mathbf{H}_1$ denotes the first order Struve function of the first kind. In the stroke plane, the averaged lift and quarter-cycle averaged lift are identical. A comparison of the instantaneous thrust, lift, and aerodynamic pitching moment and the respective quarter-cycle results are presented in Figure 3.3. The lift and thrust forces are resolved into the B frame of the FWMAV. As a result, the thrust force will not have a time average of zero, nor will the lift force be constant over a flapping cycle. If the stroke plane were identically zero, or parallel with the longitudinal axis of the body, then the lift force would be constant and the thrust would average to zero over the course of one flapping cycle.

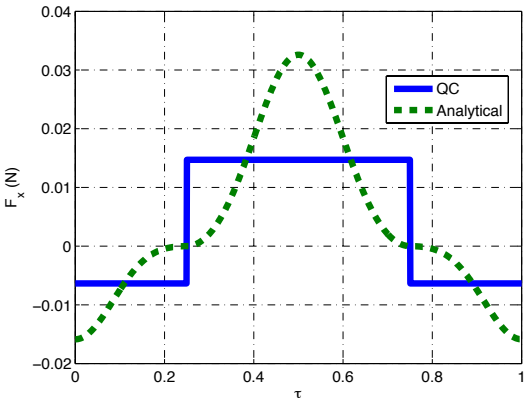

(a) Thrust Force

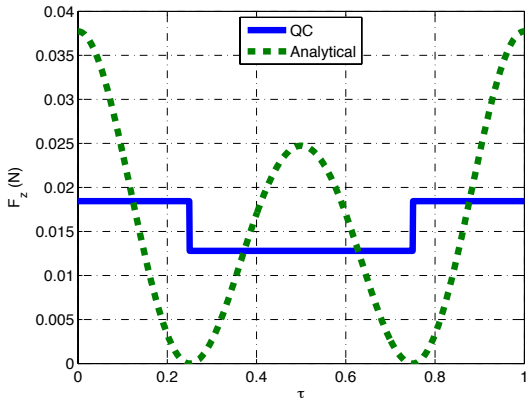

(b) Lift Force

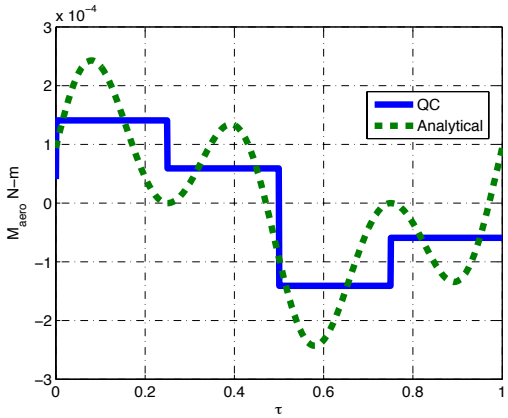

(c) Pitch Moment

Figure 3.3: Comparison of Instantaneous and Quarter-Cycle Averaged Thrust, Lift, and Aerodynamic Pitching Moment

The following three sections, 3.4.1-3.4.3, will show simulation results for three reference flight conditions: hovering flight, forward flight, and vertical flight. The simulation results won't present true reference flight conditions. The results will not be presented for an equilibrium condition of the averaged system. Due to coupling between the pitch and translational velocities, the solutions will quickly diverge from the reference flight condition. However, differences between each condition will be illustrated. The hover solution will not include effects on the aerodynamic force and moment generation from the translational velocity of the body. The forward flight presentation, in Section 3.4.2, will include the longitudinal velocity of the body included in the aerodynamic calculations. The vertical flight simulations, in Section 3.4.3, will include the vertical velocity of the body.

3.4.1 Hovering Flight

The results for quarter-cycle averaging, versus local averaging over the entire flapping cycle, are presented in the vicinity of a hover condition. The translational velocity of the body, u and w, and the pitch velocity of the body, q, are not included in the aerodynamic force and moment calculations. The aerodynamics force and moment calculations used for the hovering solutions are presented in Equations (3.35), (3.43), and (3.45). The derivation of the quarter-cycle equations for the ε^1 effects of the wings, as detailed in Sections 3.2.1-3.2.3, is presented in Appendix C. The results are vastly improved over the results from the locally averaged equations. For the same simulation parameters as presented in Section 3.3.3, the quarter-cycle averaged system is compared to the ε^1 system and the averaged system. The results are presented in Figure 3.4. The quarter-cycle system is denoted by 'QC' and represented by the solid line. The ε^1 system is represented by the dashed line. The averaged system is represented by the dash-dot line.

The quarter-cycle system does a much better job of approximating the dynamics

of the FWMAV through the use of nothing but piecewise continuous, constant functions. The inertial position in Figure 3.4(a) shows slight variation between the ε^1 and 'QC' models during the three flapping cycle duration of the simulation. The inertial position has an error of 4.9% in the x-direction and 10.4% in the z-direction, between the ε^1 system and the 'QC' system. The error between the averaged system and the ε^1 system is 100% in the x-direction and 13.5% in the z-direction. Finally, the error between the pitch angle at the end of the simulation is 100% between the averaged and ε^1 system, while the error is only 5.2% with the 'QC' system. All errors are calculated based on the difference between the initial position/orientation and the final position/orientation. The quarter cycle averaging method definitely supplies an improvement over local averaging and provides an alternative approximation technique for a nonlinear, time-varying, periodic system.

The results in Figure 3.4 only represent one flight condition, with once choice of input parameters. Figures 3.5-3.8 present the error after three flapping cycles for the distance from the initial point and the pitch angle. The initial conditions are set to zero for all of the body velocities. The initial pitch angle is zero degrees, as is the stroke plane angle, for all of the simulations. The flapping amplitude ranges from 55° to 64°, with 1° intervals. The flapping frequency is set at $24\,Hz$. The angle of attack is determined by using a bisection algorithm over the interval [0° 45°] and solving for equilibrium from Equations (3.38) and (3.39). The error in the distance from the initial condition is presented in Figure 3.5 for the quarter-cycle equations versus the first order equations of motion. The error in distance between the averaged equations and the first order equations of motion is presented in Figure 3.6.

The maximum error between the quarter-cycle equations is approximately 10% over 100 different simulation results. The minimum error for the averaged equations is approximately 40%. The error in the pitch angle between the quarter-cycle equations and the first order equations of motion is presented in Figure 3.7. The pitch angle

error for the local averaged equations is presented in Figure 3.8. The maximum error for the quarter-cycle equations for the pitch angle is approximately 4.9%. The error for the averaged equations, for every single simulation, is 100%. The quarter-cycle equations of motion definitely provide a better approximation than local averaging over a wide range of flight conditions, in vicinity of an initial hover condition.

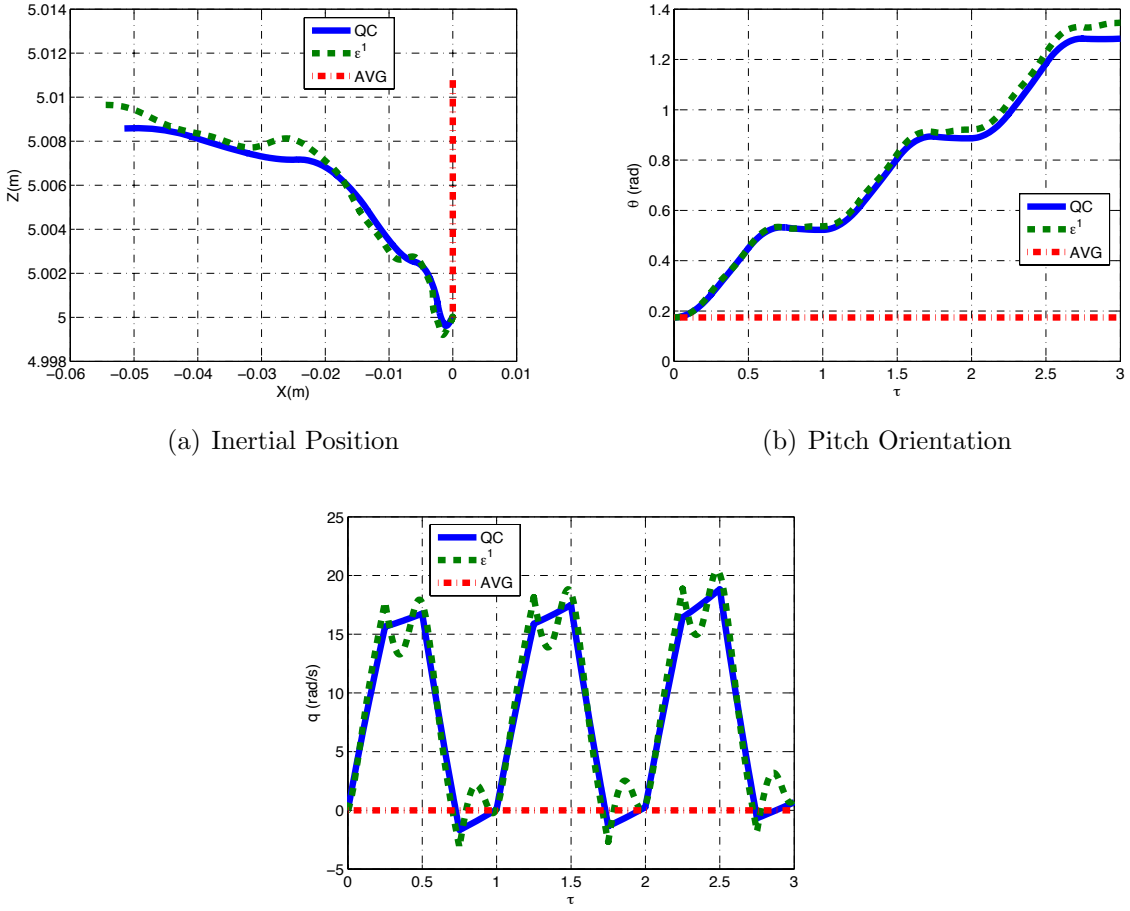

(a) Inertial Position

(b) Pitch Orientation

(c) Pitch Velocity

Figure 3.4: Simulation Results for Local Averaging and Quarter-Cycle Averaging in the Vicinity of Hover, $\beta = -10°$, $\theta_o = 10°$

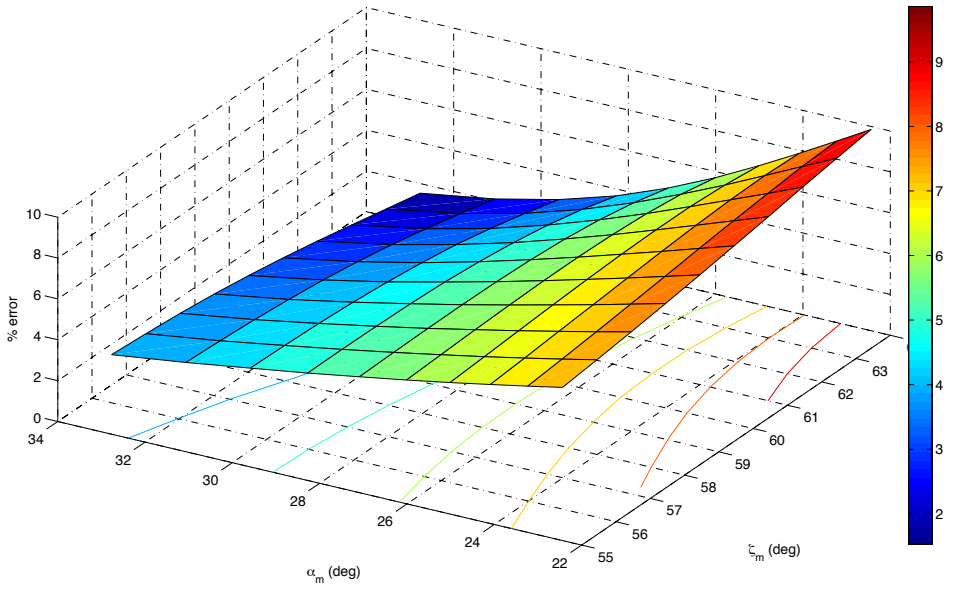

Figure 3.5: Error Results for Distance, Quarter-Cycle Averaging, Hover, $\beta = 0°$, $\theta_o = 0°$, $f = 22\,Hz$

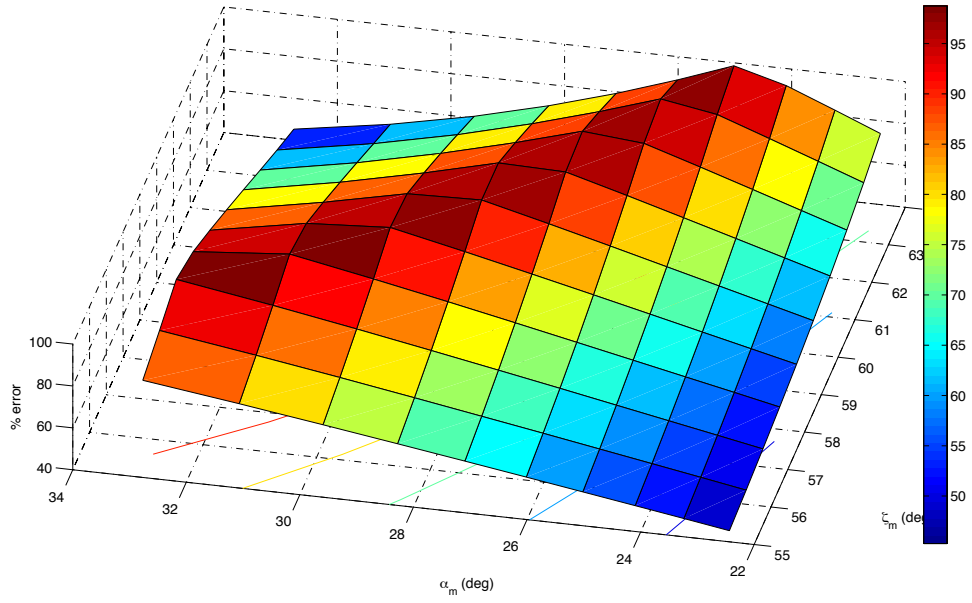

Figure 3.6: Error Results for Distance, Local Averaging, Hover, $\beta = 0°$, $\theta_o = 0°$, $f = 22\,Hz$

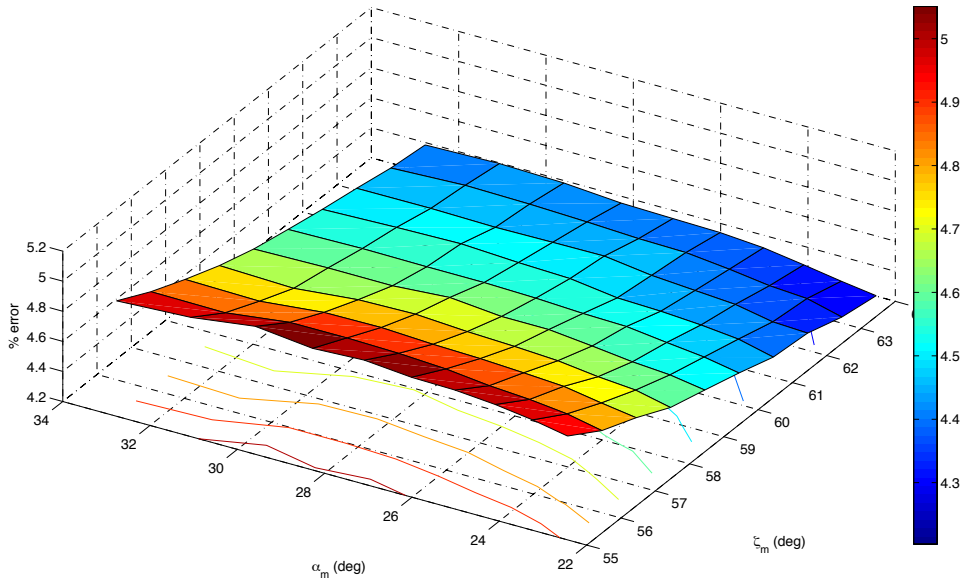

Figure 3.7: Error Results for Pitch Angle, Quarter-Cycle Averaging, Hover, $\beta = 0°$, $\theta_o = 0°$, $f = 22\,Hz$

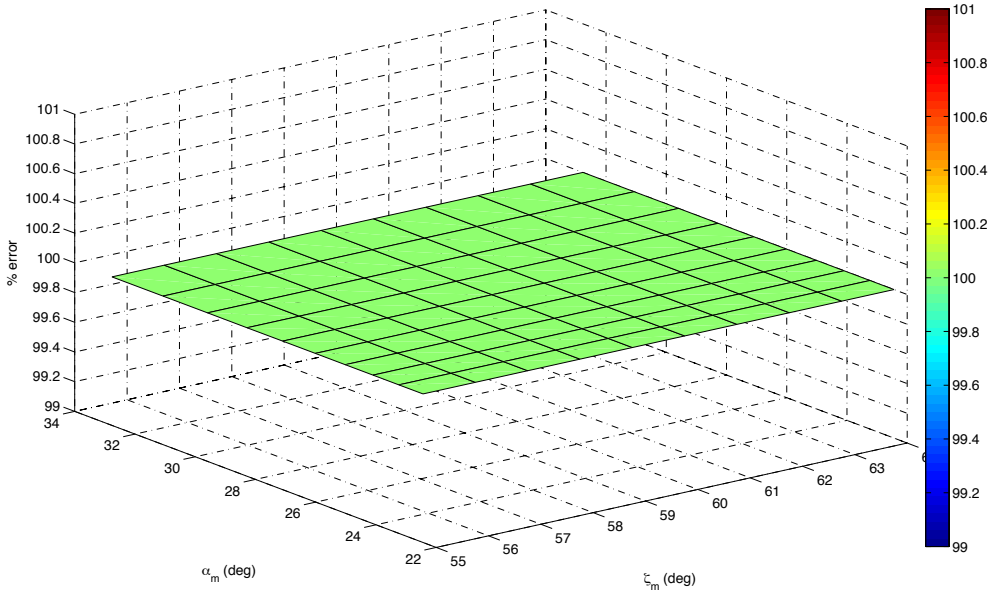

Figure 3.8: Error Results for Pitch Angle, Local Averaging, Hover, $\beta = 0°$, $\theta_o = 0°$, $f = 22\,Hz$

3.4.2 Forward Flight

To consider forward flight, we can define the total velocity of the wing, for longitudinal flight, in the wing frame according to

$$v_{wing} = \begin{bmatrix} \hat{r}_2 b\dot{\zeta} \\ 0 \end{bmatrix} + \begin{bmatrix} \cos(\zeta)\cos(\beta)u \\ \sin(\beta)u \end{bmatrix}. \tag{3.46}$$

The vertical velocity of the body (w) and the pitch velocity of the body (q) are neglected in the calculation of the aerodynamic forces and moments. The magnitude of the wing velocity is

$$||v_{wing}||^2 = \left(\hat{r}_2 b\dot{\zeta}\right)^2 + 2\hat{r}_2 b\dot{\zeta}\cos(\zeta)\cos(\beta)u + \left(\cos^2(\beta)\cos^2(\zeta) + \sin^2(\beta)\right)u^2. \tag{3.47}$$

Therefore, we can define the normal and tangential forces in the wing frame according to

$$F_T = \frac{1}{2}\rho A_w C_T ||v_{wing}||^2 \quad \text{and} \quad F_N = \frac{1}{2}\rho A_w C_N ||v_{wing}||^2. \tag{3.48}$$

The normal and tangential force coefficients, C_N and C_T, respectively are defined according to Equation (3.29). For a non-zero stroke plane, the forward velocity of the FWMAV will cause a change in the angle of attack of the wing from the geometric pitch angle defined by $\alpha(t)$. The total angle of attack, α_{total}, is a combination of the geometric angle of attack, α, and a change in angle of attack, α_Δ, defined by

$$\alpha_\Delta = \tan^{-1}\left(\frac{v_{wing}\cdot R_{w,z}}{v_{wing}\cdot R_{w,x}}\right) = \tan^{-1}\left(\frac{\sin(\beta)u}{\hat{r}_2 b\dot{\zeta} + \cos(\zeta)\cos(\beta)u}\right). \tag{3.49}$$

The additional angle of attack is assumed to act at the aerodynamic center of pressure of the wing. Although this may not be the best assumption, a thorough literature search has not discovered a viable, analytical approximation. The calculation has rarely been handled in the literature. It is mentioned in [70], but a method of the

calculation is not presented. In order to obtain an analytical solution for the 'averaged' system, we assume that α_Δ will remain 'small' in accordance with small angle approximations. As a direct result, $\tan^{-1}$ can be approximated according to

$$\alpha_\Delta = \tan^{-1}\left(\frac{\sin(\beta)u}{\hat{r}_2 b\dot{\zeta} + \cos(\zeta)\cos(\beta)u}\right) \approx \frac{\sin(\beta)u}{\hat{r}_2 b\dot{\zeta} + \cos(\zeta)\cos(\beta)u}. \tag{3.50}$$

The coefficients of the normal and tangential forces can redefined according to

$$\begin{aligned} C_{T,\alpha_\Delta} &= -0.4\,\mathrm{sgn}\left(\dot{\zeta}\right)\cos^2\left(2\left(\alpha+\alpha_\Delta\right)\right) \\ &\approx -0.4\,\mathrm{sgn}\left(\dot{\zeta}\right)\left(\cos^2\left(2\alpha\right) - 2\sin\left(2\alpha\right)\alpha_\Delta\right) \end{aligned} \tag{3.51}$$

and

$$\begin{aligned} C_{N,\alpha_\Delta} &= -3.4\,\mathrm{sgn}\left(\dot{\zeta}\right)\sin\left(\alpha+\alpha_\Delta\right) \\ &\approx -3.4\,\mathrm{sgn}\left(\dot{\zeta}\right)\left(\sin(\alpha) + \cos(\alpha)\alpha_\Delta\right). \end{aligned} \tag{3.52}$$

A further approximation is needed to handle the inclusion of α_Δ into the calculation of the aerodynamic forces and moments. The aerodynamic force calculation will result in terms with the form

$$\begin{aligned} \alpha_\Delta ||v_{wing}||^2 &= \frac{\sin(\beta)u}{\hat{r}_2 b\dot{\zeta} + \cos(\zeta)\cos(\beta)u}\left(\left(\hat{r}_2 b\dot{\zeta} + \cos(\zeta)\cos(\beta)u\right)^2 + \sin^2(\beta)u^2\right) \\ &= \sin(\beta)u\left(\hat{r}_2 b\dot{\zeta} + \cos(\zeta)\cos(\beta)u\right) + \frac{\sin^3(\beta)u^3}{\hat{r}_2 b\dot{\zeta} + \cos(\zeta)\cos(\beta)u}. \end{aligned} \tag{3.53}$$

If, for an initial analysis, forward flight speeds of less than 1 m/s are considered, the term containing u^3 will not only be small compared to its denominator, but small compared to the other terms in the aerodynamic calculations. Therefore, we choose to neglect it. The thrust force in the body frame, due to the geometric angle of attack,

can be written as

$$
\begin{aligned}
F_{x,\alpha} \;=\; & -\frac{1}{2}\cos(\beta)\mathrm{sgn}\left(\dot{\zeta}\right)\left(k_T\cos(\alpha_m)+k_N\sin(\alpha_m)\right)\left(\mathbf{J}_0\left(\zeta_m\right)+\mathbf{J}_2\left(\zeta_m\right)\right) \\
& +\frac{1}{2}\sin(\beta)\left(k_T\sin(\alpha_m)-k_N\cos(\alpha_m)\right) \\
& -\frac{1}{\pi}\cos^2(\beta)\left(k_1+k_2\right)\left(1+\frac{\sin(2\zeta_m)}{2\zeta_m}\right)u \\
& -\sin(2\beta)\mathrm{sgn}\left(\dot{\zeta}\right)\left(k_3-k_4\right)\left(\frac{\sin(\zeta_m)}{\zeta_m}\right)u \\
& -\mathrm{sgn}\left(\dot{\zeta}\right)\left(k_5+k_6\right)\left(\cos^3(\beta)\left(\frac{3}{4}\mathbf{J}_0(\zeta_m)+\frac{1}{4}\mathbf{J}_0(3\zeta_m)\right)\right. \\
& \left.+\cos(\beta)\sin^2(\beta)\mathbf{J}_0(\zeta_m)\right)u^2 \\
& +\left(k_7-k_8\right)\left(\sin(\beta)\cos^2(\beta)\left(\frac{1}{2}+\frac{1}{2}\mathbf{J}_0\left(2\zeta_m\right)\right)+\sin^3(\beta)\right)u^2,
\end{aligned}
\tag{3.54}
$$

where the constants k_i are defined in Appendix C. The inclusion of the longitudinal velocity of the central body into the aerodynamic calculations results in a thrust force that is no longer zero over the course of a flapping cycle. The term containing the constants k_1 and k_2 is constant when averaged over the course of the flapping cycle and results from the thrust force on the wings in the stroke plane. The thrust force is directly dependent on the velocity of the body. The term containing k_7 and k_8 is a result of the lift force on the wings in the stroke plane and varies with the power of u^2. The contribution to the thrust force from the change in angle of attack is

$$
\begin{aligned}
F_{x,\alpha_\Delta} \;=\; & \frac{2}{\pi}\sin(2\beta)\left(\cos(\beta)\,\mathrm{sgn}\left(\dot{\zeta}\right)\left(k_9-k_{10}\right)\left(\frac{\sin(\zeta_m)}{\zeta_m}\right)-\sin(\beta)\left(k_{11}+k_{12}\right)\right)u \\
& +\sin(2\beta)\left(\cos(\beta)\left(k_{13}-k_{14}\right)\left(1+\mathbf{J}_0\left(2\zeta_m\right)\right)\right)u^2 \\
& -\sin(2\beta)\left(\sin(\beta)\,\mathrm{sgn}\left(\dot{\zeta}\right)\left(k_{15}+k_{16}\right)\mathbf{J}_0\left(\zeta_m\right)\right)u^2.
\end{aligned}
\tag{3.55}
$$

As with the contribution to the thrust force due to the geometric angle of attack, both the thrust force and the lift force in the stroke plane result in a constant contribution

to the thrust force as a result of the velocity of the body. The lift force contribution, in the body frame, from the geometric pitch angle is

$$\begin{aligned} F_{z,\alpha} &= \frac{1}{2}\cos(\beta)\big(k_T\sin(\alpha_m) - k_N\cos(\alpha_m)\big) \\ &\quad + \frac{1}{2}\sin(\beta)\,\mathrm{sgn}\left(\dot{\zeta}\right)\big(k_T\cos(\alpha_m) + k_N\sin(\alpha_m)\big)\big(\mathbf{J}_0\left(\zeta_m\right) + \mathbf{J}_2\left(\zeta_m\right)\big) \\ &\quad + \cos^2(\beta)\,\mathrm{sgn}\left(\dot{\zeta}\right)(k_3 - k_4)\left(\frac{2}{\pi}\frac{\sin(\zeta_m)}{\zeta_m}\right)u \\ &\quad + \frac{1}{2}\sin(2\beta)\,(k_1 + k_2)\left(\frac{1}{\pi} + \frac{1}{\pi}\frac{\sin(2\zeta_m)}{2\zeta_m}\right)u \\ &\quad + \mathrm{sgn}\left(\dot{\zeta}\right)(k_5 + k_6)\left(\frac{1}{4}\sin(\beta)\cos^2(\beta)\,(3\mathbf{J}_0(\zeta_m) + \mathbf{J}_0(3\zeta_m)) + \right. \\ &\quad \left. + \sin^3(\beta)\mathbf{J}_0(\zeta_m)\right)u^2 \\ &\quad + (k_7 - k_8)\left(\cos^3(\beta)\left(\frac{1}{2} + \frac{1}{2}\mathbf{J}_0\left(2\zeta_m\right)\right) + \cos(\beta)\sin^2(\beta)\right)u^2. \end{aligned} \tag{3.56}$$

The lift contribution from the change in angle of attack is

$$\begin{aligned} F_{z,\alpha_\Delta} &= -\frac{1}{\pi}\left(\sin(2\beta)\,(k_{11} + k_{12}) + \sin^2(\beta)\,(k_9 - k_{10})\,\mathrm{sgn}\left(\dot{\zeta}\right)\left(\frac{\sin(\zeta_m)}{\zeta_m}\right)\right)u \\ &\quad - \sin(2\beta)\Big(\cos(\beta)\,\mathrm{sgn}\left(\dot{\zeta}\right)(k_{15} + k_{16})\,\mathbf{J}_0\left(\zeta_m\right)\Big)u^2 \\ &\quad + \sin(2\beta)\Big(\sin(\beta)\,(k_{14} - k_{13})\left(1 + \mathbf{J}_0\left(2\zeta_m\right)\right)\Big)u^2. \end{aligned} \tag{3.57}$$

Without considering the contribution of the body velocity on the aerodynamic forces and moments, the average of the aerodynamic pitching moment over one flapping cycle is identically zero. However, including the body velocity u results in a non-zero, time-averaged contribution to the aerodynamic pitching moment. The aerodynamic

pitching moment, due to the geometric angle of attack for one wing, is equal to

$$\begin{aligned} M_{aero,\alpha} &= \operatorname{sgn}\big(\zeta\big)\hat{r}_2 b_w\big(k_N\cos(\alpha_m)-k_T\sin(\alpha_m)\big)\frac{1}{\zeta_m}\mathbf{H}_1\left(\zeta_m\right) \\ &+\frac{1}{8}\operatorname{sgn}\left(\dot{\zeta}\right)c_w k_N\big(\mathbf{J}_0(\zeta_m)+\mathbf{J}_2(\zeta_m)\big) \\ &+\frac{1}{2}\operatorname{sgn}\left(s(2\omega)\right)\cos(\beta)\hat{r}_2 b_w\left(k_4-k_3\right)\left(\frac{2}{\pi}\frac{1-\cos(2\zeta_m)}{2\zeta_m}\right)u \\ &+\operatorname{sgn}\left(\zeta\right)\hat{r}_2 b_w\left(k_8-k_7\right)\Big(\frac{1}{4}\cos^2(\beta)\big(\mathbf{H}_0\left(\zeta_m\right)+\mathbf{H}_0\left(3\zeta_m\right)\big)+\ldots \\ &+\sin^2(\beta)\mathbf{H}_0(\zeta_m)\Big)u^2+\cos(\beta)k_{17}\left(\frac{2}{\pi}+\frac{2}{\pi}\frac{\sin(2\zeta_m)}{2\zeta_m}\right)u \\ &+\operatorname{sgn}\left(\dot{\zeta}\right)k_{18}\left(\frac{1}{4}\cos^2(\beta)\left(3\mathbf{J}_0(\zeta_m)+\mathbf{J}_0(3\zeta_m)\right)+\mathbf{J}_0(\zeta_m)\sin^2(\beta)\right)u^2. \end{aligned} \tag{3.58}$$

The contribution to the aerodynamic pitching moment due to the change in angle of attack is

$$\begin{aligned} M_{aero,\alpha_\Delta} &= \operatorname{sgn}\left(\zeta\right)\left(k_{19}+k_{20}\right)\sin(\beta)\left(\frac{2}{\pi}\frac{1-\cos(\zeta_m)}{\zeta_m}\right)u \\ &+\operatorname{sgn}\left(s(2\omega)\right)\sin(2\beta)\left(k_{21}+k_{22}\right)\mathbf{H}_0\left(2\zeta_m\right)u^2 \\ &+k_{23}\sin(\beta)\operatorname{sgn}\left(\dot{\zeta}\right)\left(\frac{2}{\pi}\frac{\sin(\zeta_m)}{\zeta_m}\right)u+k_{24}\sin(2\beta)\big(1+\mathbf{J}_0\left(2\zeta_m\right)\big)u^2. \end{aligned} \tag{3.59}$$

The pitch moment has constant contributions from the aerodynamics proportional to u, the term containing k_{17} in Equation (3.58), and u^2, the term containing k_{24} in Equation (3.59).

Case	Initial Pitch Angle $\theta_o\,(^\circ)$	Stroke Plane Angle $\beta\,(^\circ)$	Initial velocity $u_o\,(m/s)$
1	0	-20	0.25
2	0	-10	0.5
3	5	-5	-0.5
4	5	-15	-0.25

Table 3.1: Summary of Input Parameters for Forward Flight Comparison Simulations, Presented in Figures 3.9-3.12

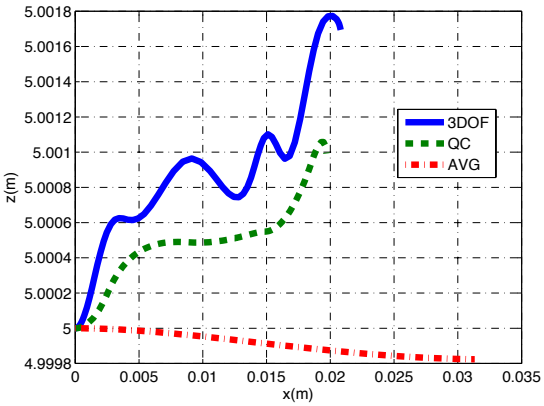

(a) Case 1: $\theta_o = 0°$, $\beta = -20°$, $u_o = 0.25$ m/s

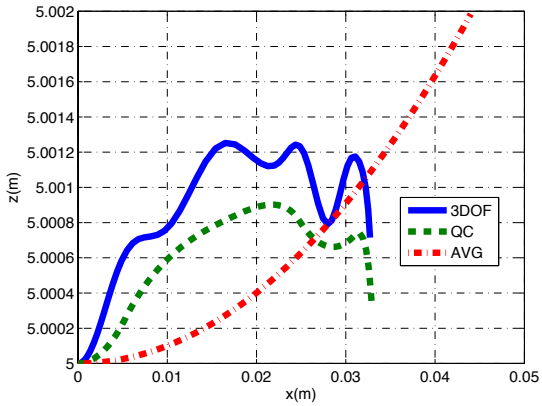

(b) Case 2: $\theta_o = 0°$, $\beta = -10°$, $u_o = 0.5$ m/s

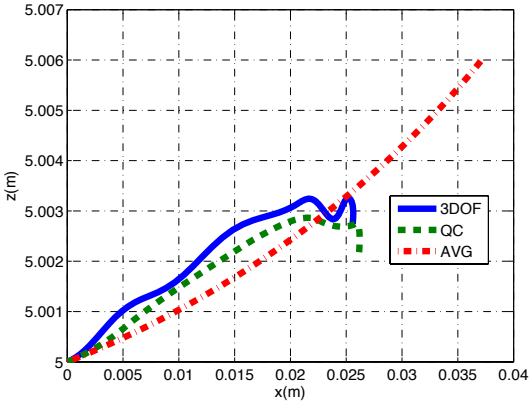

(c) Case 3: $\theta_o = 5°$, $\beta = -5°$, $u_o = 0.5$ m/s

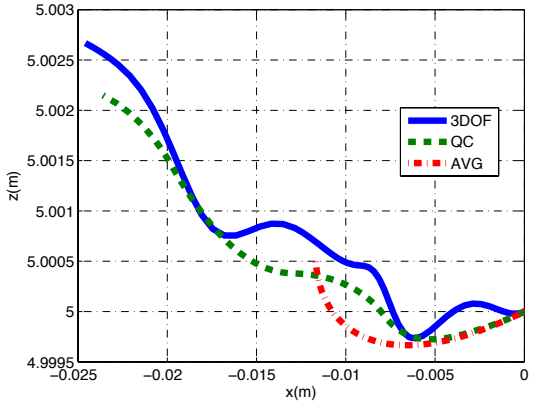

(d) Case 4: $\theta_o = 5°$, $\beta = -15°$, $u_o = -0.25$ m/s

Figure 3.9: $X - Z$ Position Simulation Results for Forward Flight: $f = 22\,Hz$, $\alpha_m = 35°$, $\zeta_m = 60°$

Figures 3.9-3.12 present simulation results for a longitudinal aircraft model, without the wing effects included, but including the body velocity u into the aerodynamic calculations. The solid line is the longitudinal aircraft model with the analytical aerodynamic model. The dash-dot line is the simulation results for the quarter-cycle model. The dotted line is the results for the averaged system. Four cases are presented in each Figure. The input parameters for the simulations are presented in Table 3.1.

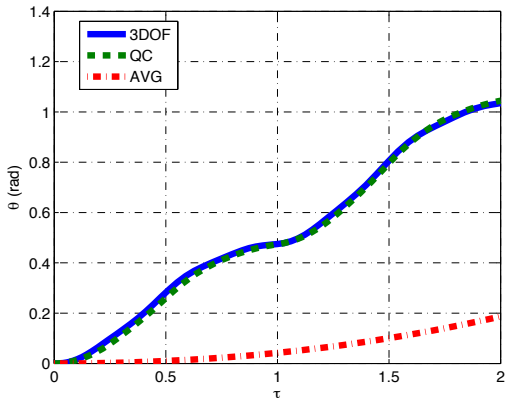

(a) Case 1: $\theta_o = 0°$, $\beta = -20°$, $u_o = 0.25$ m/s

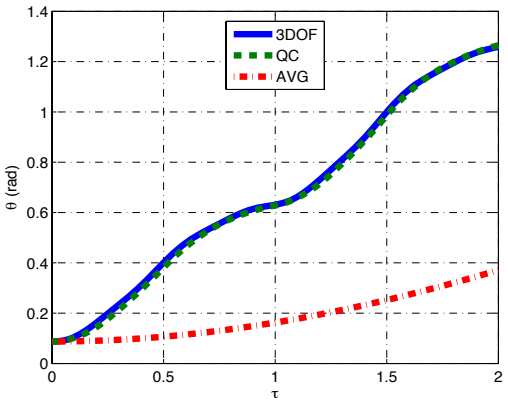

(b) Case 2: $\theta_o = 0°$, $\beta = -10°$, $u_o = 0.5$ m/s

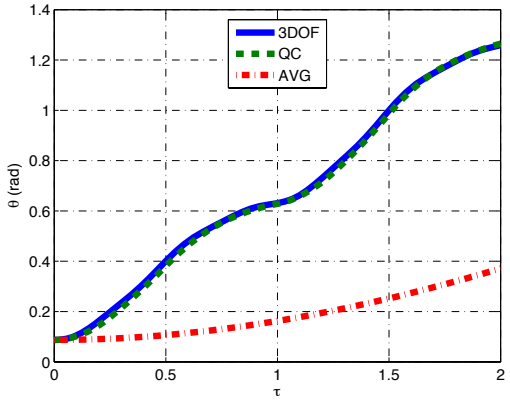

(c) Case 3: $\theta_o = 5°$, $\beta = -5°$, $u_o = 0.5$ m/s

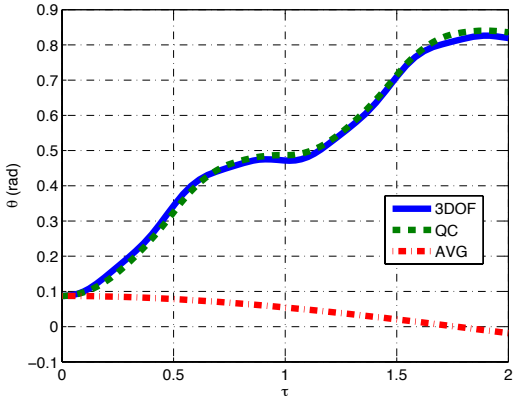

(d) Case 4: $\theta_o = 5°$, $\beta = -15°$, $u_o = -0.25$ m/s

Figure 3.10: Pitch Angle Simulation Results for Forward Flight: $f = 22\,Hz$, $\alpha_m = 35°$, $\zeta_m = 60°$

Figure 3.9 shows the inertial position of the FWMAV after two flapping cycles. The simulation results show that the quarter-cycle method predicts the actual behavior of the FWMAV better than averaging alone, consistent with the results presented in Section 3.4.1. As opposed to the hovering flight approximation, local averaging at least gets the longitudinal direction of the motion correct. For Case 1, in Fig. 3.9(a), the local averaging solution predicts a decrease in altitude while the actual solution, and the quarter-cycle solution, predict an increase in altitude. For the other cases, local averaging predicts the correct direction, but vastly overestimates (or underestimates) the amount of displacement.

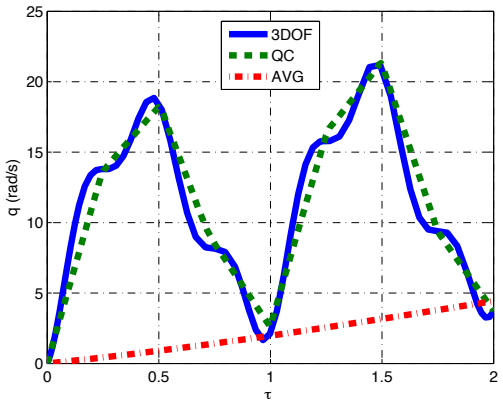

(a) Case 1: $\theta_o = 0°$, $\beta = -20°$, $u_o = 0.25$ m/s

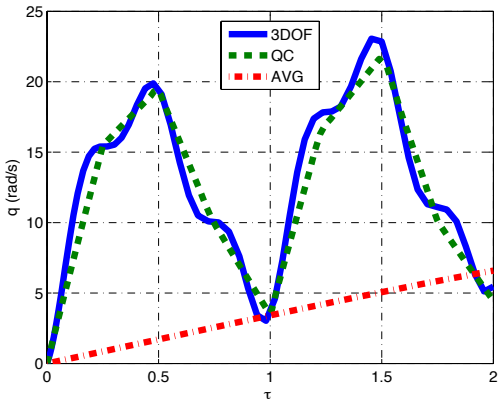

(b) Case 2: $\theta_o = 0°$, $\beta = -10°$, $u_o = 0.5$ m/s

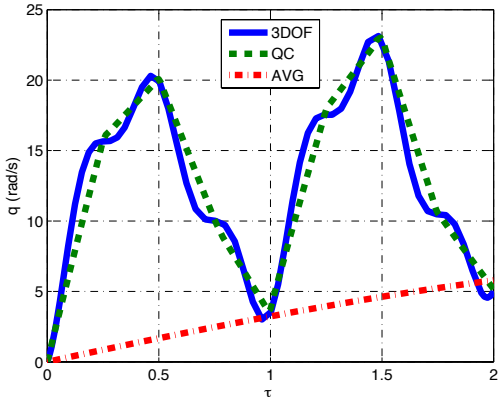

(c) Case 3: $\theta_o = 5°$, $\beta = -5°$, $u_o = 0.5$ m/s

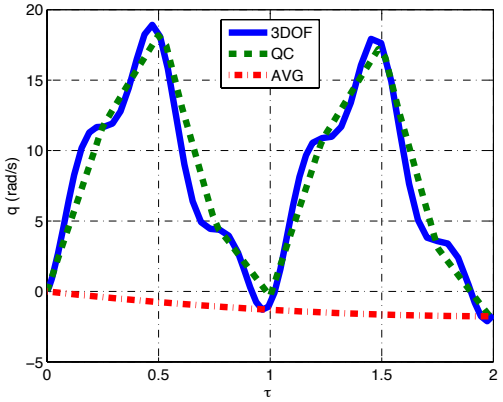

(d) Case 4: $\theta_o = 5°$, $\beta = -15°$, $u_o = -0.25$ m/s

Figure 3.11: Pitch Velocity Simulation Results for Forward Flight: $f = 22\,Hz$, $\alpha_m = 35°$, $\zeta_m = 60°$

Figures 3.10 and 3.11 show the simulation results for the pitch angle and pitch velocity of the central body. For a positive forward velocity, in Figures 3.10(a)-3.10(c), both the averaged system and the quarter-cycle system predict a positive increase in the pitch angle. However, for a negative initial velocity in Figure 3.10(d), the averaged model predicts an increase in the opposite direction from the quarter-cycle averaged system. In either case, the magnitude of the pitch angle at the end of two flapping cycles for the quarter-cycle system is much closer to the true system than to the averaged system. The results are presented for only two flapping cycles because the

pitch angle quickly reaches a nose-up orientation, at $\theta = \frac{\pi}{2}$, with the inclusion of the forward velocity in an open loop simulation.

Figure 3.12 shows the simulation results for the longitudinal velocity of the body, u, for the two flapping cycles. As with the pitch orientation and velocity, the quarter-cycle approximation performs vastly better than local averaging. As with the FW-MAV in a hover condition, the quarter-cycle approximation performs better than the local averaging method. The derivation of the equations in this section will provide a basis for the analysis of the forward flight regime and the determination of equilibrium conditions and possibly limit cycles around said equilibrium conditions.

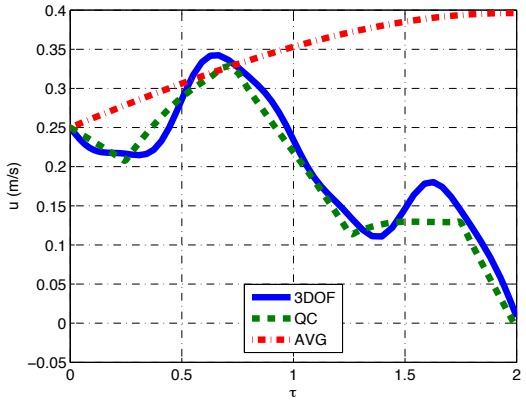

(a) Case 1: $\theta_o = 0°$, $\beta = -20°$, $u_o = 0.25$ m/s

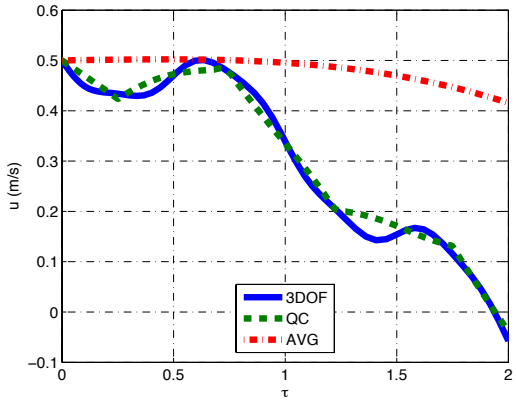

(b) Case 2: $\theta_o = 0°$, $\beta = -10°$, $u_o = 0.5$ m/s

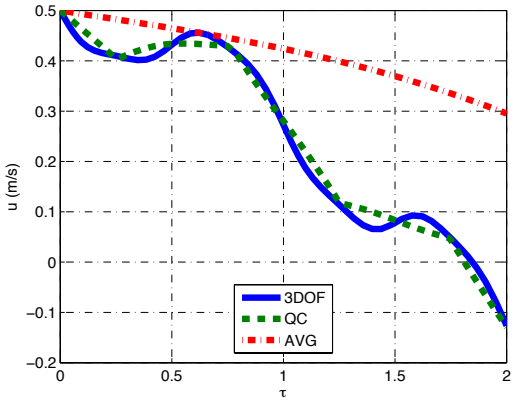

(c) Case 3: $\theta_o = 5°$, $\beta = -5°$, $w_o = 0.5$ m/s

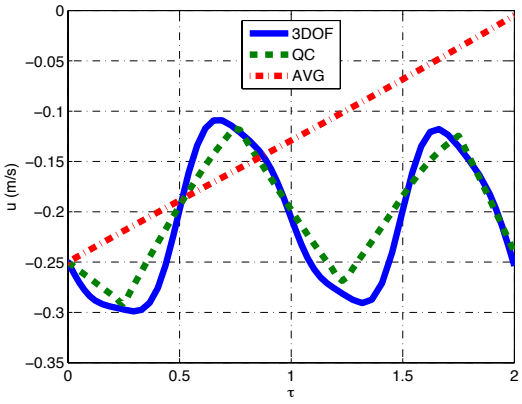

(d) Case 4: $\theta_o = 5°$, $\beta = -15°$, $w_o = -0.25$ m/s

Figure 3.12: Longitudinal Velocity Simulation Results for Forward Flight: $f = 22\,Hz$, $\alpha_m = 35°$, $\zeta_m = 60°$

3.4.3 Vertical Flight

Considering vertical flight, we define the total velocity of the wing, in the wing frame, according to

$$v_{wing} = \begin{bmatrix} \hat{r}_2 b\dot{\zeta} \\ 0 \end{bmatrix} + \begin{bmatrix} -\cos(\zeta)\sin(\beta)w \\ \cos(\beta)w \end{bmatrix}. \tag{3.60}$$

The magnitude of the wing velocity, expressed in the wing frame and relative to the inertial frame, is

$$||v_{wing}||^2 = (\hat{r}_2 b_w)^2 - 2\,\hat{r}_2 b_w \cos(\zeta)\dot{\zeta}\sin(\beta)w + \left(\cos^2(\zeta)\sin^2(\beta) + \cos^2(\beta)\right) w^2. \tag{3.61}$$

The normal and tangential forces in the wing frame are still defined according to Equation (3.48). The change in angle of attack, α_Δ, is derived in the same manner as in Equation (3.49). However, the actual result differs and is calculated according to

$$\alpha_\Delta = \tan^{-1}\left(\frac{\cos(\beta)w}{\hat{r}_2 b_w\dot{\zeta} - \cos(\zeta)\sin(\beta)w}\right) \approx \frac{\cos(\beta)w}{\hat{r}_2 b_w\dot{\zeta} - \cos(\zeta)\sin(\beta)w}. \tag{3.62}$$

The normal and tangential force coefficients are identical to those defined in Equation (3.29). The change in the force coefficients due to the change in angle of attack is the same as in the forward flight case, as defined in Equations (3.51) and (3.52). The inclusion of the α_Δ term into the calculation of the aerodynamics forces and moments for vertical flight differs from that of forward flight. The aerodynamic calculation will

result in terms calculated according to

$$\begin{aligned}\alpha_\Delta||v_{wing}||^2 &= \frac{\cos(\beta)w}{\hat{r}_2 b_w\dot{\zeta}-\cos(\zeta)\sin(\beta)w}\left(\left(\hat{r}_2 b_w\dot{\zeta}-\cos(\zeta)\sin(\beta)w\right)^2+\cos^2(\beta)w^2\right)\\ &= \cos(\beta)w\left(\hat{r}_2 b_w\dot{\zeta}-\cos(\zeta)\sin(\beta)w\right)+\frac{\cos^3(\beta)w^3}{\hat{r}_2 b_w\dot{\zeta}-\cos(\zeta)\sin(\beta)w}. \quad (3.63)\end{aligned}$$

A similar assumption is made for vertical flight as with forward flight, the terms containing w^3 are neglected for relatively slow vertical flight regimes. The thrust force, in the body frame due to the velocity of the wing, is calculated according to

$$\begin{aligned}F_{x,\alpha} &= -\frac{1}{2}\cos(\beta)\text{sgn}\left(\dot{\zeta}\right)\left(k_T\cos(\alpha_m)+k_N\sin(\alpha_m)\right)\left(\mathbf{J}_0\left(\zeta_m\right)+\mathbf{J}_2\left(\zeta_m\right)\right)\\ &\quad +\frac{1}{2}\sin(\beta)\left(k_T\sin(\alpha_m)-k_N\cos(\alpha_m)\right) \quad (3.64)\\ &\quad +\frac{1}{2}\sin(2\beta)\left(k_1+k_2\right)\left(\frac{1}{\pi}+\frac{1}{\pi}\frac{\sin(2\zeta_m)}{2\zeta_m}\right)w\\ &\quad +\sin^2(\beta)\text{sgn}\left(\dot{\zeta}\right)\left(k_4-k_3\right)\left(\frac{2}{\pi}\frac{\sin(\zeta_m)}{\zeta_m}\right)w-\left(k_5+k_6\right)\text{sgn}\left(\dot{\zeta}\right)*\\ &\quad \left(\cos(\beta)\sin^2(\beta)\left(\frac{3}{4}\mathbf{J}_0\left(\zeta_m\right)+\frac{1}{4}\mathbf{J}_0\left(3\zeta_m\right)\right)+\cos^3(\beta)\mathbf{J}_0\left(\zeta_m\right)\right)w^2\\ &\quad +\left(k_7-k_8\right)\left(\sin^3(\beta)\left(\frac{1}{2}+\frac{1}{2}\mathbf{J}_0\left(2\zeta_m\right)\right)+\sin(\beta)\cos^2(\beta)\right)w^2.\end{aligned}$$

As with the forward flight equations, the thrust force contributes constant and periodic effects proportional to w and w^2. Analysis of the thrust force shows that if $\beta\equiv 0$, then all of the constant functions will be identically zero. With a stroke plane parallel to the longitudinal axis of the body, only periodic forces will affect the longitudinal position of the body. The contribution to the thrust force from the change in angle of attack is calculated according to

$$\begin{aligned}F_{x,\alpha_\Delta} &= \frac{1}{\pi}\left(2\cos^2(\beta)\text{sgn}\left(\dot{\zeta}\right)\left(k_9-k_{10}\right)\left(\frac{\sin(\zeta_m)}{\zeta_m}\right)-\sin(2\beta)\left(k_{11}+k_{12}\right)\right)w\\ &\quad +\sin(2\beta)\left(\cos(\beta)\left(k_{14}-k_{13}\right)\left(1+\mathbf{J}_0\left(2\zeta_m\right)\right)\right)w^2 \quad (3.65)\\ &\quad +\sin(2\beta)\left(\sin(\beta)\text{sgn}\left(\dot{\zeta}\right)\left(k_{15}+k_{16}\right)\mathbf{J}_0\left(\zeta_m\right)\right)w^2.\end{aligned}$$

As with the thrust contribution from the geometric angle of attack, the constant thrust contribution due to the change in angle of attack will also be identically zero if $\beta \equiv 0$. The contribution to the lift force from the geometric angle of attack is calculated according to

$$\begin{aligned} F_{z,\alpha} &= \frac{1}{2}\cos(\beta)\big(k_T \sin(\alpha_m) - k_N \cos(\alpha_m)\big) \\ &+\frac{1}{2}\sin(\beta)\text{sgn}\left(\dot{\zeta}\right)\big(k_T \cos(\alpha_m) + k_N \sin(\alpha_m)\big)\big(\mathbf{J}_0(\zeta_m) + \mathbf{J}_2(\zeta_m)\big) \\ &+\frac{1}{2}\sin(2\beta)\text{sgn}\left(\dot{\zeta}\right)(k_4 - k_3)\left(\frac{2}{\pi}\frac{\sin(\zeta_m)}{\zeta_m}\right)w \\ &-\sin^2(\beta)\,(k_1 + k_2)\left(\frac{1}{\pi}\right)\left(1 + \frac{\sin(2\zeta_m)}{2\zeta_m}\right)w + (k_5 + k_6)\,\text{sgn}\left(\dot{\zeta}\right) * \\ &\left(\frac{1}{4}\sin^3(\beta)\,(3\mathbf{J}_0(\zeta_m) + \mathbf{J}_0(3\zeta_m)) + \sin(\beta)\cos^2(\beta)\mathbf{J}_0(\zeta_m)\right)w^2 \\ &+(k_7 - k_8)\left(\frac{1}{2}\cos(\beta)\sin^2(\beta)\,(1 + \mathbf{J}_0\,(2\zeta_m)) + \cos^3(\beta)\right)w^2. \end{aligned} \tag{3.66}$$

For a stroke plane equal to zero ($\beta \equiv 0$), the lift force will have two constant contributions: one due to the flapping velocity of the wing and one proportional to w^2. The contribution to the lift force from the change in angle of attack is

$$\begin{aligned} F_{z,\alpha_\Delta} &= \frac{1}{\pi}\left(\sin(2\beta)\text{sgn}\left(\dot{\zeta}\right)(k_{10} - k_9)\left(\frac{\sin(\zeta_m)}{\zeta_m}\right) - 2\,(k_{11} + k_{12})\cos^2(\beta)\right)w \\ &+\sin(2\beta)\left(\cos(\beta)\,(k_{15} + k_{16})\,\text{sgn}\left(\dot{\zeta}\right)\mathbf{J}_0\,(\zeta_m)\right)w^2 \\ &+\sin(2\beta)\,((k_{13} - k_{14})\sin(\beta)\,(1 + \mathbf{J}_0\,(2\zeta_m)))\,w^2. \end{aligned} \tag{3.67}$$

The lift force due to the change in angle of attack contributes a constant force proportional to w if the stroke plane is identically zero. The aerodynamic pitching moment

due to the velocity of the wing is calculated according to

$$
\begin{aligned}
M_{aero,\alpha} &= \operatorname{sgn}\big(\zeta\big)\hat{r}_2 b_w\big(k_N\cos(\alpha_m)-k_T\sin(\alpha_m)\big)\frac{1}{\zeta_m}\mathbf{H}_1\left(\zeta_m\right) \\
&+\frac{1}{8}\operatorname{sgn}\left(\dot{\zeta}\right)c_w k_N\big(\mathbf{J}_0(\zeta_m)+\mathbf{J}_2(\zeta_m)\big) \\
&+\frac{1}{2}\operatorname{sgn}\left(s(2\omega\,t)\right)\sin(\beta)\hat{r}_2 b_w\left(k_3-k_4\right)\left(\frac{2}{\pi}\frac{1-\cos(2\zeta_m)}{2\zeta_m}\right)w \\
&+\operatorname{sgn}\left(\zeta\right)\hat{r}_2 b_w\left(k_8-k_7\right)* \\
&\left(\frac{1}{4}\sin^2(\beta)\big(\mathbf{H}_0\left(\zeta_m\right)+\mathbf{H}_0\left(3\zeta_m\right)\big)+\cos^2(\beta)\mathbf{H}_0(\zeta_m)\right)w^2 \\
&-\sin(\beta)k_{17}\left(\frac{2}{\pi}+\frac{2}{\pi}\frac{\sin(2\zeta_m)}{2\zeta_m}\right)w \\
&+\operatorname{sgn}\left(\dot{\zeta}\right)k_{18}\left(\sin^2(\beta)\left(\frac{3}{4}\mathbf{J}_0(\zeta_m)+\frac{1}{4}\mathbf{J}_0(3\zeta_m)\right)+\mathbf{J}_0(\zeta_m)\cos^2(\beta)\right)w^2.
\end{aligned}
\tag{3.68}
$$

The majority of the contributions to the aerodynamic pitching moments are periodic. For a stroke plane equal to zero, the only constant contribution to the aerodynamic pitching moment from the geometric angle of attack will also be zero. The final contribution to the aerodynamic pitching moment is the contribution from the change in angle of attack due to the vertical velocity.

$$
\begin{aligned}
M_{aero,\alpha_\Delta} &= \operatorname{sgn}\left(\zeta\right)\left(k_{19}+k_{20}\right)\cos(\beta)\left(\frac{2}{\pi}\frac{1-\cos(\zeta_m)}{\zeta_m}\right)w \\
&-\operatorname{sgn}\left(s(2\omega\,t)\right)\sin(2\beta)\left(k_{21}+k_{22}\right)\mathbf{H}_0\left(2\zeta_m\right)w^2 \\
&+k_{23}\cos(\beta)\operatorname{sgn}\left(\dot{\zeta}\right)\left(\frac{2}{\pi}\frac{\sin(\zeta_m)}{\zeta_m}\right)w-k_{24}\sin(2\beta)\big(1+\mathbf{J}_0\left(2\zeta_m\right)\big)w^2.
\end{aligned}
\tag{3.69}
$$

The constant contribution, proportional to w^2, will be zero for a stroke plane equal to zero.

The quarter-cycle approximation of vertical flight equations of motion will be simulated versus the analytical system and the averaged system. Four different cases will be presented; two cases will be for ascending flight and two for descending flight. The input parameters are detailed in Table 3.2.

Case	Initial Pitch Angle $\theta_o\,(^\circ)$	Stroke Plane $\beta\,(^\circ)$	Initial velocity $w_o\,(m/s)$
1	20	-20	0.25
2	20	-20	-0.25
3	10	-10	0.5
4	10	-10	-0.5

Table 3.2: Summary of Input Parameters for Vertical Flight Comparison Simulations, Presented in Figures 3.13-3.16

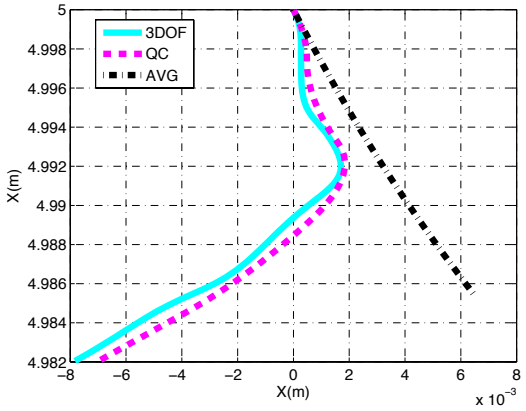

(a) Case 1: $\theta_o = 20°$, $\beta = -20°$, $w_o = 0.25$ m/s

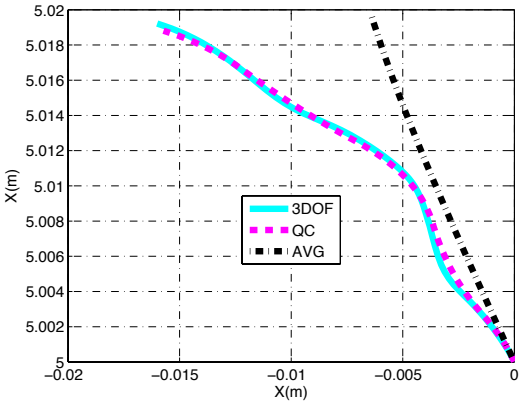

(b) Case 2: $\theta_o = 20°$, $\beta = -20°$, $w_o = -0.25$ m/s

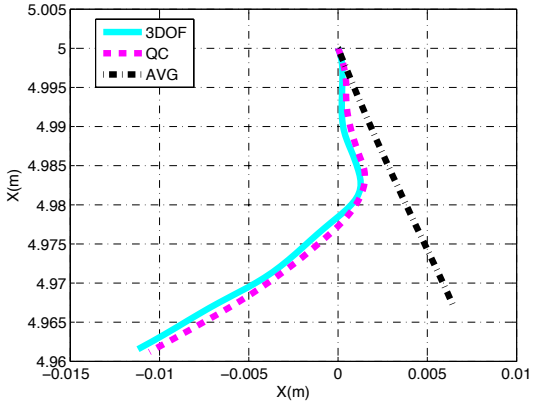

(c) Case 3: $\theta_o = 10°$, $\beta = -10°$, $w_o = 0.5$ m/s

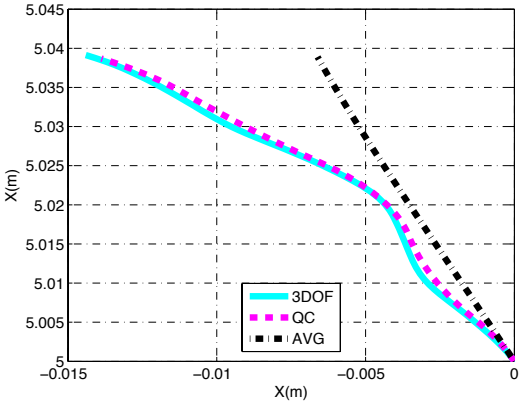

(d) Case 4: $\theta_o = 10°$, $\beta = -10°$, $w_o = -0.5$ m/s

Figure 3.13: $X - Z$ Position Simulation Results for Vertical Flight: $f = 21\,Hz$, $\alpha_m = 35°$, $\zeta_m = 60°$

The simulation results for vertical flight are presented in Figures 3.13-3.16. For ascending and descending flight, vertical flight predicts a backwards translation (neg-

ative x-direction). The inertial position for the four simulations is presented in Figure 3.13. For descending flight, in Figs. 3.13(a) and 3.13(c), the analytical and quarter-cycle approximations predict translation in the same direction. The averaged system predicts translation in the opposite direction (positive x-direction). For ascending flight, both approximations predict translation in the correct direction, but the quarter-cycle approximation is a vast improvement in accuracy over the averaged system.

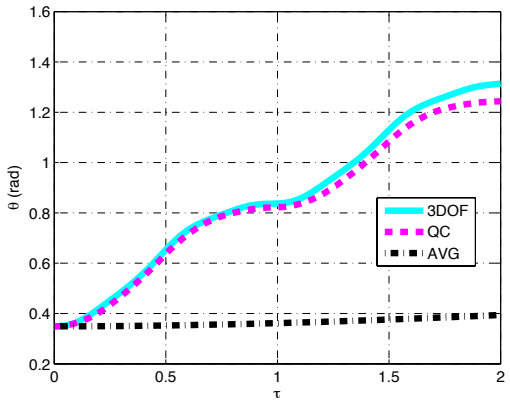

(a) Case 1: $\theta_o = 20°$, $\beta = -20°$, $w_o = 0.25$ m/s

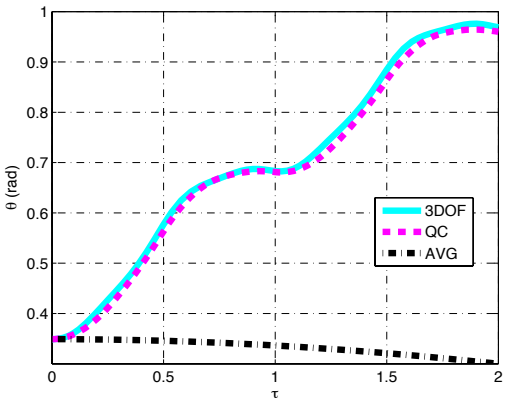

(b) Case 2: $\theta_o = 20°$, $\beta = -20°$, $w_o = -0.25$ m/s

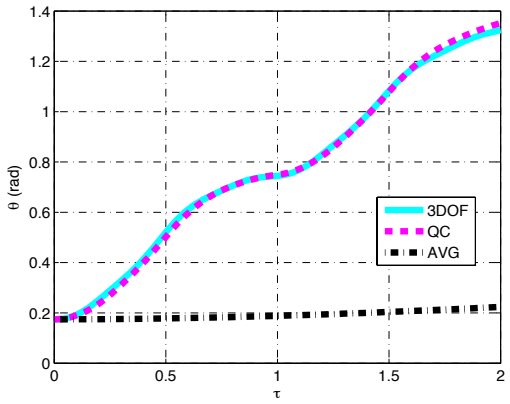

(c) Case 3: $\theta_o = 10°$, $\beta = -10°$, $w_o = 0.5$ m/s

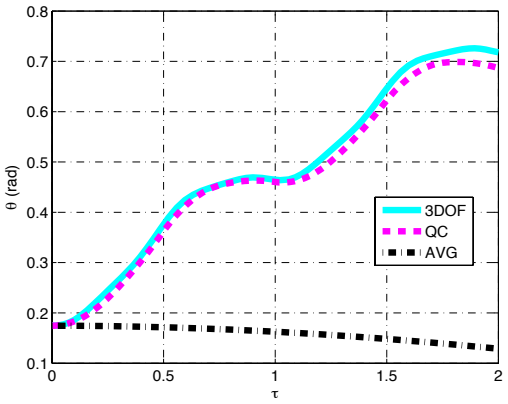

(d) Case 4: $\theta_o = 10°$, $\beta = -10°$, $w_o = -0.5$ m/s

Figure 3.14: Pitch Angle Simulation Results for Vertical Flight: $f = 21\,Hz$, $\alpha_m = 35°$, $\zeta_m = 60°$

The pitch orientation for the vertical flight simulations are presented in Figure

3.14. The pitch behavior is generally the same for all four cases presented and well approximated by the quarter-cycle equations. In the case of ascending flight, as shown in Figs. 3.14(b) and 3.14(d), the pitch prediction for the averaged system is increasing in magnitude from the actual system. For descending flight, in Figs. 3.14(a) and 3.14(c), the averaged system gets the direction of the pitch change correct but is not close in magnitude. The quarter-cycle equations also match the pitch velocity, in Figure 3.15, and vertical velocity, in Figure 3.16, well throughout the simulation of the FWMAV.

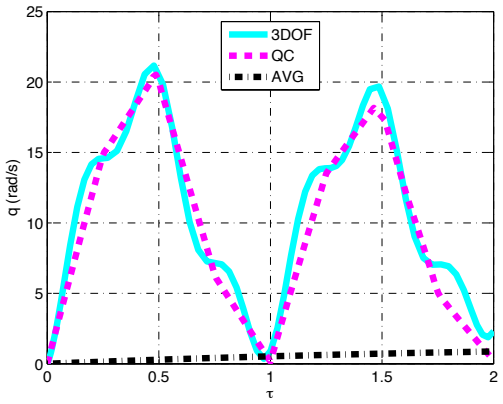

(a) Case 1: $\theta_o = 20°$, $\beta = -20°$, $w_o = 0.25$ m/s

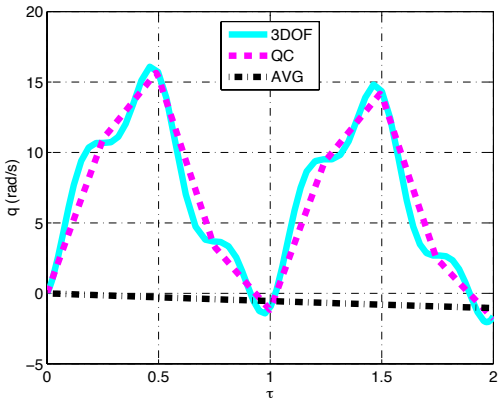

(b) Case 2: $\theta_o = 20°$, $\beta = -20°$, $w_o = -0.25$ m/s

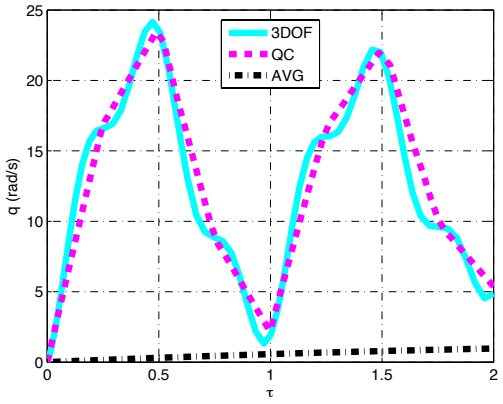

(c) Case 3: $\theta_o = 10°$, $\beta = -10°$, $w_o = 0.5$ m/s

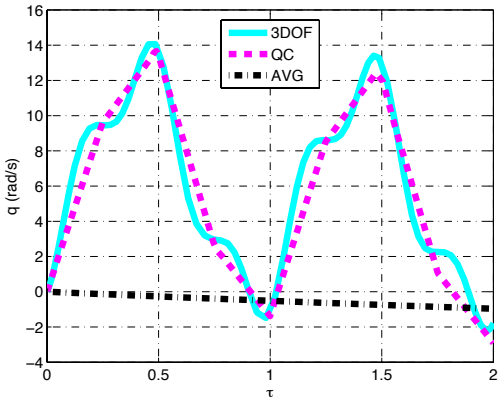

(d) Case 4: $\theta_o = 10°$, $\beta = -10°$, $w_o = -0.5$ m/s

Figure 3.15: Pitch Velocity Simulation Results for Vertical Flight: $f = 21\,Hz$, $\alpha_m = 35°$, $\zeta_m = 60°$

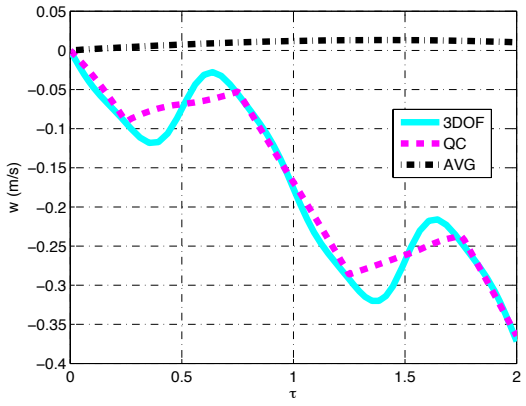

(a) Case 1: $\theta_o = 20°$, $\beta = -20°$, $w_o = 0.25$ m/s

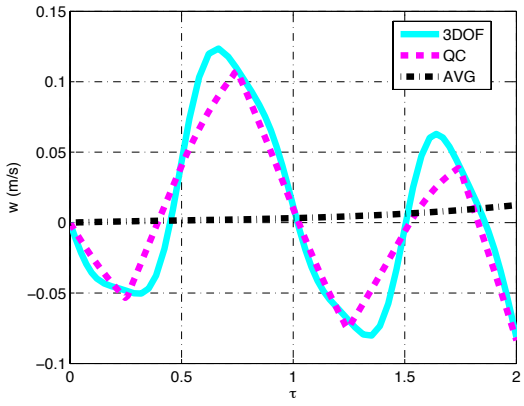

(b) Case 2: $\theta_o = 20°$, $\beta = -20°$, $w_o = -0.25$ m/s

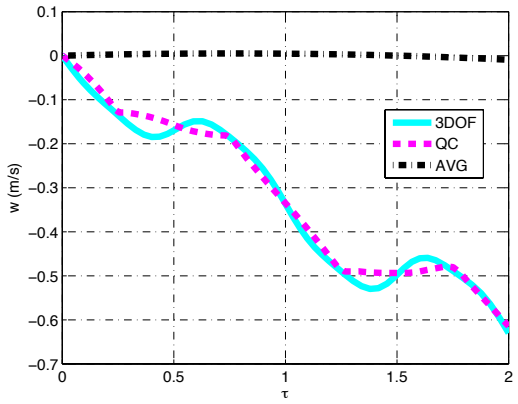

(c) Case 3: $\theta_o = 10°$, $\beta = -10°$, $w_o = 0.5$ m/s

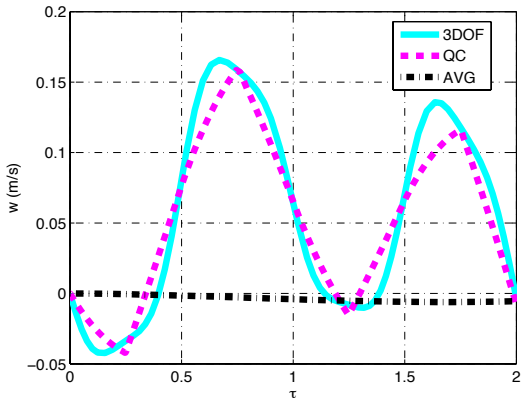

(d) Case 4: $\theta_o = 10°$, $\beta = -10°$, $w_o = -0.5$ m/s

Figure 3.16: Vertical Velocity Results for Vertical Flight: $f = 21\,Hz$, $\alpha_m = 35°$, $\zeta_m = 60°$

3.5 Error Summary and Conclusions

The chapter presented a method of approximating the behavior of a flapping wing micro air vehicle for three reference flight conditions: hover, forward flight, and vertical flight. The quarter-cycle approximation produces good results compared to the first order equations of motion and a vast improvement over the local (naïve) averaged system. It is important to note that there is no guarantee for accuracy using the local averaging method. In Section 3.4.1, error results are presented for 100 simulations of the quarter-cycle approximation versus the local averaging approximation. For the hover simulations, the stroke plane angle and initial pitch angle are both set at zero degrees. The error results are summarized in Table 3.3. The flapping amplitude is varied from 55° to 64° with increments of one degree. For each flapping amplitude, with a set frequency of 24 Hz, the require angle of attack for a trim condition of the averaged systems is calculated using a bisection algorithm. The error results for a 121

Comparison	Average Error (%)	Maximum Error (%)	Minimum Error (%)
QC - Distance	5.80	9.86	1.53
AVG - Distance	74.2	98.8	45.3
QC - Pitch	4.58	5.05	4.20
AVG - Pitch	100	100	100

Table 3.3: Error Results for Quarter-Cycle Approximation and Local Averaging Approximation for Hover

forward flight simulations are presented in Table 3.4. The simulations use a constant angle of attack set to 35°, a flapping amplitude set to 60°, and a flapping frequency of 22 Hz. The simulations are conducted for two flapping cycles. The final pitch angle and distance from the start point are compared to the first order system for the quarter-cycle approximation and the local averaging approximation. The initial longitudinal velocity is varied from -1 m/s to 1 m/s in increments of 0.2 m/s. The stroke plane angle is varied from 0° to -20° in increments of two degrees. All other initial velocities are set to zero. The same input parameters used in the forward flight

Comparison	Average Error (%)	Maximum Error (%)	Minimum Error (%)
QC - Distance	2.97	27.4	0.0171
AVG - Distance	49.78	373	11.92
QC - Pitch	2.99	12.73	0.16
AVG - Pitch	133	633	60.5

Table 3.4: Error Results for Quarter-Cycle Approximation and Local Averaging Approximation for Forward Flight

simulations for the angle of attack, the flapping amplitude, and flapping frequency are used for an evaluation of the error for the vertical flight approximations. The vertical velocity is varied over the same range as the initial longitudinal velocity. The stroke plane is varied over the same range, except the initial pitch angle is set to be the negative of the stroke plane angle. The condition on the initial pitch angle make the wings parallel to the inertial frame at the initial condition. The error results for the vertical flight approximations are presented in Table 3.5. The error results presented

Comparison	Average Error (%)	Maximum Error (%)	Minimum Error (%)
QC - Distance	1.17	3.07	0.00790
AVG - Distance	19.1	80.4	0.31
QC - Pitch	1.51	3.28	0.00239
AVG - Pitch	84.1	100	70.0

Table 3.5: Error Results for Quarter-Cycle Approximation and Local Averaging Approximation for Vertical Flight

in Tables 3.3-3.5 show that the quarter-cycle approximation technique improves the error by over an order of magnitude for all three flight conditions, when compared to local averaging. The method is effective at approximating the dynamic behavior of the first order equations of motion. The quarter-cycle equations of motion will be used for the analysis of stability derivatives and limit cycles in Chapter 4 and the importance of the wings on the position and orientation of the central body in Chapter 5.

CHAPTER 4

Hover Analysis Using Local Averaging and Quarter-Cycle Averaging

4.1 Introduction

Averaged forces and moments have been used in numerous studies to determine the stability of flight for model insects. As previously referenced in Chapter 1, numerous studies have identified the stability derivatives of insects using numerical methods. Sun and Xiong calculated the stability derivatives for a hovering bumblebee in [66]. Sun et al. calculated the stability derivatives, in vicinity of a hover condition, for four insect species (hawkmoth, cranefly, dronefly, and hovefly) in [62]. The stability derivatives are calculated using flapping cycle averaged aerodynamic forces and moments. The aerodynamic force and moment data is obtained using computational fluid dynamics in [66] and [62]. In [70], Faruque and Humbert calculate the stability derivatives for a model fruit fly using system identification. The numerical result is obtained by using the flapping cycle averaged aerodynamic forces and moments obtained from a quasi-steady/blade-element aerodynamic model. The results in [62, 66, 70] are consistent in the modal structure of the eigenvalues. The model structure contains two stable subsidence modes (one fast and one slow) and one unstable, oscillatory mode. The modal structure is consistent with the most common

structure for vertical takeoff or landing (VTOL) aircraft [70, 127]. All of the stability derivatives neglect the mass of the wings, and the associated coupling effects, in the calculation of the stability derivatives.

The chapter will present a analytically tractable method of obtaining the stability derivatives for a flapping wing micro air vehicle in the vicinity of a hover condition. The stability derivatives are obtained using a quasi-steady/blade-element aerodynamic and local averaging techniques for the standard aircraft model. The modal structure is consistent with previous studies. The stability derivatives results for the standard aircraft model are presented in [128]. Additionally, the stability derivatives for the hover condition will be presented with wing effects included. The analysis will show that inclusion of the wing effects not only changes the trim solution for hover, but increases the time constant of the unstable oscillatory mode. The same techniques will be used to calculate the control derivatives. A linear control analysis will show that not including the wing effects will not produce the desired pole locations. Finally, an approximation of a limit cycle in vicinity of a hover condition can be obtained using the averaged trim condition, coupled with proper control of the pitch velocity of the central body. The control is designed for a system without wing effects. When the control is applied to a system with the wing effects included, the desired output is not achieved.

4.2 Stability Derivatives in Vicinity of a Hover Condition: Standard Aircraft Model

For an initial analysis, the mass of the wings, and the wings' associated inertial effects on the position and orientation of the central body, are neglected. An additional assumption is that the aerodynamic model will produce identical normal and tangential forces for symmetrical flapping relative to the central body. Additionally,

under the constraint of symmetrical flapping and with the aerodynamic forces assumption, the lateral forces, roll moments, and yaw moments will be identically zero when resolved in the body frame. For longitudinal motion, the equations of motion are

$$\dot{u} = \frac{F_x}{m_{sys}} - g\sin\theta - q\,w, \tag{4.1}$$

$$\dot{w} = \frac{F_z}{m_{sys}} + g\cos\theta + q\,u, \tag{4.2}$$

$$\dot{\theta} = q, \tag{4.3}$$

and

$$\dot{q} = \frac{M}{I_{yy}}. \tag{4.4}$$

The mass of the system is denoted by m_{sys} and the moment of inertia with respect to $\hat{b}_y$ of the B frame is $I_{yy,sys}$. The wings are assumed to be mounted at joints such that their y-positions in the B frame are equal in magnitude, but opposite in sign. The x- and z-positions of the wings joints in the B frame are identically zero.

4.2.1 Aerodynamic Model

The aerodynamic model is based on the model used extensively in [39] and [89] and previously used in Chapters 2 and 3. We will make a simplifying assumption that the angle of attack is constant during each half-stroke, therefore the normal force contribution due to rotation of the wing will be zero. The assumption was previously used in [38, 79, 82, 83]. The wing is assumed to flip instantly at the end of each half-stroke. As a result, we can write the angle of attack as a function of time as

$$\alpha(t) = \text{sgn}\left(\dot{\zeta}\right)\alpha_m, \tag{4.5}$$

where $\dot{\zeta}$ denotes the time rate of change of the flapping angle of the wing. The flapping angle will be a sinusoidal function, defined by:

$$\zeta(t) = \zeta_m \sin(2\pi f t), \tag{4.6}$$

where ζ_m is half of the total flapping amplitude. The tangential and normal forces on the wing are calculated according to

$$F_T = \frac{1}{2}\rho A_w C_T U_{cp}(t)^2 \text{ and } F_N = \frac{1}{2}\rho A_w C_N U_{cp}(t)^2. \tag{4.7}$$

The coefficients for the tangential and normal forces are calculated according to

$$C_T = -0.4 \operatorname{sgn}\left(\dot{\zeta}\right) \cos^2(2\alpha_m) \tag{4.8}$$

and

$$C_N = -3.4 \sin(\alpha_m). \tag{4.9}$$

The coefficients are modified from [39] consistent with the choice of wing kinematics. In Equations (4.8) and (4.9), α_m is the constant amplitude of the angle of attack during the upstroke and the downstroke. If the translational and angular velocity of the body is neglected in the calculation of aerodynamic forces and moments, then the velocity at the center of pressure of the wing is

$$U_{cp}(t) = \hat{r}_2 b (\omega \zeta_m) \cos(\omega t). \tag{4.10}$$

The normal and tangential forces generated by the motion of the wing are transformed into the body frame. The transformation is obtained through a sequence of rotations from the wing frame to the stroke plane frame and from the stroke plane frame to the body frame. The wings are assumed to be thin, rigid flat plates with constant

chord, c, and semi-span, b. The center of pressure of the wing is calculated to be at the normalized center of pressure, $\hat{r}_2$, and $^1/_4$ of the chord from the leading edge of the wing, based on the chosen wing geometry.

4.2.2 Hover Solution

The hover solution is obtained through the use of local averaging. A treatment of local averaging is available in [117]. The aerodynamic forces and moments are averaged over one flapping cycle, according to

$$\overline{y} = \frac{1}{2\pi} \int_0^{2\pi} y(t) dt \,, \tag{4.11}$$

where $y(t)$ is representative of the aerodynamic force or moment equation. Based on the chosen aerodynamic model and representation of the flight dynamics, the averaged thrust force in the stroke plane frame is zero, identical to the result obtained in [38]. The averaged lift force in the stroke plane frame, for one wing, is equal to

$$\overline{F}_{z,sp} = \frac{1}{2} k_T \sin(\alpha_m) - \frac{1}{2} k_N \cos(\alpha_m). \tag{4.12}$$

The average of the aerodynamic pitching moment is zero, identical to the result in [38], due to the assumptions on wing joint placement. Therefore, a hover solution in the B frame is obtained when the averaged thrust is zero and the averaged lift is equal to weight. If the stroke plane is inclined relative to the longitudinal axis of the body, then the following two conditions will need to be met:

$$\overline{F}_z \cos\beta = -m_{sys} g \cos\theta_o \quad \text{and} \quad \overline{F}_z \sin\beta = m_{sys} g \sin\theta_o, \tag{4.13}$$

where θ_o denotes the nominal pitch attitude. The trim solution differs slightly from the solution presented in [70]. In [70], the wing joint placement is forward of the center

of mass of the body. The time-averaged pitching moment is trimmed appropriately to compensate for the difference.

4.2.3 Perturbed Aerodynamics

The stability derivatives are obtained using a combination of averaging and a perturbed aerodynamic model. First, the perturbed velocity of the body needs to be written in the respective wing frames according to

$$\Delta\bar{\mathbf{v}}_b^w = \mathbf{R}_\zeta \mathbf{R}_\beta \begin{bmatrix} \Delta u \\ \\ \Delta w \end{bmatrix}, \tag{4.14}$$

where $\mathbf{R}_\beta$ denotes the rotation matrix carrying the body frame to the stroke plane frame. The matrix $\mathbf{R}_\zeta$ details the rotation matrix carrying the stroke plane angle to the wing frame when the flapping angle is non-zero. In component form, the perturbed translational velocity of the body in the wing frame (neglecting the y-direction for longitudinal flight) is:

$$\Delta\bar{\mathbf{v}}_b^w = \begin{bmatrix} \cos(\zeta)\left(\cos(\beta)\Delta u - \sin(\beta)\Delta w\right) \\ \\ \sin(\beta)\Delta u + \cos(\beta)\Delta w \end{bmatrix}. \tag{4.15}$$

The pitch velocity of the body is transformed into the wing frame according to

$$\Delta\bar{\omega}_b^w = \mathbf{R}_\zeta \mathbf{R}_\beta \begin{bmatrix} 0 \\ \\ \Delta q \\ \\ 0 \end{bmatrix}. \tag{4.16}$$

The total velocity of the wing, in the wing frame, is calculated according to

$$\bar{\mathbf{v}}_{wing} = \begin{bmatrix} \hat{r}_2 b\,\dot{\zeta} \\ \\ 0 \end{bmatrix} + \Delta\bar{\mathbf{v}}_b^w + \Delta\bar{\omega}_b^w \times \bar{\rho}_{ac}^w. \tag{4.17}$$

The aerodynamic center of pressure in the wing frame, relative to the body frame, is expressed as $\bar{\rho}_{ac}^{w}$. The total velocity of the wing, in the wing frame, in component form is

$$\bar{\mathbf{v}}_{wing} = \begin{bmatrix} \hat{r}_2 b_w \dot{\zeta} + \cos(\zeta)\left(\cos(\beta)\Delta u - \sin(\beta)\Delta w\right) \\ \sin(\beta)\Delta u + \cos(\beta)\Delta w - \hat{r}_2 b_w \sin(\zeta)\Delta q \end{bmatrix}. \tag{4.18}$$

The magnitude of the wing velocity squared, neglecting Δ^2 terms, is

$$||\bar{\mathbf{v}}_{wing}||^2 = (\hat{r}_2 b\dot{\zeta})^2 + 2\hat{r}_2 b_w \cos(\zeta)\dot{\zeta}\left(\cos(\beta)\Delta u - \sin(\beta)\Delta w\right). \tag{4.19}$$

The first term, $(\hat{r}_2 b\dot{\zeta})^2$, accounts for the averaged lift/thrust force in the hover solution. Therefore, the perturbations to the aerodynamic forces and moments will result from the second and third terms. The hover solution is subtracted from the perturbed aerodynamics equations obtained from the equations of motion in vicinity of a hover condition; a more detailed treatment is available in [51] and [70]. Therefore, the velocity perturbations are accounted for in the aerodynamic force and moment calculations. After eliminating the contributions enabling the hover condition, the perturbed equations of motion can be written as:

$$\Delta\dot{u} = X_u(t)\Delta u + X_w(t)\Delta w + X_q(t)\Delta q - g\,\cos\theta_o\Delta\theta, \tag{4.20}$$

$$\Delta\dot{w} = Z_u(t)\Delta u + Z_w(t)\Delta w + Z_q(t)\Delta q - g\,\sin\theta_o\Delta\theta, \tag{4.21}$$

and

$$\Delta\dot{q} = M_u(t)\Delta_u + M_w(t)\Delta w + M_q(t)\Delta q, \tag{4.22}$$

where $X_{[.]}$, $Z_{[.]}$, and $M_{[.]}$ are nonlinear functions of the flapping angle and angle of attack. The aerodynamic perturbations do not directly affect the pitch angle of the FWMAV.

4.2.4 Stability Derivatives due to Velocity Perturbations

In [127], the perturbed hover equations for VTOL aircraft and helicopters neglect a perturbation velocity in the x-direction due to velocity in the z-direction (w). In [70], perturbations are only considered in the longitudinal direction. In this analysis, perturbations to both the longitudinal velocity, Δu, and vertical velocity, Δw, are considered. For brevity in the following equations, the following coefficients are defined:

$$c_T = 0.2\rho\, A_w \hat{r}_2 b_w\, \omega\, \zeta_m \cos^2(2\alpha_m) \tag{4.23}$$

and

$$c_N = 1.7\rho\, A_w \hat{r}_2 b_w\, \omega\, \zeta_m \sin(\alpha_m)\,, \tag{4.24}$$

which account for the effects of the tangential and normal forces generated on the wings due to motion of the central body. The stability derivatives are arranged in the following manner:

$$\begin{bmatrix} \Delta\dot{u} \\ \Delta\dot{w} \\ \Delta\dot{\theta} \\ \Delta\dot{q} \end{bmatrix} = \bar{\mathbf{A}}_{hover} \begin{bmatrix} \Delta u \\ \Delta w \\ \Delta\theta \\ \Delta q \end{bmatrix}, \tag{4.25}$$

where the system matrix is arranged according to

$$\bar{\mathbf{A}}_{hover} = \begin{bmatrix} \overline{X}_u & \overline{X}_w & \overline{X}_q & -g\,\cos(\overline{\theta}_o) \\ \overline{Z}_u & \overline{Z}_w & \overline{Z}_q & -g\,\sin(\overline{\theta}_o) \\ \overline{M}_u & \overline{M}_w & \overline{M}_q & 0 \\ 0 & 0 & 1 & 0 \end{bmatrix}. \tag{4.26}$$

The overbar denotes average with respect to time t. The mass and moment of inertia about the y-axis of the central body are absorbed into the stability derivatives in

$\bar{\mathbf{A}}_{hover}$, such that

$$\overline{X}_u = \frac{2}{m_{sys}} \left(\frac{1}{2\pi} \int_0^{2\pi} X_u(t) dt \right). \tag{4.27}$$

For example, the nonlinear function describing the effect of longitudinal velocity on the vertical dynamics of the central body, due to the tangential force on the wing is

$$\begin{aligned} Z_{u,T}(t) &= \left(\frac{1}{2} \sin(2\beta) \cos(\alpha_m) \cos^2 \zeta + \cos^2 \beta \sin(\alpha_m) \text{sgn}\left(\dot{\zeta}\right) \cos(\zeta) \right) \\ &\quad * \text{sgn}\left(\dot{\zeta}\right) c_T \cos(\omega t) \Delta u. \end{aligned} \tag{4.28}$$

The averaged result is

$$\overline{Z}_{u,T} = \frac{1}{\pi} \sin(2\beta) \cos(\alpha_m) c_T \left(1 + \frac{\sin(2\zeta_m)}{2\zeta_m} \right) \Delta u. \tag{4.29}$$

The integrals are calculated using assistance from [124] and [126]. The non-zero stability derivatives for the longitudinal motion of the body are

$$\overline{X}_u = -\frac{2}{\pi} \cos^2(\beta) \left(\cos(\alpha_m) c_T + \sin(\alpha_m) c_N \right) \left(1 + \frac{\sin(2\zeta_m)}{2\zeta_m} \right) \tag{4.30}$$

and

$$\overline{X}_w = \frac{1}{\pi} \sin(2\beta) \left(\cos(\alpha_m) c_T + \sin(\alpha_m) c_N \right) \left(1 + \frac{\sin(2\zeta_m)}{2\zeta_m} \right). \tag{4.31}$$

The non-zero stability derivatives for the vertical motion of the body are

$$\overline{Z}_u = \frac{1}{\pi} \sin(2\beta) \left(\cos(\alpha_m) c_T + \sin(\alpha_m) c_N \right) \left(1 + \frac{\sin(2\zeta_m)}{2\zeta_m} \right) \tag{4.32}$$

and

$$\overline{Z}_w = -\frac{2}{\pi} \sin^2(\beta) \left(\cos(\alpha_m) c_T + \sin(\alpha_m) c_N \right) \left(1 + \frac{\sin(2\zeta_m)}{2\zeta_m} \right). \tag{4.33}$$

The results predict that if the stroke plane is zero, namely the main flapping motion is along the longitudinal axis of the central body, then there will be no effect on the

motion of the body in the longitudinal direction to a perturbation in the vertical direction. Additionally, the effects on the vertical direction of the body are zero for perturbations in velocity in the vertical and horizontal directions. If the stroke plane angle is $\beta = -90°$, then perturbations in the longitudinal velocity will not have an effect on the stability of the system. In [127], Franklin states that the X_w derivative is traditionally neglected for vertical takeoff or landing aircraft.

The stability derivatives in the longitudinal and vertical directions, due to the pitch rate q, are both identically zero. For completeness,

$$\overline{X}_q \equiv 0 \text{ and } \overline{Z}_q \equiv 0, \tag{4.34}$$

both of which are traditionally neglected due to low magnitude in comparison with the other stability derivatives [127]. The stability derivatives resulting from change in the aerodynamic pitching moment due to perturbations in the longitudinal and vertical velocities are

$$\overline{M}_u = \frac{1}{2\pi} \cos(\beta)\ c_w\, c_N \left(1 + \frac{\sin(2\zeta_m)}{2\zeta_m}\right) \tag{4.35}$$

and

$$\overline{M}_w = -\frac{1}{2\pi} \sin(\beta)\ c_w\, c_N \left(1 + \frac{\sin(2\zeta_m)}{2\zeta_m}\right), \tag{4.36}$$

where c_w denotes the chord length of the wing. The time-average of the stability derivative from the aerodynamic pitching moment, due to change in pitch rate, is zero. We can state formally that

$$\overline{M}_q \equiv 0. \tag{4.37}$$

4.2.5 Stability Derivatives due to Change in Angle of Attack

The change in total velocity of the wing, in the wing frame, produces a change in the effective angle of attack of the wing relative to the stroke plane. For example, as detailed in [70], if the FWMAV has purely vertical velocity and increases in altitude, then the effective angle of attack and lift will be reduced. The opposite is true for a descent; the angle of attack and lift increase. The phenomenon is referred to as 'heave' damping in [70]. The change in angle of attack, $\Delta\alpha$, is either positive or negative and is obtained from:

$$\Delta\alpha = \tan^{-1}\left(\frac{v_{z,wg}}{v_{x,wg}}\right), \tag{4.38}$$

where $v_{x,wg}$ and $v_{z,wg}$ denote the total velocity of the wing, at the center of pressure, expressed in the wing frame in the x and z directions. In the vicinity of the hover condition, we assume that the change in angle of attack is small and using the small angle assumption: $\Delta\alpha = v_{z,wg}/v_{x,wg}$. The change in angle of attack is then equal to

$$\Delta\alpha = \frac{\sin(\beta)\Delta u + \cos(\beta)\Delta w - \sin(\zeta)\hat{r}_2 b_w \Delta q}{\cos(\zeta)\left(\cos(\beta)\Delta u - \sin(\beta)\Delta w\right) + \hat{r}_2 b\dot{\zeta}}. \tag{4.39}$$

The effects of $\Delta\alpha$ will manifest in the coefficients for the normal and tangential forces, previously detailed in Eqs. (4.8) and (4.9). The resulting normal and tangential lift coefficients will be equal to

$$C_{T,\Delta\alpha} = -0.4\,\mathrm{sgn}\left(\dot{\zeta}\right)\left(\cos^2(2\alpha) - 2\,\sin(4\alpha)\Delta\alpha\right) \tag{4.40}$$

and

$$C_{N,\Delta\alpha} = -3.4\,\mathrm{sgn}\left(\dot{\zeta}\right)\left(\sin(\alpha) + \cos(\alpha)\Delta\alpha\right). \tag{4.41}$$

When the coefficients are substituted into the equations for lift and drag, we make the following assumption:

$$U_{cp}(t)^2 \Delta\alpha \approx (\sin(\beta)\Delta u + \cos(\beta)\Delta w - \sin(\zeta)\hat{r}_2 b_w \Delta q)\, U_{cp}(t), \tag{4.42}$$

due to the fact that over the course of a flapping cycle, $U_{cp}(t) >> \Delta[.]$. The normal and tangential coefficients for the additional angle of attack are:

$$c_{T,\Delta\alpha} = 0.4\rho\, A_w \sin(4\alpha_m)\, (\hat{r}_2 b_w\, \omega\zeta_m) \tag{4.43}$$

and

$$c_{N,\Delta\alpha} = 1.7\rho\, A_w \cos(\alpha_m)\, (\hat{r}_2 b_w\, \omega\zeta_m)\ . \tag{4.44}$$

The stability derivative additions, due to the change in angle of attack, for the longitudinal motion of the FWMAV are:

$$\overline{X}_{u,\Delta\alpha} = -\frac{2}{\pi}\sin^2(\beta)\,(c_{T,\Delta\alpha}\sin(\alpha_m) + c_{N,\Delta\alpha}\cos(\alpha_m)) \tag{4.45}$$

and

$$\overline{X}_{w,\Delta\alpha} = -\frac{1}{\pi}\sin(2\beta)\,(c_{T,\Delta\alpha}\sin(\alpha_m) + c_{N,\Delta\alpha}\cos(\alpha_m))\,. \tag{4.46}$$

The stability derivatives affecting the vertical motion of the FWMAV are:

$$\overline{Z}_{u,\Delta\alpha} = \frac{1}{\pi}\sin(2\beta)\,(c_{T,\Delta\alpha}\sin(\alpha_m) - c_{N,\Delta\alpha}\cos(\alpha_m)) \tag{4.47}$$

and

$$\overline{Z}_{w,\Delta\alpha} = \frac{2}{\pi}\cos^2(\beta)\,(c_{T,\Delta\alpha}\sin(\alpha_m) - c_{N,\Delta\alpha}\cos(\alpha_m))\,. \tag{4.48}$$

If the stroke plane is identically zero, perturbations in the vertical velocity will now have an effect on the system. For a parallel stroke plane, when only velocity pertur-

bations are considered, there is no effect on the stability of the hover condition due to a vertical velocity perturbation. Likewise, if the stroke plane is $-90°$, longitudinal velocity perturbations will manifest in the system through the stability derivatives due to the change in angle of attack.

The stability derivative of the aerodynamic moment, due to pitch rate, is no longer identically zero. The stability derivative, $\overline{M}_{q,\Delta\alpha}$ is calculated according to:

$$\overline{M}_{q,\Delta\alpha} = -\frac{1}{\pi}\left(1 - \frac{\sin(2\zeta_m)}{2\zeta_m}\right)(\hat{r}_2 b)^2\Big(c_{T,\Delta\alpha}\sin(\alpha_m) + c_{N,\Delta\alpha}\cos(\alpha_m)\Big). \quad (4.49)$$

Without the addition of the stability derivatives due to $\Delta\alpha$, the analysis does not produce results consistent with previous studies. The system matrix with the addition of the stability derivatives due to the change in angle of attack is

$$\bar{\mathbf{A}}_{hover} = \begin{bmatrix} \overline{X}_u + \overline{X}_{u,\Delta\alpha} & \overline{X}_w + \overline{X}_{w,\Delta\alpha} & 0 & -g\cos(\theta_o) \\ \overline{Z}_u + \overline{Z}_{u,\Delta\alpha} & \overline{Z}_w + \overline{Z}_{w,\Delta\alpha} & 0 & -g\sin(\theta_o) \\ \overline{M}_u & \overline{M}_w & \overline{M}_{q,\Delta\alpha} & 0 \\ 0 & 0 & 1 & 0 \end{bmatrix}. \quad (4.50)$$

4.2.6 Results

4.2.6.1 Variation with Stroke Plane Angle

Results are presented for a FWMAV with hawkmoth type body parameters. The flapping frequency is set at 21 Hz with an amplitude $\zeta_m = 60°$. A simple bisection algorithm, between $0°$ and $45°$, is used to determine the angle of attack to maintain a hover condition. The bisection algorithm calculates an angle of attack of $35.895°$. The stability derivatives are non-dimensionalized consistent with the manner presented in [51], [62], and [66]. The reference length is c, the reference velocity is U, and the

reference time is c/U. The reference velocity, U, is defined as:

$$U = 4\zeta_m f \hat{r}_2 b. \tag{4.51}$$

The non-dimensional stability derivatives, denoted by a superscript +, are calculated in the following manner:

$$\overline{X}_{[.]}{}^{+} = \frac{\overline{X}_{[.]}}{\rho U^2 A_w}, \; \overline{Z}_{[.]}{}^{+} = \frac{\overline{Z}_{[.]}}{\rho U^2 A_w}, \text{ and } \quad \overline{M}_{[.]}{}^{+} = \frac{\overline{M}_{[.]}}{\rho U^2 A_w c}. \tag{4.52}$$

The stability derivatives due to the pitch rate, q, are non-dimensionalized by multiplying the denominator by an additional reference length. The mass of the system, mass moment of inertia, and gravity are non-dimensionalized according to:

$$m_{sys}{}^{+} = \frac{m_{sys}}{\rho A_w c}, \; I_{yy,sys}{}^{+} = \frac{I_{yy,sys}}{\rho A_w c^3}, \text{ and } g^{+} = \frac{gc}{U^2}. \tag{4.53}$$

Fig. 4.1 shows the variation of the pole locations for a hawkmoth-sized FWMAV for changes in the stroke plane angle. To maintain the equilibrium at hover, the nominal pitch angle also changes. The stroke plane angle, β, varies from $\beta \in \{0 \; -22.5 \; -45\}$ and the corresponding nominal pitch angle is $\theta_o \in \{0 \; 22.5 \; 45\}$. Both angles are given in degrees. For a pitch angle of zero degrees, the system has two stable poles and a pair of unstable, oscillatory poles. As the pitch angle increases, the magnitude of the stroke plane angle changes to maintain the equilibrium condition. The magnitude of the poles varies slightly with the change in nominal pitch angle and stroke plane angle. The modal structure is consistent with the independent results presented in [62, 66, 70].

The magnitude of the poles differs from the previous efforts. The unstable oscillatory mode has a slower time constant than the results in [62]. The slower of the two subsidence modes is faster than the results in [62]. The discrepancy in the magnitude

of the eigenvalues could be a result of the numerous assumptions used to obtain the approximate model. In [62], the Navier-Stokes equations are coupled with the flight dynamics equations to compute the equilibrium solution at hover. The aerodynamic model is a simple quasi-steady/blade-element model. The assumption on the angle of attack results in the neglect of the rotational lift effects of the wing. The wingstrokes in [62] and [70] are more complicated and biomimetic. The wing joint placement is different. The wing joints in other studies are placed forward of the center of mass of the body. The wingstroke chosen here can be replicated by current technology [80].

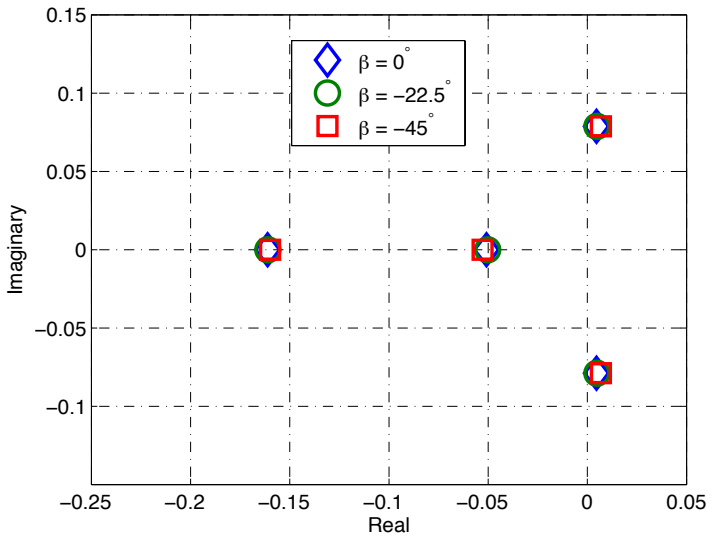

Figure 4.1: Modal Structure for Local Averaging in the Vicinity of Hover, Variation of Pole Locations with Stroke Plane Angle β

4.2.6.2 Variation of Model Insect

The modal structure for different insect models is now presented, based off of the parameters and analysis in [62] and [66]. The five model insects are a hoverfly (HF), dronefly (DF), cranefly (CF), hawkmoth (HM), and bumblebee (BB). Table 4.1 details the pertinent parameters for each model. The angle of attack for each insect

model is calculated using a bisection algorithm. For all model insects, the nominal

Model	m (mg)	b (mm)	c (mm)	$\zeta_m(^\circ)$	f (Hz)	$\alpha_m(^\circ)$
HF	27.3	9.3	2.2	45	160	23.90
DF	68.4	11.4	3.19	54.5	157	17.47
CF	11.4	12.7	2.38	60	45.5	22.11
HM	1648	51.9	18.26	60.5	26.3	24.99
BB	175	13.2	4.01	58	155	20.46

Table 4.1: Model Parameter Summary

pitch angle is set to $\theta_o = 45^\circ$ and the associated stroke plane angle is $\beta = -45^\circ$. The chosen pitch angle is close to the values presented in [62]. It's important to note that in [62], as well as much of the biology literature, the stroke plane is defined relative to the inertial frame. In the development in Chapter 2, the stroke plane is defined relative to the longitudinal axis of the body. The associated modal structure is presented in Fig. 4.2. The modal structure is consistent with the results presented in [62, 70], as stated previously. As shown in [62], the stability derivatives for the dronefly and the hoverfly are nearly identical. The magnitude of the slow subsidence mode is larger than expected from the results in [62], but the magnitude of the fast subsidence mode has less than ten percent error for all species. The results in [62] predict approximately a half to full order of magnitude difference between the slow and fast subsidence mode. The worst approximation is of the unstable oscillatory mode for the cranefly; the results differs by over an order of magnitude. The sources of discrepancy are numerous and include the wingstroke assumptions, wing planform instructions, and the simplified aerodynamic model.

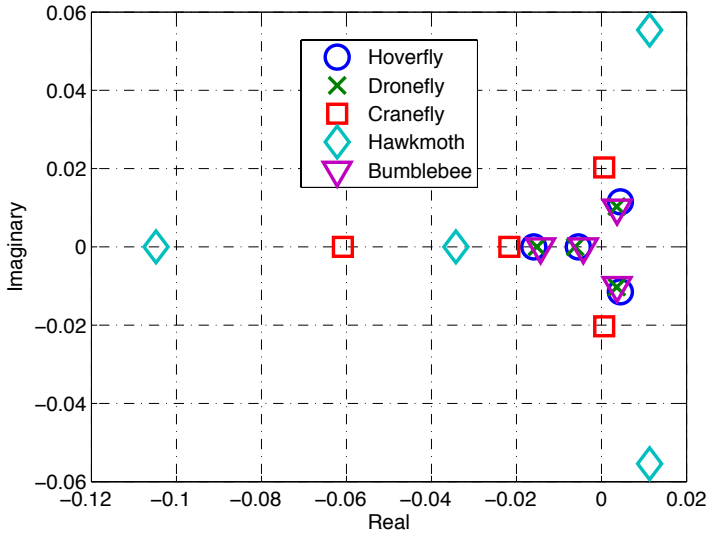

Figure 4.2: Nondimensional Modal Structure for Multiple Insect Models

4.3 Stability Derivatives in Vicinity of a Hover Condition: Multi-Body Model

The stability derivatives previously presented for hover can be expanded to include the averaged wing effects, as derived in Chapter 3. The equations of motion were previously detailed in Equations (3.38), (3.39), and (3.41). The averaged equation of motion for the longitudinal velocity of the body is

$$\begin{aligned}\dot{\bar{u}} &= \frac{\bar{F}_x}{m_{sys}} - g\sin\bar{\theta} - \bar{q}\bar{w} + \frac{2}{m_{sys}} m_w \rho_w \omega \zeta_m \sin(\alpha_m)\cos\beta \left(\frac{2}{\pi}\frac{\sin(\zeta_m)}{\zeta_m}\right)\bar{q} \\ &+ \frac{m_w \rho_w \hat{r}_2 b_w}{m_{sys} I_{yy,sys}} \big(k_T \sin(\alpha_m) - k_N \cos(\alpha_m)\big) \sin\beta \big(1 - \mathbf{J}_0(2\zeta_m) - \mathbf{J}_2(2\zeta_m)\big).\end{aligned} \tag{4.54}$$

The averaged equation of motion for the vertical velocity of the body is

$$\begin{aligned}\dot{\bar{w}} &= \frac{\bar{F}_z}{m_{sys}} + g\cos\bar{\theta} + \bar{q}\bar{u} - \frac{2}{m_{sys}} m_w \rho_w \omega \zeta_m \sin(\alpha_m)\sin\beta \left(\frac{2}{\pi}\frac{\sin(\zeta_m)}{\zeta_m}\right)\bar{q} \\ &- \frac{m_w \rho_w \hat{r}_2 b_w}{m_{sys} I_{yy,sys}} \big(k_T \sin(\alpha_m) - k_N \cos(\alpha_m)\big) \cos\beta \big(1 - \mathbf{J}_0(2\zeta_m) - \mathbf{J}_2(2\zeta_m)\big).\end{aligned} \tag{4.55}$$

As detailed in Chapter 3, the time average of the equations of motion for the pitch velocity is identically zero. Therefore, the pitch dynamics will be governed by

$$\dot{\bar{q}} = 0 \tag{4.56}$$

and

$$\dot{\bar{\theta}} = 0. \tag{4.57}$$

The equilibrium condition changes from the solution presented in Section 4.2.2. A pitch velocity of zero will continue to serve for equilibrium. However, the kinematic parameters will change slightly to handle the additional constant force resulting from the local averaging of the equations of motion. Fortunately, the additional force, which is in the second line of Equations (4.55) and (4.56), is coincident with the lift vector. Therefore, the new equilibrium condition is

$$\begin{aligned} -g\cos(\theta) &= \cos(\beta)\frac{F_{z,sp}}{m_{sys}} - \cos(\beta)\frac{m_w \rho_w \hat{r}_2 b_w}{m_{sys} I_{yy,sys}} * \\ &\quad \big(k_T \sin(\alpha_m) - k_N \cos(\alpha_m)\big)\big(1 - \mathbf{J}_0\left(2\zeta_m\right) - \mathbf{J}_2\left(2\zeta_m\right)\big) \end{aligned} \tag{4.58}$$

and

$$\begin{aligned} g\sin(\theta) &= -\sin(\beta)\frac{F_{z,sp}}{m_{sys}} + \sin(\beta)\frac{m_w \rho_w \hat{r}_2 b_w}{m_{sys} I_{yy,sys}} * \\ &\quad \big(k_T \sin(\alpha_m) - k_N \cos(\alpha_m)\big)\big(1 - \mathbf{J}_0\left(2\zeta_m\right) - \mathbf{J}_2\left(2\zeta_m\right)\big). \end{aligned} \tag{4.59}$$

The condition for the pitch velocity and pitch angle are trivially satisfied, given the nature of Equations (4.56) and (4.57). The additional stability derivatives will be a result of the term containing the pitch velocity, $\bar{q}$, in Equations (4.55) and (4.56).

The additional stability derivatives will be defined, for one wing, according to

$$\overline{X}_{q,wg} = m_w \rho_w \omega \zeta_m \sin(\alpha_m) \cos(\beta) \left(\frac{2}{\pi} \frac{\sin(\zeta_m)}{\zeta_m} \right) \tag{4.60}$$

and

$$\overline{Z}_{q,wg} = -m_w \rho_w \omega \zeta_m \sin(\alpha_m) \sin(\beta) \left(\frac{2}{\pi} \frac{\sin(\zeta_m)}{\zeta_m} \right). \tag{4.61}$$

The inclusion of the wing effects actually adds additional stability derivatives to the system matrix. The wings affect the position of the flapping micro air vehicle through the pitch velocity. In [66], Sun and Xiong state that improper phasing between the flapping and pitching motion of the wings can produce highly unstable results (in terms of the averaged system). It is an interesting result that the wing effects create, or add, stability derivatives that the previous analysis did not develop. The stability derivatives of the position of the body, X_q and Z_q, are neglected in the analysis presented in [70]. The derivatives are not neglected by Sun in [66] and [62]. With the addition of the stability derivatives due to the coupling between the wing and body motion, the system matrix now can be presented as

$$\bar{\mathbf{A}}_{hover,wg} = \begin{bmatrix} \overline{X}_u + \overline{X}_{u,\Delta\alpha} & \overline{X}_w + \overline{X}_{w,\Delta\alpha} & \overline{X}_{q,wg} & -g\cos(\theta_o) \\ \overline{Z}_u + \overline{Z}_{u,\Delta\alpha} & \overline{Z}_w + \overline{Z}_{w,\Delta\alpha} & \overline{Z}_{q,wg} & -g\sin(\theta_o) \\ \overline{M}_u & \overline{M}_w & \overline{M}_{q,\Delta\alpha} & 0 \\ 0 & 0 & 1 & 0 \end{bmatrix}. \tag{4.62}$$

In order to analyze the effects of the wings, the mass of the wings needs to be calculated for each of the model insects. The following tables presents additional data not previously presented in Table 4.1. The mass of the wings presented in Table 4.2 is for one wing. The data is taken from Ellington in [16] for the hoverfly, dronefly, and cranefly. The specimen number is listed in parenthesis. The data for the hawkmoth is from Willmott and Ellington in [21]. For the bumblebee, the data is from Dudley

Model	$m_w(\%)$	m_w (mg)	$\alpha_m(^\circ)$	$\alpha_m(^\circ)$	$\Delta\alpha_m(\%)$
HF (HF07)	1.27	0.17	23.90	23.99	0.38
DF (DF01)	1.54	0.53	17.47	17.57	0.57
CF (CF02)	4.29	0.24	22.11	22.11	0
HM (F1)	5.79	47.71	24.99	26.16	4.68
BB (BB01)	0.53	0.46	20.46	20.51	0.24

Table 4.2: Model Parameters - Wings

and Ellington in [25]. Table 4.2 details the changes in angle of attack required for the hover solution with the wing effects included. The angle of attack is determined by using a bisection algorithm. All other parameters remain the same as in Section 4.2.6. The change in angle of attack is negligible, except for the hawkmoth parameters. Tables 4.3 and 4.4 present the eigenvalues previously presented in Section 4.2.6 compared to the eigenvalue results for the system matrix and equilibrium solution with the wing effects included.

Model	λ_1	$\lambda_{1,wg}$	$\Delta\lambda_1(\%)$	λ_2	$\lambda_{2,wg}$	$\Delta\lambda_2(\%)$
HF	-0.01594	-0.01606	0.71	-0.005441	-0.005431	0.17
DF	-0.01520	-0.01532	0.77	-0.006209	-0.006201	0.12
CF	-0.06085	-0.06085	0	-0.02170	-0.02170	0
HM	-0.1048	-0.1074	2.48	-0.03425	-0.03347	2.27
BB	-0.01432	-0.01437	0.07	-0.004266	-0.004263	0.34

Table 4.3: Eigenvalue Comparison: Standard Aircraft Equations vs. Wing Effects, Subsidence Modes (Fast and Slow)

Model	$\lambda_{3,4}$	$\lambda_{3,4,wg}$	$\Delta\lambda_{3,4}(\%)$
HF	$0.004437 \pm 0.01149j$	$0.004491 \pm 0.01141j$	1.23
DF	$0.003587 \pm 0.01029j$	$0.003644 \pm 0.01026j$	1.6
CF	$0.0006144 \pm 0.02028j$	$0.0006146 \pm 0.02028j$	0.03
HM	$0.01130 \pm 0.05541j$	$0.01281 \pm 0.05560j$	13.35
BB	$0.003653 \pm 0.009903j$	$0.003677 \pm 0.009888j$	0.67

Table 4.4: Eigenvalue Comparison: Standard Aircraft Equations vs. Wing Effects, Oscillatory Mode

The addition of the wing effects introduces a noticeable change in the non-dimensional stability derivatives for the hawkmoth model. The change is minimal for the other

insect models. The changes in the subsidence modes for the cranefly were less than 0.01% and not significant. The addition of the wing effects produces an error of 13.35% for the unstable, oscillatory mode of the hawkmoth model. As detailed in Table 4.2, the mass of the wings of the hawkmoth are nearly two orders of magnitude greater than the mass of the other insect models. Furthermore, the flapping frequency is only an order of magnitude less than the bumblebee, dronefly, and cranefly. As detailed in Equations (4.55) and (4.56), the wing effects are proportional to mass and the flapping frequency, or the flapping frequency squared. Therefore, the wing effects for the hawkmoth should be more significant than for the other insect models.

4.4 Linear Control Analysis in Vicinity of Hover

In order to get a gauge of whether or not the mass of the wings is important for control studies of the averaged system, a control analysis will be conducted in vicinity of the hover condition. The input matrix will be determined by perturbations from equilibrium, as detailed in [51] and [70]. A controllability analysis for flapping wing micro air vehicles is nothing new and is widely reported. However, the analysis in the context of the wing effects has not been approached. For the control inputs, a stroke plane angle tilt can shift the lift vector and enable translation of the vehicle [70]. The stroke plane is also used as a control input in [100]. The stroke plane tilt is not available to the work presented in [79, 83], since the dynamic model does not allow for stroke plane changes. Lift can be increased (or decreased) by increasing (decreasing) the flapping frequency. The effect of the flapping frequency has been previously presented in [70] and [79]. For pitch control, a control mass will be used. The multi-body equations of motion, to include the control mass, wings, and central body, are presented in [109]. The control mass controls the pitch by creating a mass moment about the center of mass of the vehicle and directly changing the orientation. The method has been independently presented in [104] and [79]. In [104], the mass

moment is created by pitching a segmented body. In [79], the control mass is a 'bobweight' with a single degree of freedom that translates to create pitch control. The derivation presented in [109] assumes the control mass has two degrees of freedom: freedom to translate along the longitudinal and vertical axes of the body. As stated, a detailed derivation of the multi-body effects is available in [109]. The resulting moment, with one degree of freedom along the longitudinal axis, is

$$M_{cm} = -m_{cm} x_{cm}(t)\, g \cos(\theta), \tag{4.63}$$

where m_{cm} denotes the mass of the control mass and $x_{cm}(t)$ is the position of the control mass relative to the central body center of mass along $\hat{b}_x$. The position of the control mass is defined according to

$$x_{cm}(t) = x_{cm,o} + x_{cm,m} \sin\left(2\pi f_{mass} t\right), \tag{4.64}$$

where $x_{cm,o}$ denotes the initial position of the mass relative to the center of mass of the central body. The amplitude of the control mass' motion is defined by $x_{cm,m}$ and the frequency of the motion is denoted by f_{mass}. If the f_{mass} is equal to the flapping frequency, then the time averaged effect of the control mass is simply

$$\overline{M}_{cm} = -m_{cm} x_{cm,o}\, g \cos(\theta). \tag{4.65}$$

The quarter-cycle representation of the moment due to the control mass is

$$\overline{M}_{cm,QC} = -m_{cm} x_{cm,o}\, g \cos(\theta) - \operatorname{sgn}\left(\dot{\zeta}\right) m_{cm} x_{cm,m}\, g \cos(\theta). \tag{4.66}$$

The small perturbations from equilibrium for the control inputs of the averaged system are simply: $f_o + \Delta f$, $\beta_o + \Delta\beta$, and $x_{cm,o} + \Delta x_{cm,o}$. Substitution of the perturbed

control inputs into the equations of motion, coupled with subtraction of the equilibrium control inputs, will produce the control derivatives. For the system without the wing effects, the control derivatives due to change in the stroke plane are

$$\overline{X}_{\beta} = \frac{1}{2}\cos(\beta_o)\left(k_N\cos(\alpha_m) - k_T\sin(\alpha_m)\right) \tag{4.67}$$

and

$$\overline{Z}_{\beta} = \frac{1}{2}\sin(\beta_o)\left(k_N\cos(\alpha_m) - k_T\sin(\alpha_m)\right). \tag{4.68}$$

The coefficients k_N and k_T are evaluated at the trim condition. The control derivative for pitch due to a change in stroke plane, $\overline{M}_{\beta}$, is identically zero. Due to the assumption of wing joint position, a change in the stroke plane has zero effect on the pitch angle. If the wing joints were fore, or aft, of the body center of mass, then change in the stroke plane would affect the pitch velocity. The control derivatives for the position of the FWMAV due to the control mass, $\overline{X}_{cm}$ and $\overline{Z}_{cm}$, are identically zero. The control derivative for pitch, due to the control mass, is

$$\overline{M}_{x_{cm}} = -m_{cm}\,g\cos(\theta_o). \tag{4.69}$$

To efficiently define the control derivatives due to change in the flapping frequency, the following constants are defined

$$k_{T,\Delta f} = 0.2\rho_{sl}A_w\cos^2(2\alpha_m)\left(2\pi\hat{r}_2 b_w\zeta_m\right)^2 \tag{4.70}$$

and

$$k_{N,\Delta f} = 1.7\rho_{sl}A_w\sin(\alpha_m)\left(2\pi\hat{r}_2 b_w\zeta_m\right)^2. \tag{4.71}$$

The control derivatives for the position of the FWMAV due to change in flapping frequency, are

$$\overline{X}_f = -\frac{1}{2}\sin(\beta_o)\left(k_{T,\Delta f}\sin(\alpha_m) - k_{N,\Delta f}\cos(\alpha_m)\right) f_o \tag{4.72}$$

and

$$\overline{Z}_f = \frac{1}{2}\cos(\beta_o)\left(k_{T,\Delta f}\sin(\alpha_m) - k_{N,\Delta f}\cos(\alpha_m)\right) f_o. \tag{4.73}$$

The control derivative for pitch due to change in the flapping frequency is identically zero. The linear system is arranged in state-space form in the following manner:

$$\begin{bmatrix} \Delta\dot{u} \\ \Delta\dot{w} \\ \Delta\dot{q} \\ \Delta\dot{\theta} \end{bmatrix} = \bar{\mathbf{A}}_{hover} \begin{bmatrix} \Delta u \\ \Delta w \\ \Delta q \\ \Delta\theta \end{bmatrix} + \bar{\mathbf{B}}_{hover} \begin{bmatrix} \Delta\beta \\ \Delta x_{cm,o} \\ \Delta f \end{bmatrix}. \tag{4.74}$$

The system matrix, $\bar{\mathbf{A}}_{hover}$, is defined in Equation (4.50). The control input matrix is defined according to

$$\bar{\mathbf{B}}_{hover} = \begin{bmatrix} \overline{X}_\beta & \overline{X}_{x_{cm}} & \overline{X}_f \\ \overline{Z}_\beta & \overline{Z}_{x_{cm}} & \overline{Z}_f \\ \overline{M}_\beta & \overline{M}_{x_{cm}} & \overline{M}_f \\ 0 & 0 & 0 \end{bmatrix}. \tag{4.75}$$

The nominal control input for the control mass, to maintain the equilibrium conditions previously defined, is simply $x_{cm,o} = 0$ and $f_{mass} = f$. Additionally, the mass of the control mass will be set to equal the total wing mass. The controllability of the system can be checked according to one of the controllability rank conditions in [129]. The controllability matrix is calculated according to

$$\mathbb{C} = \begin{bmatrix} B & AB & A^2B & \dots & A^{n-1}B \end{bmatrix}. \tag{4.76}$$

If the rank of the controllability matrix is equal to the dimension of the system, then the system is completely controllable [129]. The dimension of the flapping wing micro air vehicle system, based on the linearized averaged dynamics, is four. Using the hawkmoth parameters as an example, the system is completely controllable. A completely controllable system can be stabilized using full state feedback. We can define a control input according to $u = -\mathbf{K}x + r$, where $\mathbf{K}$ is the gain matrix and r is a reference. The system is stabilized using pole placement and the completely controllable system allows for picking the placement of poles. Using full state feedback, the dynamics of the new system are

$$\dot{x} = (\mathbf{A} - \mathbf{BK})\, x + \mathbf{B}r \tag{4.77}$$

and the matrix $(\mathbf{A} - \mathbf{BK})$ is stable with all of the eigenvalues in the left-half side of the complex plane. Alternatively, the system is stable if the magnitude of the real parts of all of the eigenvalues is negative. Full state feedback will be used to analyze the effect of the wings on the stabilization of the unstable system of a flapping wing micro air vehicle in the vicinity of hover. The addition of wing effects changed the stability derivatives for the flapping wing micro air vehicle near hover. The addition of the wing effects will also change the control derivatives. The change is due to the constant wing force as detailed in Equations (4.55) and (4.56). The changes to the control derivatives will manifest in $\overline{X}_{\beta}$, $\overline{Z}_{\beta}$, $\overline{X}_{f}$, and $\overline{Z}_{f}$. The changes in the control derivatives due to perturbations in the stroke plane angle are

$$\overline{X}_{\beta,wg} = \frac{\cos(\beta_o)\left(k_T \sin(\alpha_m) - k_N \cos(\alpha_m)\right) \hat{r}_2 b_w m_w \rho_w \left(1 - \mathbf{J}_0(2\zeta_m) - \mathbf{J}_2(2\zeta_m)\right)}{I_{yy,sys}} \tag{4.78}$$

and

$$\overline{Z}_{\beta,wg} = \frac{\sin(\beta_o)\left(k_T \sin(\alpha_m) - k_N \cos(\alpha_m)\right)\hat{r}_2 b_w m_w \rho_w \left(1 - \mathbf{J}_0(2\zeta_m) - \mathbf{J}_2(2\zeta_m)\right)}{I_{yy,sys}}. \tag{4.79}$$

The control derivatives are evaluated at the trim condition with the nominal control input. The changes in the control derivatives due to perturbations in the flapping frequency are

$$\overline{X}_{f,wg} = \frac{\sin(\beta)\left(k_{T,\Delta f} \sin(\alpha_m) - k_{N,\Delta f} \cos(\alpha_m)\right)\hat{r}_2 b_w m_w \rho_w \left(1 - \mathbf{J}_0(2\zeta_m) - \mathbf{J}_2(2\zeta_m)\right) f_o}{I_{yy,sys}} \tag{4.80}$$

and

$$\overline{Z}_{f,wg} = -\frac{\cos(\beta)\left(k_{T,\Delta f} \sin(\alpha_m) - k_{N,\Delta f} \cos(\alpha_m)\right)\hat{r}_2 b_w m_w \rho_w \left(1 - \mathbf{J}_0(2\zeta_m) - \mathbf{J}_2(2\zeta_m)\right) f_o}{I_{yy,sys}}. \tag{4.81}$$

The control input matrix with the wing effects included is

$$\bar{\mathbf{B}}_{hover,wg} = \begin{bmatrix} \overline{X}_\beta + \overline{X}_{\beta,wg} & \overline{X}_{x_{cm}} & \overline{X}_f + \overline{X}_{f,wg} \\ \overline{Z}_\beta + \overline{Z}_{\beta,wg} & \overline{Z}_{x_{cm}} & \overline{Z}_f + \overline{Z}_{f,wg} \\ \overline{M}_\beta & \overline{M}_{x_{cm}} & \overline{M}_f \\ 0 & 0 & 0 \end{bmatrix}. \tag{4.82}$$

The pair $\left(\bar{\mathbf{A}}_{hover,wg}, \bar{\mathbf{B}}_{hover,wg}\right)$ is also controllable. Using state feedback, the gains for placing the poles at the following locations

$$P = \begin{bmatrix} -0.1077 \\ -0.0122 \pm 0.0557j \\ -0.0314 \end{bmatrix} \tag{4.83}$$

are different for the linearized, averaged system without wing effects and the linearized, averaged system with wing effects. The desired pole locations for the subsidence modes are the same as the open loop poles for the averaged system without wings. The unstable, oscillatory mode is changed to be at the same time constant and damping ratio, but with a stable magnitude. The gain matrix K_1 denotes the gains for the system without wings. The gain matrix K_2 denotes the gain matrix for the system with wings. The resulting gain matrices are

$$K_1 = \begin{bmatrix} 0.3892 & 0.1257 & -0.3737 & 0.4830 \\ -0.0224 & -0.0164 & -0.0334 & -0.0046 \\ -32.4690 & -14.3222 & 18.2678 & -7.4598 \end{bmatrix}$$

and

$$K_2 = \begin{bmatrix} 0.3719 & 0.1097 & -0.1534 & 0.4651 \\ -0.0239 & -0.0171 & -0.0357 & -0.0046 \\ -25.9670 & -12.4080 & -7.0859 & -6.2070 \end{bmatrix}.$$

The system with wing effects requires less overall control authority to achieve the desired pole locations. Figure 4.3 shows the open loop stability derivatives for the hawkmoth models with and without wing effects. Figure 4.4 shows the effects of applying the two different gain matrices to the open loop models. The diamond represents the system without wings with the correct feedback. The square represents the system with wings with the feedback calculated for the system without wings. The 'x' represents the system without wings with the feedback calculated for the system with wings. From an initial analysis, it appears applying the wrong feedback to the system with wings may results in an unstable configuration if the desired pole locations, or the pole locations due to a limited control input, are too close to the imaginary axis. For example, if the closed-loop pole locations of the oscillatory mode are placed at $-0.005 \pm 0.0557j$, applying the feedback K_1 to the system with wings

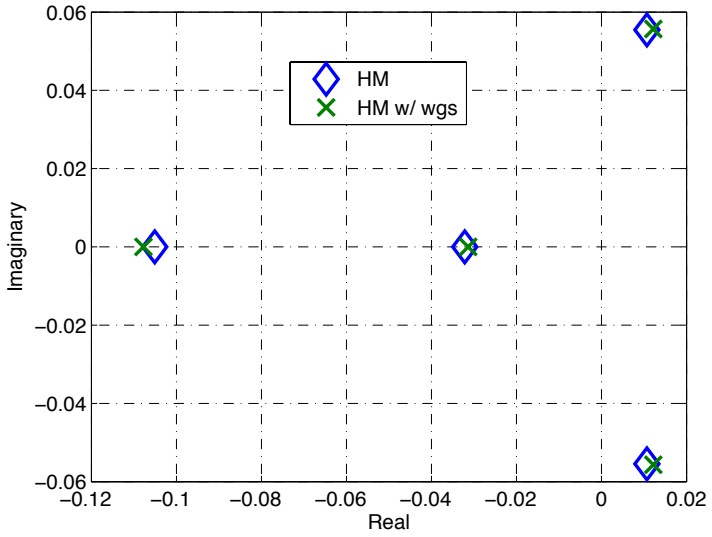

Figure 4.3: Stability Derivatives for Hawkmoth Model w/ and w/o Wing Effects. Wing effects detailed by 'w/ wgs'

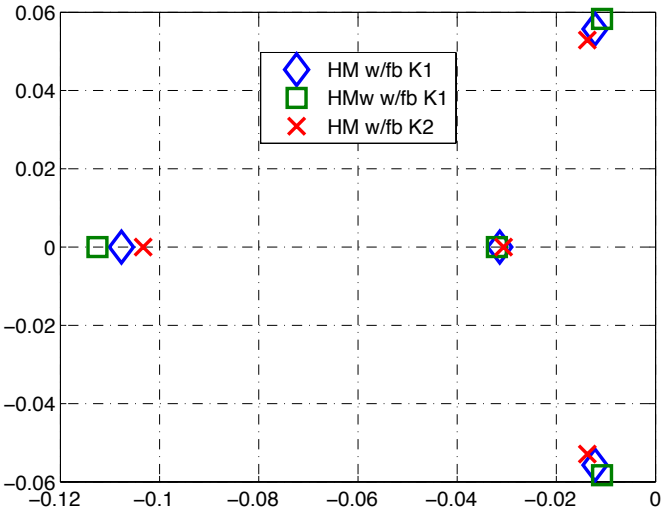

Figure 4.4: Stability Derivatives for Hawkmoth Model w/ and w/o Wing Effects with Full State Feedback

will not result in stable poles, but in marginally stable poles. The poles will have real parts equal to 0 and exist squarely on the $j\omega$-axis. If the closed-loop pole location is set at $-0.0003 \pm 0.0557j$, then the application of the feedback for the system without wings to the system with wings will result in a slowly unstable system. The unstable

oscillatory mode will be $0.0001 \pm 0.0547j$. The wide range of linear control theory could easily handle this problem, namely robust and/or adaptive control techniques that account explicitly for unknown or uncertain system parameters. However, the point is simply that the inclusion of the wing effects, for a hawkmoth sized vehicle, changes the linear dynamics. The linear dynamics are good for only small deviations from equilibrium. In Chapter 3, the method of local averaging did not produce a good approximation of the system. Furthermore, the nonlinear dynamics predict a significant difference in the position and orientation of the flapping wing micro air vehicle when the wing effects are included. The wings can have an impact on the linearization of the averaged system. The effects of the wings need to be addressed on the nonlinear dynamics to quantify, when (if) the mass effects of the wings are no longer important.

4.5 Limit Cycle Analysis in Vicinity of Hover

The quarter-cycle equations introduced in Chapter 3, coupled with the equilibrium solution, can be used to identify conditions for limit cycles. In reality, the averaged system is only an approximation of the periodic flapping wing micro air vehicle system. As stated in [74] and [82], the equilibrium condition for a flapping wing micro air vehicle is stable oscillations around an operating point. In [75], Bolender conducted an orbital stability analysis of the limit cycle behavior of a model flapping wing micro air vehicle. Bolender determined that the limit cycle is unstable. The conditions for the existence of a limit cycle can be identified for both a three degree of freedom standard aircraft model and for the three degree of freedom model with the mass and inertial effects of the wings included. As described in [66], the destabilizing effect from equilibrium is largely a result of coupling between the pitch velocity and the translational velocity of the body. The aerodynamic pitch moment, after the quarter-cycle approximation is applied, is given in Equation (3.45). The equation is repeated

here, where $\overline{M}_{aero,QC}$ is calculated according to

$$\begin{aligned}\overline{M}_{aero,QC} &= \operatorname{sgn}(\zeta)\,\hat{r}_2 b_w \frac{1}{\zeta_m}\mathbf{H}_1(\zeta_m)\left(k_N\cos(\alpha_m) - k_T\sin(\alpha_m)\right) \\ &\quad + \frac{1}{8}\operatorname{sgn}\left(\dot{\zeta}\right) c_w k_N\left(\mathbf{J}_0(\zeta_m) + \mathbf{J}_2(\zeta_m)\right).\end{aligned} \tag{4.84}$$

Taking inspiration from the control theory of feedback linearization as detailed in [121], two conditions can be set for limit cycles in vicinity of hovering. Both conditions assume that there is a control input that meets two conditions. One, the control input necessary for the limit cycle does not affect the vertical and longitudinal equilibrium of the flapping wing micro air vehicle. Alternatively, the control necessary to produce the limit cycle results in zero net thrust and lift equal to weight over the course of a flapping cycle. The second condition depends on the desired behavior. If the control can cancel out the entirety of the quarter-cycle approximation for M_{aero}, then the limit cycle behavior will only be exhibited in the longitudinal position of the flapping wing micro air vehicle. The pitch velocity will remain zero and the pitch angle will not change. Therefore, assuming the control is available, we can define M_{c1} according to

$$M_{c1} = -2\operatorname{sgn}(\zeta)\,\hat{r}_2 b_w \frac{1}{\zeta_m}\mathbf{H}_1(\zeta_m)\left(k_N\cos(\alpha_m) - k_T\sin(\alpha_m)\right). \tag{4.85}$$

The control is multiplied by two to account for the contribution of both wings. Using the same morphological parameters as in Chapter 3, the flapping wing model will be based on a hawkmoth. The flapping frequency is set at 22 Hz. With a flapping amplitude $\zeta_m = 60°$, the calculated angle of attack is 31.4923°. The angle of attack is calculated using a bisection algorithm as detailed in Section 4.2.6. The trim condition is for the averaged system without the effects of the wings. The control is applied to the analytical system and the 'quarter-cycle' approximation of the system. The position of the flapping wing micro air vehicle after four flapping cycles is presented in Fig 4.5(a). The pitch angle is presented in Fig 4.5(b).

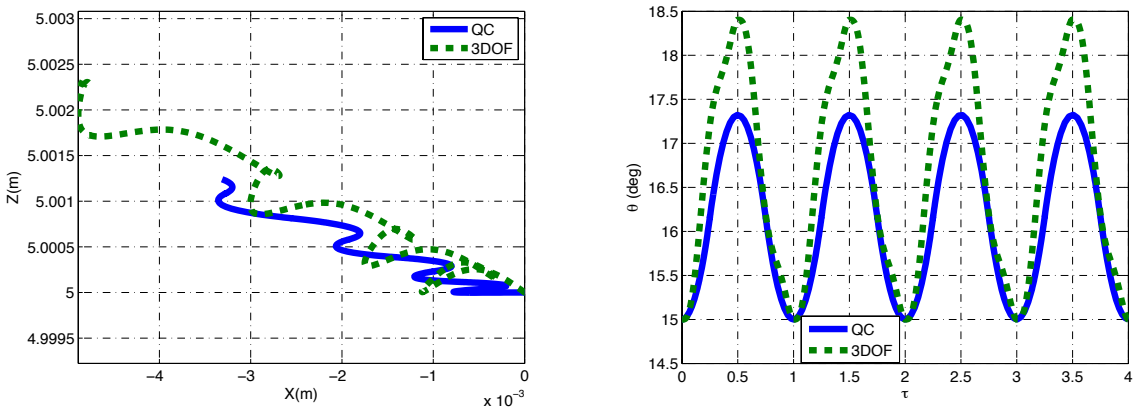

(a) $X - Z$ Position

(b) Pitch Angle

Figure 4.5: Simulation Results for Limit Cycle with M_{c1}, $\beta = -15°$, $\theta_o = 15°$

The pitch angle is stable, in the absence of perturbations. The flapping wing micro air vehicle slowly translates from the initial starting point. The piecewise linear control applied to the first order system results in a slightly larger oscillation from the initial pitch angle of 15°. The control applied is open loop and is used as a mean of identifying the conditions necessary for limit cycle type behavior of the pitch angle. If the control can only change the portion of the M_{aero} equation that is consistent with a sine wave, the sgn(ζ) portion, then the limit cycle behavior will manifest in the pitch angle only.

The applied control can also be assumed to counter the entirety of the aerodynamic pitching moment according to

$$M_{c2} = -2\overline{M}_{aero,QC}. \tag{4.86}$$

If the control is applied to the first order and quarter-cycle system, a different type of behavior manifests. The inertial position with control M_{c2} is presented in Figure 4.6. Figure 4.6(a) shows the inertial position after one flapping cycle. Figure 4.6(b) shows the inertial position after four flapping cycles. The first order system is represented

by the dashed line and labeled '3DOF.' The approximation of the first order system is represented by the solid line and labeled 'QC.'

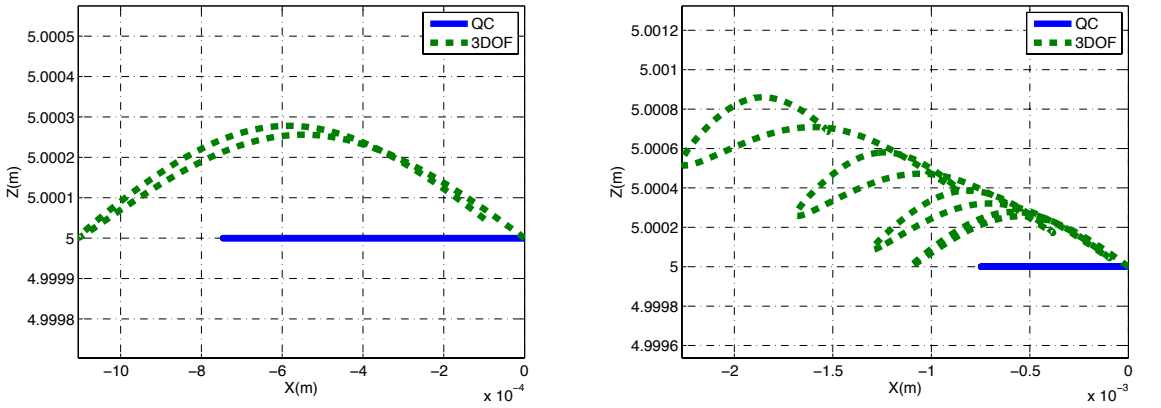

(a) $X - Z$ Position for One Flapping Cycle

(b) $X - Z$ Position for Four Flapping Cycles

Figure 4.6: $X - Z$ Position Simulation Results for Limit Cycle with M_{c2}, $\beta = -15°$, $\theta_o = 15°$

Without active control, the first order system nearly returns to the initial starting point after one flapping cycle. The aircraft slowly translates away from the initial starting point. The quarter-cycle system demonstrates the limit cycle behavior. The aircraft translates back and forth at the initial starting altitude. The pitch angle of the first order system is presented in Figure 4.7(a) and pitch angle of the quarter-cycle system is presented in Figure 4.7(b). The limit cycle about the initial pitch angle still manifests in the first order system, although it is qualitatively different from the previous result. In the absence of disturbances, the control perfectly cancels the approximation of the aerodynamic pitch moment and there is no change from the initial pitch angle.

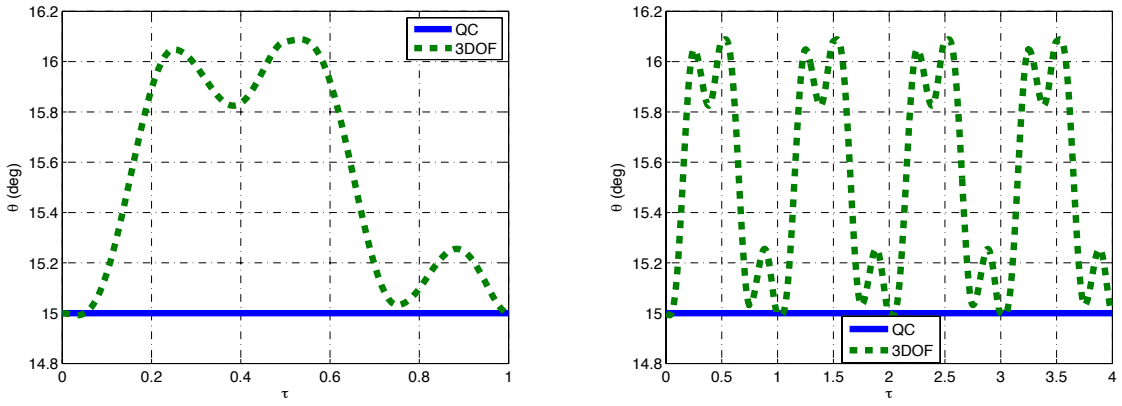

(a) Pitch Angle for One Flapping Cycle

(b) Pitch Angle for Four Flapping Cycles

Figure 4.7: Pitch Angle Simulation Results for Limit Cycle with M_{c2}, $\beta = -15°$, $\theta_o = 15°$

The same analysis can be applied to the approximation of the first order system presented in Chapter 3.4.1 and Appendix C. The results are not the same. The control is only designed to cancel the effects of the aerodynamic pitching moment and does not account for the effects of the wings. Figure 4.8 presents the $X - Z$ position results for the two controls applied to the system representations with wing effects included. The first order system is represented by the dashed line. The 'quarter-cycle' approximation is represented by the solid line. Figure 4.9 presents the simulation results for the pitch angle. The controls end up having similar performance for the presented system. The equilibrium solution is not changed from the system without wing effects. The simulations seem to predict that if the wing effects are not included in control applications, then the desired behavior of the system will not be achieved. The same controls produced limit cycle behavior in the pitch angle for both the first order and quarter-cycle system without wing effects. The same behavior does not manifest when the wing effects are included.

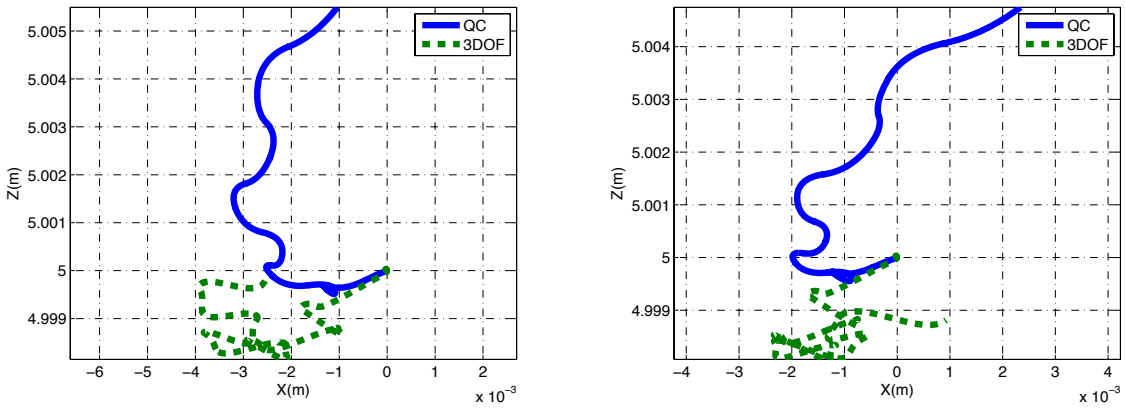

(a) Control M_{c1} (b) Control M_{c2}

Figure 4.8: $X - Z$ Inertial Position for Systems with Wing Effects, $\beta = -15°$, $\theta_o = 15°$, with Controls M_{c1} and M_{c2}

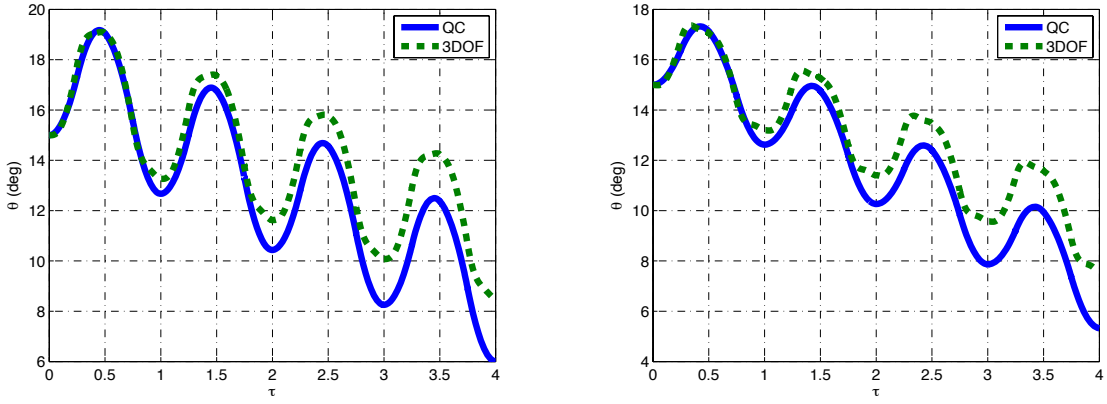

(a) Control M_{c1} (b) Control M_{c2}

Figure 4.9: Pitch Angles for Systems with Wing Effects, $\beta = -15°$, $\theta_o = 15°$, with Controls M_{c1} and M_{c2}

4.6 Conclusions

A stability and control analysis of a flapping wing micro air vehicle shows that the inertial and mass effects of the wings can have an effect on stability. Local averaging produces stability derivatives that are qualitatively consistent with modal structures for VTOL aircraft and independent analyses of insect models. When the same local averaging techniques are applied to the averaged system with wings, the hawkmoth

model exhibits error in the trim solution and the magnitude of the open loop poles. The local averaging analysis is extended to control derivatives. Improper application of control, albeit with a poor location for closed loop poles, can produce an unstable system when a stable system is desired.

The insight gained from the equilibrium condition for the averaged system is applied to the first order system and quarter-cycle system with and without the wing effects. Control application can produce limit cycle behavior for the system without wings. When the same control is applied to the systems with wings, the limit cycle behavior does not manifest. Through stability and open loop control analysis, the mass of the wings affects the behavior of the system. The next chapter will use appropriate application of scaling laws to determine when (if) the mass effects of the wings are no longer important.

CHAPTER 5

The Importance of the Wings

5.1 Introduction

The importance of the wings needs to be addressed. As detailed in Chapter 2, a multi-body model flight dynamics model for a flapping wing micro air vehicle was derived from first principles. The multi-body model predicts significant differences in the position and orientation of a flapping wing MAV model, when compared to the predictions of the standard aircraft flight dynamics model. In Section 2.5.4, the mass of the wings of the flapping wing micro air vehicle model is decreased as a percentage of the total body mass. The predicted behavior of the multi-body model approaches the predicted behavior of the standard aircraft model as the mass of the wings is decreased. However, in nature, the mass of the wings does not monotonically decrease as the total mass of the flier and the flapping frequency remain fixed. Greenwalt, in [130], states

> It follows from the wing area-wing weight relationship that the weight of the wings will comprise a steadily increasing percentage of total body weight as the size of the flying animal increases.

The first order equations of motion derived in Chapter 3 will be used to analyze the relative importance of the mass and inertial effects of the wings on the position

and orientation of the body. Allometric scaling relationships for a range of biological fliers will be used to develop relationships between the flapping frequency and mass of a model body, with the mass of the wings as a percentage of the mass of the body.

5.2 Scaling

The importance of the wings to dynamics and stability studies will expressed with the aid of scaling relationships. Scaling relationships are widely studied in regards to insects and birds. Relationships are best-exemplified by the Great Flight Diagram in [13]. The Great Flight Diagram illustrates the scaling relationship between cruising speed and weight for biological fliers as small as a fruit fly to airplanes as large as the Airbus A380. A common scaling relationship, and a focus of a high amount of study, is the relationship between body mass and flapping frequency. The work is based on the extensive compilation of insect statistics, such as their mass, wing area, and wingbeat frequency. Greenewalt conducted a seminal and often cited study of the scaling relationships of flying animals in [130]. Byrne et al. present the compilation of the body morphologies of 160 insect species in [131]. Other allometric studies of insect species include a relationship between wingbeat frequency, wing area, and body mass by Corben in [132], a study of panamanian bees by Darveau et al. in [133], and scaling relationships developed by Deakin in [134] and [135]. Comprehensive reviews of scaling relationships are available from Weis-Fogh in [136], Templin in [137] and Shyy et al. in [138]. Scaling relationships are also available in [1], [10], and [12].

There are numerous different scaling trends and no one trend is a perfect fit. Usually, the single allometric relationships have a high amount of variance in the data. Single allometric relationships relate one parameter to another, e.g. body mass to flapping frequency. Double allometric relationships correlate two variables to another, e.g. wing area and body mass to flapping frequency as detailed in [135]. The relationships can vary for interspecific and intraspecific studies. In [16], Ellington

states that the average insect does not exist in nature. However, general relationships do exist for a large range of biological fliers. The general trend, as detailed in [130, 138], is that the weight (W) of biological fliers is proportional to the cube of the total wing span (R). The relationship is easily defined according to $W \propto R^3$. The inverse of the relationship defines that $R \propto W^{1/3}$. The total wing area (S) of fliers scales with the mass of the fliers (M) according to $S \propto m^{2/3}$. In [12], the flapping frequency is proportional to different powers of the body mass, depending on the species under study and the assumptions used to determine the relationship. The relationship may be calculated according to dimensional relationships, force balances, or aerodynamic power relationships.

A general relationship does not exist for the mass of the biological fliers. Instead, there is the general trend that as the total mass of the insect flier increases, the mass percentage of the wings also increases. Likewise, the general trend is that as the total mass of the biological flier decreases, the flapping frequency increases. In a personal communication with Professor Michael Dickinson from Caltech, Dickinson states that there is not a significant scaling relationship for insect wing mass to body mass or flapping frequency. He states part of the problem is that insect wings are notoriously hard to weigh. He recommends to conduct a study by capturing insects and weighing the wings. Instead of conducting a study over a wide range of insects, the available relationships and knowledge of insects will be used to develop a design space of various combinations of wing mass percentage and flapping frequency.

There is no significant relationship for the wing thickness as a function of other parameters. In [130], Greenewalt states that wing thickness scales with wing length (b) to the 1.34 power, or $t_{wing} \propto b^{1.34}$. However, in [16], Ellington states that there is not a significant correlation between wing thickness and any other parameters for insects. Instead, Ellington recommends using the non-dimensional wing thickness parameter $\hat{h}$ to evaluate the relative mass of wings for different insect species. The

parameter $\hat{h}$ is expressed as a percentage of the wing span in [16]. The differences in thickness are generally due to the type of wing construction, largely dependent on the Order of the insect species. The wing thickness ranges from 0.015% to 0.106% of the insect wing length, with an average value of 0.0507% [16]. The only correlated study for the wing mass that a wide literature review discovered is the following relationship from [130]. Greenewalt correlates wing mass to to wing area according to $2570\, m_{wing} = S^{5/3}$, where m_{wing} is given in milligrams (mg) and the wing area is given in square millimeters (mm^2). The application of scaling relationships will be to develop a relationship between the body mass and wing mass of insects. A conclusion can be made in regards to at what point, either as percentage of body mass or flapping frequency, the wings are no longer important to the studies of dynamic, stability, and control for flapping wing micro air vehicles.

In the development of this analysis, we used combinations of multiple different scaling relationships to create a 'design space.' The application of a wide range of scaling relationships often produced spurious results. The combination of wing area, flapping frequency, and body mass would produce estimates of flapping amplitude and mid-stroke angle of attack well below values seen in nature. Alternatively, if the flapping amplitude and mid-stroke angle of attack are fixed, the resulting flapping frequency would be extremely low. In addition to the 'design space', the scaling analysis will also present results based on scaling of a specific insect species over a wide range of frequencies. Insect species from the different groups identified by Greenewalt in [130] will be used. Based on scaling relationships, e.g. $m \propto S^{3/2}$, correlation constants will be calculated for individual insects and expanded to create the design space.

Of important note is the relationship between Reynolds number for different frequencies and wing sizes. For hovering flight, the Reynolds number can be defined

according to [10]:

$$Re = \frac{\Phi\, R^2}{\nu}\left(\frac{4}{AR}\right), \tag{5.1}$$

where Φ denotes the total flapping amplitude, ν is the kinematic viscosity, R is the wing length, and AR is the aspect ratio of the wings (ratio of length to width). To fit the description of the dynamics previously presented, $\Phi = 2\zeta_m$. Shyy et al. state in [10] that the Reynolds number can be preserved over a range of sizes, for a geometrically similar wing, using the product fR^2. For the analysis of the mass and inertial effects of the wings to be presented, the aerodynamics affect the analysis indirectly. None of the terms to be analyzed are directly dependent on an aerodynamic model. Directly, an aerodynamic model could change the flapping amplitude, angle of attack, or flapping frequency. The flapping parameters are inputs into the mass and inertial wing effects. Changing the parameters will not change the analysis, as long as the parameters are consistent with insect flight. The simplified aerodynamic model presented in Section 3.3.1 will be used to trim the averaged solution of the first order equations of motion. Since a force balance will be achieved for the averaged system in hover, the flapping input parameters will be relevant and realistic. Finally, the work is motivated to present an analytical model of the equations of motion. As a direct result, an analytical aerodynamic model is necessary.

5.3 Scaling Motivation

As detailed in Chapter 2, the mass of the wings can have a significant effect on the position and orientation of the body for a hawkmoth-sized model. However, a hawkmoth is on the large end of insects in terms of mass. As a result, the flapping frequency is lower and the mass percentage of the wings is higher than a bumblebee, for example. In [62], Sun et al. stated the rigid body assumption may be inaccurate for hawkmoths and craneflies, where the mass percentage of the wings is significantly

Model	m_{sys} (mg)	m_{wg} (%)	m_{wg} (mg)	f (Hz)	b_w (mm)	c_w (mm)
BB	175	0.53	0.46	155	13.2	4.02
CF	11	4.29	0.24	45	12.7	2.31
HM	1648	5.79	47	26.3	51.9	18.6

Table 5.1: Morphological and Simulation Parameters for Insect Model Flight Dynamics Comparisons

higher and the flapping frequency is lower. Zhang and Sun present simulations in [69] to valid the rigid body assumption. Based on the analysis presented in Chapter 3, our contention is that averaging the wing effects over a flapping cycle, and neglecting those effects for averages of zero, may not be the best representation of the model. Figures 5.1 and 5.2 present simulations results for a bumblebee and cranefly model, based off of the parameters in [62] and previously used in Chapter 4. Table 5.1 presents the pertinent simulation parameters. The relevant values for the hawkmoth parameters presented in Section 2.5.2 are included for comparison. The simulation results presented in Figures 5.1 and 5.2 used input angles of the following form

$$\zeta(t) = \zeta_m \sin(\omega t), \quad \alpha(t) = \alpha_m \cos(\omega t), \quad \text{and} \quad \delta(t) = \delta_m \sin(N_\delta \omega t),$$

with $\zeta_m = 60°$, $\alpha_m = 45°$, $\delta_m = 1°$, and $N_\delta = 2$. The results are presented for three flapping cycles each. The aerodynamic model is the model developed by Deng, Schenato, et al. in [39, 89] and has been used previously in Chapters 2-4. The difference in the center of mass for the bumblebee is approximately 1/2 of the body length in Figure 5.1(b). The difference in the center of mass position for the cranefly is on order of one body length. The difference in pitch attitude are negligible for the bumblebee (Fig. 5.2(b)) and very small for the cranefly (Fig. 5.2(a)). The difference for the pitch angle for the cranefly is on order of the difference for the hawkmoth when the 'UCB' aerodynamic model is used.

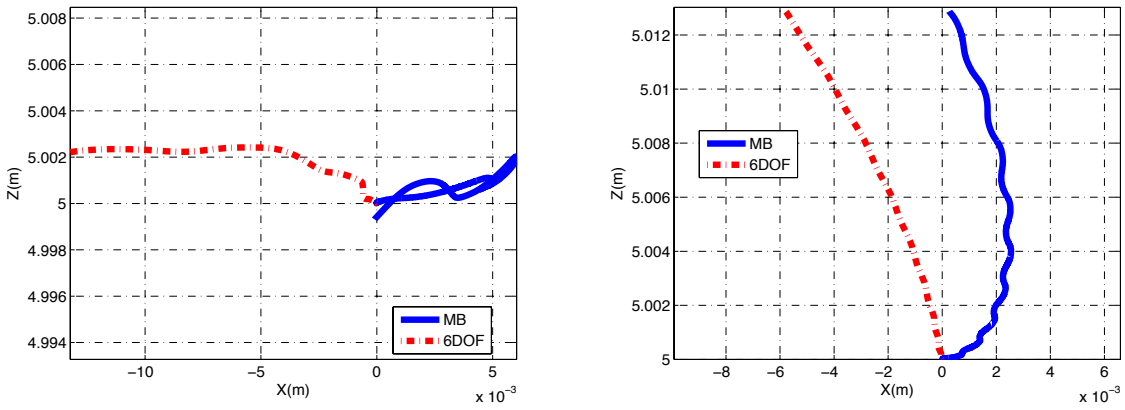

(a) Cranefly Model (b) Bumblebee Model

Figure 5.1: $X - Z$ Position Results for Model Insect Comparison, Multi-body Model and 6DOF Model. $\beta = -10°$, $\theta_o = 10°$

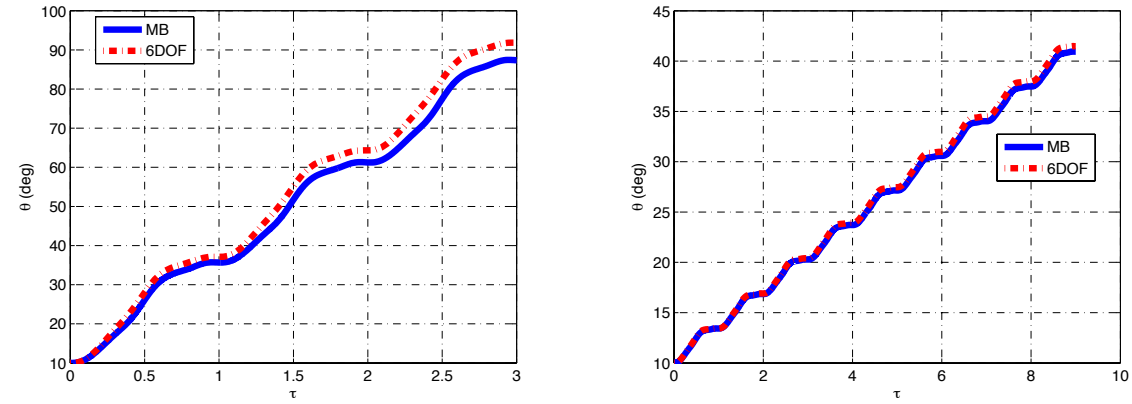

(a) Cranefly Model (b) Bumblebee Model

Figure 5.2: Pitch Angle Results for Model Insect Comparison, Multi-body Model and 6DOF Model. $\beta = -10°$, $\theta_o = 10°$

From an open loop, multi-body dynamics view point, the mass of the wings can have a significant effect on the position and orientation of the body of model insects. For a hawkmoth sized model, the effects are significant as detailed in Chapter 2. The difference in position can be on the order of two body lengths in as little as three flapping cycles. However, for the bumblebee model, the difference after three flapping cycles is negligible. For a cranefly, the difference in position is more significant. The

question needs to be answered: at what combination(s) of mass and flapping frequency can the effects of the wings be neglected for dynamics, stability, and control studies?

5.4 General Trends

The relationships for wing area and wing length can be used to calculate the mass of the wings. By fixing wing thickness as a percentage of the individual wing span, or semi-span, the wing area and wing thickness (as a function of wing span) can be used to calculate the volume of the wing. The mass of the model will be used to determine the total wing area according to the relationship defined in [139]. McMasters defines the relationship for wing area to mass from smallest insect to large aircraft in [139]. The mass of the 'aircraft' is proportional to the wing area according to $m = 15S^{3/2}$, where mass is in kilograms and wing area is in square meters. The inverse of the relationship, to be used in the present analysis, is $S = \frac{1}{15^{2/3}} m^{2/3}$.

The semi-span, or wing length, will be determined from relationships developed in [130]. In [130], the wing length for one wing can be related to the total wing area. The relationship is $b^2 = c_{span} S$, where the wing length is given in millimeters and the wing area is given in square millimeters. The proportionality constant, c_{span}, varies for different groupings of insect species and proper care is taken to ensure consistent dimensions for all units. A larger value of c_{span} will give longer wings with a narrower chord, while a smaller value of c_{span} will give short, wide wings. Greenewalt contributed the smallest value of c_{span} to butterflies and associated species. Greenewalt's work in [130] has five values of c_{span}, with $c_{span} \in \{3.39\ 2.72\ 1.88\ 1.16\ 0.66\}$. The first constant relates to *Drosophila*, the genus for small flies [140]. The second constant, $c_{span} = 2.72$, relates to the genus *Tipula*, which is a family of large values and includes the cranefly [141]. The third constant, $c_{span} = 1.88$, is for the Order *Diptera*, which consists of over 240,000 insects species, to include mosquitoes and gnats [142]. Other Orders included in the correlation for third constant are *Coleoptera* (beetles) and *Hy-*

menoptera (bees, wasps, ants) [143, 144]. The third constant encompasses the largest range of data, correlating wing area to wing length over three orders of magnitude of wing area. The family *Sphingidae* (hawkmoths) and the order *Odonata* (dragonflies, damselflies) are included in the correlation for the fourth constant, $c_{span} = 1.16$ [145, 146]. The final constant, $c_{span} = 0.66$, is a relationship for butterflies and moths [147, 148, 149]. The relationship between wing length and wing area will be used to develop different estimates of the mass percentage of the wings. The mass of the wings is calculated as a product of the wing area, wing thickness, and the density of the wings. The density of the wings is assumed to be strong cuticle and set at the value of $\rho_{wing} = 1200\, kg/m^3$. The density is referenced in [16] and [150]. The density is also used in a scaling of the flexural stiffness of wings in [151].

The analysis of the effects of the wings on the position and orientation of the body will focus on four main effects. The linear momentum effects of the wings, defined by $\ddot{\bar{\rho}}_{ci}$, will be used in conjunction with the wing acceleration (control moment) contributions, to determine the mass effect of the wings on the position of the body. The effects of the mass of the wings on the pitch orientation of the body will be assessed through the angular momentum terms, $\mathbf{I}_i\dot{\bar{\omega}}_i + \bar{\omega}_i \times \mathbf{I}_i\bar{\omega}_i$, and the wing acceleration (control moment) contribution. The quarter-cycle approximations of the wing effects are defined in Appendix C. Since the majority of the wing effects time average to zero, the value for the first quarter-cycle, from 0 to $\frac{\pi}{2}$, will be used. The calculated values will be nondimensionalized so that comparisons and general trends can be identified from changes in flapping frequency and mass percentage. The forces and moments due to the mass effects of the wings are nondimensionalized in the same manner as in Chapter 4.

In order to create a wide design space and to analyze general trends, the relationships in [130] are used to developed five design 'types': from long, thinner wings to short, wide wings. The flapping frequency is varied from 10 Hz to 300 Hz in intervals

of 10 Hz. The mass of the system is calculated from the proportional relationship $m_{sys} \propto f^{-2}$, with a proportionality constant of unity. In addition to the five wing types, the initial thickness of the wing at 10 Hz is varied between 0.04% and 0.11% of the length of one wing. The total thickness of the wing decreases according to $t_{wing} \propto b_w^{1.34}$. The area of the wings is calculated according to the general scaling law from [139]: $m_{sys} = 15\, S^{3/2}$, where m_{sys} is in kg and the wing area is in m^2. The initial set of relationships is for a flapping amplitude of 60° and an angle of attack calculated using a bisection algorithm for hover of the averaged system. The simple wingstroke presented in Chapters 3 and 4 is maintained here, since it was used to develop the quarter-cycle approximations.

The general trends are the same for all five wing choices. Depending on the wing type choice, the mass percentage of the wings varies from nearly 16.2% to 1.2% over the frequency range from 10 to 300 Hz. The contribution to the longitudinal position of the flapping wing micro air vehicle from the linear momentum of the wings is presented in Figure 5.3. The general trend shows a maximum nondimensional contribution at the lowest flapping frequency and the highest wing mass percentage. The linear momentum contribution in the x-direction is shown for $c_{span} = 3.39$. The 'thickest' wings start at 0.11% of the wing semi-span. For $c_{span} = 3.39$, the mass percentage of the wings ranges from 16.2% down to 2.72%.

The contribution from the control moment in the x-direction is presented in Figure 5.4 for $c_{span} = 2.72$. The mass percentage ranges from 14.5% to 2.44%. The contribution for the angular momentum terms to the pitch orientation is presented in Figure 5.5 for $c_{span} = 1.88$. The mass percentage ranges from 12.1% to 2.03%. The final contribution presented is for the control moment to pitch in Figure 5.6 for $c_{span} = 1.16$. The mass percentage ranges from 9.48% to 1.59%. The general trends for all of the contributions are the same. The maximum contribution is for the lowest frequency and highest mass percentage. The nondimensional forces and moments de-

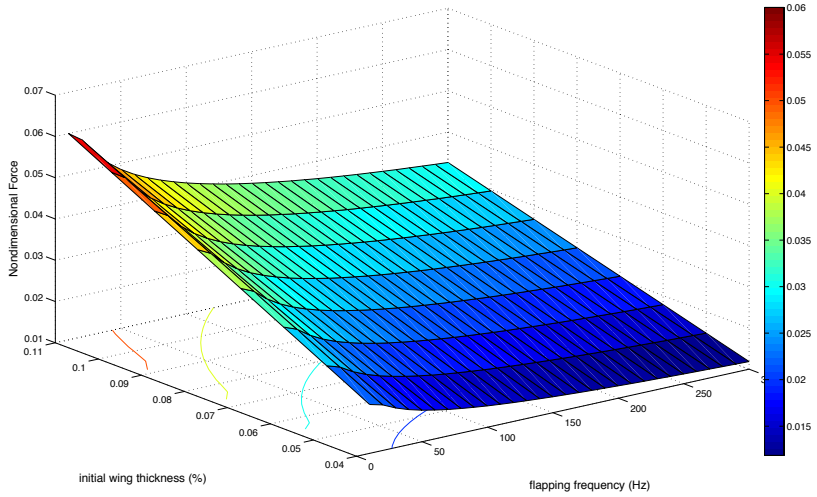

Figure 5.3: Nondimensional Force for $\bar{\rho}_{ci} \cdot \hat{b}_x$ for $c_{span} = 3.39$

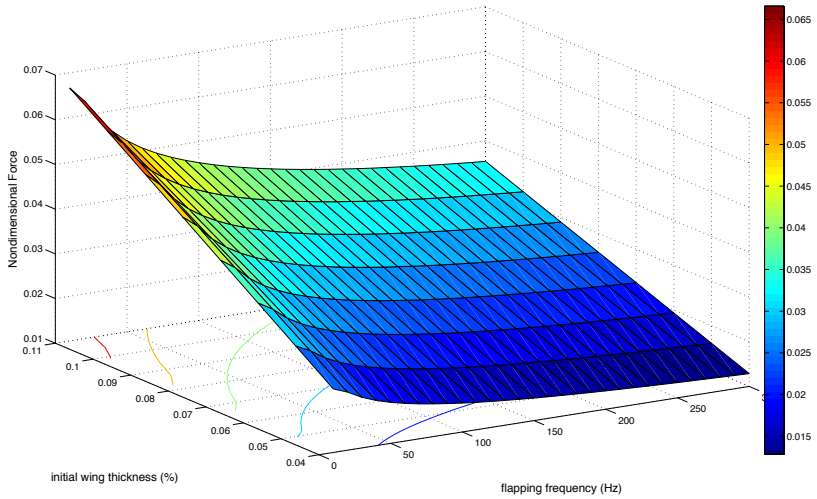

Figure 5.4: Nondimensional Force for Control Moment Contribution to $\hat{b}_x$ for $c_{span} = 2.72$

crease as the frequency increases and/or the mass percentage decreases. For a fixed frequency, the mass of the flapping wing micro air vehicle model is the same. The analysis shows that for a given frequency, the mass effects of the wings decrease as the relative mass percentage is decreased. It is also important to note that although the contributions decrease with lower mass percentage and higher frequency, so does the nondimensional force due to lift or gravity.

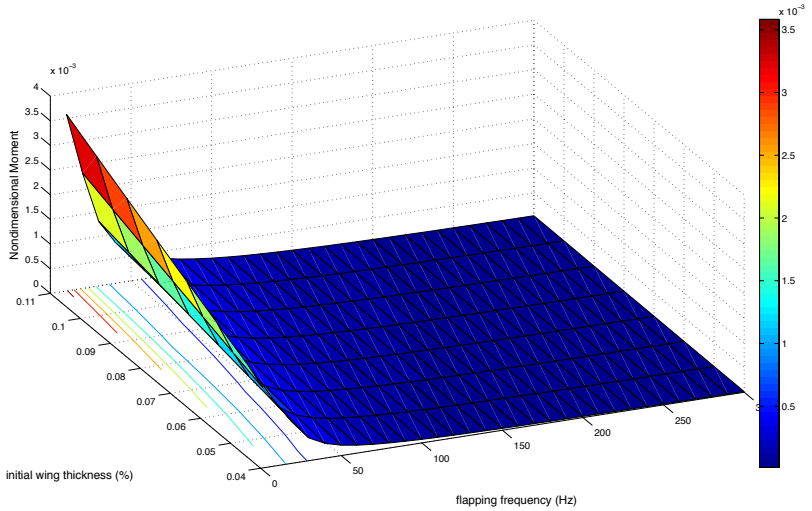

Figure 5.5: Nondimensional Moment for $\bar{\omega} \times \mathbf{I}\bar{\omega}$ for $c_{span} = 1.88$

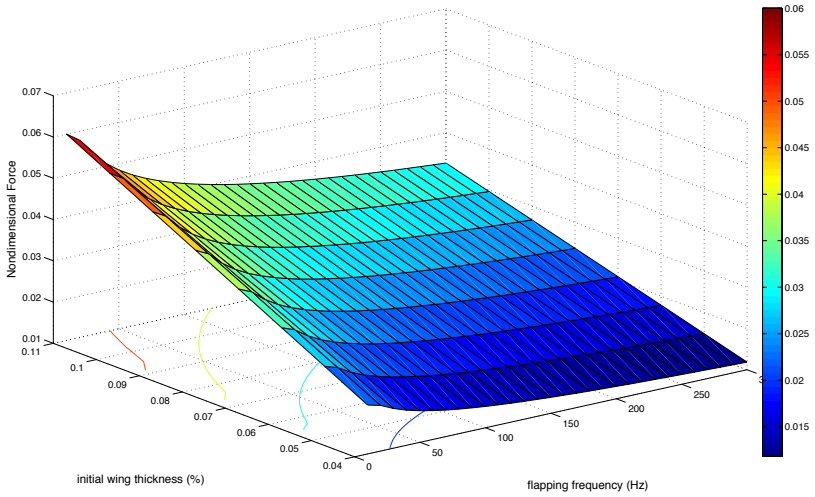

Figure 5.6: Nondimensional Moment for Control Moment Contribution to Pitch for $c_{span} = 1.16$

5.5 Scaling Analysis for Individual Insect Models

The previous scaling analysis showed that the wing effects decrease with increasing flapping frequency and/or decreasing wing mass percentage. The final scaling analysis will be conducted based on the models of the hawkmoth, bumblebee, and cranefly. For all models, the body will be assumed to be a rigid cylinder with constant radius

Model	Mass Correlation	Mass Coefficient	Wing Area Coefficient	$\hat{h}$ (%)	t_{wing} Coefficient
HM1	f^{-2}	1.1399	0.1384	0.076	0.002078
HM2	f^{-3}	29.9795	0.1384	0.076	0.002078
BB	f^{-2}	4.2044	0.0339	0.06	0.002613
CF	f^{-3}	1.0362	0.1222	0.0554	0.2401

Table 5.2: Correlation Coefficients for Scaling Analysis of Individual Insect Models

for mass moment of inertia calculations. The wings are assumed to be thin, rigid flat plates. Over a range of flapping frequencies, a single allometric relationship will be used to determine the mass of the flapping wing micro air vehicle. The chosen relationship will depend on the model insect being used. From [12], the mass of bees is proportional to f^{-2}, where m is the mass of the model in kilograms and f is the flapping frequency in Hertz. The mass of craneflies is closer to f^{-3}, while the hawkmoth is in between the two boundaries of f^{-2} and f^{-3}. For all of the model insects, the total wing area S is assumed to be proportional to the two-thirds power of the mass of the body in kilograms ($S \propto m^{2/3}$). The coefficient for the correlation will be determined for a specific insect model for the wing area to mass relationship and the mass to frequency relationship. The coefficients for the correlations of the model insects are presented in Table 5.2. The correlation coefficients are determined using the morphological parameters presented in Table 5.1. The wing thickness will be correlated according to $t_{wing} \propto c_t b^{1.34}$. The wing thickness of the model will based off of the $\hat{h}$ parameter from Ellington in [16]. The $\hat{h}$ parameters expresses the wing thickness as a percentage of the wing semi-span (wing length). The correlation constants for the wing thickness are presented in Table 5.2. The linear momentum effects for each of the insect models are presented in Figures 5.7-5.10. In Figures 5.7-5.10, the circle represents the linear momentum effects in the x-direction. The 'x' represents the linear momentum effects in the z-direction. The square represents the control moment contribution to the x-direction and the diamond to the z-direction. Finally, the plus symbol presents the body weight force.

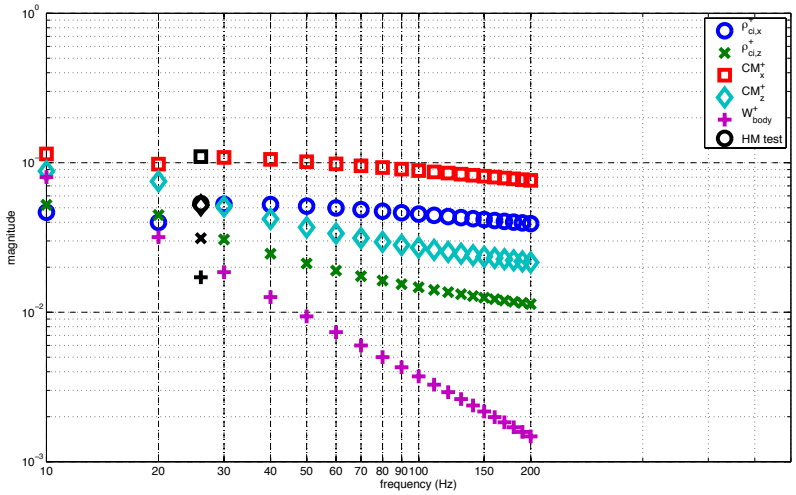

Figure 5.7: Linear Momentum Effects for Scaled Hawkmoth Model, $m_{sys} \propto f^{-2}$

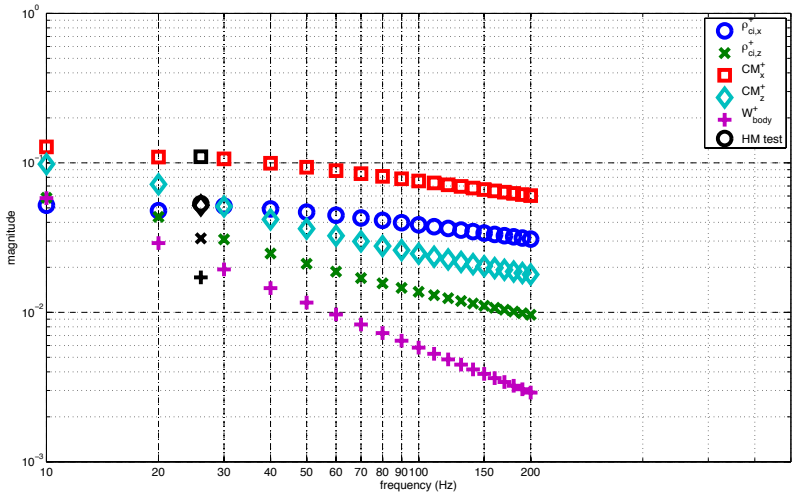

Figure 5.8: Linear Momentum Effects for Scaled Hawkmoth Model, $m_{sys} \propto f^{-3}$

The contribution from the linear momentum effects is generally of the same order of magnitude, or larger, than the nondimensional weight for the four scaled insect models. For the bumblebee model, the weight is initially greater than the linear momentum contributions at low frequencies. As the flapping frequency increases, the linear momentum contributions increase in magnitude relative to the weight. However, all of the linear momentum contributions time average to zero. The linear

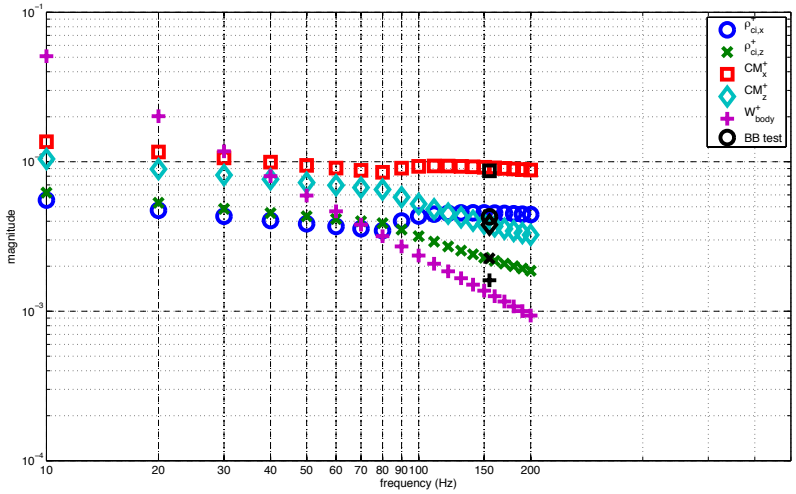

Figure 5.9: Linear Momentum Effects for Scaled Bumblebee Model, $m_{sys} \propto f^{-2}$

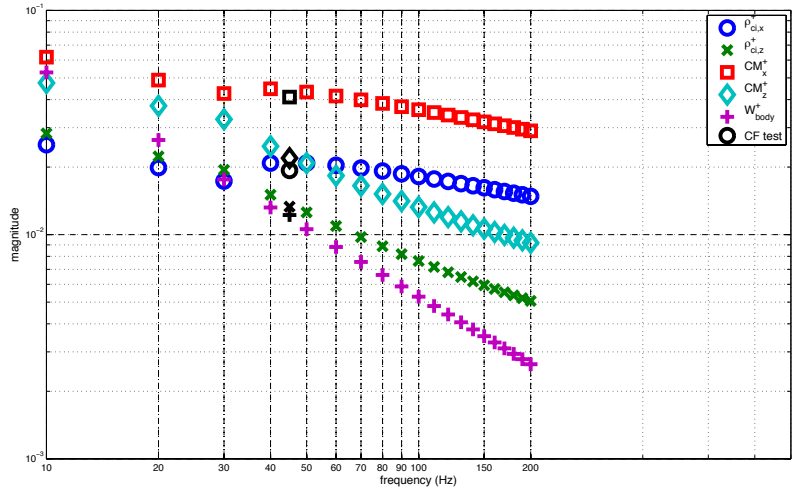

Figure 5.10: Linear Momentum Effects for Scaled Cranefly Model, $m_{sys} \propto f^{-3}$

momentum effects are not constant. Periodic forces do not affect the system in the same manner as lift and weight, which are constant forces in the averaged sense. In Figure 5.9, the bumblebee model values are plotted at 155 Hz. The wing effects on position are within an order of magnitude of the weight force. The wing effects do not have a significant effect on the position of the nominal bumblebee model, as presented in Figure 5.1(b). The linear momentum effects on the position of the bumblebee are

not negligible, either. The scaling relationships do not present a clear answer for a determination of when contributions of the linear momentum effects are no longer significant.

The hawkmoth models predict a mass percentage ranging from 6.1% to 3.1% for the scaling relationship $m \propto f^{-2}$. The mass percentage decreases, as flapping frequency increases, from 6.8% to 2.5% for the scaling relationship $m \propto f^{-3}$. Even at a frequency of 200 Hz, the mass percentage is significantly higher than seen in nature. For the bumblebee model, the mass percentage decreases from 1.2% to 0.6% as the flapping frequency increases. The mass percentage range for the cranefly model is 7.7% to 2.8%. The four insect models represent a wide range of combinations for flapping frequency and wing mass percentage. The initial conclusion is that the linear momentum effects should be included in all dynamics, stability and control studies.

The angular momentum effects are presented in Figures 5.11-5.14. The circle represents the nondimensional aerodynamic pitching moment. The 'x' represents the contributions from the control moment. The square represents the angular momentum contribution to pitch. For the system without wing effects, under a longitudinal flight condition, the only contribution to a change in pitch velocity is the aerodynamic pitching moment. Therefore, the aerodynamic pitching moment is compared to the angular momentum effects and the control moment effects.

The angular momentum effects present a different picture from the linear momentum effects. The angular momentum effects of the wings are always less than the aerodynamic pitching moment. For the given dynamics representation and aerodynamic model choice, the aerodynamic pitching moment has a time average of zero, just like all of the wing effects on the pitch orientation. It can be concluded that the aerodynamic pitching moment has the most significant effect on the orientation of the body. The other effects are less important, especially after a frequency of approximately 30-40 Hz, depending on the insect model. After 30-40 Hz, the angular

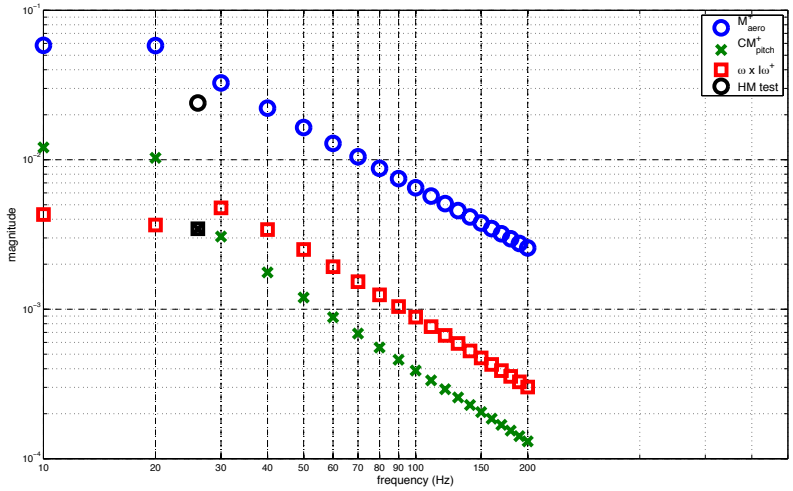

Figure 5.11: Angular Momentum Effects for Scaled Hawkmoth Model, $m_{sys} \propto f^{-2}$

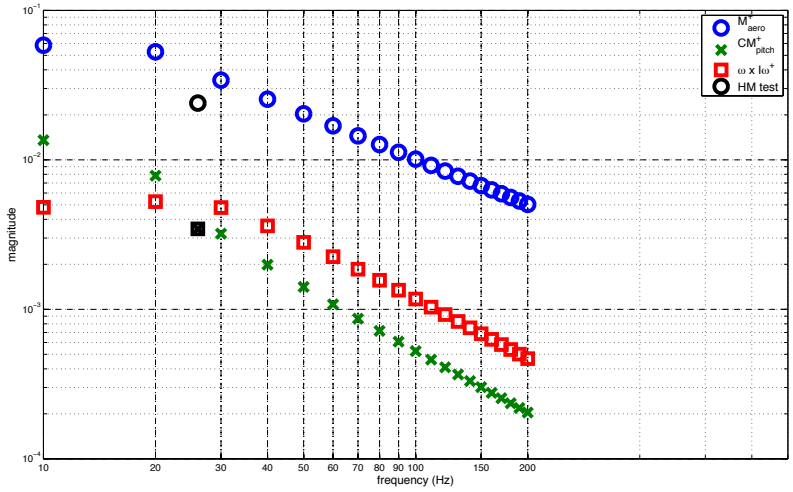

Figure 5.12: Angular Momentum Effects for Scaled Hawkmoth Model, $m_{sys} \propto f^{-3}$

momentum contribution for the hawkmoth and cranefly models decreases at a faster rate than the aerodynamic pitching moment. The rate changes at a higher flapping frequency for the bumblebee model.

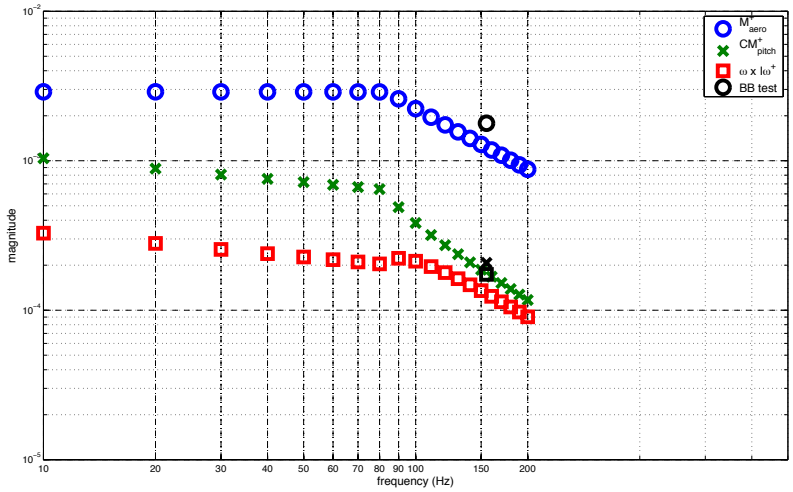

Figure 5.13: Angular Momentum Effects for Scaled Bumblebee Model, $m_{sys} \propto f^{-2}$

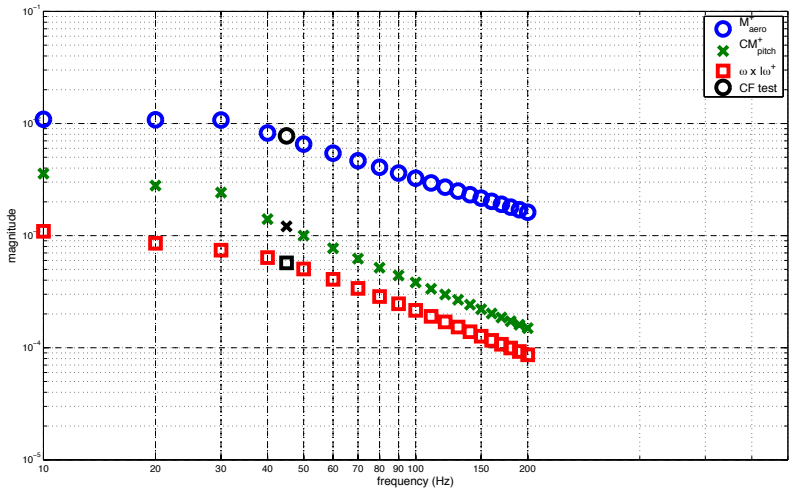

Figure 5.14: Angular Momentum Effects for Scaled Cranefly Model, $m_{sys} \propto f^{-3}$

5.6 Conclusions

The scaling relationships show that, in general, the nondimensional linear and angular momentum effects of the wings decrease in importance as the flapping frequency increases. The effects also decrease as the wing mass percentage is decreased. The most significant effects occur at high mass percentages and low flapping frequencies. The scaling conclusions are consistent for a wide ranging design space, based on dif-

ferent insect wing models and thickness relationships, as well as relationships based on individual insect models.

The linear momentum effects behave differently than the angular momentum effects, when scaling effects are considered. The linear momentum effects are generally one order of magnitude or more higher than the weight effects of the insect model. An example of the recommendation that the linear momentum effects should always be included is presented in Figure 5.15. After three flapping cycles, with a flapping

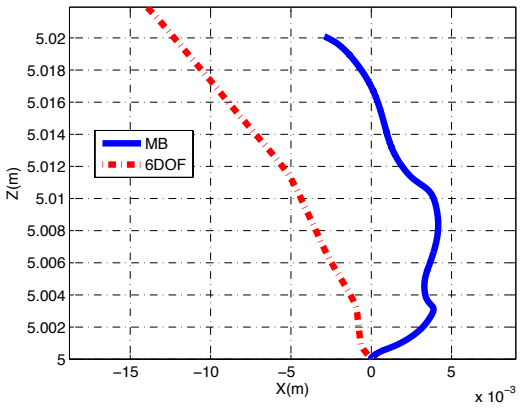

Figure 5.15: $X - Z$ Position, Scaling Example, $m_{sys} \propto f^{-2}$

frequency of 150 Hz and a wing mass percentage of 3.3%, the prediction for the center of mass of the body is off by two body lengths. In as little as 0.02 s, there is a significant difference in position. The same parameters produce virtually zero difference in the pitch orientation.

The most significant contribution to the pitch of the body is the aerodynamic pitching moment. The aerodynamic pitching moment is generally an order of magnitude to the wing effects. The angular momentum wing effects decrease significantly faster than the aerodynamic pitching moment at approximately 30-40 Hz. The scaling leads to the conclusion that the linear momentum effects of the wings should always be included in dynamics, stability, and control studies.

CHAPTER 6

Conclusion and Future Research

6.1 Summary and Contributions

The final chapter presents a summary of the work and possible future endeavors to explore the methods and techniques even further. The main contribution of the dissertation is a framework for evaluating the importance of the mass and inertial effects of the wings on the position and orientation of a flapping wing micro air vehicle. The procedure begins with a multi-body flight dynamics model. The model is transformed to first order form and approximated using the quarter-cycle averaging technique. Scaling analysis can then be used to evaluate the relative importance of the linear and angular momentum effects on the position and orientation of the body.

6.1.1 Multi-Body Flight Dynamics Model

A multi-body flight dynamics model was derived from first principles. The flight dynamics model is obtained by assuming three degrees of freedom for each wing, a stroke plane inclined relative to the body, and the inclusion of an aerodynamic model. The results from the flight dynamics model are dependent on the choice of aerodynamic model. The multi-body flight dynamics model predicts significant differences in position and orientation when compared to the standard aircraft equations of motion. The significance of the difference in position and orientation may be dependent

on the choice of aerodynamic model.

6.1.2 Quarter-Cycle Averaging

Quarter-cycle averaging was developed to approximate the first order equations of motion for a flapping wing micro air vehicle. The first order equations of motion are derived from the multi-body model using an approximate inverse and appropriate assumptions. The first order equations of motion are the standard aircraft equations of motion plus perturbations to those equations of motion due to the mass effects of the wings. The standard aircraft equations of motion do not have a general analytical solution, therefore standard averaging techniques are not available. Quarter-cycle averaging re-writes the nonlinear, time-varying equations of motion as piecewise continuous functions. The approximation error is reduced by over an order of magnitude when compared to the poor results obtained from local averaging.

6.1.3 Hover Analysis

The stability of a flapping wing micro air vehicle was analyzed in the vicinity of a hover condition. An analytical approximation of the stability derivatives for the flapping wing micro air vehicle was derived through the use of local averaging techniques. The analytical approximation predicts a modal structure for the eigenvalues that is consistent with independent, numerical analyses. The inclusion of wing effects changes the magnitude of the poles, but does not change the modal structure. The wing effects not only change the required controls for a linear analysis in the vicinity of a hover condition, but for a nonlinear analysis of the conditions for a limit cycle as well.

6.1.4 Scaling

A scaling analysis was conducted to analyze the relative importance of the wings on the position and orientation of the central body. A general design space was created using a combination of scaling techniques. The general trend is that the linear and angular momentum effects of the wings decrease with increased flapping frequency and/or decreased wing mass. For a fixed flapping frequency, the wing effects decrease as the wing mass percentage, relative to the body, is monotonically decreased. For the given dynamics model and aerodynamics model, the wing effects are generally important. There are cases where the mass effects of the wings do not have a significant effect on the position of the body. However, even for a given model at a high flapping frequency, the wings can have a significant effect on the position of the body. The angular momentum effects do not have a significant effect on the orientation of the body beyond a range of about 30-40 Hz.

6.2 Future Research Directions

The results and methods presented are obtained through the use of various assumptions. Removing some of these assumptions can provide multiple new research directions. True insect wings are not perfectly rigid. Research has shown that the flexibility of insect wings is important for lift and thrust generation. Aeroelastic effects could be important in the dynamics of the flapping wing micro air vehicle and incorporated into the model. The simulations of the flight dynamics model used a quasi-steady/blade-element model. The model could be simulated with higher fidelity aerodynamic data, either from a computational fluid dynamics solver or surrogate model, to see if the mass and inertial effects are important with a wider range of aerodynamic models.

The quarter-cycle averaging technique is conducted with a simplified wing stroke

and only two degrees of freedom. The research can be expanded to account for the deviation angle and the effects on the position and orientation of the vehicle. A more biomimetic wing stroke could be used, as well as a higher fidelity aerodynamic model. However, the inclusion of either will probably move the analysis from an analytical one to a numerical one. The quarter-cycle averaged equations to analyze stability and limit cycles in the vicinity of a hover condition could also be used to analyze other reference flight conditions as well. The stability of forward flight and vertical flight can be examined to see if the same methods produce results qualitatively consistent with other studies. Robust and/or adaptive control studies could be conducted to determine the sensitivity to modeling error of a flapping wing micro air vehicle due to the mass of the wings.

The scaling analysis could be expanded to fit additional aerodynamic models. The results may be aerodynamic model dependent. The comparison of the effects on the pitch orientation of the central body are based on the aerodynamic pitching moment, which will change dependent on the aerodynamic model chosen as an input into the system. The overall conclusion of the importance of the wings for position can be studied with nonlinear robust and/or adaptive control to determine sensitivity to modeling uncertainty. Finally, the control algorithms should be tested on a real prototype to see if the conclusions hold in the physical world.

APPENDICES

APPENDIX A

Multi-Body Derivation

The appendix presents developments used in the multi-body flight dynamics model derivation. The following are not necessary for the full derivation, but are provided for completeness in the presentation of the dynamics model. The appendix is intended to include certain important aspects of the derivation for completeness, so that the work presented previously maybe easily replicated. A summary of the numerous assumptions used in the development of the multi-body, flight dynamics model is:

- The flapping wing micro air vehicle is operating in a flat Earth environment with constant gravity.
- The Earth is not moving.
- The body and wings are rigid bodies.
- The rigid bodies have constant mass.
- The wing joints enable each wing to have three degrees of freedom relative to the stroke plane.
- The wings are modeled as thin, rectangular flat plates with constant chord.

- The aerodynamic center of pressure of the wings is calculated based on the geometry of the wings.
- The effects of wind gusts are not considered.
- Aerodynamic interactions between the wings and the body are neglected.

The rotation matrices for the left wing are defined according to

$$\mathbf{R}_{\delta_L} = \begin{bmatrix} 1 & 0 & 0 \\ 0 & \cos\delta_L & -\sin\delta_L \\ 0 & \sin\delta_L & \cos\delta_L \end{bmatrix}, \mathbf{R}_{\alpha_L} = \begin{bmatrix} \cos\alpha_L & 0 & -\sin\alpha_L \\ 0 & 1 & 0 \\ \sin\alpha_L & 0 & \cos\alpha_L \end{bmatrix},$$

and

$$\mathbf{R}_{\zeta_L} = \begin{bmatrix} \cos\zeta_L & \sin\zeta_L & 0 \\ -\sin\zeta_L & \cos\zeta_L & 0 \\ 0 & 0 & 1 \end{bmatrix}. \tag{A.1}$$

The rotation matrices for the right wing are presented in Equation (2.4). The combination of the full rotation matrix carrying the right stroke plane frame to the right wing frame, $\mathbf{R}_R$, is

$$\begin{bmatrix} \mathrm{c}\alpha_R\mathrm{c}\zeta_R + \mathrm{s}\alpha_R\mathrm{s}\delta_R\mathrm{s}\zeta_R & -\mathrm{c}\alpha_R\mathrm{s}\zeta_R + \mathrm{s}\alpha_R\mathrm{s}\delta_R\mathrm{c}\zeta_R & -\mathrm{s}\alpha_R\mathrm{c}\delta_R \\ \mathrm{c}\delta_R\mathrm{s}\zeta_R & \mathrm{c}\delta_R\mathrm{c}\zeta_R & \mathrm{s}\delta_R \\ \mathrm{s}\alpha_R\mathrm{c}\zeta_R - \mathrm{c}\alpha_R\mathrm{s}\delta_R\mathrm{s}\zeta_R & -\mathrm{s}\alpha_R\mathrm{s}\zeta_R - \mathrm{c}\alpha_R\mathrm{s}\delta_R\mathrm{c}\zeta_R & \mathrm{c}\alpha_R\mathrm{c}\delta_R \end{bmatrix}, \tag{A.2}$$

where 'c' is shorthand for cosine and 's' is shorthand for sine. The rotation matrix carrying the left stroke plane to the left wing frame, $\mathbf{R}_L$, is

$$\begin{bmatrix} \mathrm{c}\alpha_L\mathrm{c}\zeta_L + \mathrm{s}\alpha_L\mathrm{s}\delta_L\mathrm{s}\zeta_L & \mathrm{c}\alpha_L\mathrm{s}\zeta_L - \mathrm{s}\alpha_L\mathrm{s}\delta_L\mathrm{c}\zeta_L & -\mathrm{s}\alpha_L\mathrm{c}\delta_L \\ -\mathrm{c}\delta_L\mathrm{s}\zeta_L & \mathrm{c}\delta_R\mathrm{c}\zeta_L & -\mathrm{s}\delta_L \\ \mathrm{s}\alpha_L\mathrm{c}\zeta_L - \mathrm{c}\alpha_L\mathrm{s}\delta_L\mathrm{s}\zeta_L & \mathrm{s}\alpha_L\mathrm{s}\zeta_L + \mathrm{c}\alpha_L\mathrm{s}\delta_L\mathrm{c}\zeta_L & \mathrm{c}\alpha_L\mathrm{c}\delta_L \end{bmatrix}. \tag{A.3}$$

The diagonal terms for $\mathbf{R}_R$ and $\mathbf{R}_L$ are identical if the wing angles are identical. The terms in the first row, third column and third row, first column of the rotation matrices for the wings are also identical if the wing angles are equal. The remaining four terms in the rotation matrices are equal in magnitude, but opposite in sign, if the wing angles are identical. Inspection of the transpose of the rotation matrix carrying the stroke plane frame to the wing frame shows the physical intuition of the choice of 3-1-2 Euler Angles. A mass at the end of a rod can be tracked according to spherical coordinates. A point along the y-axis of the right wing frame would be tracked by the second column of ${\mathbf{R}_R}^{\mathrm{T}}$:

$$ {\mathbf{R}_R}^{\mathrm{T}} = \begin{bmatrix} \mathrm{c}\alpha_R\mathrm{c}\zeta_R + \mathrm{s}\alpha_R\mathrm{s}\delta_R\mathrm{s}\zeta_R & \mathrm{c}\delta_R\mathrm{s}\zeta_R & \mathrm{s}\alpha_R\mathrm{c}\zeta_R - \mathrm{c}\alpha_R\mathrm{s}\delta_R\mathrm{s}\zeta_R \\ -\mathrm{c}\alpha_R\mathrm{s}\zeta_R + \mathrm{s}\alpha_R\mathrm{s}\delta_R\mathrm{c}\zeta_R & \mathrm{c}\delta_R\mathrm{c}\zeta_R & -(\mathrm{s}\alpha_R\mathrm{s}\zeta_R + \mathrm{c}\alpha_R\mathrm{s}\delta_R\mathrm{c}\zeta_R) \\ -\mathrm{s}\alpha_R\mathrm{c}\delta_R & \mathrm{s}\delta_R & \mathrm{c}\alpha_R\mathrm{c}\delta_R \end{bmatrix}, \tag{A.4} $$

which is a spherical coordinate representation using the angles δ_R and ζ_R with origin at the wing root. A similar procedure can be used for the left wing, but the signs are flipped since the wing is on the opposite side of the vehicle:

$$ {\mathbf{R}_L}^{\mathrm{T}} = \begin{bmatrix} \mathrm{c}\alpha_L\mathrm{c}\zeta_L + \mathrm{s}\alpha_L\mathrm{s}\delta_L\mathrm{s}\zeta_L & -\mathrm{c}\delta_L\mathrm{s}\zeta_L & \mathrm{s}\alpha_L\mathrm{c}\zeta_L - \mathrm{c}\alpha_L\mathrm{s}\delta_L\mathrm{s}\zeta_L \\ \mathrm{c}\alpha_L\mathrm{s}\zeta_L - \mathrm{s}\alpha_L\mathrm{s}\delta_L\mathrm{c}\zeta_L & \mathrm{c}\delta_L\mathrm{c}\zeta_L & \mathrm{s}\alpha_L\mathrm{s}\zeta_L + \mathrm{c}\alpha_L\mathrm{s}\delta_L\mathrm{c}\zeta_L \\ -\mathrm{s}\alpha_L\mathrm{c}\delta_L & -\mathrm{s}\delta_L & \mathrm{c}\alpha_L\mathrm{c}\delta_L \end{bmatrix}. \tag{A.5} $$

For the left wing, the angular velocity with respect to the stroke plane is calculated according to

$$ \bar{\omega}_{3,sp} = \mathbf{R}_L \begin{bmatrix} 0 \\ 0 \\ \dot{\zeta}_L \end{bmatrix} + \mathbf{R}_{\alpha_L}\mathbf{R}_{\delta_L} \begin{bmatrix} -\dot{\delta}_L \\ 0 \\ 0 \end{bmatrix} + \mathbf{R}_{\alpha_L} \begin{bmatrix} 0 \\ \dot{\alpha}_L \\ 0 \end{bmatrix}. \tag{A.6} $$

By components, the angular velocity of the left wing is

$$\bar{\omega}_{3,sp} = \begin{bmatrix} p_{LW} \\ q_{LW} \\ r_{LW} \end{bmatrix} = \begin{bmatrix} -(\cos\alpha_L)\dot{\delta}_L - (\sin\alpha_L \cos\delta_L)\dot{\zeta}_L \\ \dot{\alpha}_L - (\sin\delta_L)\dot{\zeta}_L \\ -(\sin\alpha_L)\dot{\delta}_L + (\cos\alpha_L \cos\delta_L)\dot{\zeta}_L \end{bmatrix}. \tag{A.7}$$

As stated in Chapter 2, the reference point for the wings is chosen to be the respective wing joints. In order to track the velocity of the wing joint with respect to the inertial frame, vectors, $\bar{r}_R$ and $\bar{r}_L$, are defined from the center of mass of the central body to the wing joint. The wing joints vectors are expressed in the B frame according to

$$\bar{r}_R = R_x\hat{b}_x + R_y\hat{b}_y + R_z\hat{b}_z \quad \text{and} \quad \bar{r}_L = L_x\hat{b}_x + L_y\hat{b}_y + L_z\hat{b}_z. \tag{A.8}$$

The velocities at the wing joints are

$$\bar{\mathbf{v}}_2 = \bar{\mathbf{v}}_1 + \bar{\omega}_1 \times \bar{r}_R \quad \text{and} \quad \bar{\mathbf{v}}_3 = \bar{\mathbf{v}}_1 + \bar{\omega}_1 \times \bar{r}_L. \tag{A.9}$$

In component form, the velocity for the right wing joint is

$$\bar{\mathbf{v}}_2 = \begin{bmatrix} u + qR_z - rR_y \\ v + rR_x - pR_z \\ w + pR_y - qR_x \end{bmatrix}. \tag{A.10}$$

The velocity for the left wing joint is

$$\bar{\mathbf{v}}_3 = \begin{bmatrix} u + qL_z - rL_y \\ v + rL_x - pL_z \\ w + pL_y - qL_x \end{bmatrix}. \tag{A.11}$$

The acceleration of the right wing joint is obtained utilizing the transport theorem.

$$(\dot{\bar{\mathbf{v}}}_2)^I = (\dot{\bar{\mathbf{v}}}_2)^B + \bar{\omega}_1 \times \bar{\mathbf{v}}_2$$

$$(\dot{\bar{\mathbf{v}}}_2)^I = (\dot{\bar{\mathbf{v}}}_1)^B + \dot{\bar{\omega}}_1 \times \bar{r}_R + \bar{\omega}_1 \times \dot{\bar{r}}_R + \bar{\omega}_1 \times (\bar{\mathbf{v}}_1 + \bar{\omega}_1 \times \bar{r}_R)$$

The acceleration of the left wing joint is obtained in the same manner. In the B frame, $\dot{\bar{r}}_R \equiv 0$, and the acceleration of the right wing joint is

$$\dot{\bar{\mathbf{v}}}_2 = \begin{bmatrix} \dot{u} + \dot{q}R_z - \dot{r}R_y + qw - rv + qpR_y + rpR_z - (r^2 + q^2)R_x \\ \dot{v} + \dot{r}R_x - \dot{p}R_z + ru - pw + pqR_x + rqR_z - (p^2 + r^2)R_y \\ \dot{w} + \dot{p}R_y - \dot{q}R_x + pv - qu + prR_x + qrR_y - (p^2 + q^2)R_z \end{bmatrix}. \tag{A.12}$$

The acceleration for the left wing has the same form, except with proper substitutions of the components of $\bar{r}_L$ for the components of $\bar{r}_R$. The derivation of the acceleration of the wing reference vectors, $\ddot{\bar{\rho}}_{ci}$, results in four terms:

$$\begin{aligned} \ddot{\bar{\rho}}_{ci} &= \mathbf{R}_{\beta_k}{}^{\mathrm{T}} \mathbf{R}_k{}^{\mathrm{T}} \tilde{\omega}_{i,sp} \tilde{\omega}_{i,sp} \bar{\rho}_{ci,w} + 2\,\bar{\omega}_i \times \mathbf{R}_{\beta_k}{}^{\mathrm{T}} \tilde{\omega}_{i,sp} \bar{\rho}_{ci,w} \\ &\quad + 2\,\bar{\omega}_i \times (\bar{\omega}_i \times \bar{\rho}_{ci}) + \dot{\bar{\omega}}_i \times \bar{\rho}_{ci} + \mathbf{R}_{\beta_k}{}^{\mathrm{T}} \mathbf{R}_k{}^{\mathrm{T}} \dot{\tilde{\omega}}_{i,sp} \bar{\rho}_{ci,w} \end{aligned} \tag{A.13}$$

The acceleration terms of the right wing reference vector are obtained by setting $i = 2$ and $k = R$. The acceleration terms for the left wing reference vector are obtained by setting $i = 3$ and $k = L$.

APPENDIX B

First Order Equations of Motion

First Order Equations of Motion

The derivation of the equations of motion for a flapping wing micro air vehicle are detailed in Chapter 2 and Appendix A. In order to analyze the equations of motion and the relative importance of the wing mass, the multi-body equations need to be decoupled and placed into first order form. Due to the highly coupled nature of the system, obtaining the first order equations of motion in the traditional way, by inverting the mass matrix directly, is not tractable analytically (symbolically). Therefore, an approximate inverse is used to obtain the first order equations of motion. The use of the approximate inverse allows the analysis of the equations of motion of a FWMAV in first order form. The multi-body equations of motion can be written in the following form:

$$\mathbf{M}\dot{\bar{u}}_j = \begin{bmatrix} \bar{F}_{aero} + \bar{F}_g - \sum_{i=1}^{3}\left(\dot{\bar{\mathbf{v}}}_{i,red} + \ddot{\bar{\rho}}_{ci,red}\right) \\ \bar{M}_{aero} + \bar{M}_g - \sum_{i=1}^{3}\left(\mathbf{I}_i\bar{\omega}_1 \times \bar{\omega}_i + \bar{\omega}_i \times \mathbf{I}_i\bar{\omega}_1 + m_i\bar{\rho}_{ci} \times \dot{\bar{\mathbf{v}}}_{i,red}\right) \\ Q_{RW} - \left(\mathbf{I}_2\bar{\omega}_1 \times \bar{\omega}_2 + \bar{\omega}_2 \times \mathbf{I}_2\bar{\omega}_2 + m_2\bar{\rho}_{c2} \times \dot{\bar{\mathbf{v}}}_{2,red}\right) \\ Q_{LW} - \left(\mathbf{I}_3\bar{\omega}_1 \times \bar{\omega}_3 + \bar{\omega}_3 \times \mathbf{I}_3\bar{\omega}_3 + m_3\bar{\rho}_{c3} \times \dot{\bar{\mathbf{v}}}_{3,red}\right) \end{bmatrix}. \quad \text{(B.1)}$$

In Equation (B.1), the matrix $\mathbf{M}$ is a time-varying mass matrix, with $\mathbf{M} \in \mathbb{R}^{12x12}$. The vector $\dot{\bar{u}}_j$ represents the time-derivative of the quasi-velocities, $\bar{\mathbf{u}}_j$, defined in Equation (2.7). In order to obtain the approximate inverse, the matrix is split into two parts, A, and E, according to the following equation

$$\mathbf{M} = \mathbf{A} + \varepsilon\mathbf{E}, \tag{B.2}$$

where ε is a small parameter. For the purpose of the analysis presented in this manuscript, the small parameter ε is the mass of the wings. The approximate inverse, $\mathbf{M}^{-1}$, is obtained from the following equation:

$$\mathbf{M}^{-1} = \mathbf{A}^{-1} + \varepsilon\mathbf{A}^{-1}\mathbf{E}\mathbf{A}^{-1}. \tag{B.3}$$

The components of the mass matrix can be written as

$$\mathbf{A} = \begin{bmatrix} A_{11} & 0 & 0 & 0 \\ 0 & A_{22} & 0 & 0 \\ 0 & 0 & A_{33} & 0 \\ 0 & 0 & 0 & A_{44} \end{bmatrix} \tag{B.4}$$

and

$$\mathbf{E} = \begin{bmatrix} 0 & E_{12} & E_{13} & E_{14} \\ E_{21} & 0 & E_{23} & E_{24} \\ E_{31} & E_{32} & 0 & 0 \\ E_{41} & E_{42} & 0 & 0 \end{bmatrix}. \tag{B.5}$$

Matrix Composition and Inversion

The components of $\mathbf{A}$ and $\mathbf{E}$ can be further defined and explained. For simplicity in presentation, the ε term will be absorbed into the components of the $\mathbf{E}$ matrix. The

first term in $\mathbf{A}$ is A_{11} and describes the affect of the system mass on the translation of the central body. A_{11} is defined according to

$$A_{11} = m_{sys}\mathbb{I}^{3\text{x}3}. \tag{B.6}$$

A_{22} describes the affect of the inertia of the system on the rotation of the central body. A_{22} is calculated from

$$A_{22} = \mathbf{I}_1 + \mathbf{I}_2 + \mathbf{I}_3 + (\tilde{r}_R + \tilde{\rho}_{c2})\,\tilde{r}_R^{\mathrm{T}} + (\tilde{r}_L + \tilde{\rho}_{c3})\,\tilde{r}_L^{\mathrm{T}} + \tilde{r}_R\tilde{\rho}_{c2}^{\mathrm{T}} + \tilde{r}_L\tilde{\rho}_{c3}^{\mathrm{T}}. \tag{B.7}$$

The terms $\tilde{\rho}_{c2}$ and $\tilde{\rho}_{c3}$ are skew-symmetric matrices representing the position of the wing centers of mass in the body frame. The wing centers of mass are obtained from Equation (2.8). For example, the skew-symmetric matrix for the right wing reference vector is

$$\tilde{\rho}_{c2} = \begin{bmatrix} 0 & -\rho_{c2,z} & \rho_{c2,y} \\ \rho_{c2,z} & 0 & -\rho_{c2,x} \\ -\rho_{c2,y} & \rho_{c2,x} & 0 \end{bmatrix}, \tag{B.8}$$

where

$$\bar{\rho}_{c2} = \begin{bmatrix} \rho_{c2,x} \\ \rho_{c2,y} \\ \rho_{c2,z} \end{bmatrix} = {\mathbf{R}_{\beta_R}}^{\mathrm{T}}{\mathbf{R}_R}^{\mathrm{T}}\bar{\rho}_{c2,w}. \tag{B.9}$$

The terms $\tilde{r}_R$ and $\tilde{r}_L$ are skew-symmetric matrices representing the position of the wing joints in the body frame. The skew-symmetric matrices are simply defined according to

$$\tilde{r}_R = \begin{bmatrix} 0 & -R_z & R_y \\ R_z & 0 & -R_x \\ -R_y & R_x & 0 \end{bmatrix} \tag{B.10}$$

and

$$\tilde{r}_L = \begin{bmatrix} 0 & -L_z & L_y \\ L_z & 0 & -L_x \\ -L_y & L_x & 0 \end{bmatrix}. \tag{B.11}$$

The individual entries in the definitions of $\tilde{r}_R$ and $\tilde{r}_L$ represent the components of the wing joint reference vector in the body frame. The terms A_{33} and A_{44} describe the effects of the individual wing moments of inertia on the angular velocities of the right and left wings, respectively. The terms are calculated according to

$$A_{33} = \mathbf{R}_{\beta_R}{}^{\mathrm{T}} \mathbf{I}_2 \mathbf{R}_{\beta_R}{}^{\mathrm{T}} \quad \text{and} \quad A_{44} = \mathbf{R}_{\beta_L}{}^{\mathrm{T}} \mathbf{I}_3 \mathbf{R}_{\beta_L}{}^{\mathrm{T}}. \tag{B.12}$$

The term E_{12} represents the effects of the coupling of the rotational motion of the body and the position of the wing center of mass on the translation of the body. The term E_{21} contains the effects of the coupling of the translational motion of the body and the position of the wings centers of mass on the rotation of the body. The term E_{12} is the transpose of the term E_{21}, where

$$E_{21} = m_2 \left(\tilde{\rho}_{c2} + \tilde{r}_R \right) + m_3 \left(\tilde{\rho}_{c3} + \tilde{r}_L \right). \tag{B.13}$$

The terms E_{13} and E_{14} represent the effects of the necessary accelerations of the wings, to obtain the desired wing motion, on the translation of the central body. E_{13} and E_{14} are calculated according to

$$E_{13} = m_2 \tilde{\rho}_{c2}^{\mathrm{T}} \mathbf{R}_{\beta_R}{}^{\mathrm{T}} + \mathbf{R}_{\beta_R}{}^{\mathrm{T}} \Theta_{RW} \quad \text{and} \quad E_{14} = m_3 \tilde{\rho}_{c3}^{\mathrm{T}} \mathbf{R}_{\beta_L}{}^{\mathrm{T}} + \mathbf{R}_{\beta_L}{}^{\mathrm{T}} \Theta_{LW}. \tag{B.14}$$

The terms Θ_{RW} and Θ_{LW} represent the relationship between the acceleration of the angular velocities of the wings and the translation of the central body. The terms are obtained from the calculation of the acceleration of the wing center of mass reference

vectors, defined in Equation (2.13). Θ_{RW} results from the term ${\mathbf{R}_{\beta_R}}^{\mathrm{T}}{\mathbf{R}_R}^{\mathrm{T}}\dot{\tilde{\omega}}_{2,sp}\bar{\rho}_{c2,w}$. For a flat plate wing, where the wing is mounted at the mid-point, such that $\bar{\rho}_{c2,w} = \begin{bmatrix} 0 & \rho_2 & 0 \end{bmatrix}^{\mathrm{T}}$, Θ_{RW} is equal to

$$\Theta_{RW} = m_2\rho_2 \begin{bmatrix} {\mathbf{R}_R}^{\mathrm{T}}(1,3) & 0 & -{\mathbf{R}_R}^{\mathrm{T}}(1,1) \\ {\mathbf{R}_R}^{\mathrm{T}}(2,3) & 0 & -{\mathbf{R}_R}^{\mathrm{T}}(2,1) \\ {\mathbf{R}_R}^{\mathrm{T}}(3,3) & 0 & -{\mathbf{R}_R}^{\mathrm{T}}(3,1) \end{bmatrix}, \tag{B.15}$$

where ${\mathbf{R}_R}^{\mathrm{T}}(1,1)$ refers to the first row, first column entry of the transpose of the rotation matrix, ${\mathbf{R}_R}^{\mathrm{T}}$. In a similar manner, Θ_{LW} is equal to

$$\Theta_{LW} = m_3\rho_3 \begin{bmatrix} -{\mathbf{R}_L}^{\mathrm{T}}(1,3) & 0 & {\mathbf{R}_L}^{\mathrm{T}}(1,1) \\ -{\mathbf{R}_L}^{\mathrm{T}}(2,3) & 0 & {\mathbf{R}_L}^{\mathrm{T}}(2,1) \\ -{\mathbf{R}_L}^{\mathrm{T}}(3,3) & 0 & {\mathbf{R}_L}^{\mathrm{T}}(3,1) \end{bmatrix}. \tag{B.16}$$

The terms E_{23} and E_{24} represent the effects of the required accelerations of the wings on the rotation of the central body. E_{23} and E_{24} are calculated according to

$$E_{23} = \mathbf{I}_2{\mathbf{R}_{\beta_R}}^{\mathrm{T}} + \tilde{r}_R E_{13} \quad \text{and} \quad E_{24} = \mathbf{I}_3{\mathbf{R}_{\beta_L}}^{\mathrm{T}} + \tilde{r}_L E_{14}. \tag{B.17}$$

The terms E_{31} and E_{41} represent the effects of the translation of the central body on the wing motion. The terms are calculated according to

$$E_{31} = {\mathbf{R}_{\beta_R}}^{\mathrm{T}}\tilde{\rho}_{c2} \quad \text{and} \quad E_{41} = {\mathbf{R}_{\beta_L}}^{\mathrm{T}}\tilde{\rho}_{c3}. \tag{B.18}$$

The last two terms, E_{32} and E_{42}, represent the effects of the rotation of the central body on the wing motion. The terms are calculated according to

$$E_{32} = {\mathbf{R}_{\beta_R}}^{\mathrm{T}}\left(\mathbf{I}_2 + m_2\tilde{\rho}_{c2}\tilde{r}_R^{\mathrm{T}}\right) \quad \text{and} \quad E_{42} = {\mathbf{R}_{\beta_L}}^{\mathrm{T}}\left(\mathbf{I}_3 + m_3\tilde{\rho}_{c3}\tilde{r}_L^{\mathrm{T}}\right). \tag{B.19}$$

Using the form of the matrix approximate inverse in Equation (B.3), the approximate inverse of the matrix can be calculated according to

$$\mathbf{M}^{-1} \approx \begin{bmatrix} {A_{11}}^{-1} & {A_{11}}^{-1}E_{12}{A_{22}}^{-1} & {A_{11}}^{-1}E_{13}{A_{33}}^{-1} & {A_{11}}^{-1}E_{14}{A_{44}}^{-1} \\ {A_{22}}^{-1}E_{21}{A_{11}}^{-1} & {A_{22}}^{-1} & {A_{22}}^{-1}E_{23}{A_{33}}^{-1} & {A_{22}}^{-1}E_{24}{A_{44}}^{-1} \\ {A_{33}}^{-1}E_{31}{A_{11}}^{-1} & {A_{33}}^{-1}E_{32}{A_{22}}^{-1} & {A_{33}}^{-1} & 0 \\ {A_{44}}^{-1}E_{41}{A_{11}}^{-1} & {A_{44}}^{-1}E_{42}{A_{22}}^{-1} & 0 & {A_{44}}^{-1} \end{bmatrix}. \tag{B.20}$$

The result utilizes the fact that since the matrix $\mathbf{A}$ is block diagonal, the inverse of $\mathbf{A}$ is the inverse of each block diagonal element, such that

$$\mathbf{A}^{-1} = \begin{bmatrix} {A_{11}}^{-1} & 0 & 0 & 0 \\ 0 & {A_{22}}^{-1} & 0 & 0 \\ 0 & 0 & {A_{33}}^{-1} & 0 \\ 0 & 0 & 0 & {A_{44}}^{-1} \end{bmatrix}. \tag{B.21}$$

Comparison of the Equations of Motion

As stated in Chapter 3, the use of the approximate inverse enables the equations of motion to be placed in the following form:

$$\dot{x} = f^{(0)}(x,t) + \varepsilon^1 f^{(1)}(x,t) + \varepsilon^2 f^{(2)}(x,t). \tag{B.22}$$

Due to the highly coupled nature of the equations of motion, the full nonlinear model described in Chapter 2 can be compared to the approximate equations of motion analytically. However, through the use of simulations of the different models, the different sets of equations of motion can be compared. The different sets of equations will be compared for symmetrical flapping and with both of the aerodynamic models presented in Chapter 2. The pertinent flapping kinematic parameters are the following: $\alpha_m = 45°$, $\delta_m = 1°$, $\zeta_m = 60°$, and $f = 22Hz$. The results for the model

developed by Deng et al. are presented in Figures B.1(a), B.2(a), and B.3(a). The results for the Berman and Wang aerodynamic model are presented in Figures B.1(b), B.2(b), and B.3(b).

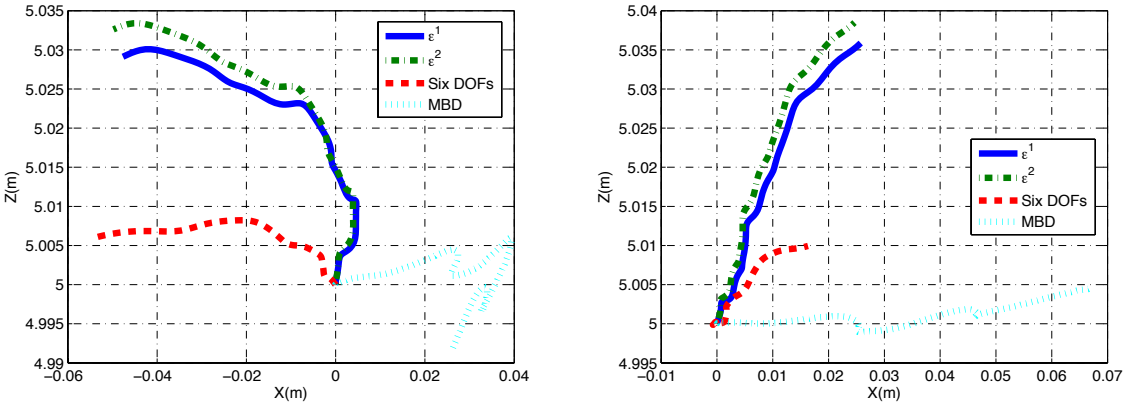

(a) UCB Aerodynamic Model (b) Berman and Wang Aerodynamic Model

Figure B.1: $X - Z$ Inertial Comparison of Dynamic Models

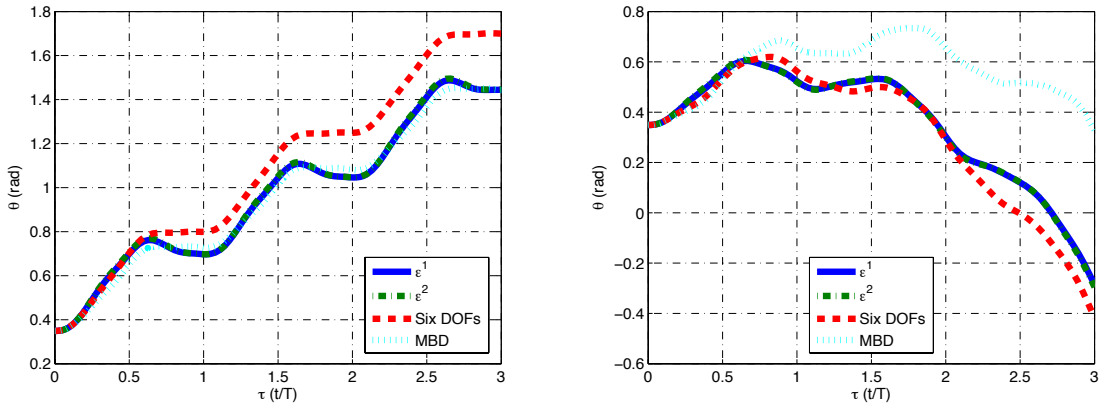

(a) UCB Aerodynamic Model (b) Berman and Wang Aerodynamic Model

Figure B.2: Pitch Angle Comparison of Dynamic Models

The approximation does not match the position when the UCB or Berman and Wang aerodynamic models are used. The approximate inverse does not simulate the full nonlinear system, but does still exhibit a difference in position with the standard aircraft equations of motion. The pitch angle does match for the UCB model when compared with the multi-body model.

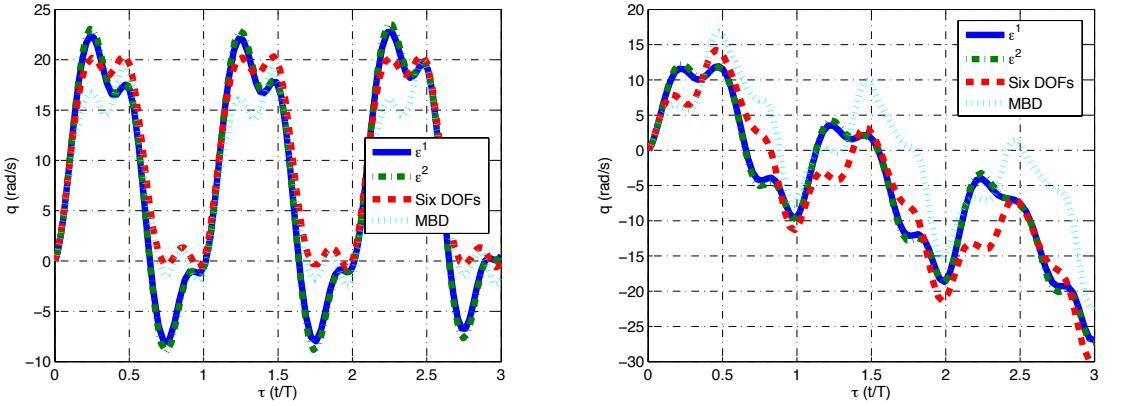

(a) UCB Aerodynamic Model

(b) Berman and Wang Aerodynamic Model

Figure B.3: Pitch Velocity Comparison of Dynamic Models

APPENDIX C

Quarter-Cycle Equations of Motion for Symmetrical Flapping

The appendix presents the details of the first order equations of motion presented in Chapter 3 and their associated quarter-cycle approximations.

Longitudinal Velocity - $\dot{u}$

The contributions to the forward velocity, stemming from $f_1^{(1)}(x,t)$, are the following. The contributions of the acceleration of the wing reference vectors are detailed in Equation (A.14). From the assumptions made in Chapter 3, we can write the skew-symmetric matrix defining the angular velocity of the wing in the stroke plane as

$$\tilde{\omega}_{2,sp} = \begin{bmatrix} 0 & -r_{RW} & 0 \\ r_{RW} & 0 & -p_{RW} \\ 0 & p_{RW} & 0 \end{bmatrix}, \tag{C.1}$$

where $p_{RW} = \sin(\alpha_R)\dot{\zeta_R}$ and $r_{RW} = -\cos(\alpha_R)\dot{\zeta_R}$. The first term from Equation (A.14), $\mathbf{R}_{\beta_R}{}^{\mathrm{T}}\mathbf{R}_R{}^{\mathrm{T}}\tilde{\omega}_{2,sp}\tilde{\omega}_{2,sp}\bar{\rho}_{c2,w}\cdot\hat{b}_x$, simplifies to $-\rho_2\cos(\beta_R)\sin(\zeta_R)\dot{\zeta}_R^2$ based on the

assumptions made in Chapter 3. The quarter cycle approximation is the following:

$$\int_{QC} \mathbf{R}_{\beta_R}{}^{\mathrm{T}} \mathbf{R}_R{}^{\mathrm{T}} \tilde{\omega}_{2,sp} \tilde{\omega}_{2,sp} \bar{\rho}_{c2,w} \cdot \hat{b}_x = -m_w \rho_w \left(\omega \zeta_m\right)^2 \cos(\beta) \left(\frac{1}{\zeta_m} \mathbf{H}_1 \left(\zeta_m\right)\right), \qquad \text{(C.2)}$$

where ρ_w is the position of the center of mass of the wing, along the $y-axis$ of the wing in the wing frame, and m_w denotes the mass of the wing. The second term of $\ddot{\bar{\rho}}_{ci,red}$ is

$$\begin{aligned} \int_{QC} \left(2\,\bar{\omega}_2 \quad \times \quad \left(\mathbf{R}_{\beta_R}{}^{\mathrm{T}} \mathbf{R}_R{}^{\mathrm{T}} \tilde{\omega}_{2,sp} \bar{\rho}_{c2,w}\right)\right) \cdot \hat{b}_x & \\ = \quad -2 m_w \rho_w (\omega \zeta_m) \sin(\beta) \operatorname{sgn}\left(\dot{\zeta}\right) \left(\frac{2}{\pi} \frac{\sin(\zeta_m)}{\zeta_m}\right) \bar{q} & \qquad \text{(C.3)} \\ -2 m_w \rho_w \left(\omega \zeta_m\right)^2 \cos(\beta) \cos(\alpha_m) \operatorname{sgn}\left(\zeta\right) \left(\frac{1}{\zeta_m} \mathbf{H}_1(\zeta_m)\right) & \\ -2 m_w \rho_w \left(\omega \zeta_m\right)^2 \sin(\beta) \sin(\alpha_m) \operatorname{sgn}\left(\mathrm{s}\left(2\omega\right)\right) \left(\frac{1}{\zeta_m} \mathbf{H}_1(\zeta_m)\right). & \end{aligned}$$

The third term of $\ddot{\bar{\rho}}_{ci,red}$ is evaluated as

$$\begin{aligned} \int_{QC} \left(\bar{\omega}_i \quad \times \quad \left(\bar{\omega}_i \times \bar{\rho}_{ci}\right)\right) \cdot \hat{b}_x & \\ = \quad m_w \rho_w \left(\omega \zeta_m\right) \left(\cos(\beta) \sin(\alpha_m) - \sin(\beta) \cos(\alpha_m) \operatorname{sgn}\left(\dot{\zeta}\right)\right) \left(\frac{2}{\pi} \frac{\sin(\zeta_m)}{\zeta_m}\right) \bar{q} & \\ -m_w \rho_w \omega^2 \zeta_m \left(\cos(\beta) \cos^2(\alpha_m) + \frac{1}{2} \sin(\beta) \sin(2\alpha_m) \operatorname{sgn}\left(\dot{\zeta}\right)\right) \operatorname{sgn}\left(\zeta\right) \mathbf{H}_1\left(\zeta_m\right) & \\ -m_w \rho_w \cos(\beta) \operatorname{sgn}\left(\zeta\right) \mathbf{H}_0\left(\zeta_m\right) \bar{q}^2. & \qquad \text{(C.4)} \end{aligned}$$

The control moment contribution, or alternatively the contribution from the acceleration of the wings, has the following form:

$$\begin{aligned} \int_{QC} \left(\left(\tilde{\rho}_{ci}^{\mathrm{T}} \mathbf{R}_{\beta_k}{}^{\mathrm{T}} + \mathbf{R}_{\beta_k}{}^{\mathrm{T}} \Theta_{RW}\right) \Omega_{RW,d}\right) \cdot \hat{b}_x = & \qquad \text{(C.5)} \\ -m_w \rho_w \omega^2 \zeta_m \operatorname{sgn}\left(\zeta\right) \left(\cos(\beta)\left(1 + \cos(\alpha_m)\right) + \operatorname{sgn}\left(\dot{\zeta}\right) \sin(\beta) \sin(\alpha_m)\right) \mathbf{H}_{-1}\left(\zeta_m\right). & \end{aligned}$$

The contribution from the coupling between the position of the wings and the aerodynamic pitching moment is

$$\begin{aligned}\int_{QC} \rho_{c2,z} M_{aero} &= \frac{1}{4}\sin(\beta)\hat{r}_2 b_w m_w \rho_w k_T \sin(\alpha_m)\big(1 - \mathbf{J}_0\left(2\zeta_m\right) - \mathbf{J}_2\left(2\zeta_m\right)\big) \\ &\quad -\frac{1}{4}\sin(\beta)\hat{r}_2 b_w m_w \rho_w k_N \cos(\alpha_m)\big(1 - \mathbf{J}_0\left(2\zeta_m\right) - \mathbf{J}_2\left(2\zeta_m\right)\big) \\ &\quad -\frac{1}{8}\sin(\beta) c_w m_w \rho_w k_N \mathrm{sgn}\left(\zeta\right)\frac{1}{2\zeta_m}\mathbf{H}_1\left(2\zeta_m\right). \end{aligned} \tag{C.6}$$

It's important to note that the previous developments are for one wing only. The total contributions need to be doubled, except for the contribution from $\rho_{c2,z} M_{aero}$, which is quadrupled.

Vertical Velocity - $\dot{w}$

The first term of $\ddot{\bar{\rho}}_{ci,red}$ contributes to the vertical velocity according to

$$\int_{QC} {\mathbf{R}_{\beta_k}}^{\mathrm{T}} {\mathbf{R}_k}^{\mathrm{T}} \tilde{\omega}_{i,sp}\tilde{\omega}_{i,sp}\bar{\rho}_{ci,w}\cdot\hat{b}_z = m_w\rho_w\left(\omega\zeta_m\right)^2\sin(\beta)\left(\frac{1}{\zeta_m}\mathbf{H}_1\left(\zeta_m\right)\right). \tag{C.7}$$

The second term of $\ddot{\bar{\rho}}_{ci,red}$ is

$$\begin{aligned}\int_{QC} \big(2\,\bar{\omega}_2 &\times \big({\mathbf{R}_{\beta_R}}^{\mathrm{T}} {\mathbf{R}_R}^{\mathrm{T}} \tilde{\omega}_{2,sp}\bar{\rho}_{c2,w}\big)\big)\cdot\hat{b}_x \\ &= -2m_w\rho_w(\omega\zeta_m)\cos(\beta)\,\mathrm{sgn}\left(\dot{\zeta}\right)\left(\frac{2}{\pi}\frac{\sin(\zeta_m)}{\zeta_m}\right)\bar{q} \\ &\quad +2m_w\rho_w\left(\omega\zeta_m\right)^2\sin(\beta)\cos(\alpha_m)\,\mathrm{sgn}\left(\zeta\right)\left(\frac{1}{\zeta_m}\mathbf{H}_1(\zeta_m)\right) \\ &\quad -2m_w\rho_w\left(\omega\zeta_m\right)^2\cos(\beta)\sin(\alpha_m)\,\mathrm{sgn}\left(\mathrm{s}\left(2\omega\right)\right)\left(\frac{1}{\zeta_m}\mathbf{H}_1(\zeta_m)\right). \end{aligned} \tag{C.8}$$

The third term of $\ddot{\bar{\rho}}_{ci,red}$ is

$$\begin{aligned}
\int_{QC} \left(\bar{\omega}_i \times (\bar{\omega}_i \times \bar{\rho}_{ci})\right) \cdot \hat{b}_x & \\
= & -m_w \rho_w (\omega\zeta_m) \left(\sin(\beta)\sin(\alpha_m) + \cos(\beta)\cos(\alpha_m)\,\mathrm{sgn}\left(\dot{\zeta}\right)\right) \left(\frac{2}{\pi}\frac{\sin(\zeta_m)}{\zeta_m}\right) \bar{q} \\
& + m_w \rho_w \omega^2 \zeta_m \left(\sin(\beta)\cos^2(\alpha_m) - \frac{1}{2}\sin(\beta)\sin(2\alpha_m)\mathrm{sgn}\left(\dot{\zeta}\right)\right) \mathrm{sgn}(\zeta)\,\mathbf{H}_1(\zeta_m) \\
& + m_w \rho_w \sin(\beta)\mathrm{sgn}(\zeta)\,\mathbf{H}_0(\zeta_m)\,\bar{q}^2. \qquad \text{(C.9)}
\end{aligned}$$

The control moment contribution (wing acceleration contribution) has the following form:

$$\begin{aligned}
& \int_{QC} \left(\left(\tilde{\rho}_{ci}^{\mathrm{T}} \mathbf{R}_{\beta_k}{}^{\mathrm{T}} + \mathbf{R}_{\beta_k}{}^{\mathrm{T}} \Theta_{RW}\right)\Omega_{RW,d}\right) \cdot \hat{b}_x = \qquad \text{(C.10)} \\
& + m_w \rho_w \omega^2 \zeta_m \mathrm{sgn}(\zeta) \left(\sin(\beta)\left(1 + \cos(\alpha_m)\right) - \mathrm{sgn}\left(\dot{\zeta}\right)\cos(\beta)\sin(\alpha_m)\right) \mathbf{H}_{-1}(\zeta_m).
\end{aligned}$$

The contribution from the coupling between the position of the wings and the aerodynamic pitching moment is

$$\begin{aligned}
\int_{QC} \rho_{c2,x} M_{aero} &= \frac{1}{4}\cos(\beta)\hat{r}_2 b_w m_w \rho_w k_N \cos(\alpha_m)\left(1 - \mathbf{J}_0(2\zeta_m) - \mathbf{J}_2(2\zeta_m)\right) \\
& - \frac{1}{4}\sin(\beta)\hat{r}_2 b_w m_w \rho_w k_T \sin(\alpha_m)\left(1 - \mathbf{J}_0(2\zeta_m) - \mathbf{J}_2(2\zeta_m)\right) \\
& + \frac{1}{8}\cos(\beta) c_w m_w \rho_w k_N \mathrm{sgn}(\zeta)\,\frac{1}{2\zeta_m}\mathbf{H}_1(2\zeta_m). \qquad \text{(C.11)}
\end{aligned}$$

Pitch Velocity - $\dot{q}$

The contribution from the the coupling between the position of the wing center of mass (differs from the aerodynamic pitching moment) and the aerodynamic force

is

$$\int_{QC} \rho_{c2,z} F_x - \rho_{c2,z} F_z = \rho_w m_w \mathrm{sgn}\left(\zeta\right) \left(k_N \cos(\alpha_m) - k_T \sin(\alpha_m)\right) \frac{1}{\zeta_m} \mathbf{H}_1\left(\zeta_m\right). \quad \text{(C.12)}$$

For symmetrical flapping, in a longitudinal, vertical, or hovering flight condition, the $\bar{\omega}_i \times \mathbf{I}_i \bar{\omega}_i$ term reduces to the following for the wings (using the right wing as the example):

$$\begin{aligned} \left(\bar{\omega}_i \times \mathbf{I}_i \bar{\omega}_i\right) \cdot \hat{b}_y &= \left(I_{xx,2} - I_{zz,2}\right) p_{RW} r_{RW} + I_{xz,2} \left({p_{RW}}^2 - {r_{RW}}^2\right) \\ &\quad + \left(I_{yz,2} p_{RW} - I_{xy,2} r_{RW}\right) q. \end{aligned} \quad \text{(C.13)}$$

The term $\mathbf{I}_2 \left(\bar{\omega}_1 \times \bar{\omega}_2\right)$ results from the calculation of $\mathbf{I}_2 \dot{\bar{\omega}}_2$. The remaining contribution is analogous to the $\ddot{\bar{\rho}}_{ci}$ terms affecting the translation of the central body. For symmetrical flapping, the term $\mathbf{I}_2 \left(\bar{\omega}_1 \times \bar{\omega}_2\right)$ reduces to

$$\mathbf{I}_2 \left(\bar{\omega}_1 \times \bar{\omega}_2\right) \cdot \hat{b}_y = \left(I_{yz,2} p_{RW} - I_{xy,2} r_{RW}\right) q. \quad \text{(C.14)}$$

The individual components of the inertia tensor (eg. $I_{xx,i}$) correspond to the transformed inertia tensor in the wing frame. The quarter cycle representation of the $\mathbf{I}_2 \left(\bar{\omega}_1 \times \bar{\omega}_2\right)$ is

$$\begin{aligned} &\int_{QC} \mathbf{I}_2 \left(\bar{\omega}_1 \times \bar{\omega}_2\right) \cdot \hat{b}_y = \quad \text{(C.15)} \\ &\frac{1}{\pi} \omega \zeta_m \cos(\alpha_m) \left(I_{xx,w} - 2 I_{yy,w} + I_{zz,w}\right) \mathrm{sgn}\left(\mathrm{s}\left(2\omega\right)\right) \left(\frac{1 - \cos(2\zeta_m)}{2\zeta_m}\right) \bar{q} \\ &+ \frac{1}{\pi} \omega \zeta_m \left(\cos(\alpha_m) \cos(2\alpha_m)\right) \left(I_{xx,w} - I_{zz,w}\right) \mathrm{sgn}\left(\mathrm{s}\left(2\omega\right)\right) \left(\frac{1 - \cos(2\zeta_m)}{2\zeta_m}\right) \bar{q} \\ &- \frac{2}{\pi} \omega \zeta_m \left(\cos(\alpha_m) \sin^2(\alpha_m)\right) \left(I_{xx,w} - I_{zz,w}\right) \mathrm{sgn}\left(\mathrm{s}\left(2\omega\right)\right) \left(\frac{1 - \cos(\zeta_m)}{\zeta_m}\right) \bar{q}. \end{aligned}$$

The quarter cycle representation for $\bar{\omega}_i \times \mathbf{I}_i \bar{\omega}_i$ is:

$$\int_{QC} \bar{\omega}_i \times \mathbf{I}_i \bar{\omega}_i \cdot \hat{b}_y = \tag{C.16}$$

$$\begin{aligned}
&-\frac{1}{4}\left(\omega\zeta_m\right)^2 \left(I_{xx,w} - I_{zz,w}\right) \sin(4\alpha_m) \operatorname{sgn}\left(\dot{\zeta}\right) \left(\mathbf{J}_0\left(\zeta_m\right) + \mathbf{J}_2\left(\zeta_m\right)\right) \\
&-\frac{1}{16}\left(\omega\zeta_m\right)^2 \left(I_{xx,w} - I_{zz,w}\right) \sin(4\alpha_m) \operatorname{sgn}\left(\dot{\zeta}\right) \left(3 + \mathbf{J}_0\left(2\zeta_m\right) + \mathbf{J}_2\left(2\zeta_m\right)\right) \\
&+\frac{1}{8}\left(\omega\zeta_m\right)^2 \left(I_{xx,w} - 2I_{yy,w} + I_{zz,w}\right) \sin(2\alpha_m) \operatorname{sgn}\left(\dot{\zeta}\right) \left(1 - \mathbf{J}_0\left(2\zeta_m\right) - \mathbf{J}_2\left(2\zeta_m\right)\right) \\
&+\int_{QC} \mathbf{I}_2 \left(\bar{\omega}_1 \times \bar{\omega}_2\right) \cdot \hat{b}_y.
\end{aligned} \tag{C.17}$$

The wing acceleration contribution to the pitch velocity, using the right wing as an example, is:

$$\left(\left(A_{22}{}^{-1} E_{23}\right) \Omega_{RW,d}\right) \cdot \hat{b}_y. \tag{C.18}$$

where A_{22} and E_{23} are previously defined in Appendix B. The quarter cycle representation is

$$\begin{aligned}
&\int_{QC} \left(\left(A_{22}{}^{-1} E_{23}\right) \Omega_{RW,d}\right) \cdot \hat{b}_y = \\
&\frac{1}{2}\omega^2 \zeta_m \left(I_{xx,w} - I_{zz,w}\right) \operatorname{sgn}\left(\dot{\zeta}\right) \sin(\alpha_m) \mathbf{J}_1\left(\zeta_m\right) \\
&+\frac{1}{2}\omega^2 \zeta_m \left(I_{xx,w} - I_{zz,w}\right) \operatorname{sgn}\left(\dot{\zeta}\right) \sin(\alpha_m) \cos(2\alpha_m) \left(\mathbf{J}_1\left(\zeta_m\right) + \frac{1}{2}\mathbf{J}_1\left(2\zeta_m\right)\right) \\
&+\frac{1}{4}\omega^2 \zeta_m \left(I_{xx,w} - 2I_{yy,w} + I_{zz,w}\right) \operatorname{sgn}\left(\dot{\zeta}\right) \sin(\alpha_m) \mathbf{J}_1\left(2\zeta_m\right).
\end{aligned} \tag{C.19}$$

The following constants results from the derivation of the contributions of the forward velocity and vertical velocity to the aerodynamic forces and moments. The constants k_1 and k_2 result from the $u(w)$ contribution of the tangential force and normal force, respectively, to the thrust force in the stroke plane as a result of the geometric angle

of attack.

$$k_1 = 0.4\rho\, A_w\, (\hat{r}_2 b_w \omega \zeta_m) \left(\frac{1}{2}\cos(\alpha_m) + \frac{1}{4}\cos(3\alpha_m) + \frac{1}{4}\cos(5\alpha_m) \right) \tag{C.20}$$

$$k_2 = 3.4\rho\, A_w\, (\hat{r}_2 b_w \omega \zeta_m) \sin^2(\alpha_m) \tag{C.21}$$

The constants k_3 and k_4 result from the $u(w)$ contribution of the tangential force and normal forces, respectively, to the lift force in the stroke plane as a result of the geometric angle of attack.

$$k_3 = 0.4\rho\, A_w\, (\hat{r}_2 b_w \omega \zeta_m) \left(\frac{1}{2}\sin(\alpha_m) - \frac{1}{4}\sin(3\alpha_m) + \frac{1}{4}\sin(5\alpha_m) \right) \tag{C.22}$$

$$k_4 = 1.7\rho\, A_w\, (\hat{r}_2 b_w \omega \zeta_m) \sin(2\alpha_m) \tag{C.23}$$

The constants k_5 and k_6 result from the $u^2(w^2)$ contribution of the tangential force and normal forces, respectively, to the lift force in the stroke plane as a result of the geometric angle of attack.

$$k_5 = 0.2\rho\, A_w \left(\frac{1}{2}\cos(\alpha_m) + \frac{1}{4}\cos(3\alpha_m) + \frac{1}{4}\cos(5\alpha_m) \right) \tag{C.24}$$

$$k_6 = 1.7\rho\, A_w \sin^2(\alpha_m) \tag{C.25}$$

The constants k_7 and k_8 result from the $u^2(w^2)$ contribution of the tangential force and normal forces, respectively, to the lift force in the stroke plane as a result of the geometric angle of attack.

$$k_7 = 0.2\rho\, A_w \left(\frac{1}{2}\sin(\alpha_m) - \frac{1}{4}\sin(3\alpha_m) + \frac{1}{4}\sin(5\alpha_m) \right) \tag{C.26}$$

$$k_8 = 0.85\rho\, A_w \sin(2\alpha_m) \tag{C.27}$$

The constants k_9 and k_{10} result from the $u(w)$ contribution of the tangential force and normal force, respectively, to the thrust force in the stroke plane as a result of the change in angle of attack.

$$k_9 = 0.2\rho\, A_w\, (\hat{r}_2 b_w \omega \zeta_m)\, \big(\sin(3\alpha_m) + \sin(5\alpha_m)\big) \tag{C.28}$$

$$k_{10} = 0.85\rho\, A_w\, (\hat{r}_2 b_w \omega \zeta_m) \sin(2\alpha_m) \tag{C.29}$$

The constants k_{11} and k_{12} result from the $u(w)$ contribution of the tangential force and normal force, respectively, to the lift force in the stroke plane as a result of the change in angle of attack.

$$k_{11} = 0.2\rho\, A_w\, (\hat{r}_2 b_w \omega \zeta_m)\, \big(\sin(3\alpha_m) - \sin(5\alpha_m)\big) \tag{C.30}$$

$$k_{12} = 1.7\rho\, A_w\, (\hat{r}_2 b_w \omega \zeta_m) \cos^2(\alpha_m) \tag{C.31}$$

The constants k_{13} and k_{14} result from the $u^2(w^2)$ contribution of the tangential force and normal force, respectively, to the thrust force in the stroke plane as a result of the change in angle of attack.

$$k_{13} = 0.05\rho\, A_w \big(\sin(3\alpha_m) + \sin(5\alpha_m)\big) \tag{C.32}$$

$$k_{14} = 0.425\rho\, A_w \sin(2\alpha_m) \tag{C.33}$$

The constants k_{15} and k_{16} result from the $u^2(w^2)$ contribution of the tangential force and normal force, respectively, to the lift force in the stroke plane as a result of the change in angle of attack.

$$k_{15} = 0.1\rho\, A_w \big(\sin(3\alpha_m) - \sin(5\alpha_m)\big) \tag{C.34}$$

$$k_{16} = 0.85\rho\, A_w \cos^2(\alpha_m) \tag{C.35}$$

The constants k_{17} and k_{18} result from the $u(w)$ and $u^2(w^2)$ contributions of the normal force to the aerodynamic pitching moment. The contributions are due to the geometric angle of attack and the normal force acting through the chord-wise component of the aerodynamic center of pressure.

$$k_{17} = 0.425\rho A_w c_w \left(\hat{r}_2 b_w \zeta_m\right) \sin(\alpha_m) \tag{C.36}$$

$$k_{18} = 0.425\rho A_w c_w \sin(\alpha_m) \tag{C.37}$$

The constants k_{19}-k_{24} result from the change in angle of attack contribution to the aerodynamic pitching moment. The constants k_{19} and k_{20} result from the $u(w)$ contribution to the tangential and normal forces, respectively, acting through the radial component of the aerodynamic center of pressure.

$$k_{19} = 0.2\rho A_w \left(\hat{r}_2 b_w\right)^2 \omega\zeta_m \big(\cos(3\alpha_m) - \cos(5\alpha_m)\big) \tag{C.38}$$

$$k_{20} = 1.7\rho A_w \left(\hat{r}_2 b_w\right)^2 \omega\zeta_m \cos^2(\alpha_m) \tag{C.39}$$

The constants k_{21} and k_{22} result from the $u^2(w^2)$ contribution to the tangential and normal forces, respectively, acting through the radial component of the aerodynamic center of pressure.

$$k_{21} = 0.05\rho A_w \hat{r}_2 b_w \big(\cos(3\alpha_m) - \cos(5\alpha_m)\big) \tag{C.40}$$

$$k_{22} = 0.425\rho A_w \hat{r}_2 b_w \cos^2(\alpha_m) \tag{C.41}$$

Finally, the constants k_{23} and k_{24} result from the $u(w)$ and $u^2(w^2)$ contributions of the normal force to the aerodynamic pitching moment. The contributions are due

to the change in angle of attack and the normal force acting through the chord-wise component of the aerodynamic center of pressure.

$$k_{23} = 0.425\rho A_w c_w \cos(\alpha_m) \left(\hat{r}_2 b_w \omega \zeta_m\right) \tag{C.42}$$

$$k_{24} = 0.10625\rho A_w c_w \cos(\alpha_m) \tag{C.43}$$

APPENDIX D

Integrals of Periodic Functions: Quarter-Cycle Representation

The appendix details the various integrals used to calculated the average and quarter-cycle equations of motion. The integrals are derived through the use of [124, 125, 126] and Wolfram Alpha. The input waveforms have two main forms: $z\sin(\theta)$ and $z\cos(\theta)$, where z denotes the amplitude of the sinusoidal or cosinusoidal wave. The first integral results in a Bessel function of the first kind, order zero. The integral has the same value over each quarter-cycle.

$$\frac{2}{\pi}\int_0^{\frac{\pi}{2}} \cos\left(z\sin\theta\right) d\theta = \frac{2}{\pi}\int_0^{\frac{\pi}{2}} \cos\left(z\cos\theta\right) d\theta = \mathbf{J}_0(z) \tag{D.1}$$

The next integral results in a Struve function of the first kind, order zero. The integral changes sign over each quarter-cycle, depending on the input wave (either sine or cosine). However, regardless of the type of input waveform, the integral is zero over the full flapping cycle from 0 to 2π.

$$\frac{2}{\pi}\int_0^{\frac{\pi}{2}} \sin\left(z\sin\theta\right) d\theta = \frac{2}{\pi}\int_0^{\frac{\pi}{2}} \sin\left(z\cos\theta\right) d\theta = \mathbf{H}_0(z) \tag{D.2}$$

For a sinusoidal input, $\sin(z\sin\theta)$, the quarter-cycle function is $\operatorname{sgn}(\sin\theta)\,\mathbf{H}_0(z)$. For a cosinusoidal input, $\sin(z\cos\theta)$, the quarter-cycle function is $\operatorname{sgn}(\cos\theta)\,\mathbf{H}_0(z)$. The next four integrals detail integrals involving the sine and cosine of a sinusoidal wave multiplied by an additional sine or cosine wave. The first integral changes sign consistent with a cosine wave:

$$\frac{2}{\pi}\int_0^{\frac{\pi}{2}}\cos(z\sin\theta)\cos\theta d\theta = \frac{2}{\pi}\frac{\sin(z)}{z}. \tag{D.3}$$

The integral is zero over the entire flapping cycle. The quarter-cycle approximation is

$$\int_{QC}\cos(z\sin\theta)\cos\theta d\theta = \operatorname{sgn}(\cos\theta)\,\frac{2}{\pi}\frac{\sin(z)}{z}. \tag{D.4}$$

The next integral changes sign consistent with a sine wave and is zero over the entire flapping cycle:

$$\frac{2}{\pi}\int_0^{\frac{\pi}{2}}\cos(z\sin\theta)\sin\theta d\theta = \mathbf{H}_{-1}(z). \tag{D.5}$$

The quarter-cycle approximation is

$$\int_{QC}\cos(z\sin\theta)\sin\theta d\theta = \operatorname{sgn}(\sin\theta)\,\mathbf{H}_{-1}(z). \tag{D.6}$$

The next integral changes sign over each quarter-cycle. The sign changes are consistent with a sine wave with double the angle.

$$\frac{2}{\pi}\int_0^{\frac{\pi}{2}}\sin(z\sin\theta)\cos\theta d\theta = \frac{2}{\pi}\frac{1-\cos(z)}{z} \tag{D.7}$$

The quarter-cycle approximation is

$$\int_0^{QC} \sin\left(z\sin\theta\right)\cos\theta d\theta = \operatorname{sgn}\left(\sin 2\theta\right)\frac{2}{\pi}\frac{1-\cos(z)}{z}. \tag{D.8}$$

The next integral is constant over all four flapping cycles. No quarter-cycle representation is necessary.

$$\frac{2}{\pi}\int_0^{\frac{\pi}{2}} \sin\left(z\sin\theta\right)\sin\theta d\theta = \mathbf{J}_1(z) \tag{D.9}$$

The next four integrals involve multiplication by double angle sinusoidal and cosinusoidal waveforms. The first integral is constant over all four quarter-cycles.

$$\frac{2}{\pi}\int_0^{\frac{\pi}{2}} \cos\left(z\sin\theta\right)\cos 2\theta d\theta = \mathbf{J}_2(z) \tag{D.10}$$

The next integral averages to zero over the flapping cycle and changes sign consistent with a double angle sine wave.

$$\frac{2}{\pi}\int_0^{\frac{\pi}{2}} \cos\left(z\sin\theta\right)\sin 2\theta d\theta = \frac{4}{\pi}\frac{\left(-1+\cos(z)+z\sin(z)\right)}{z^2} \tag{D.11}$$

The quarter-cycle representation is

$$\frac{2}{\pi}\int_0^{\frac{\pi}{2}} \cos\left(z\sin\theta\right)\sin 2\theta d\theta = \operatorname{sgn}\left(\sin 2\theta\right)\frac{4}{\pi}\frac{\left(-1+\cos(z)+z\sin(z)\right)}{z^2}. \tag{D.12}$$

The next integral changes sign consistent with a sine wave.

$$\frac{2}{\pi}\int_0^{\frac{\pi}{2}} \sin\left(z\sin\theta\right)\sin 2\theta d\theta = \frac{4}{\pi}\frac{\left(-z\cos(z)+\sin(z)\right)}{z^2} \tag{D.13}$$

The quarter-cycle representation is

$$\frac{2}{\pi}\int_0^{\frac{\pi}{2}} \sin\left(z\sin\theta\right)\sin 2\theta d\theta = \operatorname{sgn}\left(\sin\theta\right)\frac{4}{\pi}\frac{\left(-z\cos(z)+\sin(z)\right)}{z^2}. \tag{D.14}$$

The last integral changes sign consistent with a sine wave.

$$\frac{2}{\pi}\int_0^{\frac{\pi}{2}} \sin\left(z\sin\theta\right)\cos 2\theta d\theta = \frac{2}{z}\mathbf{H}_1(z) - \mathbf{H}_0(z) \tag{D.15}$$

The quarter-cycle representation is

$$\frac{2}{\pi}\int_0^{\frac{\pi}{2}} \sin\left(z\sin\theta\right)\cos 2\theta d\theta = \operatorname{sgn}\left(\sin\theta\right)\frac{2}{z}\mathbf{H}_1(z) - \mathbf{H}_0(z). \tag{D.16}$$

An interesting result happens with an integral of the form $\sin(z\sin\theta)\cos^2\theta$. Using the double angle form of $\cos^2\theta$, the integral can be evaluated according to

$$\frac{2}{\pi}\int_0^{\frac{\pi}{2}} \sin(z\sin\theta)\cos^2\theta d\theta = \frac{1}{z}\mathbf{H}_1(z). \tag{D.17}$$

BIBLIOGRAPHY

BIBLIOGRAPHY

[1] R. Dudley. *The Biomechanics of Insect Flight: Form, Function, Evolution*. Princeton University Press, Princeton, NJ, 2000.

[2] C.P. Ellington. The aerodynamics of hovering insect flight i: The quasi-steady analysis. *Philosophical Transactions of the Royal Society of London*, 305(1122):1–15, 1984.

[3] J.M. Wakeling and C.P. Ellington. Dragonfly flight i. gliding flight and steady-state aerodynamic forces. *The Journal of Experimental Biology*, 200:543–556, 1997.

[4] C.P. Ellington. The novel aerodynamics of insect flight: Applications to micro-air vehicles. *The Journal of Experimental Biology*, 202:3439–3448, 1999.

[5] K.M.E. de Clerq, R. de Kat, B. Remes, B.W. van Oudheusden, and H. Bijl. Aerodynamic experiments on delfly ii: unsteady lift enhancement. In *Proceedings of the 2009 European Micro-air Vehicle Conference and Competition 2009, Delft, Netherlands, 14-17 September 2009*, Delft, Netherlands, 2009. TU Delft.

[6] A. Conn, S. Burgess, R. Hyde, and C.S. Ling. From natural flyers to the mechanical realization of a flapping wing micro air vehicle. In *Proceedings of 2006 IEEE International Conference on Robotics and Biomimetics, December 17 - 20, 2006, Kunming, China*, pages 439–444. IEEE, 2006.

[7] M. A. A. Fenelon. Biomimetic flapping wing aerial vehicle. In *Proceedings of the 2008 IEEE International Conference on Robotics and Biomimetics, Bangkok, Thailand, 21-26 February 2009*, pages 1053–1058. IEEE, 2009.

[8] L. Yang, C. Hsu, F. Hsiao, C. Feng, and Y. Shen. A micro-aerial vehicle (mav) with figure-of-eight flapping induced by flexible wing frames. In *Proceedings of the 47th AIAA Aerospaces Science Meeting Including the New Horizons Forum and Aerospace Exposition, 5-8 January 2009*. AIAA, 2009.

[9] Aerovironment. Nano hummingbird. http://www.avinc.com/nano, March 2011.

[10] W. Shyy, Y. Lian, J. Tang, D. Viieru, and H. Liu. *Aerodynamics of Low Reynolds Number Flyers*. Cambridge University Press, New York, NY, 2008.

[11] S. Vogel. *Life in Moving Fluids*. Princeton University Press, Princeton, NJ, 1996.

[12] A. Azuma. *The Biokinetics of Flying and Swimming*. Springer-Verlag, Tokyo, 1992.

[13] H. Tennekes. *The Simple Science of Flight: From Insects to Jumbo Jets*. The MIT Press, Cambridge, MA, 2009.

[14] T. Weis-Fogh. Energetics of hovering flight in hummingbirds and drosophila. *The Journal of Experimental Biology*, 56:79–104, 1972.

[15] T. Weis-Fogh. Quick estimates of flight fitness in hovering animals, including novel mechanisms for lift production. *The Journal of Experimental Biology*, 59:169–230, 1973.

[16] C.P. Ellington. The aerodynamics of hovering insect flight ii: Morphological parameters. *Philosophical Transactions of the Royal Society of London*, 305(1122):17–40, 1984.

[17] C.P. Ellington. The aerodynamics of hovering insect flight iii: Kinematics. *Philosophical Transactions of the Royal Society of London*, 305(1122):41–78, 1984.

[18] C.P. Ellington. The aerodynamics of hovering insect flight iv: Aerodynamic mechanisms. *Philosophical Transactions of the Royal Society of London*, 305(1122):79–113, 1984.

[19] C.P. Ellington. The aerodynamics of hovering insect flight v: A vortex theory. *Philosophical Transactions of the Royal Society of London*, 305(1122):115–144, 1984.

[20] C.P. Ellington. The aerodynamics of hovering insect flight v: Lift and power requirements. *Philosophical Transactions of the Royal Society of London*, 305(1122):145–181, 1984.

[21] A.P. Willmott and C.P. Ellington. The mechanics of flight in the hawkmoth *Manduca sexta* i. kinematics of hovering and forward flight. *The Journal of Experimental Biology*, 200:2705–2722, 1997.

[22] A.P. Willmott and C.P. Ellington. The mechanics of flight in the hawkmoth *Manduca sexta* ii. aerodynamic consequences of kinematic and morphological variation. *The Journal of Experimental Biology*, 200:2723–2745, 1997.

[23] J.M. Wakeling and C.P. Ellington. Dragonfly flight ii. velocities, accelerations, and kinematics of flapping flight. *The Journal of Experimental Biology*, 200:557–582, 1997.

[24] J.M. Wakeling and C.P. Ellington. Dragonfly flight iii. lift and power requirements. *The Journal of Experimental Biology*, 200:583–600, 1997.

[25] R. Dudley and C.P. Ellington. Mechanics of forward flight in bumblebees i. kinematics and morphology. *The Journal of Experimental Biology*, 148:19–52, 1990.

[26] R. Dudley and C.P. Ellington. Mechanics of forward flight in bumblebees ii. quasi-steady lift and power requirements. *The Journal of Experimental Biology*, 148:53–88, 1990.

[27] G. Taylor and A. Thomas. Dynamic flight stability in the desert locus *Schistocerca gregaria*. *The Journal of Experimental Biology*, 206:2803–2829, 2003.

[28] M. Dickinson, F-O. Lehmann, and S. Sane. Wing rotation and the aerodynamic basis of insect flight. *Science*, 284(5422):1954–1960, 1999.

[29] S.P. Sane and M.H. Dickinson. The control of flight force by a flapping wing: Lift and drag production. *The Journal of Experimental Biology*, 204, 2001.

[30] S.P. Sane and M. H. Dickinson. The aerodynamic effects of wing rotation and a revised quasi-steady model of flapping flight. *The Journal of Experimental Biology*, 204, 2002.

[31] W. Shyy, H. Aono, S.K. Chimakurthi, P. Trizilia, C-K. Kang, C.E.S. Cesnik, and H. Liu. Recent progress in flapping wing aerodynamics and aeroelasticity. *Progress in Aerospace Sciences*, 46:284–327, 2010.

[32] S. Sane. Review: The aerodynamics of insect flight. *The Journal of Experimental Biology*, 206:4191–4208, 2003.

[33] Z. J. Wang. Dissecting insect flight. *Annual Review Fluid Mechanics*, 37:183–210, 2005.

[34] S.A. Ansari, R. Zbikowski, and K. Knowles. Aerodynamic modeling of insect-like flapping flight for micro air vehicles. *Progess in Aerospace Sciences*, 42:129–172, 2006.

[35] W. Shyy, Y. Lian, J. Tang, H. Liu, P. Trizila, B. Stanford, L. Bernal, C. Cesnik, P. Friedmann, and P. Ifju. Computational aerodynamics of low reynolds number plunging, pitching and flexible wings for mav applications. *Acta Mechanica Sinica*, 24:351–373, 2008.

[36] G.J. Berman and Z.J. Wang. Energy-minimizing kinematics in hovering insect flight. *Journal of Fluid Mechanics*, 582:153–168, 2007.

[37] M. Sun and G. Du. Lift and power requirements of hovering insect flight. *Acta Mechanica Sinica*, 19:458–469, 2003.

[38] D. Doman, M. Oppenheimer, and D. Sigthorsson. Dynamics and control of a minimally actuated biomimetic vehicle: Part i - aerodynamic model. In *Proceedings of the AIAA Guidance, Navigation, and Control Conference, Chicago, Illinois, USA, August 10-13, 2009*. AIAA, 2009.

[39] X. Deng, L. Schenato, W. Wu, and S. Sastry. Flapping flight for biomimetic robot insects: Part i - system modeling. *IEEE Transactions on Robotics*, 22(4), August 2006.

[40] S.A. Ansari, R. Zbikowski, and K. Knowles. Non-linear unsteady aerodynamic model for insect-like flapping wings in the hover. part 1: methodology and analysis. *Proceedings of the Institution of Mechanical Engineers, Part G: Journal of Aerospace Engineering*, 220(2):61–83, 2006.

[41] S.A. Ansari, R. Zbikowski, and K. Knowles. Non-linear unsteady aerodynamic model for insect-like flapping wings in the hover. part 2: implementation and validation. *Proceedings of the Institution of Mechanical Engineers, Part G: Journal of Aerospace Engineering*, 220(3):169–186, 2006.

[42] P. Trizilia, C-K. Kang, M. Visbal, and W. Shyy. A surrogate model approach in 2d versus 3d flapping wing aerodynamic analysis. In *Proceedings of the 12th AIAA/ISSMO Multidisciplinary Analysis and Optimization Conference, 10-12 September 2008, Victoria, British Columbia, Canada*. AIAA, 2008.

[43] P. Trizila, C-K. Kang, H. Aono, M. Visbal, and W.Shyy. Fluid physics and surrogate modeling of a low reynolds number flapping rigid plate. In *Proceedings of the 28th AIAA Applied Aerodynamics Conference, 28 June - 1 July 2010, Chicago, Illinois*. AIAA, 2010.

[44] D-K. Kim, J-S. Lee, and J-H. Han. Improved aerodynamic model for efficient analysis of flapping-wing flight. *AIAA Journal*, 49(4):868–872, 2011.

[45] C-K. Kang, H. Aono, C.E.S. Cesnik, and W. Shyy. A scaling parameter for the thrust generation of flapping flexible wings. In *Proceedings of the 49th AIAA Aerospace Science Meeting Including the New Horizons Forum and Aerospace Exposition, 4-7 January 2011, Orlando, Florida*. AIAA, 2011.

[46] A. Gogulapit and P. P. Friedmann. Approximate aerodynamic and aeroelastic modeling of flapping wings in hover and forward flight. In *Proceedings of the 52nd AIAA/ASME/AHS/ASC Structures, Structural Dynamics and Materials Conference, 4-7 April 2011, Denver, Colorado*. AIAA, 2011.

[47] S.A. Ansari, K. Knowles, and R. Zbikowski. Insectlike flapping wings in the hover part 1: Effect of wing kinematics. *Journal of Aircraft*, 45(6):1945–1954, 2008.

[48] S.A. Ansari, K. Knowles, and R. Zbikowski. Insectlike flapping wings in the hover part 2: Effects of wing geometry. *Journal of Aircraft*, 45(6):1976–1990, 2008.

[49] Z. Khan and S. Agrawal. Optimal hovering kinematics of flapping wings for micro air vehicles. *Journal of Aircraft*, 49(2):257–268, 2011.

[50] C. Chabalko, D. Snyser, P. Beran, and G. Parker. The physics of an optimized flapping wing micro air vehicle. In *Proceedings of the 47th AIAA Aerospace Science Meeting Including the New Horizons Forum and Aerospace Exposition, 5-8 January 2009, Orlando, Florida*. AIAA, 2009.

[51] B. Etkin and L.D. Reid. *Dynamics of Flight: Stability and Control*. John Wiley & Sons, Inc., New York, NY, 1996.

[52] Z. Khan and S. Agrawal. Modeling and simulation of flapping wing micro air vehicles. In *Proceedings of IDETC/CIE'2005 2005 ASME International Design Engineering Technical Conferences, Long Beach, California, USA, September 24-28, 2005*. American Society of Mechanical Engineers, 2005.

[53] H. Duan and Q. Li. Dynamic model and attitude control of flapping wing micro aerial vehicle. In *Proceedings of the 2009 IEEE International Conference on Robotics and Biomimetics, 19-23 December 2009, Guilin, China*. IEEE, 2009.

[54] M. Lasek and K. Sibilski. Modelling and simulation of flapping wing control for a micromechanical flying insect (entomopter). In *Proceedings of the AIAA Modeling and Simulation Technologies Conference and Exhibit, 5-8 August 2002, Monterrey, California*. AIAA, 2002.

[55] W. Buler, L. Loroch, K. Sibilski, and A. Zyluk. Modeling and simulation of the nonlinear dynamic behavior of a flapping wings micro-aerial-vehicle. In *Proceedings of the 42nd AIAA Aerospace Sciences Meeting and Exhibit, Reno, Nevada, USA, 5-8 November 2004*. American Institute of Aeronautics and Astronautics, 2004.

[56] J. Jackson, R. Bhattacharya, and T. Strganac. Modeling and suboptimal trajectory generation for a symmetric flapping wing vehicle. In *Proceedings of the AIAA Guidance, Navigation, and Control Conference and Exhibit, Honolulu, Hawaii, USA, 18-21 August 2008*. American Institute of Aeronautics and Astronautics, 2008.

[57] J.A. Grauer and J.E. Hubbard. A multibody model of an ornithopter. In *Proceedings of the 47th Aerospace Sciences Meeting Including the New Horizons Forum and Aerospace Exposition, 5-8 January 2009, Orlando, FL*. AIAA, 2009.

[58] J.A. Grauer and J.E. Hubbard. Multibody model of an ornithopter. *AIAA Journal of Guidance, Control and Dynamics*, 32(5):1675–1679, 2009.

[59] J. Grauer, E. Ulrich, J. Hubbard Jr., D. Pines, and J.S. Humbert. Testing and system identification of an ornithopter in longitudinal flight. *Journal of Aircraft*, 48(2):660–667, 2011.

[60] M. A. Bolender. Rigid multi-body equations-of-motion for flapping wing mavs using kane's equations. In *Proceedings of the AIAA Guidance, Navigation, and Control Conference, Chicago, Illinois, USA, August 10-13, 2009*. AIAA, 2009.

[61] G. Gebert, P. Gallmeier, and J. Evers. Equations of motion for flapping flight. In *Proceedings of the AIAA Atmospheric Flight Mechanics Conference, 5-8 August 2002, Monterey, CA, USA*. AIAA, 2002.

[62] M. Sun, J.K. Wang, and Y. Xiong. Dynamic flight stability of hovering insects. *Acta Mechanica Sinica*, 208:447–459, 2007.

[63] W. Dickson, A. Straw, C. Poelma, and M. Dickinson. An integrative model of insect flight control. In *Proceedings of the 44th AIAA Aerospace Sciences Meeting and Exhibit, Reno, Nevada, USA, 9-12 January 2006*. AIAA, 2006.

[64] W. Dickson, A. Straw, and M. Dickinson. Integrative model of *drosophila* flight. *AIAA Journal*, 46(9):2150–2164, 2008.

[65] G. Taylor, R. Bomphrey, and J. Hoen. Insect flight dynamics and control. In *Proceedings of the 44th AIAA Aerospace Sciences Meeting and Exhibit, 9-12 January 2006, Reno, Nevada, USA*. AIAA, 2006.

[66] M. Sun and Y. Xiong. Dynamic flight stability of a hovering bumblebee. *The Journal of Experimental Biology*, 208:447–459, 2005.

[67] Y. Xiong and M. Sun. Dynamic flight stability of a bumblebee in forward flight. *Acta Mechanica Sinica*, 24:25–36, 2008.

[68] J.H. Wu, Y. L. Zhang, and M. Sun. Hovering of model insects: Simulation by coupling equations of motion with navier-stokes equations. *The Journal of Experimental Biology*, 212:3313–3329, 2009.

[69] Y-L. Zhang and M. Sun. Dynamic flight stability of hovering model insects: theory versus simulation using equations of motion coupled with navier-stokes equations. *Acta Mechanica Sinica*, 26:509–520, 2010.

[70] I. Faruque and J. Humbert. Dipteran insect flight dynamics. part 1: longitudinal motion about hover. *Journal of Theoretical Biology*, 264:538–552, 2010.

[71] N. Gao, H. Aono, and H. Liu. A numerical analysis of dynamic flight stability of hawkmoth hovering. *Journal of Biomechanical Science and Engineering*, 4(1):105–116, 2009.

[72] I. Faruque and J. Humbert. Dipteran insect flight dynamics. part 2: lateral-directional motion about hover. *Journal of Theoretical Biology*, 265:306–313, 2010.

[73] Y-L. Zhang and M. Sun. Dynamic flight stability of a hovering model insect: lateral motion. *Acta Mechanica Sinica*, 26:175–190, 2010.

[74] T. L. Hedrick, B. Cheng, and X. Deng. Wingbeat time and the scaling of passive rotational damping in flapping flight. *Science*, 324:252–255, 2009.

[75] M. A. Bolender. Open-loop stability of flapping flight in hover. In *Proceedings of the AIAA Guidance, Navigation, and Control Conference, 2-5 August 2010, Toronto, Ontario, Canada*. AIAA, 2010.

[76] J.M. Dietl and E. Garcia. Ornithopter flight stabilization. In *Proceedings of Active and Passive Smart Structures and Integrated Systems 2007, 19 March 2007, San Diego, California, USA*, volume 6525. The International Society of Optical Engineering, 2007.

[77] J.M. Dietl and E. Garcia. Stability in hovering ornithopter flight. In *Proceedings of Industrial and Commercial Applications of Smart Structure Technologies 2008, 10 March 2008, San Diego, California, USA*, volume 6930. SPIE, 2008.

[78] J.M. Dietl and E. Garcia. Stability in ornithopter longitudinal dynamics. *Journal of Guidance, Control, and Dynamics*, 31(4):1157–1162, July-August 2008.

[79] M. Oppenheimer, D. Doman, and D. Sigthorsson. Dynamics and control of a minimally actuated biomimetic vehicle: Part ii - control. In *Proceedings of the AIAA Guidance, Navigation, and Control Conference, Chicago, Illinois, USA, August 10-13, 2009*. AIAA, 2009.

[80] R.J. Wood. The first takeoff of a biologically inspired at-scale robotic insect. *IEEE Transactions on Robotics*, 24(2):341–347, 2007.

[81] D. Doman, M. Oppenheimer, and D. Sigthorsson. Wingbeat shape modulation for flapping-wing micro-air-vehicle control during hover. *Journal of Guidance, Control, and Dynamics*, 33(3):724–739, 2010.

[82] M. Oppenheimer, D. Doman, and D. Sigthorsson. Dynamics and control of a biomimetic vehicle using biased wingbeat forcing functions: Part i - aerodynamic model. In *Proceedings of the 48th AIAA Aerospace Sciences Meeting Including the New Horizons Forum and Exposition, Orlando, Florida, USA, January 4-7, 2010*. AIAA, 2010.

[83] D. Doman and M. Oppenheimer D. Sigthorsson. Dynamics and control of a biomimetic vehicle using biased wingbeat forcing functions: Part ii - control. In *Proceedings of the 48th AIAA Aerospace Sciences Meeting Including the New Horizons Forum and Exposition, Orlando, Florida, USA, January 4-7, 2010*. AIAA, 2010.

[84] M. Oppenheimer, D. Doman, and D. Sightorsson. Dynamics and control of a biomimetic vehicle using biased wingbeat forcing functions. *Journal of Guidance, Control, and Dynamics*, 34(1):204–217, 2011.

[85] A. Serrani. Robust hovering control of a single-dof flapping mav. In *Proceedings of the 2010 American Control Conference, 30 June - 02 July 2010, Baltimore, MD*, pages 1302–1307. IEEE, 2010.

[86] A. Serrani. Robust control of a 3-dof flapping wing micro air vehicle. In *Proceedings of the AIAA Guidance, Navigation, and Control Conference, 2-5 August 2010, Toronto, Ontario, Canada*. AIAA, 2010.

[87] X. Deng, L. Schenato, and S. Sastry. Hovering flight control of a micromechanical flying insect. In *Proceedings of the 40th IEEE Conference on Decision and Control, Orlando, Florida, USA, December 2001*. IEEE, 2001.

[88] L. Schenato, D. Campolo, and S. Sastry. Controllability issues in flapping flight for biomimetic micro air vehicles (mavs). In *Proceedings of the 42nd IEEE Conference on Decision and Control, Maui, Hawaii USA, December 2003*. IEEE, 2003.

[89] X. Deng, L. Schenato, and S. Sastry. Flapping flight for biomimetic robot insects: Part ii - flight control design. *IEEE Transactions on Robotics*, 22(4), August 2006.

[90] M. Hu, R. Wei, W. Zhou, and X. Cui. Control of insect-like flapping wing micro air vehicles i: Control mechanic. In *Proceedings of the 26th Chinese Control Conference, 26-31 July 2007, Zhangjiajie, Hunan, China*. IEEE, 2007.

[91] M. Hu, R. Wei, Z. Dong, and X. Cui. Control of insect-like flapping wing micro air vehicles ii: Control parameter. In *Proceedings of the 26th Chinese Control Conference, 26-31 July 2007, Zhangjiajie, Hunan, China*. IEEE, 2007.

[92] M. Hu, R. Wei, T. Dai, L. Zou, and T. Li. Control strategy for insect-like flapping wing micro air vehicles: Attitude control. In *Proceedings of the 7th World Congress on Intelligent Control and Automation, 25-27 June 2008, Chongqing, China*. IEEE, 2008.

[93] M. Hu, R. Wei, Z. Shi, and L. Zou. Controllability issues for insect like flapping wing micro-air vehicle. In *Proceedings of the 7th World Congress on Intelligent Control and Automation, 25-27 June 2008, Chongqing, China*. IEEE, 2008.

[94] M. Sun and J.K. Wang. Flight stabilization control of a hovering model insect. *The Journal of Experimental Biology*, 210:2714–2722, 2007.

[95] Y. Xiong and M. Sun. Stabilization control of a bumblebee in hovering and forward flight. *Acta Mechanica Sinica*, 25:13–21, 2009.

[96] J. Wu and M. Sun. Control for going from hovering to small speed flight of a model insect. *Acta Mechanica Sinica*, 25:295–302, 2009.

[97] B. Cheng and X. Deng. Near-hover dynamics and attitude stabilization of an insect model. In *Proceedings of the 2010 American Control Conference, 30 June - 02 July 2010, Baltimore, MD*, pages 39–44. IEEE, 2010.

[98] H. Rifaï, N. Marchand, and G. Poulin. Bounded control of a flapping wing micro drone in three dimensions. In *Proceedings of the 2008 IEEE International Conference on Robotics and Automation, 19-23 May 2008, Pasadena, California*. IEEE, 2008.

[99] J. Humbert and I. Faruque. Analysis of insect-inspired wingstroke kinematic perturbations for longitudinal control. *Journal of Guidance, Control, and Dynamics*, 34(2):618–622, 2011.

[100] J. Geder, R. Ramamurti, W. Sandberg, and A. Flynn. Modeling and control design for a flapping-wing nano air vehicle. In *Proceedings of the AIAA Guidance, Navigation, and Control Conference, 2-5 August 2010, Toronto, Ontario, Canada*. AIAA, 2010.

[101] Q. Guo, M. Hu, R. Wei, J. Xu, and H. Song. Hovering control based on fuzzy neural networks for biomimetic flying robotic. In *Proceedings of the 2008 IEEE International Conference on Information and Automation, 20-23 June 2008, Zhangjiajie, China*. IEEE, 2008.

[102] S-J. Chung and M. Dorothy. Neurobiologically inspired control of engineered flapping flight. *Journal of Guidance, Control, and Dynamics*, 33(2):440–453, 2010.

[103] S. Boddhu and J. Gallagher. Evolving non-autonomous neuromorphic flight control for a flapping-wing mechanical insect. In *Proceedings of the IEEE Workshop on Evolvable and Adaptive Hardware, 2009, 30 April - 02 May 2009, Nashville, TN*, pages 9–16. IEEE, 2009.

[104] K. H. Loh and M. V. Cook. Flight dynamic modelling and control design for a flapping wing micro aerial vehicle at hover. In *Proceedings of the AIAA Atmospheric Flight Mechanics Conference and Exhibit, 11-14 August 2003, Austin, Texas*. AIAA, 2003.

[105] D. T. Greenwood. *Advanced Dynamics*. Cambridge University Press, Cambridge, UK, 2006.

[106] D. T. Greenwood. *Principles of Dynamics*. Prentice Hall, Upper Saddle River, NJ, 1988.

[107] H Baruh. *Analytical Dynamics*. WCB McGraw-Hill, Boston, MA, 2006.

[108] C. Orlowski, A. Girard, and W. Shyy. Derivation and simulation of the nonlinear dynamics of a flapping wing micro-air vehicle. In *Proceedings of the 2009 European Micro-air Vehicle Conference and Competition 2009, Delft, Netherlands, 14-17 September 2009*, Delft, Netherlands, 2009. TU Delft.

[109] C. Orlowski, A. Girard, and W. Shyy. Open loop pitch control of a flapping wing micro-air vehicle using a tail and control mass. In *Proceedings of the*

2010 American Control Conference, Baltimore, Maryland, USA, 30 June - 02 July 2010, pages 536–541, Washington, DC, 2010. Institute of Electrical and Electronics Engineers.

[110] C. Orlowski, A. Girard, and W. Shyy. Four wing flapping wing micro air vehicles - dragonflies or xwings? In *Proceedings of the 2010 AIAA Guidance, Navigation, and Control Conference, Toronto, Ontario, Canada, 2-5 August 2010*. AIAA, 2010.

[111] C. Orlowski and A. Girard. Modeling and simulation of nonlinear dynamics of flapping wing micro air vehicles. *AIAA Journal*, 49(5):969–981, 2011.

[112] T.L. Hedrick and T.L. Daniel. Flight control in the hawkmoth *Manducta sexta*: the inverse problem of hovering. *The Journal of Experimental Biology*, 206:3114–3130, 2006.

[113] J. Underwood and C.P. Ellington. The aerodynamics of revolving wings i. model hawkmoth wings. *The Journal of Experimental Biology*, 205:1547–1564, 2002.

[114] J. Underwood and C.P. Ellington. The aerodynamics of revolving wings ii. propeller force coefficients from mayfly to quail. *The Journal of Experimental Biology*, 205:1565–1576, 2002.

[115] N. M. Krylov and N.N. Bogoliubov. *Introduction to Non-linear Mechanics*. Princeton University Press, Princeton, NJ, 1947.

[116] N.N. Bogoliubov and Y. A. Mitropolsky. *Asymptotic Methods in the Theory of Non-linear Oscillations*. Gordon and Beach Science Publishers, New York, NY, 1961.

[117] J.A. Sanders, F. Verhulst, and J. Murdock. *Averaging Methods in Nonlinear Dynamical Systems Second Edition*. Springer Science, 2007.

[118] A. Gelb and W. Vander Velde. *Multiple-Input Describing Functions and Nonlinear System Design*. McGraw Hill, New York, NY, 1968.

[119] Z. Vukic, L. Kuljaca, D. Donlagic, and S. Tesnjak. *Nonlinear Control Systems*. Marcel Dekker, Inc., New York, NY, 2003.

[120] J-J. Slotine and W. Li. *Applied Nonlinear Control*. Prentice Hall, Upper Saddle River, NJ, 1991.

[121] H. Khalil. *Nonlinear Systems*. Prentice Hall, Upper Saddle River, NJ, 2002.

[122] M. Van Dyke. *Perturbation Methods in Fluid Mechanics*. The Parabolic Press, Stanford, CA, 1975.

[123] P. Kokotovic, H. Khalil, and J. O'Reilly. *Singular Perturbation Methods in Control: Analysis and Design*. Academic Press, London, 1986.

[124] W. Gröbner and N. Hofreiter. *Integraltafel*. Springer-Verlag, Vienna, Austria, 1949.

[125] N. W. McLachlan. *Bessel Functions for Engineers Second Edition*. Oxford University Press, Glasgow, Britain, 1955.

[126] I.S. Gradshteyn and I.M. Ryzhik. *Table of Integrals, Series, and Products $Fifth\,Edition$*. Academic Press, Limited, San Diego, CA, 1994.

[127] J. Franklin. *Dynamics, Control, and Flying Qualities of V/STOL Aircraft*. American Institute of Aeronautics and Astronautics, Reston, VA, 2002.

[128] C. Orlowski and A. Girard. Stability derivatives for a flapping wing mav in a hover condition using local averaging. In *Proceedings of the 2011 American Control Conference, 29 June - 01 July 2011, San Francisco, CA, USA*. IEEE, 2011.

[129] C-T. Chen. *Linear Systems Theory*. Oxford University Press, New York, NY, 1999.

[130] C.H. Greenewalt. Dimensional relationships for flying animals. *Smithsonian Miscellaneous Collections*, 144(2):1–46, 1962.

[131] D. Byrne, S. Buchmann, and H. Spangler. Relationship between wing loading, wingbeat frequency, and body mass in homopterous insects. *The Journal of Experimental Biology*, 135:9–23, 1988.

[132] H. Corben. Wing-beat frequencies, wing-areas and masses of flying insects and hummingbirds. *The Journal of Theoretical Biology*, 102:611–632, 1983.

[133] C-A. Darveau, P. Hochachka, Jr. K. Welch, D. Roubik, and R. Suarez. Allometric scaling of flight energetics in panamanian orchid bees: a comparative phylogenetic approach. *The Journal of Experimental Biology*, 208:3581–3591, 2005.

[134] M. Deakin. The physics and physiology of insect flight. *American Journal of Physics*, 38(8):1003–1005, 1970.

[135] M. Deakin. Formulae for insect wingbeat frequency. *Journal of Insect Science*, 10(96):1–9, 2010.

[136] T. Weis-Fogh. Dimensional analysis of hovering flight. *Scale Effects in Animal Locomotion*, 1977.

[137] R.J. Templin. The spectrum of animal flight: insects to pterosaurs. *Progress in Aerospace Sciences*, 36:393–436, 2000.

[138] W. Shyy, M. Berg, and D. Ljungqvist. Flapping and flexible wings for biological micro air vehicles. *Progress in Aerospace Sciences*, 35:455–505, 1999.

[139] J. McMasters. Reflections of a paleoaerodynamicist. *Perspectives in Biology and Medicine*, 29(3):331–384, 1986.

[140] Wikipedia. Drosophila. http://en.wikipedia.org/wiki/Drosophila, April 2011.

[141] Wikipedia. Tipula. http://en.wikipedia.org/wiki/Tipula, April 2011.

[142] Wikipedia. Diptera. http://en.wikipedia.org/wiki/Diptera, April 2011.

[143] Wikipedia. Coleoptera. http://en.wikipedia.org/wiki/Coleoptera, April 2011.

[144] Wikipedia. Hymenoptera. http://en.wikipedia.org/wiki/Hymenoptera, April 2011.

[145] Wikipedia. Sphingidae. http://en.wikipedia.org/wiki/Sphingidae, April 2011.

[146] Wikipedia. Odonata. http://en.wikipedia.org/wiki/Odonata, April 2011.

[147] Wikipedia. Butterfly. http://en.wikipedia.org/wiki/Butterfly, April 2011.

[148] Wikipedia. Differences between butterflies and moths. http://en.wikipedia.org/wiki/Differences_between_butterflies_and_moths, April 2011.

[149] Wikipedia. Bombycidae. http://en.wikipedia.org/wiki/Bombycidae, April 2011.

[150] S.A. Wainwright, W.D. Biggs, J.D. Currey, and J.M. Gosline. *Mechanical Design of Organisms*. Princeton University Press, Princeton, NJ, 1982.

[151] S.A. Combes and T.L. Daniel. Flexural stiffness in insect wings i. scaling and wing venation. *The Journal of Experimental Biology*, 206:2979–2987, 2003.